DOCTOR OF PHILOSOPHY

Thermodynamically consistent modelling and computational methods for multiphase flows

Guo, Zhenlin

Award date:
2014

Thermodynamically consistent modelling and computational methods for multiphase flows

By

Zhenlin Guo

A Thesis submitted for the degree of Doctor of Philosophy

Division of Mathematics

University of Dundee

Dundee

Date: 19/Sep/2014

Contents

List of Figures

Acknowledgements

I would first and foremost like to thank Professor Ping Lin for giving me the opportunity to work with him. I am very grateful for all his supervision, input into my work and support. I am also grateful for his generosity and good humour. Due to his excellent supervision, my PhD was completed very smoothly and I thoroughly enjoyed the path to completion.

I am grateful to my family for the encouragement and support they have given me during my studies. I would also like to thank Mrs Yuchun Ji for providing the warm care and help whenever I need it.

I would also like to thank Prof. John Lowengrub for the helpful and patient discussions concerning various aspects of the multiphase flows modelling. These discussions were of great importance in the development of my understanding of these issues. I would like to thank my collaborators Mr. Yongyue Jiang for some discussions on the designing of numerical methods.

I would like to extend my gratitude and appreciation to all the members of staff of the Division of Mathematics, in particular Mr Nick Dawes for providing me with many software packages and Mrs Shirley Fox for helping me with lots of paper work along

the way. I would also like to thank Dr Mariya Ptashnyk for numerous helpful discussions with regards to numerical analysis.

I would also like to pay special thanks to my fellow PhD students and the postdoctoral researchers here in Dundee (past and present). In particular, I would like to mention the names of Niall Deakin, Dr. Simon Candelaresi, Jialing Chen, and Elaine Mitchell, Dr. Yujing Yang, Dr. Gibin Powathil. It was delightful to have your company during my studies.

I would also like to thank to my friends all around the world to spend some time with me and to give me so much pleasent distractions, which are really helpful and warm. I would like to mention the names of Ji Qi, Shuo Cai, Meng Zhang, Lei Mu, Hanchu Yin, Kangning Wang, Huicong Ding, Biao Wang, Chunrui Li, Dong Zhang, Qing Cao and Nannan Wang.

Last, but not least, I would like gratefully acknowledge the support of the China Scholarship Council (CSC) Grant No.2011646021 for supporting my studies in the University of Dundee.

Abstract

This thesis presents the research of my PhD, which is the study of two-phase flows by using the phase-field methods. The key point for this work is the thermodynamic consistency. We begin by introducing an extension of the Model H to study the two-phase flows with thermocapilliary effects, where we assume that the coefficient of the surface tension is temperature dependent, and the classical energy equation is coupled with the Model H. We then investigate numerically an established phase-field model (Quasi-incompressible NSCH model) for the two-phase flows with varible density. We design a numerical method where the energy law of the model is preserved at the discrete level. Fianlly we develop a new model to study the two-phase flows with thermocapilliary effects where the model allows the two fluids to have different physical properties meanwhile maintaining the thermodynamic consistency. The pillbox argument is employed to show that our model can reduce to the sharp-interface model where the jump conditions can be recovered.

Chapter 1

Introduction

Multiphase flows play an increasingly important role in many current scientific and engineering applications. In recent years, there have been both extensive theoretical and experimental studies, yet the area remains an active interdisciplinary research field. Improved numerical algorithms have resulted in direct numerical simulations of multiphase phenomena leading to improvement in predicting the behaviour of multiphase flows. The available numerical methods for multiphase flows can roughly be divided into two categories: interface tracking and interface capturing methods. In interface tracking methods, the position of the interface is explicitly tracked, which requires meshes that track the interfaces and are updated as the flow evolves. Boundary integral methods (see the review [64]), front-tracking methods (see the review [118, 67]), and immersed boundary methods (see the review [91]) are examples of this type. In the context of the multiphase flow with thermocapillary (Marangoni) effects, e.g., the thermocapillary migration and thermocapillary instabilities, several works have been performed by using interface tracking methods. Here we refer [136, 20, 102] as examples for boundary-integral methods, [115, 94, 93, 128] for front-tracking methods, and [99, 23] for immersed-boundary methods. In interface capturing methods, on the other

hand, the interface is not tracked explicitly, but instead is implicitly defined through an interface function (e.g. level-set, color or phase-field function). This means that the computations are based on fixed spatial domains and thus eliminate the problem of updating the meshes encountered in interface tracking methods. For example, volume-of-fluid (VOF) methods (see [104] for the review, and see [44, 88] as examples for thermocapillary effects), level-set methods (see [95, 108] for the review, and see [58, 62] as examples for thermocapillary effects) are of this type.

Another interface capturing method is the phase-field method, or diffuse-interface method (see the review [8, 40, 75]), which has now emerged as a powerful method to simulate many types of multiphase flows, including drop coalescence, break-up, rising and deformations in shear flows [68, 78, 79, 26, 85, 15, 130, 77, 131, 35, 109, 65, 54], phase separation [15, 76, 74], contact line dynamics [69, 59, 45, 16, 71], and dynamics of interface with surfactants adsorption [120, 116] and thermocapillary effects [70, 24, 25, 113, 55, 53]. Phase-field methods are based on models of fluid free energy which goes back to the work of van der Waals [121], Gibbs [46] and Cahn *et. al*. [28, 27]. The basic idea for phase-field method is to treat the multiphase fluid as one fluid with variable material properties. An order parameter is employed to characterize the different phases, which varies continuously over thin interfacial layers and is mostly uniform in the bulk phases. Sharp interfaces are then replaced by the thin but non-zero thickness transition regions where the interfacial forces are smoothly distributed. A set of governing equations of the fluid flows of the whole computational domain can be derived variationally from its energy density field, where the order parameter fields satisfy an advection-diffusion equation (usually the advective Cahn-Hilliard equations) and are coupled to the Navier-Stokes equations through extra reactive stresses that mimic surface tension.

The classical phase-field model, in the case of two incompressible, viscous Newtonian fluids, is the so-called Model H [63], which couples fluid flow with Cahn-Hilliard

diffusion through a conserved parameter. It has been successfully used to simulate complicated mixing flows involving a binary incompressible fluid with the same densities for both components (see [29] for example). Gurtin *et al*. [56] re-derived this model in the framework of classical continuum mechanics and showed that it is consistent with the second law of thermodynamics in a mechanical version based on a local dissipation inequality.

One of the fundamental assumptions when deriving Model H is that the binary fluid is incompressible, more precisely, its total density as well as the densities for each component are constant. Therefore this model is restricted to the density matched case and cannot be used for the case if the two incompressible fluids have different densities. To treat the problems with small density ratios, a Boussinesq approximation is often used, where the small density difference is neglected except in the gravitational force. The achieved model maintains thermodynamic consistency (see [65] as an example). This approach however is no longer valid when the density ratio is not small. Several generalizations of Model H for the case of different densities have been presented and discussed by Lowengrub and Truskinovsky [87], Boyer [26], Ding *et al*. [35], Shen and Yang [110], and most recently by Abels *et al*. [2]. Benchmark computations for three of them, namely the models of Boyer [26], Ding *et al*. [35], and Abels *et al*. [2], were carried out by Aland and Voigt [5]. Thermodynamic consistency however could only be shown for the models proposed in [2, 87]. Antanovskii [12] derived a quasi-incompressible phase-field model for two-phase flow with different densities. The extended model was presented by Lowengrub and Truskinovsky [87], where they employed the pressure rather than density as an independent variable and worked with a Gibbs free energy. In their model, the two fluids of different densities are assumed to be mixed and compressible along the interfacial region (introducing the

quasi-incompressibility into the model). The flow in the interfacial region is in general nonsolenoidal ($\nabla \cdot \mathbf{v} \neq 0$), resulting in an expansion or contraction flow. Thermodynamic consistency is maintained within the resulting system (quasi-incompressible NSCH) where the Navier-Stokes equations are coupled with the Cahn-Hilliard equations, and the kinetic fluid pressure and variable density are introduced into the chemical potential. Very recently, a numerical method for the quasi-incompressible NSCH system with a discrete thermodynamic law (energy law) was presented by Guo *et. al.* [54], where the quasi-incompressibility (the non-solenoidal velocity) near interfaces was captured. Namely, the numerical results reveal that away from interfaces the fluid is incompressible, while near interfaces waves of expansion and contraction are observed (See chapter 4 for details).

Another assumption for Model H is that the fluid flow is isothermal. However, for the case that considers thermocapillary (Marangoni) effects, the surface tension gradient is produced by the inhomogeneous distribution of the temperature, so that the system can't be assumed to be isothermal and the transport of temperature field can't be ignored. The extension of Model H to the non-isothermal case was presented by Jasnow and Vinals [70], where, to study the thermocapillary migration of droplets, a constant, externally imposed temperature gradient is considered. Several other works, as mentioned above, have also been devoted to the use of the phase-field method to simulate the dynamics of interface with thermocapillary effects [24, 25, 113, 55]. For most of these models, the system equations of flow field (the Navier-Stokes equations with extra stress) and phase-field (the advective Cahn-Hilliard equations) are usually derived from the free energy functional that depends on temperature. The energy equations, however, were not derived together with the system equations. Instead, the classical energy transport equations are incorporated into the system directly, or the temperature fields are assumed to be fixed so that the energy equations are not needed. In these treatments, thermodynamic consistency can be hardly achieved. It turns out that

the concept of thermodynamic consistency plays an important role for the phase-field modeling. As the phase-field model can be derived through variational procedures, thermodynamic consistency of the model equations can serve as a justification for the model. In addition, it ensures the model to be compatible with the laws of thermodynamics, and to have a strict relaxational behaviour of the free energy, hence the models are more than a phenomenological description of an interfacial problem. In [12], Antanovskii presented a phase-field model to study the thermocapillary flow in a gap, where to obtain a free energy that depends on the temperature, the Cahn-Hilliard gradient term associated with the phase-field is introduced into the entropy functional of the system, which leads to a corresponding extra term appearing in the energy equation. The resulting system of equations were derived together through the local balance laws and thermodynamic relations, which maintains thermodynamic consistency. A similar gradient entropy term was considered by Anderson and McFadden [7] to study a single compressible fluid with different phases near its critical point. In their work, the phase-field model was derived through a thermodynamic formalism [107] based on entropy generation. Through a similar thermodynamic framework, Verschueren *et al*. [122] presented a phase-field model for two-phase flow with thermocapillary effects in a Hele-Shaw cell. The system equations maintains thermodynamic consistency, in which the energy equation contains an extra term associated with the variations of the phase field. In [53], Guo *et al*. developed a new phase-field model for two-phase flows with thermocapillary effects, where the model equations are derived through the theromdynamic framework based on the entropy generation that guarantees thermodynamic consistency. (See chapter 5 for details).

Several numerical methods have been used to solve the phase-field model including spectral methods ([30, 36, 79, 85, 110, 127]), adaptive moving mesh methods ([89, 18, 133, 134]), finite element methods and adaptive finite element methods ([31, 37, 42, 48, 65, 131, 132]) and finite difference methods ([32, 76, 77]), and we refer

to [43] and references therein for some recent discussions on adaptive methods for the long time simulation of the Cahn-Hilliard equation. In particular, the phase-field model can be derived from an energy variational approach. With thermodynamic consistency, an energy law is naturally associated with the well-posed nonlinearly coupled system. Note that the energy law can be preserved in the fully discretized system. It is highly desirable to have a numerical scheme that preserves the accurate energy law at the discrete level, in order to ensure the stability of the numerical algorithm and the accuracy of the solution, especially when a rapid change or a singularity occurs in the solution, such as occurs in non-Newtonian hydrodynamic systems ([83, 84]). When the underlining energy law is preserved in the fully discretized system, it is also possible to use a relatively coarse mesh in the simulation. Consequently such a method can reduce the cost of computations while resolving the prominent features of the flow. Recently, Hua *et al*. [65] introduced a C^0 finite elements formulation for a phase-field model in which the energy law of the system was well preserved at the discrete level. They obtained more accurate results for interface motion on coarser grids than another scheme that does not obey the energy law at the discrete level.

In this thesis, we will focus on two aspects of the generalizations of the classical phase-field model for two-phase flows (Model H). One is the variable density flows where the two fluids are assumed to have different densities. The other one is the two-phase flows with thermocapillary effects. In chapter 2, we present background for phase-field modelling, thermocapillary effects and continuum mechanics. In chapter 3, we develop a phase-field model for two-phase flows with thermocapillary effects by using an energetic variational procedure, where the two fluids are assumed to have the same densities. Through the examples of thermocapillary convection in the two-layer fluid system, we show that our phase-field model can reflect the mechanism of the threom-capillary convection appropriately. In chapter 4, we present a numerical method for

an established model for two-phase flows with variable density (quasi-incompressible NSCH model by Lowengrub & Truskinovsky [87]). We first show that the energy law (thermodynamic consistency) can be derived from the model equations. Under the weak formulation, we design a C^0 finite element method and a special temporal scheme where the energy law is preserved at the discrete level. Such a discrete energy law (almost the same as the continuous energy law) for this variable density two-phase flow model has never been established before with C^0 finite elements. Some numerical experiments are carried out using the adaptive mesh to investigate the scenario of coalescing and rising drops with differing density ratio. The snapshots for the evolution of the interface together with the adaptive mesh at different times are presented to show that the evolution, including the break-up/pinch-off of the drop, can be handled smoothly by our numerical scheme. In chapter 5, we develop a thermodynamically consistent phase-field model for two-phase flows with thermocapillary effects, which allows for the binary incompressible fluid (quasi-incompressible fluid) to have different densities, viscousities and thermal conductivities for each component. This model can be seen as a non-isothermal extension of the quasi-incmopressible NSCH model (Lowengrub & Truskinovsky [87]). The model equations, including the Navier-Stokes equation with extra stress, an advective Cahn-Hilliard equation and energy equation are derived under a thermodynamic framework (Anderson and McFadden [7]). To the best of our knowledge, such a thermodynamically consistent phase-field model for binary incompressible fluid with thermocapillary effects, which allows for different physical properties of each component is new. To validate our model, we first show that thermodynamic consistency are maintained in both models. We also show that our model equations satisfy the Galilean invariance and the Onsager's reciprocal relations. We then analyze the model in the sharp-interface limit to show that the governing equations and interfacial conditions of the classical sharp-interface model can be recovered from our phase-field models, which reveals the underlying physical mechanisms of

phase-field model. To validate our model, we also compute two examples, including thermcapillary convection in a two-layer fluid system and thermocapillary migration of a bubble in a medium fluid. The numerical results for both examples are consistent with the corresponding analytical solutions [98] or theoretical predictions [129]. Moreover, another example is computed to study the effects of the Marangoni number. Finally, concluding remarks and discussion about future work are given in chapter 6.

Chapter 2

Background

2.1 Phase-field methods

2.1.1 Surface energy and Cahn-Hilliard equations

In phase-field models, the interface is represented as a thin layer of finite thickness and an auxiliary phase-field function is used to indicate the phases. The phase-field function varies smoothly between distinct values in both phases and the interface can be associated with an intermediate level set of the phase-field function. Phase fields can be constructed by physical arguments if one has an expression for the free energy of the system. A typical choice for the energy associated to a fluid-fluid interface is the Cahn-Hilliard free energy given by:

$$E_s = \int_\Omega \frac{1}{\varepsilon} F(\phi) + \frac{\varepsilon}{2} |\nabla \phi|^2. \tag{2.1}$$

Here Ω is the computational domain, ϕ is the phase field (mass or volume concentration of one phase, or the concentration differences between the two phases), ε is related

to the thickness of the diffuse interface, $F(\phi) = \phi^2(\phi^2 - 1)/4$ is the double well potential having local minima in those values of ϕ which represent the bulk phases. The second term in (2.1) is the squared gradient energy that was introduced by Cahn & Hilliard [28, 27] to describe the process of phase separation.

In a system described by Eq.(2.1), thermodynamic equilibrium can be characterized by a state of the phase variable ϕ that minimizes the Cahn-Hilliard free energy. This requires the variational derivative of E_s to vanish, such that

$$\frac{\delta E_s}{\delta \phi} = \frac{1}{\varepsilon}\frac{\partial F(\phi)}{\partial \phi} - \varepsilon\Delta\phi = 0. \tag{2.2}$$

Here we define the chemical potential by

$$\mu = \frac{\delta E_s}{\delta \phi} = \frac{1}{\varepsilon}\frac{\partial F(\phi)}{\partial \phi} - \varepsilon\Delta\phi. \tag{2.3}$$

Since ϕ represents a concentration or the concentration difference, it must satisfy the conservation law

$$\frac{\partial \phi}{\partial t} = -\nabla \cdot J, \tag{2.4}$$

where the flux term J can be defined through Fick's law

$$J = M\nabla\mu, \tag{2.5}$$

and M is a constant standing for the mobility of the diffuse interface. Combing Eqs.(2.3), (2.4) and (2.5) gives the Cahn-Hilliard equation

$$\frac{\partial \phi}{\partial t} = -\nabla \cdot \left(M\nabla(\frac{1}{\varepsilon}\frac{\partial F(\phi)}{\partial \phi} - \varepsilon\Delta\phi) \right). \tag{2.6}$$

In the 1D case, we assume the boundary conditions

$$\phi(-a) = 0, \quad \phi(b) = 1. \tag{2.7}$$

where a and b are the boundary of this 1D problem. The solution at equilibrium for Eq.(2.2) with respect to (2.7) can then be given as

$$\phi = \frac{1}{2}\tanh\left(\frac{x}{2\sqrt{2}\varepsilon}\right) + \frac{1}{2},$$

where we can see that the interface thickness really depends on how we define it, e.g., it could be the width of the set $\{x|\phi(x) \in [0:2;0:8]\}$ or the set $\{x|\phi(x) \in [0:05;0:95]\}$. For $\phi(x)$ between these two ranges the thickness of interface would be $4-10$ times of the value. Therefore ε is a small parameter related to the interface thickness.

2.1.2 Phase-field model for two-phase flows

In the context of the binary fluid flows, the Navier-Stokes equation is typically coupled with the advective Cahn-Hilliard equation, where an extra stress tensor appears in NS equation to mimic the surface tension. The classical phase-field model, in the case of two incompressible, viscous Newtonian fluids, is the so-called Model H [63]. In the case of constant physical properties (density, viscosity and surface tension), the model

reads:

$$\partial_t \mathbf{u} + (\mathbf{u}\cdot\nabla\mathbf{u}) + \nabla p - \mu\nabla\cdot D(\mathbf{u}) + \tilde{\sigma}\varepsilon\nabla\cdot(\nabla\phi\otimes\nabla\phi) = g(x), \tag{2.8}$$

$$\nabla\cdot\mathbf{u} = 0, \tag{2.9}$$

$$\partial_t\phi + \mathbf{u}\cdot\nabla\phi = -\nabla\cdot(M\nabla\mu), \tag{2.10}$$

$$\mu = \tilde{\sigma}\varepsilon^{-1}F(\phi) - \tilde{\sigma}\varepsilon\Delta\phi, \tag{2.11}$$

with the boundary conditions may be posed at $\partial\Omega$

$$\mathbf{u} = 0, \quad \text{no slip}, \tag{2.12}$$

$$\mathbf{n}\cdot\nabla c = 0,\ \mathbf{n}\cdot\nabla\mu = 0,\ \text{no flux}, \tag{2.13}$$

in the domain Ω. $\mathbf{n}\cdot\nabla\mu = 0$ is the no flux boundary condition for μ. Here $\mathbf{u}$, p, ϕ and μ are the velocity, pressure, phase-field variable and chemical potential, respectively. The function $F(\phi) = \phi^2(\phi^2-1)/4$ is the double well potential energy, such that $\phi \approx 1$ in Ω_1 and $\phi \approx 0$ in Ω_2, M is a constant standing for the mobility of the diffuse interface, μ is the viscosity and g is the body force. The parameter ε is related to the thickness of the diffuse interface, $\tilde{\sigma}$ is the surface tension which is related to the physical surface tension σ through a ratio parameter η, such that $\sigma = \eta\tilde{\sigma}$ (See section 5.6.6 for details).

2.2 Thermocapillary effects

When the interface separating two fluids is exposed to a temperature gradient, the variations of surface tension along the interface leads to shear stresses that act on the fluid through viscous forces, and thus induce a motion of the fluids in the direction of the temperature gradient. For most of the fluids, the surface tension generally decreases

with the increasing temperature, and is normally a linear decreasing function of temperature, such that

$$\sigma(T) = \sigma_0 - \sigma_T(T - T_0), \tag{2.14}$$

where σ_0 is the interfacial tension at the reference temperature T_0, σ_T is the rate of change of interfacial tension with temperature, defined as $\sigma_T = \partial\sigma(T)/\partial T$. The non-uniformity of surface tension then drives the fluids to move from the region with higher temperature to that with lower temperature. This effect is known as the thermocapillary (Marangoni) effect [80], and it plays an important role in various industrial applications involving microgravity [112] or microdevices [33], where the surface forces become dominant.

One example for thermocapillary effects is the thermocapillary convection in a two-layer fluid system (thermocapillary instabilities), where the system is typically confined between two parallel plates and subjected to a temperature gradient. Due to the perturbations in the temperature, velocity field as well as the interface position, surface tension gradients will occur at the interface and drive the fluid to motion. The instabilities then set in and leads to the convective motion, where a typical convection pattern is the hexagonal cell formation found by Bénard [14]. The thermocapillary instabilities are widely studied which can be traced back to some pioneering works performed by Block [22], Pearson [97], and Sternling and Scriven [111, 106]. Literature reviews of recent experimental and analytical work on instabilities in thermocapillary convection are provided by Schatz and Neitzel [105], Davis [34] and Andereck *et al*. [6].

The mechanism of thermocapillary convection in a two layer fluid system, which is heated from above has been summarized by Johnson and Narayanan [72] (Figure 2.1). In both diagrams, the two-layer fluid systems are all heated from above, with a constant temperature gradient between two horizontal plates. In the upper diagram (Case 1), a perturbation in the interface towards the low temperature side is assumed (bottom

boundary). This local temperature reduction of interface lowers the surface tension and leads to a surface tension gradient along the interface due to its temperature dependence, with the largest surface tension in the centre of the interface. For the upper layer, this local gradient drags the fluid towards the centre of the interface. This is then replaced by hot fluid flowing downward from the top boundary to the edge of the interface, reinforcing the perturbation. Meanwhile, as the flow of lower fluid is coupled, there is upwelling of cold fluid from the bottom boundary to the edge of the interface, which tends to lower the local temperature and dampen the perturbation.
The lower diagram (Case 2 in Figure 3.1) just shows the opposite scenario, in which the perturbation in the interface towards the high temperature side (top boundary) is assumed. Again, the convection sets in, with the flow in the upper layer reinforcing the instability and reducing it in the lower layer.

Another example for thermocapillary effects is the thermocapillary migration of drops, where the drops are set in a liquid possessing a temperature gradient, and will move toward the hot region due to the thermocapillary effects. The thermocapillary migration of a drop was first examined experimentally by Young *et al*. [129], who derived an analytical expression for the terminal velocity of a single spherical drop in a constant temperature gradient by assuming the convective transport of momentum and energy are negligible. Since then, extensive works were carried out experimentally, analytically and numerically in order to investigate this phenomenon, where many of them are summarized by Subramanian and Balasubramaniam [112]. In chapter 3 and 5, we will study the thermocapillary effects for two-phase flows by using phase-field models.

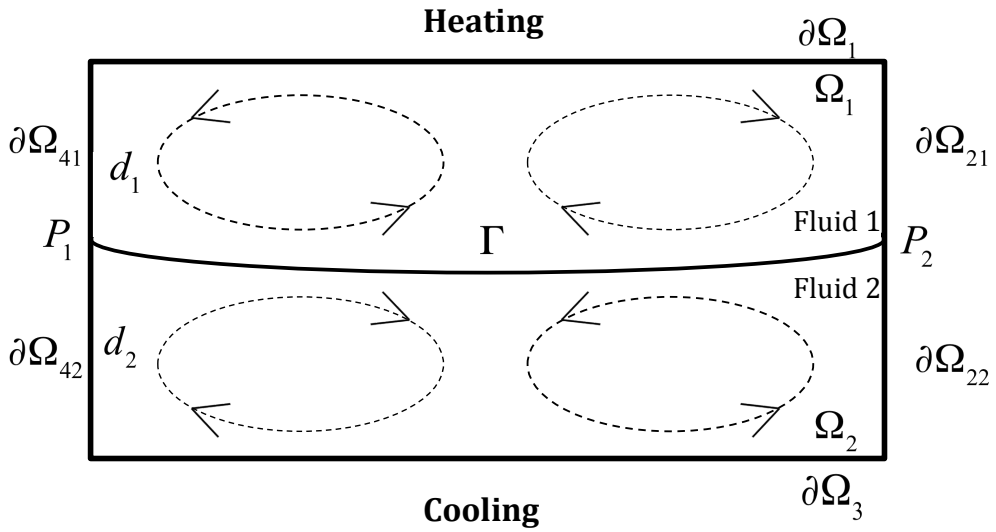

Case 1

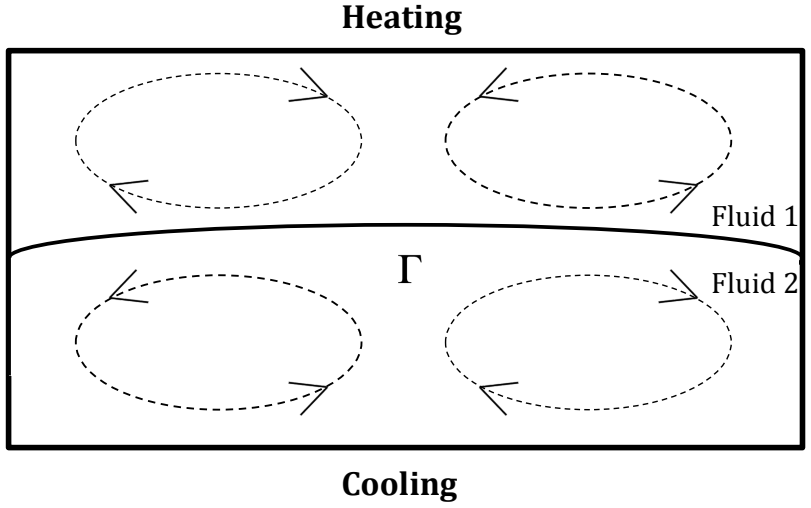

Case 2

Figure 2.1: Sketch for two cases of Marangoni-Bénard convection in a two-layer fluid system heated from above.

2.3 Continuum mechanics

In this section, we introduce the basic knowledge of the continuum mechanics, which would be used in Chapter 3 and Chapter 5.

2.3.1 Tensor algebra

We first give a brief introduction to the tensor algebra. In order to represent vectors and tensors in component form, we first introduce a right-handed system of rectangular Cartesian axes $Ox_1x_2x_3$, and the unit basis vectors $\hat{\mathbf{e}}_1$, $\hat{\mathbf{e}}_2$, $\hat{\mathbf{e}}_3$. In terms of this basis, an arbitrary vector $\mathbf{v}$ can be given in component form by

$$\mathbf{v} = v_1\hat{\mathbf{e}}_1 + v_2\hat{\mathbf{e}}_2 + v_3\hat{\mathbf{e}}_3 = \sum_{i=1}^{3} v_i\hat{\mathbf{e}}_i. \tag{2.15}$$

For simplicity, we agree that whenever a subscript appears exactly twice in a given term, that subscript will take on the values 1, 2, 3 successively, and the resulting terms summed. In the tensor algebra, this assumption is called "summation convention". Therefore Eq.(2.15) can be written as

$$\mathbf{v} = \sum_{i=1}^{3} v_i\hat{\mathbf{e}}_i = v_i\hat{\mathbf{e}}_i, \tag{2.16}$$

where we have deleted entirely the summation symbol $\sum$. For the basis vectors, we have the following properties

$$\hat{\mathbf{e}}_i \cdot \hat{\mathbf{e}}_j = \begin{cases} 1 & \text{if } \ i = j, \\ 0 & \text{if } \ i \neq j. \end{cases} \tag{2.17}$$

Therefore, we introduce the Kronecker delta defined by

$$\delta_{ij} = \begin{cases} 1 & \text{if } \; i = j, \\ 0 & \text{if } \; i \neq j, \end{cases} \tag{2.18}$$

and we have that

$$\hat{\mathbf{e}}_i \cdot \hat{\mathbf{e}}_j = \delta_{ij} \quad (i, j = 1, 2, 3). \tag{2.19}$$

Further, the dot product of vector $\mathbf{u} \cdot \mathbf{v}$ may be written as

$$\mathbf{u} \cdot \mathbf{v} = u_i \hat{\mathbf{e}}_i \cdot v_j \hat{\mathbf{e}}_j = u_i v_j \hat{\mathbf{e}}_i \cdot \hat{\mathbf{e}}_j = u_i v_j \delta_{ij} = u_i v_i. \tag{2.20}$$

We now introduce the permutation symbol ε_{ijk}, which can be given as

$$\varepsilon_{ijk} = \begin{cases} 1 & \text{if numerical value of } \; ijk \; \text{ appear as in the sequence } \quad 12312, \\ -1 & \text{if numerical value of } \; ijk \; \text{ appear as in the sequence } \quad 32132, \\ 0 & \text{if numerical value of } \; ijk \; \text{ appear as in any other sequence .} \end{cases}$$

Now, based on the above definition, the cross product of the basis vectors $\hat{\mathbf{e}}_i \; (i = 1, 2, 3)$ can be written as

$$\hat{\mathbf{e}}_i \times \hat{\mathbf{e}}_j = \varepsilon_{ijk} \hat{\mathbf{e}}_k \quad (i, j, k = 1, 2, 3) \tag{2.21}$$

And further the vector cross product becomes

$$\mathbf{u} \times \mathbf{v} = u_i \hat{\mathbf{e}}_i \times v_j \hat{\mathbf{e}}_j = u_i v_j \hat{\mathbf{e}}_i \times \hat{\mathbf{e}}_j = \varepsilon_{ijk} u_i v_j \hat{\mathbf{e}}_k. \tag{2.22}$$

2.3.2 Particles, configurations, deformation and motion

Continuum mechanics considers the material bodies in the form of gas, liquids or solids. We begin by describing the model used to represent such material bodies. We first define a material body B as the set of elements X, called particles or material points, which can be put into a one-to-one mapping correspondence with the points of a regular region of physical space. Note that whereas a particle of classical mechanics has an assigned mass, a continuum particle is essentially a material point for which a density is defined. The specification of the position of all of the particles of B with respect to a fixed origin at some instant of time is said to define the configuration of the body at that instant. Mathematically, this is expressed by the mapping

$$\mathbf{x} = \kappa(X), \tag{2.23}$$

in which the vector function κ relates the position of $\mathbf{x}$ to each original particle X of the body. Here we assume that this mapping is uniquely invertible and differentiable as many times as required (two or three times). The inverse can be written as

$$X = \kappa^{-1}(\mathbf{x}). \tag{2.24}$$

A motion of body B is a continuous time sequence of displacements that carries the set of particles X into various configurations in a stationary space. Such a motion may be expressed by the equation

$$\mathbf{x} = \kappa(X,t) \tag{2.25}$$

which gives the position $\mathbf{x}$ for each particle X at any time t, where $t \in [0,+\infty)$. The initial configuration which the body occupies at time $t = 0$, is normally chosen as the reference configuration. The current configuration is the one which the body occupies

at the current time t.

2.3.3 Material and spatial coordinates

Consider the reference configuration prescribed by some mapping function Φ, and the position vector (material coordinates) $\mathbf{X}$ of particle X can be represented as

$$\mathbf{X} = \Phi(X). \tag{2.26}$$

Here the position vector $\mathbf{X}$ can be expressed in terms of the base vectors as

$$\mathbf{X} = X_A \hat{\mathbf{I}}_A, \tag{2.27}$$

where the component X_A are the material coordinates, or referential coordinate of the particle X, and I_A are the unit vectors. Moreover, we define an inverse mapping

$$X = \Phi^{-1}(\mathbf{X}). \tag{2.28}$$

Substituting into Eq.(2.25). we obtain

$$\mathbf{x} = \kappa[\Phi^{-1}(\mathbf{X}), t] = \chi(\mathbf{X}, t), \tag{2.29}$$

which defines the motion of the body in physical space relative to the reference configuration prescribed by the mapping function Φ. In particular, at $t = 0$, Eq. (2.29) defines the initial configuration which is often adopted as the reference configuration, and this results in the initial spatial coordinates being identical with the material coordinates, such that

$$\mathbf{x} = \chi(\mathbf{X}, 0) = \mathbf{X} \tag{2.30}$$

at time $t = 0$. Note that Eq.(2.29) maps the particle at $\mathbf{X}$ in the reference configuration onto the point $\mathbf{x}$ in the current configuration at time t, this can be expressed as

$$\mathbf{x} = x_i \hat{\mathbf{e}}_i, \tag{2.31}$$

where the components x_i are called the spatial coordinates of the particles. For Eq.(2.29), it is common practice in continuum mechanics to write these equations in the alternative forms

$$\mathbf{x} = \mathbf{x}(\mathbf{X}, t), \tag{2.32}$$

where the symbol $\mathbf{x}$ on the right-hand side of the equation represents the function whose arguments are $\mathbf{X}$ and t, while the same symbol on the left-hand side represents the value of the function, that is, a point in space. We shall use this notation frequently in the text that follows.

The velocity $\mathbf{v}$ of the particle along its path can then be defined as the time rate of change of position,

$$\mathbf{v} = \frac{\mathrm{d}\mathbf{x}}{\mathrm{d}t} = \frac{\partial \chi(\mathbf{X}, t)}{\partial t} = \frac{\partial \mathbf{x}(\mathbf{X}, t)}{\partial t}. \tag{2.33}$$

Here we assume that no two particles can occupy the same location in space at a given time, and furthermore, in the smooth motions we consider here, any two particles arbitrarily close in the reference configuration remain arbitrarily close in all other configurations. Therefore, the function χ in Eq.(2.29) must be single-valued and continuous, and must possess continuous derivatives with respect to space and time to whatever order is required, usually to the second or third. Moreover, we assume the inverse

function as

$$\mathbf{X} = \chi^{-1}(\mathbf{x}, t) \tag{2.34}$$

to be endowed with the same properties as χ. Then the Jacobian determinant J can be defined as

$$J = |\frac{\partial x_i}{\partial X_A}| = |\frac{\partial \chi_i}{\partial X_A}|, \tag{2.35}$$

and the mathematical condition that guarantees the existence of such an inverse function is the non-vanishing of the Jacobian deternimant, say $J \neq 0$.

2.3.4 Lagrangian and Eulerian descriptions

If a physical property of the body B such as its density ρ, or velocity $\mathbf{v}$, is expressed in terms of the material coordinates $\mathbf{X}$, and the time t, we say that property is given by the referential or material description. When the referential configuration is taken as the actual configuration at time $t = 0$, this description is usually called the Lagrangian description. For examples, we have

$$\rho = \rho(X_A, t) \qquad \text{or} \qquad \rho = \rho(\mathbf{X}, t), \tag{2.36}$$

and

$$v_i = v_i(X_A, t) \qquad \text{or} \qquad \mathbf{v} = \mathbf{v}(\mathbf{X}, t). \tag{2.37}$$

In contrast, if the properties ρ and $\mathbf{v}$ are given as functions of the spatial coordinates $\mathbf{x}$ and time t, we say that those properties are expressed by a spatial description, or as it

is sometimes called, by the Eulerian description. In view of Eq. (2.34) it is clear that Eq.(2.36) and Eq.(2.37) may be converted to express the same properties in the spatial description, such that

$$\rho = \rho(\mathbf{X},t) = \rho[\chi^{-1}(\mathbf{x},t),t] = \rho(\mathbf{x},t), \tag{2.38}$$

and

$$\mathbf{v} = \mathbf{v}(\mathbf{X},t) = \mathbf{v}[\chi^{-1}(\mathbf{x},t),t] = \mathbf{v}(\mathbf{x},t). \tag{2.39}$$

We note that in the material description, attention is focused on what is happening to the individual particles during the motion, whereas in the spatial description the emphasis is directed to the events taking place at specific points in space.

2.3.5 The material derivative

We first use a general symbol p to represent any physical or kinematic property of a continuum body, (e.g., scalar, vector or tensor property). We then have the material description

$$p = p(\mathbf{X},t), \tag{2.40}$$

or spatial description

$$p = p(\mathbf{x},t). \tag{2.41}$$

The material derivative of any such property is the time rate of change of that property for a specific collection of particles (one or more) of the continuum body. This derivative can be thought of as the rate at which p changes when measured by an observer

travelling with the particle or group of particles. We use the differential operator $\mathrm{d}/\mathrm{d}t$, or the superpositioned dot $\dot{}$ to denote a material derivative. When p is given in the material description of Eq.(2.40), the material derivative is simply the partial derivative with respect to time,

$$\frac{\mathrm{d}}{\mathrm{d}t}[p(\mathbf{X},t)] = \frac{\partial}{\partial t}[p(\mathbf{X},t)], \tag{2.42}$$

where, as it is mentioned above, the material coordinates $\mathbf{X}$ do not change with time. For the spatial form, we note that the particle will change the position, and we must use the chain rule of differentiation of the calculus to obtain

$$\frac{\mathrm{d}}{\mathrm{d}t}[p(\mathbf{x},t)] = \frac{\partial}{\partial t}p(\mathbf{x},t) + \frac{\partial}{\partial x_i}p(\mathbf{x},t)\frac{dx_i}{dt}, \tag{2.43}$$

where the first term on the right-hand side gives the change occurring in the property at position $\mathbf{x}$, known as the local rate of change; the second term results from the particles changing position in space and is referred to as the convective rate of change. Having in mind of the definition of the velocity, Eq.(2.43) may be written as

$$\frac{\mathrm{d}}{\mathrm{d}t}[p(\mathbf{x},t)] = \frac{\partial}{\partial t}p(\mathbf{x},t) + \frac{\partial}{\partial x_i}p(\mathbf{x},t)v_i = \frac{\partial}{\partial t}p(\mathbf{x},t) + \mathbf{v}\cdot\nabla p(\mathbf{x},t), \tag{2.44}$$

from which we deduce the material derivative operator for properties expressed in the spatial description

$$\frac{\mathrm{d}}{\mathrm{d}t} = \frac{\partial}{\partial t} + \mathbf{v}\cdot\nabla, \tag{2.45}$$

where ∇ is the gradient operator.

2.3.6 Deformation gradients

In deformation analysis we confine our attention to two stationary configurations, the initial (referential) and the final deformed configuration, and we ignore the sequence between the two configurations. Accordingly, the mapping function is not dependent upon time as a variable, so that Eq.(2.29) takes the form

$$\mathbf{x} = \chi(\mathbf{X}). \tag{2.46}$$

We now consider two neighboring particles of the body situated at two points P and Q in the referential configuration, such that Q is located with respect to P by the relative differential position vector

$$\mathrm{d}\mathbf{X} = \mathrm{d}X_A \mathbf{I}_A. \tag{2.47}$$

Under the mapping of function χ, the particles originally at P and Q move to the position p and q, respectively, in the deformed configuration such that their relative position vector is now

$$\mathrm{d}\mathbf{x} = \mathrm{d}x_i \mathbf{e}_i. \tag{2.48}$$

As we assume the mapping function $\mathbf{x}$ in Eq.(2.46) is continuous, so that

$$\mathrm{d}x_i = \frac{\partial \chi_i}{\partial X_A}\mathrm{d}X_A = x_{i,A}\mathrm{d}X_A, \tag{2.49}$$

where $x_{i,A} = F_{iA}$ is called the deformed gradient tensor or the deformation gradient. Therefore Eq.(2.49) can be written as

$$\mathrm{d}\mathbf{x} = \mathbf{F}\mathrm{d}\mathbf{X}, \tag{2.50}$$

where $\mathbf{F} = (F_{iA})$ is a matrix from Eq.(2.35), we obtain that

$$\det(\mathbf{F}) = J. \tag{2.51}$$

2.3.7 Material derivative of volumes

We consider a volume element $\mathrm{d}V^\circ$ defined in the referential configuration. Recall that the magnitude of the scalar triple product equals the area of a parallelogram with the vectors for sides, we have that the volume element defined in the referential configuration

$$\mathrm{d}V^\circ = \mathrm{d}\mathbf{X}^{(1)} \cdot \mathrm{d}\mathbf{X}^{(2)} \times \mathrm{d}\mathbf{X}^{(3)} = \varepsilon_{ABC}\mathrm{d}X_A^{(1)}\mathrm{d}X_B^{(2)}\mathrm{d}X_C^{(3)}, \tag{2.52}$$

and for the deformed volume element be given by

$$\mathrm{d}V = \mathrm{d}\mathbf{x}^{(1)} \cdot \mathrm{d}\mathbf{x}^{(2)} \times \mathrm{d}\mathbf{x}^{(3)} = \varepsilon_{ijk}\mathrm{d}x_i^{(1)}\mathrm{d}x_j^{(2)}\mathrm{d}x_k^{(3)}. \tag{2.53}$$

Note that to derive Eq.(2.52) and Eq.(2.53), we have used the following identity for the vector dot and cross product

$$\mathbf{I}_A \cdot \mathbf{I}_B \times \mathbf{I}_C = \varepsilon_{ABC}. \tag{2.54}$$

For the motion $\mathbf{x} = \mathbf{x}(\mathbf{X}, t)$, $\mathrm{d}\mathbf{x} = \mathbf{F}\mathrm{d}\mathbf{X}$ so the current volume is the box product

$$\mathrm{d}V = [\mathbf{F}\mathrm{d}\mathbf{X}^{(1)}, \mathbf{F}\mathrm{d}\mathbf{X}^{(2)}, \mathbf{F}\mathrm{d}\mathbf{X}^{(3)}] = \varepsilon_{ijk}x_{i,A}x_{j,B}x_{k,C}\mathrm{d}X_A^{(1)}\mathrm{d}X_B^{(2)}\mathrm{d}X_C^{(3)} = J\mathrm{d}V^\circ, \tag{2.55}$$

which gives the current volume element in terms of its original size. Here we have used the following identity

$$\varepsilon_{ijk}x_{i,A}x_{j,B}x_{k,C} = \varepsilon_{ABC}\det(\mathbf{F}) = \varepsilon_{ABC}J \tag{2.56}$$

To determine the time rate of change of dV, we take the material derivative as follows [90]

$$(\mathrm{d}V)^{\cdot} = \dot{J}\mathrm{d}V^{\circ} = J\nabla\cdot\mathbf{v}\mathrm{d}V^{\circ} = \nabla\cdot\mathbf{v}\mathrm{d}V \tag{2.57}$$

where, for the incompressible fluid flow, we have that

$$\nabla\cdot\mathbf{v} = 0 \tag{2.58}$$

Let P be any scalar, vector, or tensor property of the collection of particles occupying the current volume V, we then have the expression in the terms of the integral,

$$P(t) = \int_V p(\mathbf{x},t)\mathrm{d}V, \tag{2.59}$$

where p represents the distribution of the property per unit volume and has continuous derivatives as necessary. The material derivative of this property is given in both spatial and material forms,

$$\frac{\mathrm{d}P(t)}{\mathrm{d}t} = \frac{\mathrm{d}}{\mathrm{d}t}\int_V p(\mathbf{x},t)\mathrm{d}V = \frac{\mathrm{d}}{\mathrm{d}t}\int_{V^{\circ}} p[\mathbf{x}(\mathbf{X},t),t]J\mathrm{d}V^{\circ} \tag{2.60}$$

Since V° is a fixed volume in the referential configuration, the differentiation and integration commute, and the differentiation can be performed inside the integral sign.

Using chain rule, we obtain,

$$\begin{aligned}\frac{\mathrm{d}P(t)}{\mathrm{d}t} &= \frac{\mathrm{d}}{\mathrm{d}t}\int_{V^\circ} p[\mathbf{x}(\mathbf{X},t),t]J\mathrm{d}V^\circ = \int_{V^\circ}\frac{\mathrm{d}}{\mathrm{d}t}\Big(p[\mathbf{x}(\mathbf{X},t),t]J\Big)\mathrm{d}V^\circ \\ &= \int_{V^\circ}\Big(\dot{p}[\mathbf{x}(\mathbf{X},t),t]J + p[\mathbf{x}(\mathbf{X},t),t]\dot{J}\Big)\mathrm{d}V^\circ \\ &= \int_{V^\circ}\Big(\dot{p}[\mathbf{x}(\mathbf{X},t),t] + v_{k,k}p[\mathbf{x}(\mathbf{X},t),t]\Big)J\mathrm{d}V^\circ \\ &= \int_{V}\Big(\dot{p}[\mathbf{x}(\mathbf{X},t),t] + v_{k,k}p[\mathbf{x}(\mathbf{X},t),t]\Big)\mathrm{d}V \end{aligned} \tag{2.61}$$

where we have used the identity $J\mathrm{d}V^\circ = \mathrm{d}V$ to convert back to the spatial formulation. With the help of the material derivative operator given in [90], the above equation can be written in the form

$$\begin{aligned}\frac{\mathrm{d}P(t)}{\mathrm{d}t} &= \int_V\left(\frac{\partial p[\mathbf{x}(\mathbf{X},t),t]}{\partial t} + \mathbf{v}\cdot\nabla p[\mathbf{x}(\mathbf{X},t),t] + (\nabla\cdot\mathbf{v})p[\mathbf{x}(\mathbf{X},t),t]\right)\mathrm{d}V \\ &= \int_V\Big(p_t + \nabla\cdot(\mathbf{v}p)\Big)\mathrm{d}V \end{aligned} \tag{2.62}$$

This gives the material derivative within a control volume.

Chapter 3

Continuous finite element schemes for a phase-field model in two-layer fluid thermocapillary (Bénard-Marangoni) convection computations

3.1 Introduction

In this chapter, we study a phase-field model for a two-layer fluid where the temperature dependence of both the density (buoyancy forces) and the surface tension (thermocapillary effects) is considered. The phase-field model consisting of a modified NS equation, an advective Cahn-Hilliard equation and an energy transport equation is derived through an energetic variational procedure. An appropriate variational form and a continuous finite element method are adopted to maintain any possible underlying energy law to its greatest extent. Several examples for Bénard-Marangoni convection in an Acetonitrile and an n-Hexane two-layer fluid system heated from above will be

computed to justify our phase-field model. In addition, an interesting numerical experiment will be performed to show the competition between the thermocapillary effects and the buoyancy forces.

3.2 A phase-field model with thermocapillary effects and energetic variational procedure

We consider a phase-field model with thermocapillary effects for mixtures in two isotropic fluids of different densities because of their simplicity in the practical implementation. After applying the Bousssinesq approximation (where the small density difference is neglected except that in the gravitational force) and assuming that two fluids hold the same physical properties, i.e. dynamic viscosity, thermal conductivity, the governing system of equations can be given as the following:

$$\rho_0\Big(\mathbf{u}_t+(\mathbf{u}\cdot\nabla)\mathbf{u}\Big)+\nabla p-\mu\nabla\cdot D(\mathbf{u}) \\ +\nabla\cdot\Big(\lambda(\theta)\nabla\phi\otimes\nabla\phi+\frac{\lambda(\theta)}{2}|\nabla\phi|^2\mathbf{I}+\lambda(\theta)F(\phi)\mathbf{I}\Big)=\mathbf{s}(\phi,\theta), \quad (3.1)$$

$$\nabla\cdot\mathbf{u}=0, \quad (3.2)$$

$$\phi_t+(\mathbf{u}\cdot\nabla)\phi+\gamma\Delta\Big(\Delta\phi-f(\phi)\Big)=0, \quad (3.3)$$

$$\rho_0 c_p\Big(\theta_t+(\mathbf{u}\cdot\nabla)\theta\Big)=k\Delta\theta, \quad (3.4)$$

where the vector $\mathbf{u}$ represents the velocity of the fluid mixture, p is the hydrostatic pressure, ϕ represents the "phase" of the mixture ($\phi=1$: fluid 1; $\phi=-1$: fluid 2), and θ stands for the temperature, μ is the dynamic viscosity coefficient, $D(\mathbf{u})=1/2((\nabla\mathbf{u})+(\nabla\mathbf{u})^T)$ is the stretching tensor, $f(\phi)$ is the variation of the bulk mixing energy density $F(\phi)=(|\phi|^2-1)/4\varepsilon^2$, in which the ε is related to the capillary width (width of the mixing

layer), $\lambda = \varepsilon\sigma = \varepsilon(\sigma_0 - \sigma_1(\theta - \theta_0))$, σ is the surface tension parameter σ, where σ, by Eötvös rule [96], is a linear function of the temperature with σ_0 and σ_1 being the constant, and θ_0 is the reference temperature. The term $\nabla\phi \otimes \nabla\phi$ is the usual tensor product, i.e. $(\nabla\phi \otimes \nabla\phi)_{ij} = \nabla_i\phi\nabla_j\phi$, $\mathbf{I}$ is the identity matrix, $\mathbf{s}(\phi,\theta) = -\rho(\phi)\eta(\theta)g\boldsymbol{j}$ stands for the buoyancy force with gravity g, where the density function of mixtures is defined as $\rho(\phi) = (\rho_1(1-\phi)/2 + \rho_2(1+\phi)/2)$ with the density ρ_1 and ρ_2 for fluid 1 and fluid 2 respectively, $\eta = (1 - \alpha(\theta - \theta_0))$ according to the temperature-dependence of density. In addition, γ represents the elastic relaxation time of the system, c_p is the specific heat capacity and k the heat conductivity coefficient.

The initial conditions for the system is given as

$$\mathbf{u}\big|_{t=0} = \mathbf{u}_0,\ \phi\big|_{t=0} = \phi_0,\ \theta\big|_{t=0} = \theta_0, \tag{3.5}$$

and the Dirichlet boundary condition for $\mathbf{u}(= \mathbf{b}_\mathbf{u})$, and the Neumann boundary condition for ϕ in the Cahn-Hilliard equation: $\nabla\phi \cdot \mathbf{n} = 0, \nabla\Delta\phi \cdot \mathbf{n} = 0$, where $\mathbf{n}$ is the unit outward normal vector of the boundary.

When taking the surface tension λ as a constant (isothermal case), and neglecting the energy transport equation (3.4), the above system equations reduce to the classical phase-field model, Model H, that was employed to study binary incompressible fluid flows (e.g., [65, 85]). For the homogeneous case (i.e. the buoyancy force is negligible $s(\phi) = 0$ and the boundary value $\mathbf{b}_\mathbf{u} = 0$), the system obeys an energy dissipation law. Multiplying (3.1) by $\mathbf{u}$ and (3.3) by $-(\Delta\phi - f(\phi))$, the corresponding system gives the following energy estimate [65, 85]:

$$\frac{dE}{dt} = -\left(\mu||\nabla\mathbf{u}||^2_{\mathbf{L}^2(\Omega)} + \lambda\gamma||\nabla(\Delta\phi - f(\phi))||^2_{\mathbf{L}^2(\Omega)}\right), \tag{3.6}$$

where

$$E = \frac{1}{2}\rho_0 ||\mathbf{u}||^2_{\mathbf{L}^2(\Omega)} + \frac{\lambda}{2}||\nabla\phi||^2_{\mathbf{L}^2(\Omega)} + \lambda \int_\Omega F(\phi), \tag{3.7}$$

is the total energy of the reduced system.

In the case of λ as a function of both the time and space, we can still consider the following action functional [113]:

$$A(\mathbf{x}) = \int_0^T \int_{\Omega_0} \left\{ \frac{\rho_0}{2}|\mathbf{x}_t(\mathbf{X},t)|^2 - \lambda(\mathbf{x}(\mathbf{X},t)) \left[\frac{1}{2}|\mathbf{F}^{-T}\nabla_X \phi(\mathbf{x}(\mathbf{X},t),t)|^2 \right.\right. \\ \left.\left. + F(\phi(\mathbf{x}(\mathbf{X},t),t)) \right] \right\} J dV^\circ dt, \tag{3.8}$$

where Ω_0 is the initial domain occupied by the fluid, $\mathbf{X}$ can be viewed as the Lagrangian (initial) material coordinate and $\mathbf{x}(\mathbf{X},t)$ the Eulerian (reference) coordinate. The Jacobian matrix J and the control volume V° are introduced in section 2.3.7. Further the notation $\phi(\mathbf{x}(\mathbf{X},t),t)$ and $\lambda(\mathbf{x}(\mathbf{X},t),t)$ indicates that ϕ and λ are transported by the flow field. For an incompressible fluid, we look at the volume preserving flow map $\mathbf{x}(\mathbf{X},t)$ such that

$$\mathbf{x}_t(\mathbf{X},t) = \mathbf{u}(\mathbf{x}(\mathbf{X},t),t), \qquad \mathbf{x}(\mathbf{X},0) = \mathbf{X}, \tag{3.9}$$

and $\mathbf{F} = \nabla_{\mathbf{X}}\mathbf{x}$, as introduced in section 2.3.6, is the deformation tensor satisfying the following property [57, 90, 101]:

$$\nabla_{\mathbf{X}} = \mathbf{F}^{-1}\nabla_{\mathbf{x}}, \quad \nabla_{\mathbf{x}} = \mathbf{F}^{-T}\nabla_{\mathbf{X}}, \tag{3.10}$$

where the corresponding Jacobin determinant $J = \det\mathbf{F} = 1$ due to the incompressible constraint.

Based on the least action principle, the linear momentum equation shall be the least

action state. Here, a one parameter family of maps $\mathbf{x}^\eta$ is employed, such that,

$$\mathbf{x}^0 = \mathbf{x} \quad \text{and} \quad \frac{d\mathbf{x}^\eta}{d\eta} = \mathbf{y}, \tag{3.11}$$

where $\mathbf{y}$ is an arbitrary vector field that $\mathbf{y}|_{t=0,T} = 0$ (see [21] as an example). The deformation tensor $\mathbf{F}^\eta$, again, satisfies the property (3.10). The Jacobian $J^\eta = \det \mathbf{F}^\eta = 1$ or $\nabla \cdot \mathbf{y} = 0$ due to the incompressible constraint.

Applying the least action principle $\delta A(\mathbf{x}) = 0$, say $\frac{dA(\mathbf{x})}{d\eta} = 0|_{\eta=0}$, we can obtain the following:

$$\frac{\mathrm{d}}{\mathrm{d}\eta}\Big|_{\eta=0} A(\mathbf{x}) = \frac{\mathrm{d}}{\mathrm{d}\eta}\Big|_{\eta=0} \int_0^T \int_{\Omega_0} \left\{ \frac{\rho_0}{2} |\mathbf{x}_t^\eta(\mathbf{X},t)|^2 - \lambda(\mathbf{x}^\eta(\mathbf{X},t)) \left[\frac{1}{2} |\nabla_{\mathbf{x}^\eta} \phi(x^\eta(\mathbf{X},t),t)|^2 + F(\phi(\mathbf{x}^\eta(\mathbf{X},t),t)) \right] \right\} J dV^\circ dt = 0. \tag{3.12}$$

Further computation for the kinetic energy part leads to [126]:

$$\frac{\mathrm{d}}{\mathrm{d}\eta}\Big|_{\eta=0} \int_0^T \int_{\Omega_0} \frac{\rho_0}{2} |\mathbf{x}_t^\eta(\mathbf{X},t)|^2 J dV^\circ dt = \int_0^T \int_{\Omega_0} \rho_0 \mathbf{x}_t(\mathbf{X},t) \cdot \mathbf{y}_t J dV^\circ dt. \tag{3.13}$$

Integrating by parts gives us that

$$\begin{aligned}
&\int_0^T \int_{\Omega_0} \rho_0 \mathbf{x}_t \cdot \mathbf{y}_t J dV^\circ dt = -\int_0^T \int_{\Omega_0} \rho_0 \mathbf{x}_{tt} \cdot \mathbf{y} J dV^\circ dt \\
&= -\int_0^T \int_{\Omega_0} \rho_0 \mathbf{u}_t(\mathbf{x}(\mathbf{X},t),t) \cdot \mathbf{y} J dV^\circ dt \\
&= -\int_0^T \int_{\Omega_t} \rho_0 \Big(\mathbf{u}_t + \mathbf{x}(\mathbf{X},t)_t \cdot \nabla_{\mathbf{x}} \mathbf{u} \Big) \cdot \mathbf{y} dV dt \\
&= -\int_0^T \int_{\Omega_t} \left(\rho_0 \Big(\mathbf{u}_t + \mathbf{u} \cdot \nabla \mathbf{u} \Big) \right) \cdot \mathbf{y} dV dt,
\end{aligned} \tag{3.14}$$

where we have used Eq.(2.55). The elastic energy part leads to:

$$
\begin{aligned}
&\frac{\mathrm{d}}{\mathrm{d}\eta}\Big|_{\eta=0}\int_0^T\int_{\Omega_0}\left\{-\lambda(\mathbf{x}^\eta(\mathbf{X},t))\left[\frac{1}{2}|\nabla_{\mathbf{x}^\eta}\phi(\mathbf{x}^\eta(\mathbf{X},t),t)|^2+F(\phi(\mathbf{x}^\eta(\mathbf{X},t),t))\right]\right\}JdV^\circ dt\\
&=\int_0^T\int_{\Omega_0}\left\{-\left[\frac{1}{2}|\mathbf{F}^{-T}\nabla_{\mathbf{X}}\phi(\mathbf{x}(\mathbf{X},t),t)|^2+F(\phi(\mathbf{x}(\mathbf{X},t),t))\right]\mathbf{F}^{-T}\nabla_{\mathbf{X}}\lambda(\mathbf{x}(\mathbf{X},t),t)\cdot\mathbf{y}\right.\\
&\quad-\lambda(\mathbf{x}(\mathbf{X},t),t)\left[\mathbf{F}^{-T}\nabla_{\mathbf{X}}\phi(\mathbf{x}(\mathbf{X},t),t)\cdot\frac{d}{d\eta}\Big|_{\eta=0}\left(\nabla_{\mathbf{x}^\eta}\phi(\mathbf{x}^\eta(\mathbf{X},t),t)\right)\right.\\
&\quad\left.\left.+\mathbf{F}^{-T}\nabla_{\mathbf{X}}F(\phi(\mathbf{x}(\mathbf{X},t),t))\cdot\mathbf{y}\right]\right\}JdV^\circ dt\\
&=\int_0^T\int_{\Omega_0}\left\{-\left[\frac{1}{2}|\mathbf{F}^{-T}\nabla_{\mathbf{X}}\phi(\mathbf{x}(\mathbf{X},t),t)|^2+F(\phi(\mathbf{x}(\mathbf{X},t),t))\right]\mathbf{F}^{-T}\nabla_{\mathbf{X}}\lambda(\mathbf{x}(\mathbf{X},t),t)\cdot\mathbf{y}\right.\\
&\quad-\lambda(\mathbf{x}(\mathbf{X},t),t)\left[\mathbf{F}^{-T}\nabla_{\mathbf{X}}\phi(\mathbf{x}(\mathbf{X},t),t)\cdot\frac{d}{d\eta}\Big|_{\eta=0}\left(\nabla_{\mathbf{x}}\phi(\mathbf{x}^\eta(\mathbf{X},t),t)\nabla_{\mathbf{x}^\eta}\mathbf{x}\right)\right.\\
&\quad\left.\left.+\mathbf{F}^{-T}\nabla_{\mathbf{X}}F(\phi(\mathbf{x}(\mathbf{X},t),t))\cdot\mathbf{y}\right]\right\}JdV^\circ dt\\
&=\int_0^T\int_{\Omega_0}\left\{-\left[\frac{1}{2}|\mathbf{F}^{-T}\nabla_{\mathbf{X}}\phi(\mathbf{x}(\mathbf{X},t),t)|^2+F(\phi(\mathbf{x}(\mathbf{X},t),t))\right]\mathbf{F}^{-T}\nabla_{\mathbf{X}}\lambda(\mathbf{x}(\mathbf{X},t),t)\cdot\mathbf{y}\right.\\
&\quad-\lambda(\mathbf{x}(\mathbf{X},t),t)\left[\mathbf{F}^{-T}\nabla_{\mathbf{X}}\phi(\mathbf{x}(\mathbf{X},t),t)\cdot\left(\frac{d(\mathbf{F}^\eta)^{-T}}{d\eta}\Big|_{\eta=0}\nabla_{\mathbf{X}}\phi(\mathbf{x}(\mathbf{X},t),t)\right.\right.\\
&\quad\left.\left.\left.+\mathbf{F}^{-T}\nabla_{\mathbf{X}}\mathbf{F}^{-T}\nabla_{\mathbf{X}}\phi(\mathbf{x}(\mathbf{X},t),t)\cdot\mathbf{y}\right)+\mathbf{F}^{-T}\nabla_{\mathbf{X}}F(\phi(\mathbf{x}(\mathbf{X},t),t))\cdot\mathbf{y}\right]\right\}JdV^\circ dt\\
&=\int_0^T\int_{\Omega_t}\left\{-\left[\frac{1}{2}|\nabla_{\mathbf{x}}\phi(\mathbf{x},t)|^2+F(\phi(\mathbf{x},t))\right]\nabla_{\mathbf{x}}\lambda(\mathbf{x},t)\cdot\mathbf{y}\right.\\
&\quad\left.-\lambda(\mathbf{x},t)\left[\nabla_{\mathbf{x}}\phi(\mathbf{x},t)\cdot\left(-\nabla_{\mathbf{x}}^T\mathbf{y}\nabla_{\mathbf{x}}\phi(\mathbf{x},t)+\nabla_{\mathbf{x}}\left(\nabla_{\mathbf{x}}\phi(\mathbf{x},t)\right)\cdot\mathbf{y}\right)+\nabla_{\mathbf{x}}F(\phi(\mathbf{x},t))\cdot\mathbf{y}\right]\right\}dVdt
\end{aligned}
$$

$$
\begin{aligned}
&= \int_0^T \int_{\Omega_t} \Bigg\{ - \left[\frac{1}{2} |\nabla \phi|^2 + F(\phi) \right] \nabla \lambda \cdot \mathbf{y} \\
&\quad - \left[\nabla \cdot \left(\lambda \nabla \phi \otimes \nabla \phi \right) \cdot \mathbf{y} + \lambda \left(\nabla \phi \cdot \nabla \Big(\nabla \phi \cdot y \Big) + \nabla F(\phi) \right) \cdot \mathbf{y} \right] \Bigg\} dV dt \\
&= \int_0^T \int_{\Omega_t} \left\{ - \nabla \cdot \left(\lambda \nabla \phi \otimes \nabla \phi + \frac{\lambda}{2} |\nabla \phi|^2 \mathbf{I} + \lambda F(\phi) \mathbf{I} \right) \cdot \mathbf{y} \right\} dV dt. \qquad (3.15)
\end{aligned}
$$

Here we have used the property of the invertible matrix that ([50] P 171):

$$
\frac{d(\mathbf{F}^\eta)^{-T}}{d\eta} = -(\mathbf{F}^\eta)^{-T} \frac{d(\mathbf{F}^\eta)^T}{d\eta} (\mathbf{F}^\eta)^{-T}. \qquad (3.16)
$$

Further computation gives that:

$$
-(\mathbf{F}^\eta)^{-T} \frac{d(\mathbf{F}^\eta)^T}{d\eta} (\mathbf{F}^\eta)^{-T} \Big|_{\eta=0} = -\mathbf{F}^{-T} \nabla_{\mathbf{X}}^T \mathbf{y} \mathbf{F}^{-T} = -(\nabla_{\mathbf{X}} \mathbf{y} \mathbf{F}^{-1})^T \mathbf{F}^{-T} = -\nabla_{\mathbf{x}}^T \mathbf{y} \mathbf{F}^{-T}, \qquad (3.17)
$$

where the property (3.10) is used. By substituting (3.14), (3.15) into (3.12), we arrive at:

$$
\int_0^T \int_{\Omega_t} \left\{ \left[\rho_0 \Big(\mathbf{u}_t + \Big(\mathbf{u} \cdot \nabla \Big) \mathbf{u} \Big) + \nabla \cdot \left(\lambda \nabla \phi \otimes \nabla \phi + \frac{\lambda}{2} |\nabla \phi|^2 \mathbf{I} + \lambda F(\phi) \mathbf{I} \right) \right] \cdot \mathbf{y} \right\} dV dt = 0. \qquad (3.18)
$$

Having in mind that $\mathbf{y}$ is an arbitrary divergence free vector field, (3.18) can only be valid provided that :

$$
\rho_0 (\mathbf{u}_t + (\mathbf{u} \cdot \nabla) \mathbf{u}) + \nabla p + \nabla \cdot (\lambda \nabla \phi \otimes \nabla \phi + \frac{\lambda}{2} |\nabla \phi|^2 \mathbf{I} + \lambda F(\phi) \mathbf{I}) = 0. \qquad (3.19)
$$

Assuming the surface tension parameter is a linear function of temperature, and adding the viscous term and the external forces term together as complement, we finally get the momentum equation (3.1):

$$\rho_0(\mathbf{u}_t + (\mathbf{u}\cdot\nabla)\mathbf{u}) + \nabla p - \mu\nabla\cdot D(u) + \nabla\cdot\Big(\lambda(\theta)\nabla\phi\otimes\nabla\phi + \frac{\lambda(\theta)}{2}|\nabla\phi|^2\mathbf{I} + \lambda(\theta)F(\phi)\mathbf{I}\Big) = \mathbf{s}(\phi,\theta).$$

Note that the similar energetic variational procedures were also used in [81, 85, 113, 126].

3.3 Non-Dimensionalization

Consider a two-layer fluid in a two-dimensional domain, Ω, sketched in Figure 3.1. To simplify the study of thermocapillary effects, we non-dimensionalize the phase-field model (3.1)-(3.4) as follows. Let the distance between the plates $d = d_1 + d_2$ denote the length scale. The velocity scale is chosen to be κ/d, where $\kappa = k/\rho c_p$ is the thermal diffusivity, k the thermal conductivity and c_p the specific heat capacity. This then gives d^2/κ and $\mu\kappa/d^2$ as time and stress scales, in which μ is the dynamic viscosity. Correspondingly, the interface length is non-dimensionalized by $\bar{\varepsilon} = \varepsilon/d$, $\bar{\theta} = (\theta - \theta_0)/\theta_l$ is chosen as the temperature scale, where ε and θ are the dimensional parameter and variable in the dimensional system (3.1)-(3.4), θ_0 is the reference temperature (in the present work, it is set to be zero), θ_l is the temperature difference between the top and bottom boundaries. Dropping the bar notations, the non-dimensional phase-field

model with the thermocapillary effects can be rewritten as :

$$\frac{1}{Pr}\Big(\mathbf{u}_t+\Big(\mathbf{u}\cdot\nabla\Big)\Big)\mathbf{u}+\nabla p-\Delta\mathbf{u}+\nabla\cdot\Big(\Big(\frac{1}{Ca}-Ma\theta\Big)\Big(\nabla\phi\otimes\nabla\phi+\frac{|\nabla\phi|^2}{2}\mathbf{I}+F(\phi)\mathbf{I}\Big)\Big)$$
$$=\rho_r(Ra\theta-G)\boldsymbol{j}, \quad (3.20)$$

$$\nabla\cdot\mathbf{u}=0, \quad (3.21)$$

$$\phi_t+\Big(\mathbf{u}\cdot\nabla\Big)\phi+Pe\Delta\Big(\Delta\phi-f(\phi)\Big)=0, \quad (3.22)$$

$$\theta_t+\Big(\mathbf{u}\cdot\nabla\Big)\theta=\Delta\theta, \quad (3.23)$$

where the non-dimensional parameters are the Prandtl number, Pr, the capillary number, Ca, the Marangoni number, Ma, the Galileo number, G, the Rayleigh number, Ra, and the Peclect number, Pe, defined by

$$Pr=\frac{\nu}{\kappa},\quad Ca=\frac{\mu\kappa}{\varepsilon\sigma_0 d},\quad Ma=\frac{\varepsilon\sigma_1\theta_l d}{\mu\kappa},\quad G=\frac{gd^3}{\nu\kappa},\quad Ra=\frac{g\alpha d^3\theta_l}{\nu\kappa},\quad Pe=\frac{\kappa}{\gamma d^2},$$

in which $\nu=\mu/\rho_l$ is the Kinematic viscosity. When comparing our non-dimensional parameters (i.e. capillary number, Ca, and Marangoni number, Ma) with those in the sharp interface model (see [115] as example), the capillary width ε is considered in our parameters to reflect the effects of the mixing layer of non-zero width. The density ratio, ρ_r, appearing in the system to be evaluated, is

$$\rho_r=\frac{\Big(1+\phi\Big)}{2}+\frac{\Big(1-\phi\Big)}{2}\frac{\rho_2}{\rho_1},$$

so that, in liquid 1($\phi=1$) $\rho_r=1$, and $\rho_r=\rho_2/\rho_1$ in liquid 2 ($\phi=-1$). In addition, for the main system in the isothermal case, we non-dimensionalize the energy of the system (3.6),

$$E=\frac{1}{2}\rho_0||\mathbf{u}||^2_{\mathbf{L}^2(\Omega)}+\frac{\lambda}{2}||\nabla\phi||^2_{\mathbf{L}^2(\Omega)}+\lambda\int_\Omega F(\phi)$$

by rescaling $\bar{E} = E \times d^2/\alpha\mu \times 1/d^2$ based on the energy scale given in [87]. Dropping the bar notation, we can obtain:

$$E = \frac{1}{2Pr}||\mathbf{u}||^2_{\mathbf{L}^2(\Omega)} + \frac{1}{2Ca}||\nabla\phi||^2_{\mathbf{L}^2(\Omega)} + \frac{1}{Ca}\int_\Omega F(\phi), \tag{3.24}$$

and the corresponding non-dimensional energy dissipation law:

$$\frac{dE}{dt} = -\left(||\nabla\mathbf{u}||^2_{\mathbf{L}^2(\Omega)} + \frac{Pe}{Ca}||\nabla(\Delta\phi - f(\phi))||^2_{\mathbf{L}^2(\Omega)}\right). \tag{3.25}$$

3.4 Weak Form

As it can be implemented easily and many existing codes may be incorporated to reduce various complications, a C^0(conforming) finite element method will be employed to solve the problem. To use this method, we will reformulate the phase-field model to obtain a weak form where both trial and test functions are involved with only the first order derivatives.

We first consider the Cahn-Hilliard phase-field equation (3.22):

$$\phi_t + \Big(\mathbf{u}\cdot\nabla\Big)\phi + Pe\Delta\Big(\Delta\phi - f(\phi)\Big) = 0.$$

Due to the bi-harmonic operator in the equation, it is necessary to introduce an extra variable and use the mixed formulation to arrive at the weak form. Hence Eq.(3.22) can be rewritten into the following system (e.g., [65, 127, 131]):

$$\phi_t + \Big(\mathbf{u}\cdot\nabla\Big)\phi = \frac{Pe}{\varepsilon^2}\Delta\Big(\omega + c\phi\Big), \tag{3.26}$$

$$\omega = -\varepsilon^2 \Delta\phi + \Big(\phi^2 - 1 - c\Big)\phi, \tag{3.27}$$

where the positive constant c is introduced to enhance the stability of the numerical method (see [131] as an example).

Now we consider the momentum equation (3.20):

$$\begin{aligned}\frac{1}{Pr}\Big(\mathbf{u}_t + \big(\mathbf{u}\cdot\nabla\big)\Big)\mathbf{u} + \nabla p - \Delta\mathbf{u} + \nabla\cdot\Big(\Big(\frac{1}{Ca} - Ma\theta\Big)\Big(\nabla\phi\otimes\nabla\phi + \frac{|\nabla\phi|^2}{2}\mathbf{I} + F(\phi)\mathbf{I}\Big)\Big)& \\ = \rho_r\Big(Ra\theta - G\Big)\boldsymbol{j}.& \end{aligned} \tag{3.28}$$

A further computation for the surface tension part shows:

$$\begin{aligned}&\nabla\cdot\Big(\Big(\frac{1}{Ca} - Ma\theta\Big)\Big(\nabla\phi\otimes\nabla\phi + \frac{|\nabla\phi|^2}{2}\mathbf{I} + F(\phi)\mathbf{I}\Big)\Big)\\ =& -Ma\Big(\nabla\theta\cdot\nabla\phi\Big)\nabla\phi + \Big(\frac{1}{Ca} - Ma\theta\Big)\Delta\phi\nabla\phi + \Big(\frac{1}{Ca} - Ma\theta\Big)\nabla|\nabla\phi|^2\\ &- Ma\nabla\theta\frac{|\nabla\phi|^2}{2} - Ma\nabla\theta F(\phi) + \Big(\frac{1}{Ca} - Ma\theta\Big)\nabla F(\phi).\end{aligned} \tag{3.29}$$

Note that a second order derivative term is present in the momentum equation, which implies that a C^1 finite element method would normally be required to solve the problem. To avoid this case, we rewrite (3.27) as follows:

$$\Delta\phi = -\frac{1}{\varepsilon^2}\Big(\omega + c\phi\Big) + \frac{1}{\varepsilon^2}\Big(\phi^2 - 1\Big)\phi. \tag{3.30}$$

Now the surface tension term can be rewritten as:

$$\begin{aligned}&\nabla\cdot\Big(\Big(\frac{1}{Ca} - Ma\theta\Big)\Big(\nabla\phi\otimes\nabla\phi + \frac{|\nabla\phi|^2}{2}\mathbf{I} + F(\phi)\mathbf{I}\Big)\Big)\\ =& \Big(-Ma\nabla\theta\cdot\nabla\phi\Big)\nabla\phi - \Big(\frac{1}{Ca} - Ma\theta\Big)\Big(\frac{1}{\varepsilon^2}\Big(\omega + c\phi\Big)\Big)\nabla\phi + \Big(\frac{1}{Ca} - Ma\theta\Big)\nabla|\nabla\phi|^2\end{aligned}$$

$$-Ma\nabla\theta\frac{|\nabla\phi|^2}{2}-Ma\nabla\theta F(\phi)+2\Big(\frac{1}{Ca}-Ma\theta\Big)\nabla F(\phi). \tag{3.31}$$

Substituting the above relation to the momentum equation (3.20), we end up with a modified N-S equation without $\Delta\phi$.

Let Ω be a bounded domain in $\mathbb{R}^2$, suppose $\partial\Omega$ is the boundary of Ω, which is sufficient smooth (for example, Lipschitz-continuous). The following spaces are denoted as $\mathbf{W}^{1,3}(\Omega)=(W^{1,3}(\Omega))^2, \mathbf{W}^{1,3}_{\mathbf{b}}=\{\mathbf{u}\in\mathbf{W}^{1,3}(\Omega), \mathbf{u}=\mathbf{b}_u, \text{ on } \Omega\}, \mathbf{L}^2(\Omega)=(L^2(\Omega))^2$ and $L^2_0(\Omega)=\{p\in L^2(\Omega), \int_\Omega p d\mathbf{x}=0\}$.

By multiplying test functions $\mathbf{v}$, ψ, χ and ζ to the equation (3.20), (3.26), (3.27) and (3.23), respectively, the weak form for the system reads : Find $\mathbf{u}\in\mathbf{W}^{1,3}_{\mathbf{b_u}}(\Omega), p\in\mathbf{L}^2_0(\Omega), \phi\in\mathbf{W}^{1,3}(\Omega), \omega\in\mathbf{W}^{1,3}(\Omega)$ and $\theta\in\mathbf{W}^{1,3}(\Omega)$:

$$\begin{aligned}\int_\Omega\Bigg(&\frac{1}{Pr}\mathbf{u}_t\cdot\mathbf{v}+\frac{1}{Pr}\Big(\mathbf{u}\cdot\nabla\Big)\mathbf{u}\cdot\mathbf{v}+\nabla\mathbf{u}:\nabla\mathbf{v}-p\Big(\nabla\cdot\mathbf{v}\Big)-Ma\Big(\nabla\theta\cdot\nabla\phi\Big)\Big(\nabla\phi\cdot\mathbf{v}\Big)\\&-\frac{1}{\varepsilon^2}\Big(\frac{1}{Ca}-Ma\theta\Big)\Big(\omega+c\phi\Big)\Big(\nabla\phi\cdot\mathbf{v}\Big)+Ma\frac{|\nabla\phi|^2}{2}\Big(\nabla\theta\cdot\mathbf{v}\Big)\\&-\Big(\frac{1}{Ca}-Ma\theta\Big)|\nabla\phi|^2\Big(\nabla\cdot\mathbf{v}\Big)-Ma\,\mathrm{F}(\phi)\Big(\nabla\theta\cdot\mathbf{v}\Big)\\&+2\Big(\frac{1}{Ca}-Ma\theta\Big)f(\phi)\Big(\nabla\cdot\mathbf{v}\Big)\Bigg)d\mathbf{x}=\int_\Omega\Big(\rho_r\Big(Ra\theta-G\Big)\boldsymbol{j}\cdot\mathbf{v}\Big)d\mathbf{x},\end{aligned} \tag{3.32}$$

$$\int_\Omega\Big(\Big(\nabla\cdot\mathbf{u}\Big)q\Big)d\mathbf{x}=0, \tag{3.33}$$

$$\int_\Omega\Big(\phi_t\psi+\Big(\mathbf{u}\cdot\nabla\Big)\phi\psi+\frac{Pe}{\varepsilon^2}\nabla\Big(\omega+c\phi\Big)\cdot\nabla\psi\Big)d\mathbf{x}=0, \tag{3.34}$$

$$\int_\Omega\Big(\omega\chi-\varepsilon^2\nabla\phi\cdot\nabla\chi-\Big(\phi^2-1-c\Big)\phi\chi\Big)d\mathbf{x}=0, \tag{3.35}$$

$$\int_\Omega\Big(\theta_t\zeta+\Big(\mathbf{u}\cdot\nabla\Big)\theta\zeta+\nabla\theta\cdot\nabla\zeta\Big)d\mathbf{x}=0. \tag{3.36}$$

In the homogenous case, taking $\mathbf{v} = \mathbf{u}$, $q = p$, $\psi = \Big(\omega + c\phi\Big)/Ca$ and $\chi = \phi_t/\varepsilon^2 Ca$ in (3.32) (3.34) and (3.35) respectively and summing them up, we obtain the following energy law for the isothermal case,

$$\frac{d}{dt}\left(\frac{1}{2Pr}||\mathbf{u}||^2_{\mathbf{L}^2} + \frac{1}{2Ca}||\nabla\phi||^2_{\mathbf{L}^2} + \frac{1}{Ca}\int_\Omega F(\phi)\right) = -\left(||\nabla\mathbf{u}||^2_{\mathbf{L}^2} + \frac{Pe}{\varepsilon^4 Ca}||\nabla(\omega + c\phi||^2_{\mathbf{L}^2}\right). \quad (3.37)$$

3.5 Numerical Methods

For our computations, a finite difference scheme in time and a conformal C^0 finite element method in space are used to approximate the solutions of the weak problem. In the temporal direction, since phase-field models are highly nonlinear, explicit-implicit (or semi-implicit) first order schemes are usually adopted, where a part of the nonlinear term is treated explicitly and the rest is treated implicitly. We will use a modified midpoint scheme [65, 83, 84], which is originally designed for a liquid crystal model, to compute the advective Cahn-Hilliard equations. With this method, a discrete energy law can be obtained and consistent to the continuous one. However, Hua et. al. [65] observed some non-physical oscillations of the solution at the interface defined by $\phi = 0$, which were caused by the time discretization using this midpoint method. A remedy was proposed that a lower order scheme (say, implicit backward Euler) was used at the initial time step and the modified midpoint scheme for other ones. The corresponding algorithm will be adopted in the present work.

Let

$$\mathbf{W} = \mathbf{W}^{1,3}_{\mathbf{b_u}}(\Omega) \times L^2_0(\Omega) \times W^{1,3}(\Omega) \times W^{1,3}(\Omega),$$

then we seek the weak solutions of the resulting variational forms in $\mathbf{W}^h = \mathbf{U}^h \times P^h \times \mathbf{H}^h \times \mathbf{T}^h$, which is a subspace of $\mathbf{W}$ given by a finite element discretization of Ω, $\mathbf{W}_0^h$ represents the space $\mathbf{W}^h$ satisfying the homogeneous Dirichlet boundary condition.

If $(\mathbf{u}_h^n, p_h^n, \phi_h^n, \omega_h^n, \theta_h^n) \in \mathbf{W}^h$ is an approximation of $\mathbf{u}(t^n) = \mathbf{u}(n\Delta t), p(t^n) = p(n\Delta t)$, $\phi(t^n) = \phi(n\Delta t)$, $\omega(t^n) = \omega(n\Delta t)$ and $\theta(t^n) = \theta(n\Delta t)$ at time t^n with Δt representing the time step size, then the approximation at time $t^{n+1} = (n+1)\Delta t$ can be denoted as, $(\mathbf{u}_h^{n+1}, p_h^{n+1}, \phi_h^{n+1}, \omega_h^{n+1}, \theta_h^{n+1}) \in \mathbf{W}^h$ and can be computed by the following finite element methods:

$$
\begin{aligned}
\int_\Omega \Bigg(& \frac{1}{Pr}\Big(\mathbf{u}_{\bar{t}}^{n+1} \cdot \mathbf{v} + \Big(\mathbf{u}_h^{n+\frac{1}{2}} \cdot \nabla\Big)\mathbf{u}_h^{n+\frac{1}{2}} \cdot \mathbf{v} + \frac{1}{2}\Big(\nabla \cdot \mathbf{u}_h^{n+\frac{1}{2}}\Big)\mathbf{u}_h^{n+\frac{1}{2}} \cdot \mathbf{v}\Big) + \nabla \mathbf{u}_h^{n+\frac{1}{2}} : \nabla \mathbf{v} \\
& - p_h^{n+\frac{1}{2}}\Big(\nabla \cdot \mathbf{v}\Big) - Ma\Big(\nabla \theta_h^{n+\frac{1}{2}} \cdot \nabla \phi_h^{n+\frac{1}{2}}\Big)\nabla \phi_h^{n+\frac{1}{2}} \cdot \mathbf{v} \\
& - \frac{1}{\varepsilon^2}\Big(\frac{1}{Ca} - Ma\theta_h^{n+\frac{1}{2}}\Big)\Big(\omega_h^{n+\frac{1}{2}} + c\phi_h^{n+\frac{1}{2}}\Big)\nabla \phi_h^{n+\frac{1}{2}} \cdot \mathbf{v} + \frac{Ma}{2}\left|\nabla \phi_h^{n+\frac{1}{2}}\right|^2 \nabla \theta_h^{n+\frac{1}{2}} \cdot \mathbf{v} \\
& - \Big(\frac{1}{Ca} - Ma\theta_h^{n+\frac{1}{2}}\Big)\left|\nabla \phi_h^{n+\frac{1}{2}}\right|^2 \Big(\nabla \cdot \mathbf{v}\Big) - MaF_h(\phi_h^{n+1}, \phi_h^n)\nabla \theta_h^{n+\frac{1}{2}} \cdot \mathbf{v} \\
& + \frac{2}{\varepsilon^2}\Big(\frac{1}{Ca} - Ma\theta_h^{n+\frac{1}{2}}\Big)g_h(\phi_h^{n+1}, \phi_h^n)\theta_h^{n+\frac{1}{2}} \cdot \mathbf{v}\Bigg) d\mathbf{x} \\
& = \int_\Omega \Bigg(\rho_r(\phi_h^{n+\frac{1}{2}})\Big(Ra\theta_h^{n+\frac{1}{2}} - G\Big)\boldsymbol{j} \cdot \mathbf{v}\Bigg) d\mathbf{x}, \qquad (3.38)
\end{aligned}
$$

$$
\int_\Omega \Bigg(\Big(\nabla \cdot \mathbf{u}_h^{n+\frac{1}{2}}\Big)q\Bigg) d\mathbf{x} = 0, \qquad (3.39)
$$

$$
\int_\Omega \Bigg(\phi_{\bar{t}}^{n+1}\psi + \Big(\mathbf{u}_h^{n+\frac{1}{2}} \cdot \nabla\Big)\phi_h^{n+\frac{1}{2}}\psi + \frac{Pe}{\varepsilon^2}\nabla\Big(\omega_h^{n+\frac{1}{2}} + c\phi_h^{n+\frac{1}{2}}\Big) \cdot \nabla\psi\Bigg) d\mathbf{x} = 0, \qquad (3.40)
$$

$$
\int_\Omega \Bigg(\Big(\omega_h^{n+\frac{1}{2}} + c\phi_h^{n+\frac{1}{2}}\Big)\chi - \varepsilon^2 \nabla \phi_h^{n+\frac{1}{2}} \cdot \nabla\chi - g_h(\phi_h^{n+1}, \phi_h^n)\chi\Bigg) d\mathbf{x} = 0, \qquad (3.41)
$$

$$
\int_\Omega \Bigg(\theta_{\bar{t}}^{n+1}\zeta + \Big(\mathbf{u}_h^{n+\frac{1}{2}} \cdot \nabla\Big)\theta_h^{n+\frac{1}{2}}\zeta + \nabla \theta_h^{n+\frac{1}{2}} \cdot \nabla\zeta\Bigg) d\mathbf{x} = 0, \qquad (3.42)
$$

for all $(\mathbf{v}, q, \psi, \chi, \zeta) \in \mathbf{W}_0^h$, where $\mathbf{u}_{\bar{t}}^{n+1} = \frac{1}{\Delta t}(\mathbf{u}_h^{n+1} - \mathbf{u}_h^n), \mathbf{u}_h^{n+\frac{1}{2}} = \frac{1}{2}(\mathbf{u}_h^{n+1} + \mathbf{u}_h^n)$, $p_h^{n+\frac{1}{2}} = \frac{1}{2}(p_h^{n+1} + p_h^n), \phi_{\bar{t}}^{n+1} = \frac{1}{\Delta t}(\phi_h^{n+1} - \phi_h^n), \phi_h^{n+\frac{1}{2}} = \frac{1}{2}(\phi_h^{n+1} + \phi_h^n), \omega_h^{n+\frac{1}{2}} = \frac{1}{2}(\omega_h^{n+1} + \omega_h^n), \theta_{\bar{t}}^{n+1} = \frac{1}{\Delta t}(\theta_h^{n+1} - \theta_h^n), \theta_h^{n+\frac{1}{2}} = \frac{1}{2}(\theta_h^{n+1} + \theta_h^n)$, and the other two terms, $\mathrm{F}_h(\phi_h^{n+1}, \phi_h^n) = \frac{1}{16\varepsilon^2}((|\phi_h^{n+1}|^2 - 1) + (|\phi_h^n|^2 - 1))^2$, $\mathrm{g}_h(\phi_h^{n+1}, \phi_h^n) = \frac{1}{4}((|\phi_h^{n+1}|^2 - 1) + (|\phi_h^n|^2 - 1))(\phi_h^{n+1} + \phi_h^n)$, are the approximations of the nonlinear function $F(\phi)$ and $g(\phi) = (|\phi|^2 - 1)\phi$ respectively.

Note that, the divergence free equation (3.39) will be replaced by the following formulation corresponding to the penalty method:

$$\int_\Omega \left((\nabla \cdot \mathbf{u}_h^{n+\frac{1}{2}} + \delta p_h^{n+\frac{1}{2}}) q \right) d\mathbf{x} = 0, \tag{3.43}$$

in which a small term containing the pressure is added. In our computations, the coefficient δ is chosen to be 10^{-6} to enforce the divergence free condition. When it is necessary to use a larger δ in order to improve the stability and accuracy a sequential regularisation formulation (see [82]) may be used to replace the penalty formulation. The divergence of the velocity, however, is no longer exactly zero after the above replacement. In order to maintain the possible underlying energy law, a term $\frac{1}{2}(\nabla \cdot \mathbf{u}_h^{n+\frac{1}{2}})\mathbf{u}_h^{n+\frac{1}{2}}$ is added in (3.38), corresponding to an additional zero term $\frac{1}{2}(\nabla \cdot \mathbf{u})\mathbf{u}$ to (3.1) following the pseudo-compressibility method that was mentioned in [117].

Those three terms in (3.38), i.e. $F_h(\phi_h^{n+1}, \phi_h^n)$, $g_h(\phi_h^{n+1}, \phi_h^n)$ and $\frac{1}{2}(\nabla \cdot \mathbf{u}_h^{n+\frac{1}{2}})\mathbf{u}_h^{n+\frac{1}{2}}$, based on the modified midpoint scheme, are so designed that when taking the surface tension coefficient as a constant (isotherm case, say, $\lambda_1 = 0$) and ignoring the external forces term (e.g. the gravitational term), an accurate discrete energy law for the fully

discrete system can still be derived:

$$\left(\frac{1}{2Pr}||\mathbf{u}_h^{n+1}||^2_{\mathbf{L}^2}+\frac{1}{2Ca}||\nabla\phi_h^{n+1}||^2_{\mathbf{L}^2}+\frac{1}{Ca}\int_\Omega F(\phi_h^{n+1})\right)_{\bar{t}}$$
$$=-\left(||\nabla\mathbf{u}_h^{n+\frac{1}{2}}||^2_{\mathbf{L}^2}+\frac{Pe}{\varepsilon^4 Ca}||\nabla(\omega_h^{n+\frac{1}{2}}+c\phi_h^{n+\frac{1}{2}}||^2_{\mathbf{L}^2}\right), \quad (3.44)$$

in which way, our methods are trying to maintain such a possible underlying energy law at its greatest extent for the case where the surface tension is assumed to be temperature dependent.

3.6 Implementation issues

In this section, we consider the iterative algorithm to compute the solutions of the modified midpoint scheme. Since the system (3.20)-(3.23) is a strongly coupling system, including a modified N-S equation, an advective Cahn-Hilliard equation and an energy transport equation, a linearisation is needed so that the solutions can be computed by solving a linear system at each time step. In [113], Newton's method was employed to linearise a similar complicated system, which led to a linear system depending on time. A different linear system had to be solved for every time step, indicating that the process would be highly time-consuming. In the present work, a fixed point iteration is used as a linearisation for all the nonlinear terms, so that we can get a linear system which is symmetric and, more importantly, does not depend on time. Then the Cholesky factorisation is needed only once to factorize the symmetric linear system at the initial time step, since after that the coefficient matrix will remain the same. So the solution of the implicit scheme can be computed as if it is an explicit scheme at any time step other than the initial one.

The algorithm is designed as the following:

Starting with $(\mathbf{u}^n, p^n, \phi^n, \omega^n, \theta^n)$ as the initial guesses at the $(n+1)$th time step, we can find the solutions $(\mathbf{u}_{k+1}^{n+1}, p_{k+1}^{n+1}, \phi_{k+1}^{n+1}, \omega_{k+1}^{n+1}, \theta_{k+1}^{n+1})$ (which can be seen as approximations for $\mathbf{u}^{n+1}, p^{n+1}, \phi^{n+1}, \omega^{n+1}$ and θ^{n+1}, respectively) by interactively solving the variational equations:

(a) for the initial estimate, the Backward Euler method is employed:

$$
\begin{aligned}
&\int_\Omega \Bigg(\frac{1}{Pr}\Big(\frac{\mathbf{u}_{k+1}^{n+1}-\mathbf{u}^n}{\Delta t}\cdot\mathbf{v} + \Big(\mathbf{u}_k^{n+1}\cdot\nabla\Big)\mathbf{u}_k^{n+1}\cdot\mathbf{v} + \frac{1}{2}\Big(\nabla\cdot\mathbf{u}_k^{n+1}\Big)\mathbf{u}_k^{n+1}\cdot\mathbf{v}\Big) \\
&+ \nabla\frac{\mathbf{u}_{k+1}^{n+1}+\mathbf{u}^n}{2} : \nabla\mathbf{v} - \frac{p_{k+1}^{n+1}+p^n}{2}\Big(\nabla\cdot\mathbf{v}\Big) - Ma\Big(\nabla\theta_k^{n+1}\cdot\nabla\phi_k^{n+1}\Big)\Big(\nabla\phi_k^{n+1}\cdot\mathbf{v}\Big) \\
&- \frac{1}{\varepsilon^2}\Big(\frac{1}{Ca} - Ma\theta_k^{n+1}\Big)\Big(\omega_k^{n+1}+c\phi_k^{n+1}\Big)\Big(\nabla\phi_k^{n+1}\cdot\mathbf{v}\Big) \\
&+ \frac{Ma}{2}\Big|\nabla\phi_k^{n+1}\Big|^2\Big(\nabla\theta_k^{n+1}\cdot\mathbf{v}\Big) - \Big(\frac{1}{Ca} - Ma\theta_k^{n+1}\Big)|\nabla\phi_k^{n+1}|^2\Big(\nabla\cdot\mathbf{v}\Big) \\
&- MaF_h(\phi_k^{n+1},\phi^n)\Big(\nabla\theta_k^{n+1}\cdot\mathbf{v}\Big) + \frac{2}{\varepsilon^2}\Big(\frac{1}{Ca} - Ma\theta_k^{n+1}\Big)g_h(\phi_k^{n+1},\phi^n)\Big(\nabla\theta_k^{n+1}\cdot\mathbf{v}\Big)\Bigg)d\mathbf{x} \\
&= \int_\Omega \Big(\rho_r(\phi_k^{n+1})\Big(Ra\theta_k^{n+1}-G\Big)\boldsymbol{j}\cdot\mathbf{v}\Big)d\mathbf{x}, \qquad (3.45)
\end{aligned}
$$

$$
\int_\Omega \Big(\Big(\nabla\cdot\frac{\mathbf{u}_{k+1}^{n+1}+\mathbf{u}^n}{2} + \delta\frac{p_{k+1}^{n+1}+p^n}{2}\Big)q\Big)d\mathbf{x} = 0, \qquad (3.46)
$$

$$
\int_\Omega \Big(\frac{\phi_{k+1}^{n+1}-\phi^n}{\Delta t}\psi + \Big(\mathbf{u}_k^{n+1}\cdot\nabla\Big)\phi_k^{n+1}\psi + \frac{Pe}{\varepsilon^2}\nabla\Big(\omega_{k+1}^{n+1}+c\phi_{k+1}^{n+1}\Big)\cdot\nabla\psi\Big)d\mathbf{x} = 0, \qquad (3.47)
$$

$$
\int_\Omega \Big(\Big(\omega_{k+1}^{n+1}+c\phi_{k+1}^{n+1}\Big)\chi - \varepsilon^2\nabla\phi_{k+1}^{n+1}\cdot\nabla\chi - g_h(\phi_k^{n+1},\phi^n)\chi\Big)d\mathbf{x} = 0, \qquad (3.48)
$$

$$
\int_\Omega \Big(\frac{\theta_{k+1}^{n+1}-\theta^n}{\Delta t}\zeta + \Big(\mathbf{u}_k^{n+1}\cdot\nabla\Big)\theta_k^{n+1}\zeta + \nabla\theta_{k+1}^{n+1}\cdot\nabla\zeta\Big)d\mathbf{x} = 0. \qquad (3.49)
$$

(b) for the other iteration steps, a modified midpoint method is used. And then the

resulting nonlinear system is solved by a fixed point iteration, evaluating all the nonlinear terms as the previous iteration.

$$
\begin{aligned}
&\int_\Omega \Bigg(\frac{1}{Pr}\Big(\frac{\mathbf{u}_{k+1}^{n+1}-\mathbf{u}^n}{\Delta t}\cdot\mathbf{v} + \Big(\frac{\mathbf{u}_k^{n+1}+\mathbf{u}^n}{2}\cdot\nabla\Big)\frac{\mathbf{u}_k^{n+1}+\mathbf{u}^n}{2}\cdot\mathbf{v} + \frac{1}{2}\Big(\nabla\cdot\frac{\mathbf{u}_k^{n+1}+\mathbf{u}^n}{2}\Big)\frac{\mathbf{u}_k^{n+1}+\mathbf{u}^n}{2}\Big) \\
&\quad + \nabla\frac{\mathbf{u}_{k+1}^{n+1}+\mathbf{u}^n}{2} : \nabla\mathbf{v} - \frac{p_{k+1}^{n+1}+p^n}{2}\Big(\nabla\cdot\mathbf{v}\Big) + \frac{Ma}{2}\left|\nabla\frac{\phi_k^{n+1}+\phi^n}{2}\right|^2\Big(\nabla\frac{\theta_{k-1}^{n+1}+\theta^n}{2}\cdot\mathbf{v}\Big) \\
&\quad - Ma\Big(\nabla\frac{\theta_k^{n+1}+\theta^n}{2}\cdot\nabla\frac{\phi_k^{n+1}+\phi^n}{2}\Big)\Big(\nabla\frac{\phi_k^{n+1}+\phi^n}{2}\cdot\mathbf{v}\Big) \\
&\quad - \frac{1}{\varepsilon^2}\Big(\frac{1}{Ca} - Ma\frac{\theta_k^{n+1}+\theta^n}{2}\Big)\Big(\frac{\omega_k^{n+1}+\omega^n}{2} + c\frac{\phi_k^{n+1}+\phi^n}{2}\Big)\Big(\nabla\frac{\phi_k^{n+1}+\phi^n}{2}\cdot\mathbf{v}\Big) \\
&\quad - \Big(\frac{1}{Ca} - Ma\frac{\theta_k^{n+1}-\theta^n}{2}\Big)|\nabla\frac{\phi_k^{n+1}+\phi^n}{2}|^2\Big(\nabla\cdot\mathbf{v}\Big) - MaF_h(\phi_k^{n+1},\phi^n)\nabla\frac{\theta_k^{n+1}+\theta^n}{2}\cdot\mathbf{v} \\
&\quad + \frac{2}{\varepsilon^2}\Big(\frac{1}{Ca} - Ma\frac{\theta_k^{n+1}+\theta^n}{2}\Big)g_h(\phi_k^{n+1},\phi^n)\nabla\frac{\theta_k^{n+1}+\theta^n}{2}\cdot\mathbf{v}\Bigg)d\mathbf{x} \\
&= \int_\Omega \Bigg(\rho_r(\frac{\phi_k^{n+1}+\phi^n}{2})\Big(Ra\frac{\theta_k^{n+1}+\theta^n}{2} - G\Big)\boldsymbol{j}\cdot\mathbf{v}\Bigg)d\mathbf{x} = 0, \qquad (3.50)
\end{aligned}
$$

$$
\int_\Omega \Bigg(\Big(\nabla\cdot\frac{\mathbf{u}_{k+1}^{n+1}+\mathbf{u}^n}{2} + \delta\frac{p_{k+1}^{n+1}+p^n}{2}\Big)q\Bigg)d\mathbf{x} = 0, \qquad (3.51)
$$

$$
\begin{aligned}
&\int_\Omega \Bigg(\frac{\phi_{k+1}^{n+1}-\phi^n}{\Delta t}\psi + \Big(\frac{\mathbf{u}_k^{n+1}+\mathbf{u}^n}{2}\cdot\nabla\Big)\frac{\phi_k^{n+1}+\phi^n}{2}\psi \\
&\quad + \frac{Pe}{\varepsilon^2}\nabla\Big(\frac{\omega_{k+1}^{n+1}+\omega^n}{2} + c\frac{\phi_{k+1}^{n+1}+\phi^n}{2}\Big)\cdot\nabla\psi\Bigg)d\mathbf{x} = 0, \qquad (3.52)
\end{aligned}
$$

$$
\int_\Omega \Bigg(\Big(\frac{\omega_{k+1}^{n+1}+\omega^n}{2} + c\frac{\phi_{k+1}^{n+1}+\phi^n}{2}\Big)\chi - \varepsilon^2\nabla\frac{\phi_{k+1}^{n+1}+\phi^n}{2}\cdot\nabla\chi - g_h(\phi_k^{n+1},\phi^n)\chi\Bigg)d\mathbf{x} = 0, \qquad (3.53)
$$

$$
\int_\Omega \Bigg(\frac{\theta_{k+1}^{n+1}-\theta^n}{\Delta t}\zeta + \Big(\frac{\mathbf{u}_k^{n+1}+\mathbf{u}^n}{2}\cdot\nabla\Big)\frac{\theta_k^{n+1}+\theta^n}{2}\zeta + \nabla\frac{\theta_{k+1}^{n+1}+\theta^n}{2}\cdot\nabla\zeta\Bigg)d\mathbf{x} = 0. \qquad (3.54)
$$

Considering the following stopping criteria for the iteration, if

$$(||\mathbf{u}_{k+1}^{n+1}-\mathbf{u}_{k}^{n+1}||_{\mathbf{L}^2}^2+||\phi_{k+1}^{n+1}-\phi_{k}^{n+1}||_{\mathbf{L}^2}^2+||\omega_{k+1}^{n+1}-\omega_{k}^{n+1}||_{\mathbf{L}^2}^2+||\theta_{k+1}^{n+1}-\theta_{k}^{n+1}||_{\mathbf{L}^2}^2)^{\frac{1}{2}}$$
$$\leqslant tolerance, \tag{3.55}$$

then the solutions for the $(k+1)$th time step can be defined as

$$(\mathbf{u}^{n+1},p^{n+1},\phi^{n+1},\omega^{n+1},\theta^{n+1})=(\mathbf{u}_{k+1}^{n+1},p_{k+1}^{n+1},\phi_{k+1}^{n+1},\omega_{k+1}^{n+1},\theta_{k+1}^{n+1}), \tag{3.56}$$

otherwise, the current iteration would be continued. As it can be seen that the stiffness matrix is independent of the time step n and the number s of the fixed point iterations, and is symmetric if $c=0$. Therefore in our computations, the Cholesky factorisation was only used to solve the NS equations (3.50), (3.51), and the direct solver (UMFPACK) is used to solve the CH (3.52), (3.53) and heat equations (3.54). Moreover, the system (3.50)-(3.51) for $\mathbf{u}$ and p, the system (3.52)-(3.53) for ϕ and ω and also (3.54) for θ are separated automatically, which means that ϕ_{k+1}^{n+1} and ω_{k+1}^{n+1} can be obtained first by solving (3.52)-(3.53), then followed by solving (3.54) to obtain θ_{k+1}^{n+1}, the NS equation would be solved finally in order to get $\mathbf{u}_{k+1}^{n+1}$ and p_{k+1}^{n+1}. This procedure further reduces the size of the system and the cost of computations. It could also be an efficient way to achieve time-domain parallelization.

3.7 Numerical experiments for Bénard-Marangoni convection for heating from above

Since two immiscible liquids (Acetonitrile and n-Hexane) share the similar physical properties, the system consisting of an Acetonitrile and an n-Hexane can be solved by

Property	Acetonitrile	n-Hexane
$\rho(10^3\ kgm^{-3})$	0.776	0.655
$\nu(10^{-6}\ m^2s^{-1})$	0.476	0.458
$k(10^{-1}\ Jm^{-1}s^{-1}K^{-1})$	1.88	1.20
$c_p(10^3\ Jkg^{-1}K^{-1})$	2.23	2.27
$\alpha(10^{-3}\ K^{-1})$	1.41	1.41
$\sigma_0(10^{-3}\ Nm^{-1})$	28.66	17.89
$\sigma_1(10^{-5}\ Nm^{-1}K^{-1})$	12.63	10.22

Table 3.1: Physical properties of the Acetonitrile and n-Hexane.

our phase-field model, where all the properties (except the density) of the two liquids can be assumed to be the same (here we employ the parameters of n-Hexane for both fluids). We will compute a few examples for Bénard-Marangoni convection in such a two-layer fluid system heated from above, with the physical properties reported by Jule ([73], see the following table). Note that a similar simulation was also performed by Cliffe and Tanvern [115], in which a sharp interface was assumed.

3.7.1 Mechanism for Bénard-Marangoni convection

The mechanism of heating from above, as sketched in Figure 3.1, has been summarized by Johnson and Narayanan [72]. In both diagrams, the two-layer fluid systems are all heated from above, with a constant temperature gradient between the two horizontal plates. In the upper diagram (Case 1), a perturbation in the interface towards the low temperature side is assumed (bottom boundary). This local temperature reduction of interface lowers the surface tension and leads to a surface tension gradient along the interface due to its temperature dependence, with the largest surface tension in the centre of the interface. For the upper layer, this local gradient drags the fluid towards the centre of the interface. This is then replaced by hot fluid flowing downward from the top boundary to the edge of the interface, reinforcing the perturbation. Meanwhile, as the flow of the lower fluid is viscously coupled, there is upwelling of cold fluid

from the bottom boundary to the edge of the interface, which tends to lower the local temperature and dampen the perturbation.

The lower diagram (Case 2 in Figure 3.1) just shows the opposite scenario, in which the perturbation in the interface towards the high temperature side (top boundary) is assumed. Again, the convection set in, with the flow in the upper layer reinforcing the instability and reducing it in the lower layer.

As shown in Figure 3.1, a rectangular domain is defined that $\Omega = \Omega_1 \cup \Omega_2 = [0,2] \times [0,1]$. Let $\partial\Omega = \partial\Omega_1 \cup \partial\Omega_{21} \cup \partial\Omega_{22} \cup \partial\Omega_3 \cup \partial\Omega_{41} \cup \partial\Omega_{42}$ denote the boundary of Ω_r, $d = d_1 + d_2$ is the distance between two horizontal plates, P_1, P_2 denote two intersection points between boundary $\partial\Omega$ and the horizontal midline Γ, where Γ is also adopted as the initial interface for the two-layer fluid. Now we give the boundary and initial conditions for the problem.

Boundary and Initial conditions for velocity

$$\mathbf{u}|_{\partial\Omega} = 0, \quad \mathbf{u}_0(x) = p_0(x) = 0 \qquad (x \in \Omega). \tag{3.57}$$

Boundary and Initial conditions for phase

$$\phi|_{P_1 \cup P_2} = 0, \quad \phi|_{\partial\Omega_1 \cup \partial\Omega_{21} \cup \partial\Omega_{41} \setminus (P_1 \cup P_2)} = 1, \quad \phi|_{\partial\Omega_3 \cup \partial\Omega_{22} \cup \partial\Omega_{42} \setminus (P_1 \cup P_2)} = -1, \tag{3.58}$$

$$\phi_0(x) = 1 \ (x \in \Omega_1), \quad \phi_0(x) = -1 \ (x \in \Omega_2), \quad \phi_0(x) = 0 \ (x \in \Gamma). \tag{3.59}$$

Since in the present work, the experiments are carried out to test our phase-field model with thermocapillary effects, a Dirichlet boundary condition for ϕ is assigned, implying that the intersection points between the phase interface and boundary $\partial\Omega$, on which $\phi = 0$, are fixed. When it is necessary to consider the effects where the fluid-fluid interface intersects the plates, the moving contact line problem will be involved. The generalized Navier boundary condition for the velocity $\mathbf{u}$ and a dynamic boundary condition for the phase variable ϕ can be imposed to supplement the phase-field model

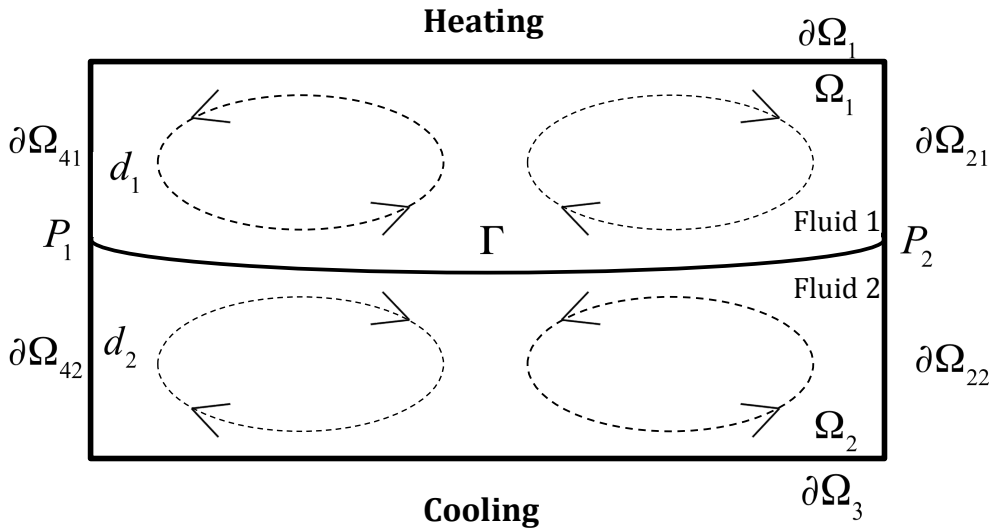

Case 1

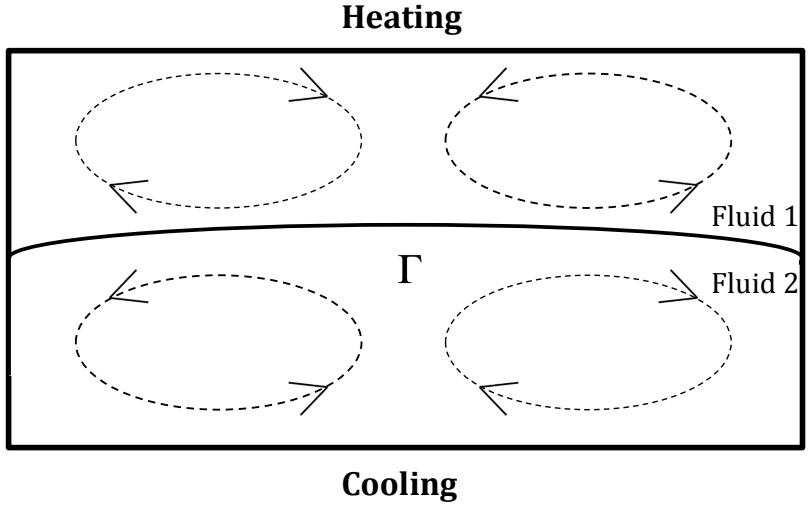

Case 2

Figure 3.1: Sketch for two cases of Marangoni-Bénard convection in a two-layer fluid system heated from above.

(see [45] as an example). Further, Γ is assumed to be the initial position of the interface

$$\Gamma = \Gamma_m + \Gamma_p,$$

where Γ_m is the midline of the domain, and Γ_p is the perturbation added in the interface. Based on the work done by Tavener et. al. [115], a half cycle of a sine wave is added as a perturbation, say, $\Gamma_p = a_1 \sin(k \times 2\pi x) + c_1$ for Case 1, and $\Gamma_p = a_2 \sin(k \times 2\pi x) + c_2$ for Case 2, where $a_1 = 0.1, c_1 = -0.05, a_2 = -0.1, c_2 = 0.05$ and $k = 0.5$.

Boundary and Initial conditions for temperature

For top heating and bottom cooling, the temperature boundary conditions for the two horizontal plates can be given as:

$$\theta|_{\partial\Omega_1} = 1, \quad \theta|_{\partial\Omega_3} = 0, \tag{3.60}$$

since the two vertical plates are assumed to be adiabatic, Neumann boundary conditions are specified:

$$\frac{d\theta}{dx}|_{\partial\Omega_2} = \frac{d\theta}{dx}|_{\partial\Omega_4} = 0 \tag{3.61}$$

for the two vertical plates. Note that the temperature boundary conditions are not specified on $\partial\Omega_{21}$, $\partial\Omega_{22}$, $\partial\Omega_{41}$ and $\partial\Omega_{42}$.

The initial condition for temperature is given as:

$$\theta_0(x) = A\hat{e}_T \cdot \mathbf{r} \quad (x \in \Omega), \tag{3.62}$$

where a temperature gradient of the above form is imposed, A is a constant, $\hat{e}_T$ is the unit vector in the direction of the temperature gradient and $\mathbf{r} = (x, y)$ is the spatial coordinate. Based on our top and bottom temperature boundary condition, a constant temperature gradient between two horizontal plates is assumed, say, $A = 1, \hat{e}_T = (0, 1)$.

Numerical Results

Considering the boundary and initial conditions (3.57)-(3.62), we compute a few examples for Bénard-Marangoni convection in an Acetonitrile and an n-Hexane system heated from above to justify our phase-field model and further to demonstrate our method. A 60×30 grid will be used for all the examples. The computations are carried out with the help of the freefem++ platform ([61]) and MATLAB. We apply the fixed point iterative method (cf. (3.45)-(3.49) and (3.50)-(3.54)) with a sufficiently small tolerance. All computations are carried out using the P_2 (piecewise polynomial of degree two) finite element space for the velocity $\mathbf{u}$, the phase variables ϕ, ω and the temperature variable θ, and the P_1 finite element space for the pressure p. All the computations are performed with the following parameter values if not otherwise stated, $Pr = 5.76, Ca = 10^{-3}, G = 5\times10^{4}, Ra = 2\times10^{3}, \rho_r = 1.2, \varepsilon = 10^{-2}, Pe = 2.5\times10^{-3}, \delta t = 10^{-4}$. Note that our numerical method works well and can converge within several iteration steps (e.g., 10-15 iteration stpes) with this set of parameter values. However, when we chagne the parameter value (for example, increasing *Pe* or reducing ε), our numerical method seems to converge hardly. The reason is that as we increase the value of *Pe*, the diffusivity of the diffuse interface is increased as well. The fast changes of the interface can be a challenge to convergence of the numerical methods. On the other hand, as we decrease the value of ε, the thickness of the diffuse interface is decreased correspondingly, a finer remeshment is required so that the thin interfacial region can be resovled. Therefore, for a larger value of *Pe* a smaller time step is suggested, and for a smaller value of ε a finer mesh (especially for the interfacial region) is required.

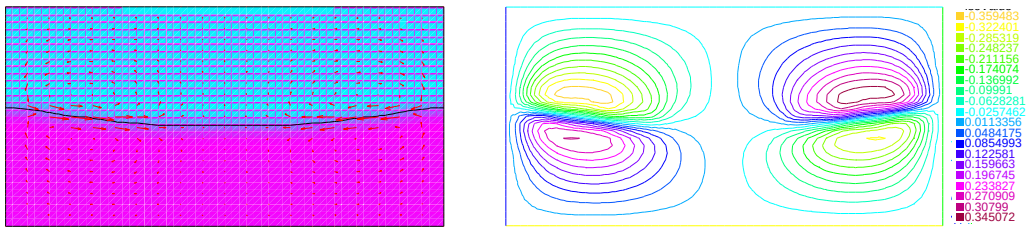

$t = 10\delta t$

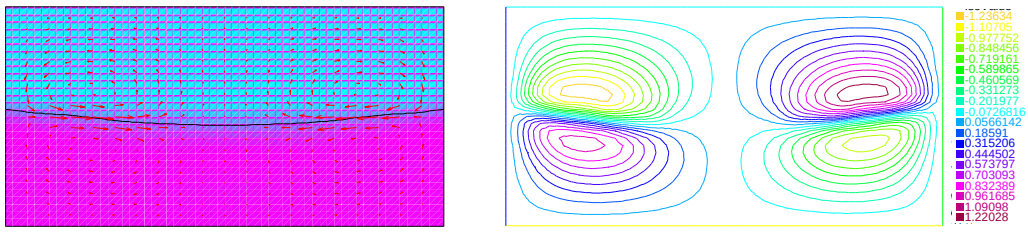

$t = 100\delta t$

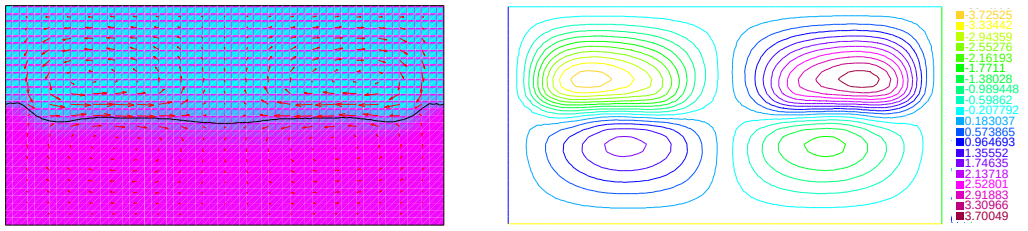

$t = 400\delta t$

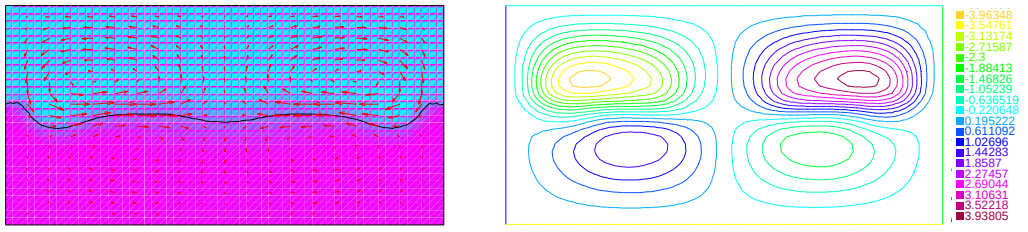

$t = 500\delta t$

Figure 3.2: Flow field with deformed interface and Streamlines for Bénard-Marangoni convection with $Ma = 80$ in Case 1. Positive values of the stream function indicate clockwise circulation and negative values indicate anti-clockwise circulation. $Pr = 5.76, Ca = 2.5 \times 10^{-3}, G = 5 \times 10^{4}, Ra = 2 \times 10^{3}, \rho_r = 1.2, \varepsilon = 10^{-2}$ and $Pe = 2.5 \times 10^{-3}$.

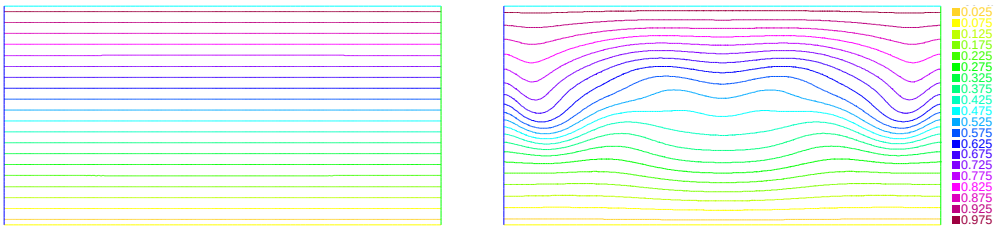

$t = 0$ $t = 500\delta t$

Figure 3.3: Isotherms for Bénard-Marangoni convection with $Ma = 80$ in Case 1. $Pr = 5.76, Ca = 2.5 \times 10^{-3}, G = 5 \times 10^{4}, Ra = 2 \times 10^{3}, \rho_r = 1.2, \varepsilon = 10^{-2}$ and $Pe = 2.5 \times 10^{-3}$.

3.7.2 Ma=80 for Case 1

We first compute an example for Case 1. The velocity field and the deformation of the interface are shown on the left in Figure 3.2, while on the right is the streamlines. As can be seen that, the Marangoni forces dominate the convection for $Ma = 80$. As the two pairs of anti-rotating convection set in, the fluid is dragged from both the edge to the middle of the domain, producing downwelling along the centreline of the lower fluid and upwelling of the upper fluid. As time progresses, the pair of rolls in the upper layer dominates the convection, leading to a slight deformation of the interface.

Figure 3.3 shows the corresponding isotherms. For $t = 500\delta t$, we can see that, the isotherm lines in the upper and lower layers are distorted strongly further away from each other along the centreline, and closer to each other along the edges. Due to the strong heat convection in both layers, the local temperature of the middle of the interface is kept lower than that of the edges, despite the slight deformation of the interface.

3.7.3 Ma=80 for Case 2

This time, we compute the flow with the perturbation in Case 2, where all the values of parameters including Marangoni number are kept the same as in §3.7.1.

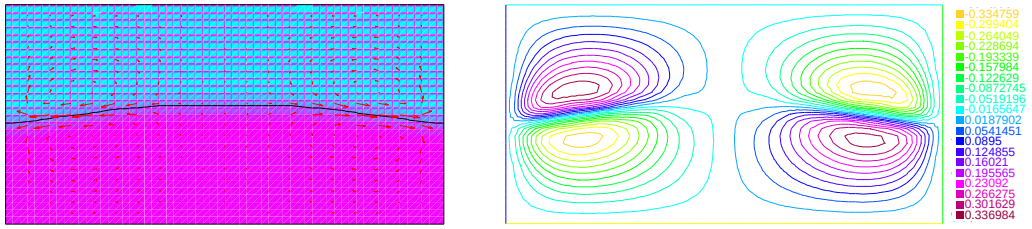

$t = 10\delta t$

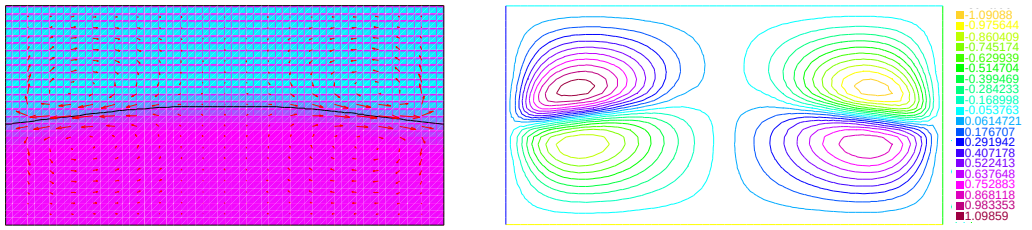

$t = 100\delta t$

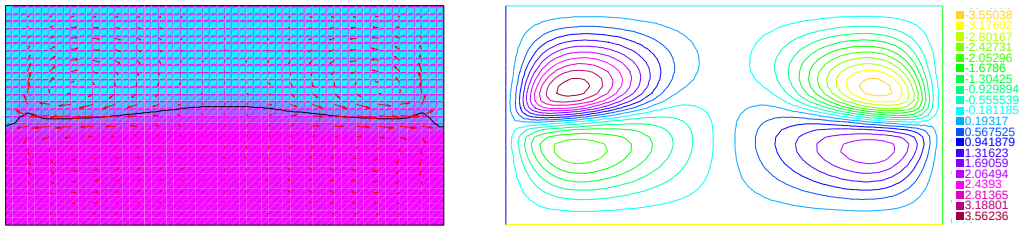

$t = 400\delta t$

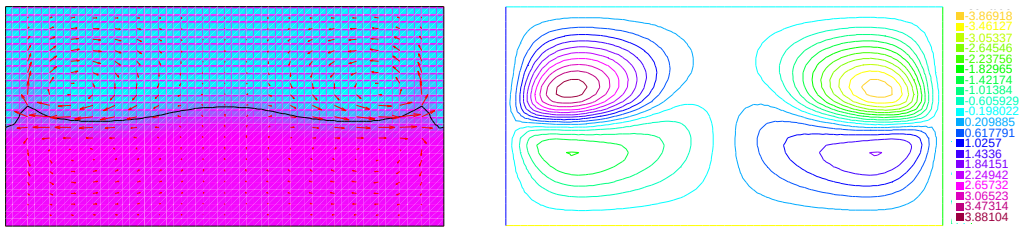

$t = 500\delta t$

Figure 3.4: Flow field with deformed interface and streamlines for Bénard-Marangoni convection with $Ma = 80$ in case 2. Positive values of the stream function indicate clockwise circulation and negative values indicate anti-clockwise circulation. $Pr = 5.76, Ca = 2.5 \times 10^{-3}, G = 5 \times 10^{4}, Ra = 2 \times 10^{3}, \rho_r = 1.2, \varepsilon = 10^{-2}$ and $Pe = 2.5 \times 10^{-3}$.

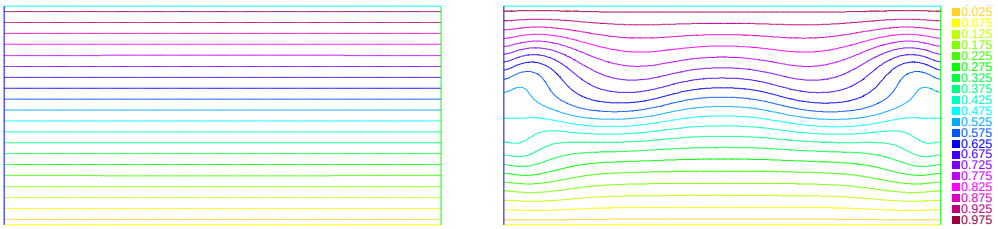

$t = 0$ $t = 500\delta t$

Figure 3.5: Isotherms Bénard-Marangoni convection with $Ma = 80$ in case 2. $Pr = 5.76, Ca = 2.5 \times 10^{-3}, G = 5 \times 10^{4}, Ra = 2 \times 10^{3}, \rho_r = 1.2, \varepsilon = 10^{-2}$ and $Pe = 2.5 \times 10^{-3}$.

Figure 3.4 shows the reversed situation for Case 2. Again, there are two pairs of anti-rotating convection. However, the fluid is dragged from the middle of the domain to both of the edges. The isotherms, from Figure 3.5 for $t = 500\delta t$, are distorted closer to each other in the middle, and further away on both of the edges of the interface.

Thus, we computed two cases of the Bénard-Marangoni convection in an Acetonitrile and an n-Hexane two-layer fluid system heated from above, the computing results show the physics of the convection and consequently, it justices that our phase-field model derived from the energetic variational procedure reflects the mechanism of Bénard-Marangoni convection in the two-layer fluid system.

3.7.4 Thermocapillary-driven Convection

To validate our phase-field model numerically, we now investigate the thermocapillary-driven convection in a heated micro-channel with two-layer superimposed fluids with a planar interface [98]. Note that the dimensional formulations (3.1)-(3.1) will be computed for this example. Our numerical results will be compared with analytical solutions obtained in [98]. Note that a similar comparison are also carried out in section 5.7.3. Considering two-layer fluids (figure 3.6), where the heights of the fluid A (upper) and fluid B (lower) are a and b, respectively, and the fluids are of infinite extension in the horizontal direction. The physical properties of the fluids are their densities, viscosities and heat conductivities. The temperature variations in the present study are considered to be small enough so that the thermophysical properties of each fluid are assumed to remain constant, with the exception of surface tension. The temperature of the lower and upper plates are

$$T^b(x,-b) = T_h + T_0\cos(\omega x) \text{ and } T^a(x,a) = T_c \tag{3.63}$$

respectively, where $T_h > T_c > T_0 > 0$, and $\omega = 2\pi/l$ is a wave number with l being the channel length. The above temperature boundary conditions establish a temperature field that is periodic in the horizontal direction with a period of l. Therefore, it is only sufficient to focus on the solution in one period, i.e.,$-l/2 < x < l/2$. In the limit of zero Marangoni number and small Reynolds number, it is possible to ignore the convective transport of momentum and energy. In addition, we assume that the interface is to remain flat. By solving the simplified sharp-interface governing equations with the corresponding jump boundary conditions at the interface, Pendes *et al*, [98] obtained the analytical solutions for temperature field $\bar{T}(x,y)$ and stream-function

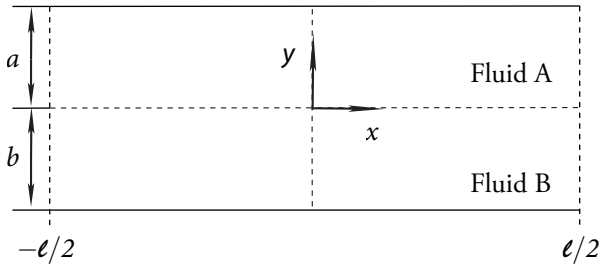

Figure 3.6: The schematic diagram showing two immiscible fluids in a microchannel. The temperatures of the lower and upper plates are $T^b(x,-b) = T_h + T_0 cos(kx)$ and $T^a(x,a) = T_c$, respectively, where $T_h > T_c > T_0$ and $k = 2\pi/l$ is the wave number, and a and b are the heights of the fluid A and B respectively.

$\bar{\psi}(x,y)$, where for the upper fluid

$$\bar{T}^A(x,y) = \frac{(T_c - T_h)y + \tilde{k}T_c b + T_h a}{a + \tilde{k}b} + T_0 f(\alpha,\beta,\tilde{k})\,\sinh(\alpha - \omega y)\,\cos(\omega x), \tag{3.64}$$

$$\bar{\psi}^A(x,y) = \frac{U_{max}}{\omega}\frac{1}{\sinh^2(\alpha) - \alpha^2}\Big\{\omega y\,\sinh^2(\alpha)\cosh(\omega y) - \frac{1}{2}\Big[2\alpha^2 + \omega y\Big(\sinh(2\alpha) - 2\alpha\Big)\Big]\sinh(\omega y)\Big\}\sin(\omega x), \tag{3.65}$$

and for the lower fluid

$$\bar{T}^B(x,y) = \frac{\tilde{k}(T_c - T_h)y + \tilde{k}T_c b + T_h a}{a + \tilde{k}b} + T_0 f(\alpha,\beta,\tilde{k})\,\Big[\sinh(\alpha)\cosh(\omega y) - \tilde{k}\sinh(\omega y)\cosh(\alpha)\Big]\,\cos(\omega x), \tag{3.66}$$

$$\bar{\psi}^B(x,y) = \frac{U_{max}}{\omega}\frac{1}{\sinh^2(\beta) - \beta^2}\Big\{\omega y\,\sinh^2(\beta)\cosh(\omega y) - \frac{1}{2}\Big[2\beta^2 - \omega y\Big(\sinh(2\beta) - 2\beta\Big)\Big]\sinh(\omega y)\Big\}\sin(\omega x). \tag{3.67}$$

	$\varepsilon = 0.02$	$\varepsilon = 0.01$	$\varepsilon = 0.005$	$\varepsilon = 0.002$
$\frac{\|\|\psi-\bar{\psi}\|\|_{L^2}}{\|\|\bar{\psi}\|\|_{L^2}}$	6.037×10^{-2}	1.538×10^{-2}	3.904×10^{-3}	8.292×10^{-4}

Table 3.2: L^2 norm of the relative difference between the numerical results and the analytical solutions for section 3.7.3

In the above equations the unknowns are defined by $\tilde{k} = k_A/k_B$, $\alpha = a\omega$, $\beta = b\omega$, $f(\alpha,\beta,\tilde{k}) = 1/(\tilde{k}\sinh(\beta)\cosh\alpha + \sinh(\alpha)\cosh\beta)$, $g(\alpha,\beta,\tilde{k}) = \sinh(\alpha)f(\alpha,\beta,\tilde{k})$ and

$$U_{max} = -\left(\frac{T_0\sigma_T}{\mu_B}\right) g(\alpha,\beta,\tilde{k})h(\alpha,\beta,\tilde{\mu}),$$

$$h(\alpha,\beta,\tilde{\mu}) = \frac{\Big(\sinh^2(\alpha)-\alpha^2\Big)\Big(\sinh^2(\beta)-\beta^2\Big)}{\tilde{k}\Big(\sinh^2(\beta)-\beta^2\Big)\Big(\sinh(2\alpha)-2\alpha\Big) + \Big(\sinh^2(\alpha)-\alpha^2\Big)\Big(\sinh(2\beta)-2\beta\Big)}.$$

Based on their work, the simulations for our phase-field model are carried out in a 2D domain $[-l/2, l/2] \times [-b, a]$ with $l = 1.6 \times 10^{-4}$, and $a = b = 4 \times 10^{-5}$. As the interface between the two fluids is assumed to be flat and rigid, the initial conditions for the phase-field is only depending on y, and can be given in the form

$$\phi(y) = \tanh\Big(\frac{y}{2\sqrt{2}\varepsilon}\Big), \text{ for } y \in (-b, a), \tag{3.68}$$

where ε is related to the thickness of the diffuse interface. The periodic boundary conditions are applied on the left and right sides of the domain. On the top and bottom walls, the no-slip boundary conditions are imposed such that

$$\mathbf{u} = 0 \text{ for } y = a, -b. \tag{3.69}$$

Eq.(3.63) are used as the boundary conditions for temperature with $T_h = 20$, $T_c = 10$ and $T_0 = 4$. Moreover, the fluid properties are set as $\rho_0 = 1$, $c_p = 1$, $\mu_A = \mu_B = 0.2$, $k = 0.2$, $\sigma_0 = 2.5 \times 10^{-1}$, $\sigma_T = -5 \times 10^{-3}$ (at $T_{ref} = T_c$). The contours of stream

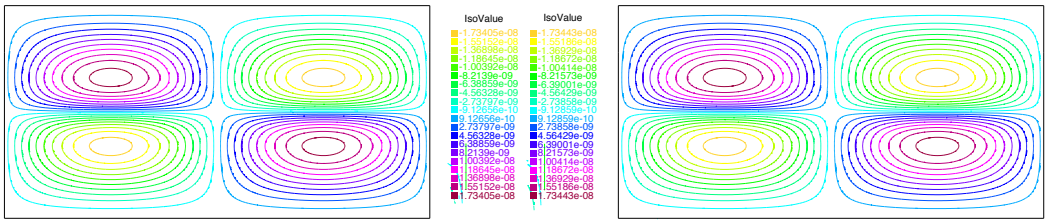

Figure 3.7: Streamlines of the numerical results and analytical solutions for the example of thermocapillary convection in two-layer fluid system. Positive (negative) values of the stream-function indicate the clockwise (the counterclockwise) circulation.

function with $\varepsilon = 0.002$ are shown in figure **??**. It can be seen that our numerical results are in good agreement with the analytical solutions. In order to show that our phase-field model approaches to the sharp-interface model as the thickness of diffuse interface goes to zero, the computations are carried out by using four different values of $\varepsilon(= 0.02, 0.01, 0.005, 0.002)$. The L^2 norm of the relative difference between the numerical results and analytical solutions are shown in table 2. We can observe that as the value of ε decreases, the L^2 norm of relative difference decreases for stream functions. Note that a more detailed description of ths numerical experiment will be provided in section 5.7.3.

3.8 Numerical experiments for thermocapillary effects

To illustrate the thermocapillary effects, two interesting numerical experiments were carried out in [30]. In their experiments, a square domain with a circle inside was occupied by a two-layer fluid. When applying two different temperature boundary conditions: one is heating inside (on the circle boundary) and cooling outside (on the square boundary); and the other one, conversely, is heating outside and cooling inside, some thermocapillary effects can be observed. Due to the temperature dependence of

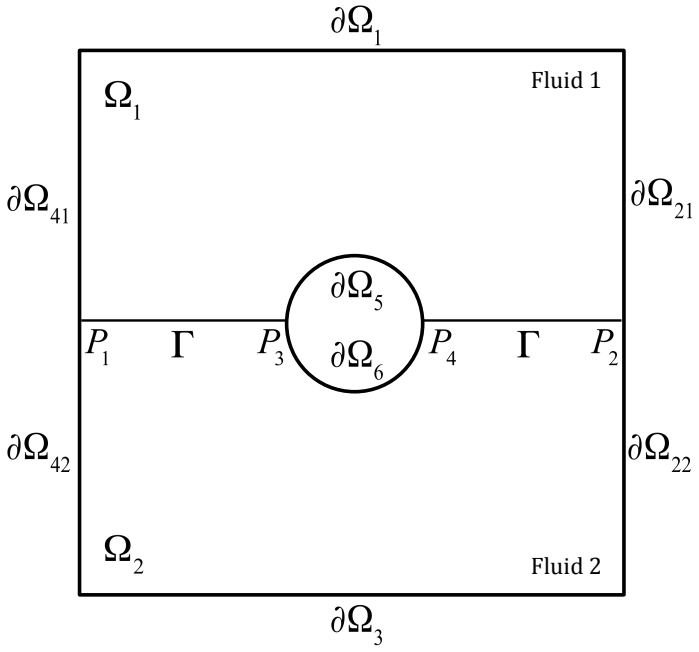

Figure 3.8: Domain Ω for flow with thermocapillary effects.

the surface tension, the horizontal interface between the two layers deformed, presenting sine/cosine-like curves. However, no further analysis about the mechanism was reported. Moreover, for a simpler numerical treatment, they employed an Allen-Cahn equation to describe the phase-field equation rather than Cahn-Hilliard equation, which involves fourth-order differential operators.

In the present work, we will repeat this experiment with our phase-field model, in which the Cahn-Hilliard phase-field equation is employed. Equipped with one of their temperature boundary conditions (heating inside and cooling outside), we will provide analysis about the mechanism that results in the sine/cosine-like curve, the corresponding computational results will be compared to show the reliability of our methods.

As shown in Figure 3.8, a squared domain with a circle inside is defined, $\Omega = [0,2] \times [0,2] \cap \{(x,y)|(x-1)^2+(y-1)^2 \geqslant 0.25\}$. Let $\partial\Omega = \partial\Omega_o \cup \partial\Omega_i$ denote the boundary of Ω_s, with $\partial\Omega_o = \partial\Omega_1 \cup \partial\Omega_{21} \cup \partial\Omega_{22} \cup \partial\Omega_3 \cup \partial\Omega_{41} \cup \partial\Omega_{42}$ and $\partial\Omega_i = \Omega_5 \cup \Omega_6$ representing the outer boundary and inner boundary respectively, P_1, P_2, P_3 and P_4 denote four intersection points between boundary $\partial\Omega$ and the horizontal midline Γ, where Γ

is also adopted as the initial interface for the two-layer fluid.

Note that, the non-dimensionlized system for this experiment is kept the same with that for Bénard-Marangoni convection, (3.20)-(3.23), except that the distance between two parallel plates (horizontal or vertical) is chosen as the length scale, and $\theta = (\theta^* - \theta_0)/\theta_l$ as the temperature scale, where θ_0 is the reference temperature (in the present work, it is set to be zero), θ_l is the temperature difference between the square and circle boundaries.

Now we introduce boundary conditions and initial conditions for non-dimensional phase-field model (3.20)-(3.23) in domain Ω.

Boundary and Initial conditions for velocity

$$\mathbf{u}|_{\partial\Omega} = 0, \qquad \mathbf{u}_0(x) = p_0(x) = 0 \quad (x \in \Omega). \tag{3.70}$$

Boundary and Initial conditions for phase

$$\phi|_{P_1 \cup P_2 \cup P_3 \cup P_4} = 0, \quad \phi|_{(\partial\Omega_1 \cup \partial\Omega_{21} \cup \partial\Omega_{41}) \setminus (P_1 \cup P_2) \cup \partial\Omega_5 \setminus (P_3 \cup P_4)} = 1,$$

$$\phi|_{(\partial\Omega_3 \cup \partial\Omega_{22} \cup \partial\Omega_{42}) \setminus (P_1 \cup P_2) \cup \partial\Omega_6 \setminus (P_3 \cup P_4)} = -1, \tag{3.71}$$

$$\phi_0(x) = 1 \ (x \in \Omega_1), \quad \phi_0(x) = -1 \ (x \in \Omega_2), \quad \phi_0(x) = 0 \ (x \in \Gamma). \tag{3.72}$$

Again a Dirichlet boundary condition for ϕ is assigned to fix the intersection points. The horizontal line Γ is assumed to be the initial position of the interface.

Specic boundary and initial conditions for temperature

Case 1 : Heating inside and cooling outside

$$\theta|_{\partial\Omega_i} = 1 \ \textit{and} \ \ \theta|_{\partial\Omega_0} = 0; \quad \theta_0(x)|_{\partial\Omega_i} = 1 \ \text{ and } \ \theta_0(x) = 0 \quad \text{elsewhere}. \tag{8.3}$$

As a first try, we let $Ma = 80$, $Ra = 0$, and the other parameters are kept the same with those in Section 3.7, say $Pr = 5.76, Ca = 2.5 \times 10^{-3}, G = 5 \times 10^4, Ra = 2 \times 10^3, \rho_r =$

$1.2, \varepsilon = 10^{-2}, Pe = 2.5 \times 10^{-3}$. However, as the time progresses, no deformation of the interface is observed, the corresponding streamlines are shown in Figure 3.9a. As it can be seen that, like Bénard-Marangoni convection in Case 2 of Section 3.7, two pairs of anti-rotating convection set in, the fluid is dragged from both the middle to both edges of the domain, producing downwelling along the centreline of the upper fluid and upwelling of the lower fluid. Since the initial interface is assumed to be flat and no buoyancy forces are considered ($Ra = 0$), the strength of the two pairs of convective rolls are of the same degree and no deformation of the interface can be caused. As we increase the Rayleigh number say $Ra = 500, 1000, 5000$, the balance of the convection rolls is broken, with the Buoyancy forces gradually dominating the convection over the thermocapillary effects. Streamlines for the flow at time $t = 100\delta t$ with different values of Ra are shown in Figure (3.9b)-Figure (3.9d), with the increasing Ra, the two pairs of convection rolls disappeared with one pair rolls gradually controlling the flow, which is caused by the increasing effects of buoyancy. Figure 3.10 shows that the interface eventually evolves to a sine/cosine-like curve with $Ma = 80$ and $Ra = 5000$, when time marches longer, this curve turns out to be steeper, which are similar with those reported in [113], where the Allen-Cahn phase-field equation is employed. Therefore we conclude that the competition between the Buoyancy forces (Ra) and the thermocapillary effects (Ma) can be shown in this interesting experiment, where the interface deforms and presents the sine/cosine curve with buoyancy forces dominating the convection over the thermocapillary effects.

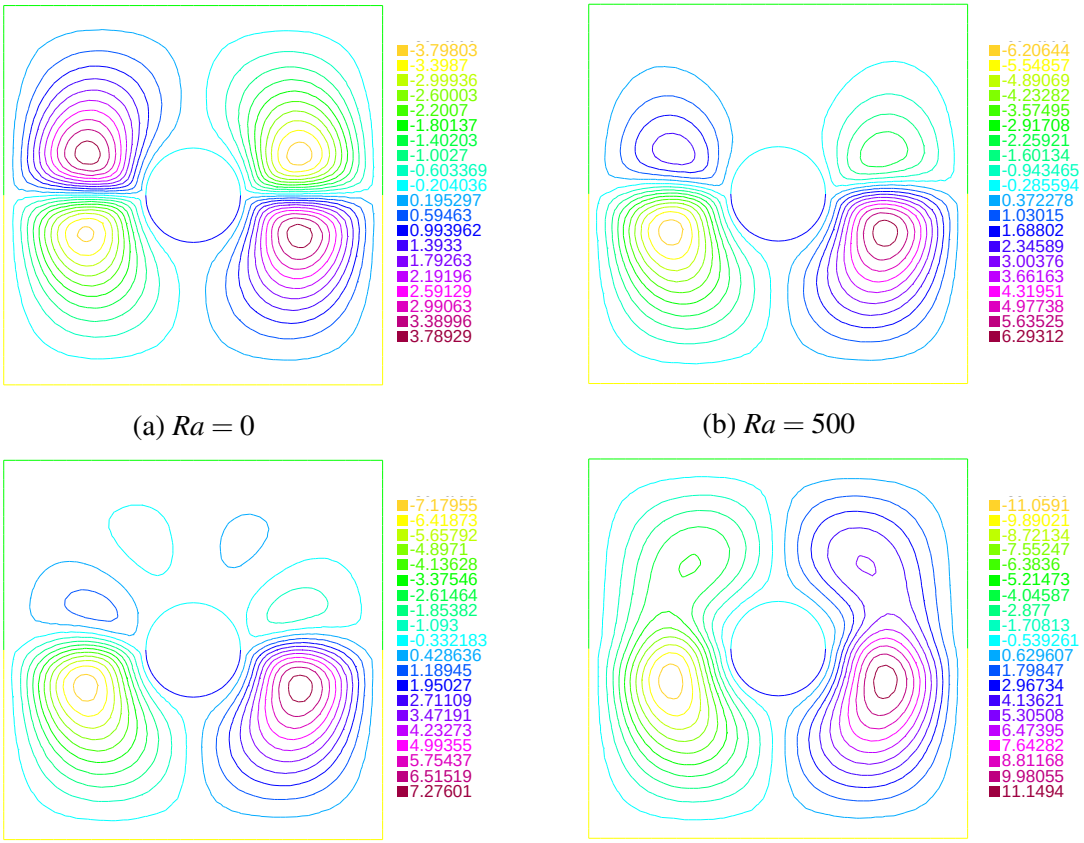

(a) $Ra = 0$

(b) $Ra = 500$

(c) $Ra = 1000$

(d) $Ra = 5000$

Figure 3.9: Streamlines for the flow with thermocapillary effects for different values of the Rayleigh number at $t = 100\delta t$. Positive values of the stream function indicate clockwise circulation and negative values indicate anti-clockwise circulation. $Pr = 5.76, Ca = 2.5 \times 10^{-3}, Ma = 80, G = 5 \times 10^4, Ra = 2 \times 10^3, \rho_r = 1.2, \varepsilon = 10^{-2}$ and $Pe = 2.5 \times 10^{-3}$.

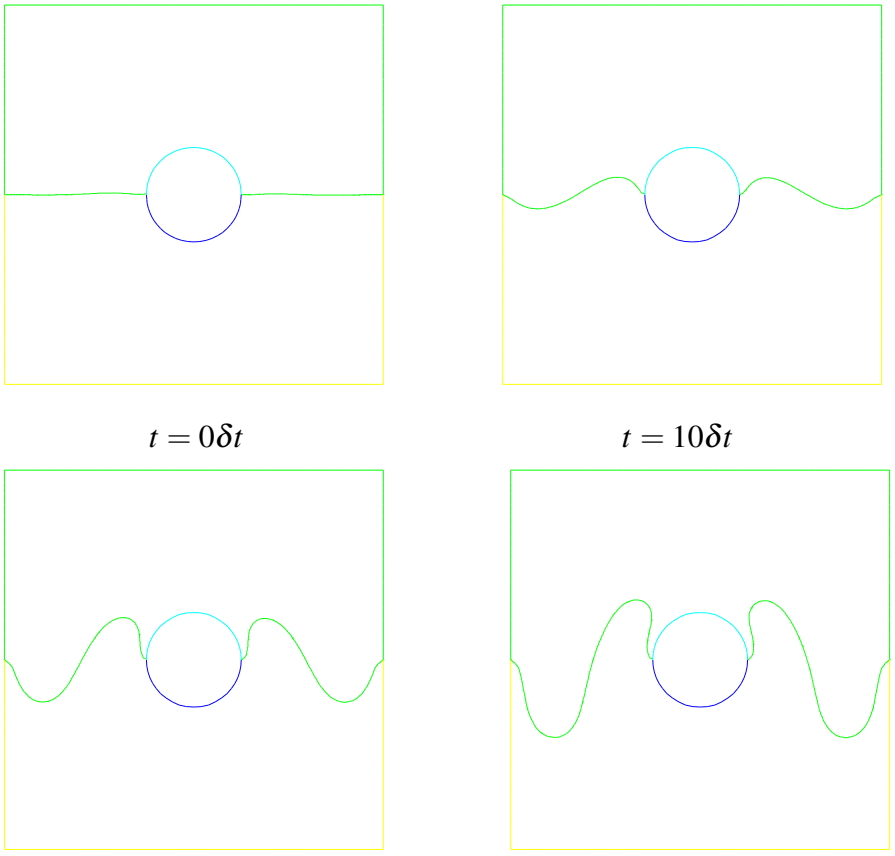

Figure 3.10: Deformation of the interface with of $Ra = 5 \times 10^3$, $Pr = 5.76, Ca = 10^{-3}, Ma = 80, G = 5 \times 10^4, \rho_r = 1.2, \varepsilon = 10^{-2}$ and $Pe = 2.5 \times 10^{-3}$.

3.9 Discussion

In this chapter, we studied a phase-field model consisting of a modified N-S equation, a Cahn-Hilliard phase-field equation and an energy transport equation. The modified N-S equation was derived through an energetic variational procedure, in which a special surface tension part was considered to serve as the temperature dependent surface tension (thermocapillary effects). An appropriate variational form and a modified midpoint method which preserve the possible underlying energy law to its greatest extent are adopted to compute the strong nonlinear system. By solving the non-dimensional system, a few examples of Bénard-Marangoni convections in an Acetonitrile and an n-Hexane system heated from above were carried out. The results presented were in a good agreement with the physics for two-layer Bénard-Marangoni convections summarized by [72]. In addition, we computed an example for thermocapillary effects that was originally carried out in [113] where an Allen-Cahn phase-field equation was employed. Comparing to those in [113], we present similar results to show the reliability of our methods. By developing the results further, we provided an analysis of the mechanism about the deformation of the interface, turning out that the experiment exhibited the competition between the thermocapillary effects and buoyancy forces. Based on our results, we conclude that our phase-field model reflects the mechanism of Bénard-Marangoni convection in the two-layer fluid system, and the modified midpoint methods for the phase-field model performs well with the interface deformation in a two-layer fluid.

Chapter 4

A numerical method for the quasi-incompressible Cahn-Hilliard-Navier-Stokes equations for variable density flows with a discrete energy law

4.1 Introduction

In this chapter, we investigate numerically a diffuse interface model for the Navier-Stokes equation with fluid-fluid interface when the fluids have different densities [87]. Under minor reformulation of the system, we show that there is a continuous energy law underlying the system, assuming that all variables have reasonable regularities. It is shown in the literature that an energy law preserving method will perform better

for multiphase problems [65, 83, 84]. Thus for the reformulated system, we design a C^0 finite element method and a special temporal scheme where the energy law is preserved at the discrete level. Such a discrete energy law (almost the same as the continuous energy law) for this variable density two-phase flow model has never been established before with C^0 finite element. Newton's method is introduced to linearise the highly non-linear system of our discretization scheme. Some numerical experiments are carried out using an adaptive mesh to investigate the scenario of coalescing and rising drops with differing density ratio. The snapshots for the evolution of the interface together with the adaptive mesh at different times are presented to show that the evolution, including the break-up/pinch-off of the drop, can be handled smoothly by our numerical scheme. The discrete energy functional for the system is examined to show that the energy law at the discrete level is preserved by our scheme.

4.2 Quasi-Incompressible NSCH System

We consider the following non-dimensional Navier-Stokes Cahn-Hilliard (NSCH) system with variable density governing the motion of a two-phase fluid:

$$\nabla \cdot \mathbf{u} = \frac{\alpha}{Pe}\Delta\mu, \text{ or } \dot{\rho} = -\rho\nabla\cdot\mathbf{u}, \tag{4.1a, 4.1b}$$

$$\rho\dot{\mathbf{u}} = -\frac{1}{M}\Big(\nabla p + C\nabla\cdot(\rho\nabla c\otimes\nabla c)\Big) + \nabla\cdot(\frac{1}{Re}\nabla\mathbf{u}) + \nabla\Big(\frac{1}{3Re}(\nabla\cdot\mathbf{u})\Big) - \frac{1}{Fr^2}(\rho-\rho_0)\hat{\mathbf{j}}, \tag{4.2}$$

$$\rho\dot{c} = \nabla\cdot(\frac{1}{Pe}\nabla\mu), \tag{4.3}$$

$$\mu = f(c) - \frac{\partial\rho}{\partial c}\frac{p}{\rho^2} - \frac{C}{\rho}\nabla\cdot(\rho\nabla c) - \frac{M\rho_0\alpha}{Fr^2}y, \tag{4.4}$$

where

$\dot{x} = x_t + (\mathbf{u} \cdot \nabla)x$	the material derivative,
$\mathbf{u}$	the velocity of mixtures,
p	the pressure,
c	phase variable ($c = 1$: fluid 1; $c = 0$: fluid 2),
$\rho = \rho(c)$	the variable density of the mixture, a function of c,
μ	the chemical potential,
ρ_0	a constant representing the "background" or reference density,
$\mathbf{x} = (x, y)$	the Cartesian coordinate system,
$\hat{\mathbf{j}}$	the vertical component of the unit vector in Cartesian coordinate system,
y	the vertical coordinate,
$F(c) = c^2(c-1)^2/4$	double-well potential (free energy),
$f(c)$	the derivative of F,
$\nabla c \otimes \nabla c$	extra reactive stress,
C	the capillary number measuring the thickness of the interface,
M	an analogue of the Mach number measuring the relative strength of the surface tension and chemical energies,
Re	the Reynolds number,
Fr	the Froude number measuring the relative strengths of inertial and gravitational forces,
Pe	the diffusional Peclet number measuring the relative strengths of (chemical) diffusion and advection.

Note that, as the gravitational effects are considered here, the system (4.1)-(4.4) we investigate in this paper is modified from the quasi-incompressible NSCH system in [87]. Comparing to the system of equations in [87], a gravitational force $-(\rho - \rho_0)\hat{\mathbf{j}}/Fr^2$ is

added to our momentum equation (4.2). Further, in order to maintain the thermodynamic consistency of our system, an extra term $-\rho_0 g\alpha y/Fr^2$ corresponding to the gravitational forces is added to the chemical potential equation (4.4) (See Remark 4.2.1 for details).

Following Lowengrub and Truskinovsky [87], a simple mixture assumption is used and the variable density is given by a harmonic interpolation of the densities of the two incompressible constituents:

$$\frac{1}{\rho(c)} = \frac{c}{\rho_1} + \frac{1-c}{\rho_2},$$

where c is the mass concentration (phase variable), and ρ_1, ρ_2 are constants representing the densities of the two incompressible fluids respectively. Further we have

$$\frac{\partial \rho}{\partial c} = -\alpha\rho^2, \tag{4.5}$$

where $\alpha = (\rho_2 - \rho_1)/\rho_2\rho_1$ is a constant. Note that the above variable density model is different from the most other models, where in the most other models the density is assumed to be a linear function of c. This is a good approximation of the simple mixture formulation if the densities are nearly matched. The harmonic interpolation means that the volume of the mixture is preserved (see [13] and [19] for comprehensive reviews). Moreover, by considering Eq.(4.3), we obtain

$$\nabla \cdot \mathbf{u} = -\frac{1}{\rho}\frac{\partial \rho}{\partial c}\dot{c} = \frac{\alpha}{Pe}\Delta\mu. \tag{4.6}$$

It can be observed that the two continuous equations in Eq.(4.1) are equivalent

$$\dot{\rho} = -\rho\nabla \cdot \mathbf{u} \iff \nabla \cdot \mathbf{u} = \frac{\alpha}{Pe}\Delta\mu. \tag{4.7}$$

It is well known that for the incompressible flows, the velocity field satisfies the divergence free condition,

$$\nabla \cdot \mathbf{u} = 0. \tag{4.8}$$

In this variable density model, however, this condition is no longer valid. Due to the variation of c, a mixture of two incompressible fluids with different densities can be compressible across the interface. In [87], such binary fluids satisfying Eq.(4.1) are termed as quasi-incompressible. Note that the energy law preserving numerical method is designed in this paper corresponding to either Eq.(4.1a) or Eq.(4.1b), where in practice the method with Eq.(4.1a) is chosen for our computations. By presenting the distribution of $\nabla \cdot \mathbf{u}$, the compressibility of quasi-incompressible flows along the interface is demonstrated in §4.6 (Fig. 4.4 and Fig. 4.5).

The system is supplied with the initial conditions:

$$\mathbf{u}|_{t=0} = \mathbf{u}_0,\ c|_{t=0} = c_0,$$

the Dirichlet boundary conditions for the velocity: $\mathbf{u}(= \mathbf{b}_\mathbf{u})$ and the Neumann boundary conditions for the phase variable c and μ: $\nabla c \cdot \hat{\mathbf{n}} = 0$ and $\nabla \mu \cdot \hat{\mathbf{n}} = 0$, where $\hat{\mathbf{n}}$ is the unit outward normal vector of the boundary.

Remark 4.2.1. *Based on entropy production, the quasi-incompressible NSCH system [87] was derived through an energetic variational procedure. It is thermodynamically consistent with an energy functional E,*

$$E = \int_\Omega \left(\frac{1}{2}\rho |\mathbf{u}|^2 + \frac{1}{M}\rho F(c) + \frac{C}{2M}\rho |\nabla c|^2 \right) \mathrm{d}\mathbf{x}, \tag{4.9}$$

where $\rho|\mathbf{u}|^2/2$ is the kinetic energy, and $\rho F(c)/M + C\rho|\nabla c|^2/2M$ is the Cahn-Hilliard free energy. For simplicity, we only consider the two-dimensional case in this paper.

Here $\mathbf{x} = (x, y)$ *is the two dimensional Cartesian coordinate system. Note that the potential energy is not considered in the original system.*

In this paper, as the effects of gravity are considered, we consider the modified system (4.1)-(4.4), where the corresponding non-dimensional total energy $\hat{E}$ *for the system (4.1)-(4.4) now can be defined as*

$$\begin{aligned}\widehat{E} &= E + E_g \\ &= \int_\Omega \left(\frac{1}{2}\rho |\mathbf{u}|^2 + \frac{1}{M}\rho F(c) + \frac{C}{2M}\rho |\nabla c|^2 + \frac{1}{Fr^2}\rho y \right) \mathrm{d}\mathbf{x} \end{aligned} \tag{4.10}$$

in which E *is from the original system (Eq.(4.9)) and* E_g *is the gravitational potential energy,*

$$E_g = \int_\Omega \left(\frac{1}{Fr^2}\rho y \right) \mathrm{d}\mathbf{x}, \tag{4.11}$$

where Ω *is a bounded domain and y is the coordinate in vertical direction.*

We now rederive the system of equations with respect to the total energy $\hat{E}$ *(Eq.(4.10)). Differentiating* E_g *with respect to time (associated with the the variational procedure) we obtain*

$$\frac{\mathrm{d}E_g}{\mathrm{d}t} = \int_\Omega \left(-\frac{1}{Fr^2}\nabla \cdot (\rho \mathbf{u}) y \right) \mathrm{d}\mathbf{x}, \tag{4.12}$$

where Eq.(4.1b) is used. Note that, for the sake of convenience, a reference density ρ_0 *is subtracted off from the gravitational forces in the NS equation (4.2). In order to derive the gravitational force* $-(\rho - \rho_0)\hat{\mathbf{j}}/Fr^2$ *within a thermodynamically consistent*

framework, we multiply Eq.(2.1a) by $-\rho_0 y/Fr^2$ *to obtain*

$$-\int_\Omega \left(\frac{1}{Fr^2}\rho_0 y \nabla \cdot \mathbf{u} - \frac{1}{Fr^2}\rho_0 y \alpha \nabla \cdot (\frac{1}{Pe}\nabla \mu) \right) \mathrm{d}\mathbf{x} = 0. \tag{4.13}$$

Adding Eq.(4.13) to Eq.(4.12) and using integration by parts, we obtain

$$\begin{aligned} \frac{\mathrm{d}E_g}{\mathrm{d}t} = &-\int_{\partial\Omega} \left(\frac{1}{Fr^2}(\rho-\rho_0) y\mathbf{u} - \frac{\alpha y \rho_0}{Fr^2 Pe}\nabla\mu \right) \cdot \hat{\mathbf{n}}\, \mathrm{d}\mathbf{x} \\ &+ \int_\Omega \left(\frac{1}{Fr^2}(\rho-\rho_0)\mathbf{u} - \frac{\rho_0\alpha}{Fr^2 Pe}\nabla\mu \right) \cdot \hat{\mathbf{j}}\, \mathrm{d}\mathbf{x}, \end{aligned} \tag{4.14}$$

where $\hat{\mathbf{n}}$ *is the unit outward normal vector of the boundary* $\partial\Omega$ *and*

$$\hat{\mathbf{j}} = \nabla y = \binom{0}{1} \tag{4.15}$$

is the vertical component of the unit vector in Cartesian coordinate system. With the homogeneous boundary conditions that the interface is assumed to have no intersections with the boundary $\partial\Omega$*, we arrive at*

$$\frac{\mathrm{d}E_g}{\mathrm{d}t} = \int_\Omega \left(\frac{1}{Fr^2}(\rho-\rho_0)\hat{\mathbf{j}}\cdot\mathbf{u} - \frac{1}{MPe}\nabla\mu\cdot\nabla(\frac{M\rho_0\alpha y}{Fr^2}) \right) \mathrm{d}\mathbf{x}, \tag{4.16}$$

where, we notice that, with the reference density, not only the gravity but also the chemical potential contribute to the time rate of the change of the potential energy. Based on the entropy production and the variational procedure that is used in [87], the first term at the right hand side will result in the gravitational forces $-(\rho-\rho_0)\hat{\mathbf{j}}/Fr^2$ *in the NS equation (4.2), acting as the external forces of our the system, and the second term at the right hand side will contribute to the entropy production and will result in* $-M\rho_0\alpha y/Fr^2$ *in the chemical potential (4.4) of our system. We thus obtain a new chemical potential (4.4), which differs in the original model derived in [87] that an*

extra term $-M\rho_0\alpha y/Fr^2$ appears to account for the potential energy associated with the gravitational force. In what follows (section 4.3), we will derive the energy law with respect to the total energy $\widehat{E}$ (Eq.(4.10)) to show that the thermodynamic consistency is maintained in our new system.

4.3 Energy Law Preserving Weak Form

We note that, only first order derivatives of $\mathbf{u}$, p, $\hat{u}$, c, μ_C are present so that the C^0 finite element method can be used to solve the problem under this weak form. For simplicity, we only consider the two-dimensional case in this paper. The results can be straightforwardly extended to three dimensions. Let Ω be a bounded domain. We denote the boundary of Ω by $\partial\Omega$ and suppose that $\partial\Omega$ is sufficiently smooth (for example, Lipschitz-continuous). Denote the following spaces as $\mathbf{W}^{1,3}(\Omega) = (W^{1,3}(\Omega))^2$, $\mathbf{W}^{1,3}_{\mathbf{b}}(\Omega) = \{\mathbf{u} \in \mathbf{W}^{1,3}(\Omega), \mathbf{u} = \mathbf{b} \text{ on } \partial\Omega\}$. Note that in order to obtain a meaningful weak form, we require ρ is positive and $\rho \in L^\infty(\Omega)$, and $\rho\mathbf{u} \in \mathbf{W}^{1,3}(\Omega)$. A direct variational or weak form may be derived straightforwardly by multiplying Eq.(4.1a) with a test function q, Eq.(4.2) with $\mathbf{v}$, Eq.(4.3) with ψ and Eq.(4.4) with χ. Using integration by parts, we obtain the weak form as the following: Find $\mathbf{u} \in \mathbf{W}^{1,3}_{\mathbf{b}}(\Omega)$, $p \in W^{1,3/2}(\Omega)$, $c \in W^{1,3}(\Omega)$, $\mu \in W^{1,3}(\Omega)$ such that

$$\int_\Omega \left(\mathbf{u}\cdot\nabla q - \frac{\alpha}{Pe}\nabla\mu\cdot\nabla q \right) \mathrm{d}\mathbf{x} = 0, \qquad \forall q \in W^{1,3/2}(\Omega), \tag{4.17}$$

$$\int_\Omega \left(\rho\dot{\mathbf{u}}\cdot\mathbf{v} + \frac{1}{M}\mathbf{v}\cdot\nabla p - \frac{C}{M}(\rho\nabla c\otimes\nabla c) : \nabla\mathbf{v} + \frac{1}{Re}\nabla\mathbf{u} : \nabla\mathbf{v} + \frac{1}{3Re}(\nabla\cdot\mathbf{u})(\nabla\cdot\mathbf{v}) \right.$$
$$\left. + \frac{1}{Fr^2}(\rho-\rho_0)\hat{\mathbf{j}}\cdot\mathbf{v} \right) \mathrm{d}\mathbf{x} = 0, \qquad \forall \mathbf{v} \in \mathbf{W}^{1,3}_0(\Omega), \tag{4.18}$$

$$\int_\Omega \left(\rho \dot{c} \psi + \frac{1}{Pe} \nabla \mu \cdot \nabla \psi \right) \mathrm{d}\mathbf{x} = 0, \qquad \forall \psi \in W^{1,3/2}(\Omega), \quad (4.19)$$

$$\int_\Omega \left(\mu \chi - f(c)\chi + \frac{\partial \rho}{\partial c} \frac{p}{\rho^2} \chi + \frac{C}{\rho} (\nabla \rho \cdot \nabla c)\chi - C \nabla c \cdot \nabla \chi + \frac{M \rho_0 \alpha}{Fr^2} y \chi \right) \mathrm{d}\mathbf{x} = 0,$$

$$\forall \chi \in W^{1,3}(\Omega). \quad (4.20)$$

At most, only first order derivatives of $\mathbf{u}$, p, c, μ, $\mathbf{v}$, q, ψ and χ are required so that the C^0 (conforming) finite element method can be used to solve the problem in this variational form. In the case of homogeneous boundary conditions, there is an energy law that underlies the system [87]. We now formally rederive the continuous energy law using the weak form (4.17)-(4.20) (with homogeneous boundary conditions for $\mathbf{u}$), which is useful in deriving the discrete energy law preserving numerical scheme later. For the momentum equation (4.18), by setting $\mathbf{v} = \mathbf{u}$ and using integration by parts, we obtain

$$\int_\Omega \left(\rho \frac{\mathrm{d}}{\mathrm{d}t} \frac{1}{2} (\mathbf{u} \cdot \mathbf{u}) - \nabla \cdot (\rho \mathbf{u}) \frac{1}{2} (\mathbf{u} \cdot \mathbf{u}) \right) \mathrm{d}\mathbf{x} = \int_\Omega \left(\frac{1}{M} p (\nabla \cdot \mathbf{u}) + \frac{C}{M} (\rho \nabla c \otimes \nabla c) : \nabla \mathbf{u} \right.$$

$$\left. - \frac{1}{Fr^2} (\rho - \rho_0) \hat{\mathbf{j}} \cdot \mathbf{u} \right) \mathrm{d}\mathbf{x} - \frac{1}{Re} ||\nabla \mathbf{u}||_{L^2}^2 - \frac{1}{3Re} ||\nabla \cdot \mathbf{u}||_{L^2}^2, \quad (4.21)$$

where we used the following identity under homogeneous boundary conditions

$$\int_\Omega \left(\rho (\mathbf{u} \cdot \nabla) \mathbf{u} \cdot \mathbf{u} \right) \mathrm{d}\mathbf{x} = \int_\Omega \left(- \nabla \cdot (\rho \mathbf{u}) \frac{1}{2} (\mathbf{u} \cdot \mathbf{u}) \right) \mathrm{d}\mathbf{x} \quad \text{for } \mathbf{u}|_{\partial\Omega} = 0.$$

For the Cahn-Hilliard equation (4.19), we set $\psi = \mu/M - \alpha(\rho-\rho_0)y/Fr^2 - \alpha\rho\mathbf{u}\cdot\mathbf{u}/2 - \alpha\rho F(c)/M - \alpha\rho C(\nabla c\cdot\nabla c)/2M - \alpha p/M$ to obtain

$$\int_\Omega \left(\frac{1}{M}\rho\dot{c}\mu + \frac{\rho_0\alpha}{Fr^2}y\rho\dot{c} + \frac{1}{Fr^2}y\dot{\rho} + \frac{1}{2}\mathbf{u}\cdot\mathbf{u}\dot{\rho} + \frac{1}{M}F(c)\dot{\rho} + \frac{C}{2M}\nabla c\cdot\nabla c\dot{\rho} + \frac{1}{M}\frac{p}{\rho}\dot{\rho}\right)\mathrm{d}\mathbf{x}$$
$$= \int_\Omega \frac{\alpha}{Pe}\nabla\mu\cdot\nabla\left(\frac{\rho-\rho_0}{Fr^2}y + \frac{1}{2}\rho\mathbf{u}\cdot\mathbf{u} + \frac{1}{M}\rho F(c) + \frac{C}{2M}\rho\nabla c\cdot\nabla c + \frac{p}{M}\right)\mathrm{d}\mathbf{x} - \frac{1}{M}\frac{1}{Pe}||\nabla\mu||^2_{L^2}. \tag{4.22}$$

For the chemical potential equation (4.20), we set $\chi = \rho\dot{c}/M$ to obtain

$$\int_\Omega \left(\frac{1}{M}\rho\frac{\mathrm{d}}{\mathrm{d}t}F(c) - \frac{1}{M}\nabla\cdot(\rho\mathbf{u})F(c) + \frac{C}{2M}\rho\frac{\mathrm{d}}{\mathrm{d}t}(\nabla c\cdot\nabla c) - \frac{C}{2M}\nabla\cdot(\rho\mathbf{u})(\nabla c\cdot\nabla c)\right)\mathrm{d}\mathbf{x}$$
$$= \int_\Omega \left(\frac{1}{M}\frac{p}{\rho}\dot{\rho} - \frac{C}{M}(\rho\nabla c\otimes\nabla c):\nabla\mathbf{u} + \frac{1}{M}\rho\dot{c}\mu + \frac{\rho_0\alpha}{Fr^2}y\rho\dot{c}\right)\mathrm{d}\mathbf{x}, \tag{4.23}$$

where, for the term $\int_\Omega(\rho f(c)\dot{c}/M)\mathrm{d}\mathbf{x}$, we have

$$\int_\Omega \left(\frac{1}{M}\rho f(c)\dot{c}\right)\mathrm{d}\mathbf{x} = \int_\Omega \left(\frac{1}{M}\rho\frac{\mathrm{d}}{\mathrm{d}t}F(c) + \frac{1}{M}\rho(\mathbf{u}\cdot\nabla)F(c)\right)\mathrm{d}\mathbf{x}$$
$$= \int_\Omega \left(\frac{1}{M}\rho\frac{\mathrm{d}}{\mathrm{d}t}F(c) - \frac{1}{M}\nabla\cdot(\rho\mathbf{u})F(c)\right)\mathrm{d}\mathbf{x}. \tag{4.24}$$

And for the term $\int_\Omega(C\rho\nabla c\cdot\nabla\dot{c}/M)\mathrm{d}\mathbf{x}$, we have

$$\int_\Omega \left(\frac{C}{M}\rho\nabla c\cdot\nabla\dot{c}\right)\mathrm{d}\mathbf{x} = \int_\Omega \left(\frac{C}{2M}\rho\frac{\mathrm{d}}{\mathrm{d}t}(\nabla c\cdot\nabla c) + \frac{C}{M}\rho\nabla c\cdot\nabla\Big((\mathbf{u}\cdot\nabla)c\Big)\right)\mathrm{d}\mathbf{x}$$
$$= \int_\Omega \left(\frac{C}{2M}\rho\frac{\mathrm{d}}{\mathrm{d}t}(\nabla c\cdot\nabla c) - \frac{C}{2M}\nabla\cdot(\rho\mathbf{u})(\nabla c\cdot\nabla c) + \frac{C}{M}(\rho\nabla c\otimes\nabla c):\nabla\mathbf{u}\right)\mathrm{d}\mathbf{x}, \tag{4.25}$$

in which the following identity is used,

$$\nabla\cdot(\rho\nabla c\otimes\nabla c)=\nabla\cdot(\rho\nabla c)\nabla c+\frac{1}{2}\rho\nabla(\nabla c\cdot\nabla c), \tag{4.26}$$

such that

$$\begin{aligned}
&\int_\Omega\left(\frac{C}{M}\rho\nabla c\cdot\nabla\Big((\mathbf{u}\cdot\nabla)c\Big)\right)\mathrm{d}\mathbf{x}\\
&=\int_\Omega\left(-\frac{C}{M}\nabla\cdot(\rho\nabla c)(\mathbf{u}\cdot\nabla)c-\frac{C}{2M}\rho\mathbf{u}\cdot\nabla(\nabla c\cdot\nabla c)+\frac{C}{2M}\rho\mathbf{u}\cdot\nabla(\nabla c\cdot\nabla c)\right)\mathrm{d}\mathbf{x}\\
&=\int_\Omega\left(-\frac{C}{M}\nabla\cdot(\rho\nabla c\otimes\nabla c)\cdot\mathbf{u}-\frac{C}{2M}\nabla\cdot(\rho\mathbf{u})(\nabla c\cdot\nabla c)\right)\mathrm{d}\mathbf{x}\\
&=\int_\Omega\left(\frac{C}{M}(\rho\nabla c\otimes\nabla c):\nabla\mathbf{u}-\frac{C}{2M}\nabla\cdot(\rho\mathbf{u})(\nabla c\cdot\nabla c)\right)\mathrm{d}\mathbf{x}.
\end{aligned}\tag{4.27}$$

By adding Eqs.(4.21)-(4.23) together, we obtain

$$\begin{aligned}
&\frac{\mathrm{d}}{\mathrm{d}t}\left(\frac{1}{2}||\sqrt{\rho}\mathbf{u}||_{L^2}^2+\frac{C}{2M}||\sqrt{\rho}\,\nabla c||_{L^2}^2+\int_\Omega\Big(\frac{1}{M}\rho F(c)\Big)\mathrm{d}\mathbf{x}\right)\\
&=-\frac{1}{Re}||\nabla\mathbf{u}||_{L^2}^2-\frac{1}{3Re}||\nabla\cdot\mathbf{u}||_{L^2}^2-\frac{1}{MPe}||\nabla\mu||_{L^2}^2\\
&-\int_\Omega\left(\frac{1}{Fr^2}(\rho-\rho_0)\hat{\mathbf{j}}\cdot\mathbf{u}+\frac{\rho_0\alpha}{Fr^2Pe}\hat{\mathbf{j}}\cdot\nabla\mu+(\nabla\cdot\mathbf{u})\Big(\frac{1}{2}\rho\mathbf{u}\cdot\mathbf{u}+\frac{1}{M}\rho F(c)+\frac{C}{2M}\rho(\nabla c\cdot\nabla c)\right.\\
&\left.+\frac{1}{M}p\Big)+\frac{\alpha}{Pe}\nabla\mu\cdot\nabla\Big(\frac{1}{2}\rho\mathbf{u}\cdot\mathbf{u}+\frac{1}{M}\rho F(c)+\frac{C}{2M}\rho\nabla c\cdot\nabla c+\frac{1}{M}p\Big)\right)\mathrm{d}\mathbf{x}.
\end{aligned}\tag{4.28}$$

For the continuous equation (4.17), we set $q = \rho\mathbf{u}\cdot\mathbf{u}/2+\rho F(c)/M+\rho C(\nabla c\cdot\nabla c)/2M+p/M+(\rho-\rho_0)y/Fr^2$, through integration by parts we obtain

$$0 = -\int_\Omega \Bigg((\nabla\cdot\mathbf{u})\Big(\frac{1}{2}\rho\mathbf{u}\cdot\mathbf{u}+\frac{1}{M}\rho F(c)+\frac{C}{2M}\rho(\nabla c\cdot\nabla c)+\frac{1}{M}p+\frac{\rho-\rho_0}{Fr^2}y\Big) - \frac{\alpha}{Pe}\nabla\mu\cdot\nabla\Big(\frac{1}{2}\rho\mathbf{u}\cdot\mathbf{u}+\frac{1}{M}\rho F(c)+\frac{C}{2M}\rho\nabla c\cdot\nabla c+\frac{1}{M}p+\frac{\rho-\rho_0}{Fr^2}y\Big)\Bigg)\mathrm{d}\mathbf{x}. \tag{4.29}$$

By adding Eq.(4.29) to Eq.(4.28), having in mind Eq.(4.15) and the following identity under the homogeneous boundary conditions for $\mathbf{u}$

$$\int_\Omega \left(\frac{1}{Fr^2}(\rho-\rho_0)\hat{\mathbf{j}}\cdot\mathbf{u}\right)\mathrm{d}\mathbf{x} = -\int_\Omega \left(\frac{1}{Fr^2}\nabla\cdot\Big((\rho-\rho_0)\mathbf{u}\Big)y\right)\mathrm{d}\mathbf{x}, \tag{4.30}$$

we finally obtain the continuous energy law for the quasi-incompressible NSCH system with respect to the total energy $\widehat{E}$ (defined in Eq.(4.10)),

$$\begin{aligned}\frac{\mathrm{d}\widehat{E}}{\mathrm{d}t} &= \frac{\mathrm{d}}{\mathrm{d}t}\left(\frac{1}{2}||\sqrt{\rho}\mathbf{u}||_{L^2}^2+\frac{C}{2M}||\sqrt{\rho}\,\nabla c||_{L^2}^2+\int_\Omega\Big(\frac{1}{M}\rho F(c)+\frac{1}{Fr^2}\rho y\Big)\mathrm{d}\mathbf{x}\right)\\ &= -\frac{1}{Re}||\nabla\mathbf{u}||_{L^2}^2-\frac{1}{3Re}||\nabla\cdot\mathbf{u}||_{L^2}^2-\frac{1}{MPe}||\nabla\mu||_{L^2}^2.\end{aligned} \tag{4.31}$$

By using Eq.(4.16), we obtain

$$\begin{aligned}\frac{\mathrm{d}E}{\mathrm{d}t} &= \frac{\mathrm{d}}{\mathrm{d}t}\left(\frac{1}{2}||\sqrt{\rho}\mathbf{u}||_{L^2}^2+\frac{C}{2M}||\sqrt{\rho}\,\nabla c||_{L^2}^2+\int_\Omega\Big(\frac{1}{M}\rho F(c)\Big)\mathrm{d}\mathbf{x}\right)\\ &= -\frac{1}{Re}||\nabla\mathbf{u}||_{L^2}^2-\frac{1}{3Re}||\nabla\cdot\mathbf{u}||_{L^2}^2-\frac{1}{MPe}||\nabla\mu||_{L^2}^2\\ &\quad-\int_\Omega\left(\frac{1}{Fr^2}(\rho-\rho_0)\hat{\mathbf{j}}\cdot\mathbf{u}+\frac{\rho_0\alpha}{Fr^2Pe}\hat{\mathbf{j}}\cdot\nabla\mu\right)\mathrm{d}\mathbf{x},\end{aligned} \tag{4.32}$$

for the original energy E (Eq.(4.9)), without the potential energy. Note that two energy laws (4.31) and (4.32) are equivalent in the continuous case, whereas, at the discrete level, this equivalence relation depends on the discretization of the numerical methods. In section 4.4, two energy law preserving numerical methods are developed corresponding to the energy law (4.31) and (4.32) respectively. The method (based on Eq.(4.1a)) with respect to the energy law (4.31) is used for our computations, and the other method (based on Eq.(4.1b)) that preserves the energy law (4.32) at the discrete level is presented in Remark 4.2.

From Eqs.(4.22), (4.25) and (4.29) we notice that, in deriving the energy law, the terms $C\rho\nabla c\cdot\nabla[(\mathbf{u}\cdot\nabla)c]/M$ and $-\alpha C\nabla\mu\cdot\nabla(\rho\nabla c\cdot\nabla c)/2MPe$ are involved, implying that a higher regularity than $c\in W^{1,3}$ is needed and that more complicated C^1 finite elements are needed. To ensure the energy law with the lower regularity $c\in W^{1,3}$, we need to reformulate the equations of the system (4.1)-(4.4), so that only first order derivatives of c are required during the derivation so that an energy law preserving C^0 finite element method can be derived.

4.4 Reformulation and the Numerical Method that Accurately Preserve the Energy Law

We first reformulate the momentum equation (4.2) and the chemical potential equation (4.4) in order that a rigorous energy law can be derived using lower regularity requirements so that the continuous (C^0) finite element can be used. We emphasise C^0 finite elements because they are much simpler than the finite elements with a higher degree of smoothness and are available in most existing finite element software packages, which reduces various complications. Based on the weak form of reformulated system, we then develop a special numerical scheme such that a discrete energy law can

be rigorously obtained that is very similar to the continuous one (4.31). This feature not only immediately implies the stability of the numerical scheme, but also ensures the accuracy of the solutions.

4.4.1 New Formulation of the Momentum Equation

In order to obtain an accurate discrete energy law, we first consider the continuous equation (4.1b)

$$\rho_t + \nabla \cdot (\rho \mathbf{u}) = 0,$$

by multiplying $\mathbf{u}/2$, we obtain

$$\frac{1}{2}\rho_t \mathbf{u} + \frac{1}{2}\nabla \cdot (\rho \mathbf{u})\mathbf{u} = 0.$$

By adding this term to Eq.(4.2), we obtain

$$\sqrt{\rho}(\sqrt{\rho}\mathbf{u})_t + \rho(\mathbf{u}\cdot\nabla)\mathbf{u} + \frac{1}{2}\nabla\cdot(\rho\mathbf{u})\mathbf{u} = -\frac{1}{M}\Big(\nabla p + C\nabla\cdot(\rho\nabla c\otimes\nabla c)\Big) + \nabla\cdot(\frac{1}{Re}\nabla\mathbf{u}) + \nabla\Big(\frac{1}{3Re}(\nabla\cdot\mathbf{u})\Big) - \frac{1}{Fr^2}(\rho-\rho_0)\hat{\mathbf{j}}. \quad (4.33)$$

We next consider the chemical potential equation (4.4) and rewrite it as

$$\mu - f(c) + \frac{\partial\rho}{\partial c}\frac{p}{\rho^2} + \frac{C}{\rho}\nabla\cdot(\rho\nabla c) + \frac{M\rho_0\alpha}{Fr^2}y = 0,$$

by multiplying $\rho\nabla c/M$ and using Eq.(4.26), we obtain

$$\frac{1}{M}\rho\nabla c\mu - \frac{1}{M}\rho\nabla F(c) + \frac{1}{M}\frac{p}{\rho}\nabla\rho + \frac{C}{M}\nabla\cdot(\rho\nabla c\otimes\nabla c) \\ - \frac{C}{2M}\rho\nabla(\nabla c\cdot\nabla c) + \frac{\rho_0\alpha}{Fr^2}y\rho\nabla c = 0. \tag{4.34}$$

By introducing a new pressure $\hat{p}$,

$$\hat{p} = p + \rho F(c) + \frac{C}{2}\rho|\nabla c|^2, \tag{4.35}$$

we obtain

$$p = \hat{p} - \rho F(c) - \frac{C}{2}\rho|\nabla c|^2. \tag{4.36}$$

Adding Eq.(4.34) to Eq.(4.33) and using in mind of Eq.(4.36), we obtain a new formulation of the momentum equation

$$\sqrt{\rho}(\sqrt{\rho}\mathbf{u})_t + \rho(\mathbf{u}\cdot\nabla)\mathbf{u} + \frac{1}{2}\nabla\cdot(\rho\mathbf{u})\mathbf{u} = -\frac{1}{M}\rho\nabla(\frac{\hat{p}}{\rho}) + \frac{1}{M}\rho\mu\nabla c \\ + \nabla\cdot(\frac{1}{Re}\nabla\mathbf{u}) + \nabla\Big(\frac{1}{3Re}(\nabla\cdot\mathbf{u})\Big) + \frac{\rho_0\alpha}{Fr^2}y\rho\nabla c - \frac{1}{Fr^2}(\rho-\rho_0)\hat{\mathbf{j}}. \tag{4.37}$$

Note that the similar treatment for the variable density terms can be found in [110], where a different phase-field model has been studied and a variable $\sigma = \sqrt{\rho}$ was introduced.

4.4.2 New Formulation of the Chemical Potential Equation

For the chemical potential equation (4.4), by multiplying ρ on both sides and substituting (4.36) we obtain

$$\rho\mu = \rho f(c) - \frac{\partial\rho}{\partial c}\frac{\hat{p}}{\rho} + \frac{\partial\rho}{\partial c}F(c) + \frac{\partial\rho C}{\partial c}\frac{}{2}(\nabla c\cdot\nabla c) - C\nabla\cdot(\rho\nabla c) - \frac{M\rho_0\alpha}{Fr^2}y\rho.$$

Note that the reason we introduce a new pressure $\hat{p}$ and reformulate Eq.(4.2) and Eq.(4.4) is that, in the weak form presented later, we can derive an accurate discrete energy law while keeping the variables in appropriate functional spaces as we assume at the beginning of section 4.3.

4.4.3 New System and Weak Form

Now we obtain the new system for the quasi-incompressible NSCH system for variable density flows,

$$\nabla\cdot\mathbf{u} = \frac{\alpha}{Pe}\Delta\mu, \tag{4.38}$$

$$\sqrt{\rho}(\sqrt{\rho}\mathbf{u})_t + \rho(\mathbf{u}\cdot\nabla)\mathbf{u} + \frac{1}{2}\nabla\cdot(\rho\mathbf{u})\mathbf{u} = -\frac{1}{M}\rho\nabla(\frac{\hat{p}}{\rho}) + \frac{1}{M}\rho\mu\nabla c$$
$$+\nabla\cdot(\frac{1}{Re}\nabla\mathbf{u}) + \nabla\Big(\frac{1}{3Re}(\nabla\cdot\mathbf{u})\Big) + \frac{\rho_0\alpha}{Fr^2}y\rho\nabla c - \frac{1}{Fr^2}(\rho-\rho_0)\hat{\mathbf{j}}, \tag{4.39}$$

$$\rho\dot{c} = \nabla\cdot(\frac{1}{Pe}\nabla\mu), \tag{4.40}$$

$$\rho\mu = \rho f(c) - \frac{\partial\rho}{\partial c}\frac{\hat{p}}{\rho} + \frac{\partial\rho}{\partial c}F(c) + \frac{\partial\rho C}{\partial c}\frac{}{2}(\nabla c\cdot\nabla c) - C\nabla\cdot(\rho\nabla c) - \frac{M\rho_0\alpha}{Fr^2}y\rho. \tag{4.41}$$

The corresponding new weak form reads: find $\mathbf{u} \in \mathbf{W}_{\mathbf{b}}^{1,3}(\Omega)$, $\hat{p}/\rho \in W^{1,3/2}(\Omega)$, $c \in W^{1,3}(\Omega)$ and $\mu \in W^{1,3}(\Omega)$ such that

$$\int_\Omega \left(-\mathbf{u}\cdot\nabla q \right) \mathrm{d}\mathbf{x} = \int_\Omega \left(-\frac{\alpha}{Pe}\nabla\mu\cdot\nabla q \right) \mathrm{d}\mathbf{x}, \qquad \forall q \in W^{1,3/2}(\Omega), \tag{4.42}$$

$$\begin{aligned}\int_\Omega \Big(\sqrt{\rho}(\sqrt{\rho}\mathbf{u})_t\cdot\mathbf{v} + \rho(\mathbf{u}\cdot\nabla)\mathbf{u}\cdot\mathbf{v} + \frac{1}{2}\nabla\cdot(\rho\mathbf{u})\mathbf{u}\cdot\mathbf{v} \Big) \mathrm{d}\mathbf{x} = \int_\Omega \Big(& -\frac{1}{M}\rho(\mathbf{v}\cdot\nabla)\frac{\hat{p}}{\rho} \\ & -\frac{1}{Re}\nabla\mathbf{u}:\nabla\mathbf{v} - \frac{1}{3Re}(\nabla\cdot\mathbf{u})(\nabla\cdot\mathbf{v}) + \frac{1}{M}\rho(\mathbf{v}\cdot\nabla)c\mu + \frac{\rho_0\alpha}{Fr^2}y\rho\mathbf{v}\cdot\nabla c \\ & -\frac{1}{Fr^2}(\rho-\rho_0)\hat{\mathbf{j}}\cdot\mathbf{v} \Big) \mathrm{d}\mathbf{x}, \qquad \forall \mathbf{v} \in \mathbf{W}_0^{1,3}(\Omega),\end{aligned} \tag{4.43}$$

$$\int_\Omega \left(\rho\dot{c}\psi \right) \mathrm{d}\mathbf{x} = \int_\Omega \left(-\frac{1}{Pe}\nabla\mu\cdot\nabla\psi \right) \mathrm{d}\mathbf{x}, \qquad \forall \psi \in W^{1,3/2}(\Omega), \tag{4.44}$$

$$\begin{aligned}\int_\Omega \left(\rho\mu\chi \right) \mathrm{d}\mathbf{x} = \int_\Omega \Big(& \rho f(c)\chi - \frac{\partial\rho}{\partial c}\frac{\hat{p}}{\rho}\chi + \frac{\partial\rho}{\partial c}F(c)\chi + \frac{\partial\rho}{\partial c}\frac{C}{2}(\nabla c\cdot\nabla c)\chi + C\rho\nabla c\cdot\nabla\chi \\ & -\frac{M\rho_0\alpha}{Fr^2}y\rho\chi \Big) \mathrm{d}\mathbf{x}, \qquad \forall \chi \in W^{1,3}(\Omega).\end{aligned} \tag{4.45}$$

If we let $\mathbf{v} = \mathbf{u}$, $\psi = \mu/M - (\rho-\rho_0)\alpha y/Fr^2 - \alpha\hat{p}/M$, $\chi = c_t/M$ and $q = \hat{p}/M$, we can still obtain the continuous energy law

$$\begin{aligned}\frac{\mathrm{d}\widehat{E}}{\mathrm{d}t} &= \frac{\mathrm{d}}{\mathrm{d}t}\left(\frac{1}{2}||\sqrt{\rho}\mathbf{u}||_{L^2}^2 + \frac{C}{2M}||\sqrt{\rho}\,\nabla c||_{L^2}^2 + \int_\Omega \Big(\frac{1}{M}\rho F(c) + \frac{1}{Fr^2}\rho y \Big) \mathrm{d}\mathbf{x} \right) \\ &= -\frac{1}{Re}||\nabla\mathbf{u}||_{L^2}^2 - \frac{1}{3Re}||\nabla\cdot\mathbf{u}||_{L^2}^2 - \frac{1}{MPe}||\nabla\mu||_{L^2}^2.\end{aligned}$$

From Sobolev's embedding theorem [3] (page 85), we know that

$$||f||_{L^q(\Omega)} \leq C||\nabla f||_{L^p(\Omega)},\ \forall f \in W^{1,p},\ 1 \leq p < q \leq \frac{np}{n-p},$$

where C is a generic constant. As mentioned earlier, we only consider the problem in 2D cases. By setting $f = c^3$, $n = 2$, $p = 1$ and $q = np/(n-p)$, we have

$$||c^4||^{3/4}_{L^{3/2}} = ||c^3||_{L^2} \leq C||3c^2\nabla c||_{L^1} \leq C||c||^2_{L^3}||\nabla c||_{L^3}\ ,$$

where the Hölder's inequality is used ($||fg||_{L^1} \leq ||f||_{L^{3/2}}||g||_{L^3}$). Hence, in the third term at the right hand side, $F(c) \in L^{3/2}$. In the fourth term at the right hand side, it is obvious that $\nabla c \cdot \nabla c \in L^{3/2}$ when $c \in W^{1,3}$ by Hölder's inequality. Bearing in mind $\rho \in L^\infty(\Omega)$ and Eq.(4.5), we obtain

$$\frac{\partial \rho}{\partial c}F(c) \in L^{3/2} \text{ and } \frac{\partial \rho}{\partial c}\nabla c \cdot \nabla c \in L^{3/2}, \tag{4.46}$$

and thus both integrals are finite when $c \in W^{1,3}$ and $\chi \in W^{1,3}$.

Next we present a special temporal scheme where an accurate discrete energy law can be obtained. If C^0 finite elements are used and if time remains continuous, the finite element solution belongs to the functional spaces required in weak form (4.42)-(4.45).

4.4.4 A Special Temporal Scheme with an Accurate Discrete Energy Law

We seek to solve the weak problem (4.42)-(4.45) using a finite difference scheme in time and a conformal C^0 finite element method in space. Let

$$\mathbf{W}_b = \mathbf{W}_b^{1,3}(\Omega) \times W^{1,3/2}(\Omega) \times W^{1,3}(\Omega) \times W^{1,3}(\Omega),$$

and $\mathbf{W}_b^h = \mathbf{U}_b^h \times P^h \times H^h \times H^h$, be a finite dimensional subspace of $\mathbf{W}_b$ given by a finite element discretization of Ω. Let $\Delta t > 0$ represent the time step size and $(\mathbf{u}_h^n, \hat{p}_h^n, c_h^n, \mu_h^n) \in \mathbf{W}_b^h$ be an approximation of $\mathbf{u}(t^n) = \mathbf{u}(n\Delta t)$, $\hat{p}(t^n) = p(\Delta t)$, $c(t^n) = c(\Delta t)$ and $\mu(t^n) = \mu(\Delta t)$. The approximation at time $t^{n+1} = (n+1)\Delta t$ is denoted as $(\mathbf{u}_h^{n+1}, \hat{p}_h^{n+1}, c_h^{n+1}, \mu_h^{n+1}) \in \mathbf{W}_b^h$ and is computed by the following finite element scheme

$$\int_\Omega \left(-(\sqrt{\rho}\mathbf{u})_h^{n+1} \cdot \nabla q \right) \mathrm{d}\mathbf{x} = \int_\Omega \left(-\frac{\alpha}{Pe} \nabla \mu_h^{n+\frac{1}{2}} \cdot \nabla q \right) \mathrm{d}\mathbf{x}, \tag{4.47}$$

$$\begin{aligned}
&\int_\Omega \Bigg(\sqrt{\rho}_h^{n+\frac{1}{2}} (\sqrt{\rho}\mathbf{u})_{\bar{t}}^{n+1} \cdot \mathbf{v} + \rho_h^{n+\frac{1}{2}} \Big((\sqrt{\rho}\mathbf{u})_h^{n+1} \cdot \nabla \Big) (\sqrt{\rho}\mathbf{u})_h^{n+1} \cdot \mathbf{v} \\
&\qquad + \frac{1}{2} \nabla \cdot \Big(\rho_h^{n+\frac{1}{2}} (\sqrt{\rho}\mathbf{u})_h^{n+1} \Big) (\sqrt{\rho}\mathbf{u})_h^{n+1} \cdot \mathbf{v} \Bigg) \mathrm{d}\mathbf{x} \\
&= \int_\Omega \Bigg(-\frac{1}{M} \rho_h^{n+\frac{1}{2}} (\mathbf{v} \cdot \nabla) \frac{\hat{p}_h^{n+\frac{1}{2}}}{\rho_h^{n+\frac{1}{2}}} - \frac{1}{Re} \nabla (\sqrt{\rho}\mathbf{u})_h^{n+1} : \nabla \mathbf{v} - \frac{1}{3Re} \Big(\nabla \cdot (\sqrt{\rho}\mathbf{u})_h^{n+1} \Big) \Big(\nabla \cdot \mathbf{v} \Big) \\
&\quad - \frac{1}{M} \frac{1}{\alpha \rho_h^{n+\frac{1}{2}}} (\mathbf{v} \cdot \nabla) \rho_h^{n+\frac{1}{2}} \mu_h^{n+\frac{1}{2}} - \frac{\rho_0 \alpha}{Fr^2} y \frac{1}{\alpha \rho_h^{n+\frac{1}{2}}} \mathbf{v} \cdot \nabla \rho_h^{n+\frac{1}{2}} - \frac{1}{Fr^2} (\rho_h^{n+\frac{1}{2}} - \rho_0) \hat{\mathbf{j}} \cdot \mathbf{v} \Bigg) \mathrm{d}\mathbf{x},
\end{aligned} \tag{4.48}$$

$$\int_\Omega \Bigg(-\frac{r(c_h^{n+1}, c_h^n)}{\alpha \rho_h^{n+\frac{1}{2}}} c_{\bar{t}}^{n+1} \psi + \frac{1}{2\rho_h^{n+\frac{1}{2}}} \Big((\rho_h^{n+1})^2 (\sqrt{\rho}\mathbf{u})_h^{n+1} \cdot \nabla c_h^{n+1}$$

$$+(\rho_h^n)^2(\sqrt{\rho}\mathbf{u})_h^{n+1}\cdot\nabla c_h^n\Big)\psi\Bigg)\mathrm{d}\mathbf{x}=\int_\Omega\Bigg(-\frac{1}{Pe}\nabla\mu_h^{n+\frac{1}{2}}\cdot\nabla\psi\Bigg)\mathrm{d}\mathbf{x}, \tag{4.49}$$

$$\int_\Omega\Bigg(-\frac{r(c_h^{n+1},c_h^n)}{\alpha\rho_h^{n+\frac{1}{2}}}\mu_h^{n+\frac{1}{2}}\chi\Bigg)\mathrm{d}\mathbf{x}=\int_\Omega\Bigg(\rho_h^{n+\frac{1}{2}}g(c_h^{n+1},c_h^n)\chi-\frac{1}{\rho_h^{n+\frac{1}{2}}}r(c_h^{n+1},c_h^n)\hat{p}_h^{n+\frac{1}{2}}\chi$$
$$+\frac{1}{2}\Big(F(c_h^{n+1})+F(c_h^n)\Big)r(c_h^{n+1},c_h^n)\chi+\frac{C}{4}(\nabla c_h^{n+1}\cdot\nabla c_h^{n+1}+\nabla c_h^n\cdot\nabla c_h^n)r(c_h^{n+1},c_h^n)\chi$$
$$+C\rho_h^{n+\frac{1}{2}}\nabla c_h^{n+\frac{1}{2}}\cdot\nabla\chi+\frac{r(c_h^{n+1},c_h^n)}{\rho_h^{n+\frac{1}{2}}}\frac{M\rho_0}{Fr^2}y\chi\Bigg)\mathrm{d}\mathbf{x}, \tag{4.50}$$

for all $(\mathbf{v},q,\psi,\chi)\in\mathbf{W}_0^h$, where $\mathbf{W}_0^h$ represents the space $\mathbf{W}_b^h$ $(b=0)$ satisfying homogeneous Dirichlet boundary conditions and

$$\rho_h^{n+1}=\frac{\rho_1\rho_2}{(\rho_2-\rho_1)c_h^{n+1}+\rho_1},\qquad \rho_h^{n+\frac{1}{2}}=\frac{\rho_h^{n+1}+\rho_h^n}{2},\qquad \sqrt{\rho}_h^{n+\frac{1}{2}}=\frac{\sqrt{\rho_h^{n+1}}+\sqrt{\rho_h^n}}{2},$$
$$\hat{p}_h^{n+\frac{1}{2}}=\frac{\hat{p}_h^{n+1}+\hat{p}_h^n}{2},\quad (\sqrt{\rho}\mathbf{u})_h^{n+1}=\frac{\sqrt{\rho_h^{n+1}}\mathbf{u}_h^{n+1}+\sqrt{\rho_h^n}\mathbf{u}_h^n}{\sqrt{\rho_h^{n+1}}+\sqrt{\rho_h^n}},\quad (\sqrt{\rho}\mathbf{u})_{\bar{t}}^{n+1}=\frac{\sqrt{\rho_h^{n+1}}\mathbf{u}_h^{n+1}-\sqrt{\rho_h^n}\mathbf{u}_h^n}{\Delta t},$$
$$c_{\bar{t}}^{n+1}=\frac{c_h^{n+1}-c_h^n}{\Delta t},\qquad c_h^{n+\frac{1}{2}}=\frac{c_h^{n+1}+c_h^n}{2},\qquad \mu_h^{n+\frac{1}{2}}=\frac{\mu_h^{n+1}+\mu_h^n}{2}.$$

Further,

$$g(c_h^{n+1},c_h^n)=\frac{1}{4}\Big(c_h^{n+1}(c_h^{n+1}-1)+c_h^n(c_h^n-1)\Big)(c_h^{n+1}+c_h^n-1) \tag{4.51}$$

is an approximation to the nonlinear function $F'(c)=f(c)=c(c-1)(c-1/2)$, where we note the identity,

$$F(c_h^{n+1})-F(c_h^n)=g(c_h^{n+1},c_h^n)(c_h^{n+1}-c_h^n). \tag{4.52}$$

Here

$$r(c_h^{n+1}, c_h^n) = -\frac{\rho_1\rho_2(\rho_2-\rho_1)}{\Big((\rho_2-\rho_1)\Big)c_h^{n+1}+\rho_1)\Big((\rho_2-\rho_1)c_h^n+\rho_1\Big)}, \tag{4.53}$$

is an approximation of the nonlinear function

$$\frac{\partial\rho(c)}{\partial c} = -\alpha\rho^2(c) = -\frac{\rho_1\rho_2(\rho_2-\rho_1)}{\Big((\rho_2-\rho_1)c+\rho_1\Big)^2}, \tag{4.54}$$

where we note the identity

$$\rho(c_h^{n+1}) - \rho(c_h^n) = r(c_h^{n+1}, c_h^n)(c_h^{n+1} - c_h^n). \tag{4.55}$$

And we use

$$-\frac{r(c_h^{n+1}, c_h^n)}{\alpha\rho_h^{n+\frac{1}{2}}},\ \frac{(\rho_h^{n+1})^2}{\rho_h^{n+\frac{1}{2}}} \text{ and } \frac{(\rho_h^n)^2}{\rho_h^{n+\frac{1}{2}}} \tag{4.56}$$

to approximate $\rho(c)$.

Theorem 4.4.1. *In the case of homogeneous boundary conditions, the solution of scheme (4.47)-(4.50) satisfies the following discrete energy law, which is analogous to that obtained in the continuous case in Eq.(4.31),*

$$\begin{aligned}\widehat{E}_{\bar{t}}^{n+1} &= \left(\frac{1}{2}||\sqrt{\rho_h^{n+1}}\mathbf{u}_h^{n+1}||_{L^2}^2 + \frac{C}{2M}||\sqrt{\rho_h^{n+1}}\nabla c_h^{n+1}||_{L^2}^2 + \int_\Omega\Big(\frac{1}{M}\rho_h^{n+1}F(c_h^{n+1})\right.\\ &\left.+\frac{1}{Fr^2}\rho_h^{n+1}y\Big)\mathrm{d}\mathbf{x}\right)_{\bar{t}}\\ &= -\frac{1}{Re}||\nabla(\sqrt{\rho}\mathbf{u})_h^{n+1}||_{L^2}^2 - \frac{1}{3Re}||\nabla\cdot(\sqrt{\rho}\mathbf{u})_h^{n+1}||_{L^2}^2 - \frac{1}{MPe}||\nabla\mu_h^{n+\frac{1}{2}}||_{L^2}^2.\end{aligned} \tag{4.57}$$

Proof. According to the continuous energy law, by setting $\mathbf{v} = (\sqrt{\rho}\mathbf{u})_h^{n+1}$ *in Eq.(4.48) and using integration by parts, we have*

$$\begin{aligned}
&\left(\frac{1}{2}||\sqrt{\rho_h^{n+1}}\mathbf{u}_h^{n+1}||_{L^2}^2\right)_{\bar{t}} = \int_\Omega \left(\frac{1}{M}\frac{\hat{p}_h^{n+\frac{1}{2}}}{\rho_h^{n+\frac{1}{2}}}\nabla\cdot\left(\rho_h^{n+\frac{1}{2}}(\sqrt{\rho}\mathbf{u})_h^{n+1}\right)\right.\\
&-\frac{1}{M}\frac{\rho_0 y}{\alpha\rho_h^{n+\frac{1}{2}}}(\sqrt{\rho}\mathbf{u})_h^{n+1}\cdot\nabla\rho_h^{n+\frac{1}{2}} - \frac{1}{M}\frac{1}{\alpha\rho_h^{n+\frac{1}{2}}}(\sqrt{\rho}\mathbf{u})_h^{n+1}\cdot\nabla\rho_h^{n+\frac{1}{2}}\mu_h^{n+\frac{1}{2}}\\
&\left.+\frac{1}{Fr^2}(\rho_h^{n+\frac{1}{2}}-\rho_0)\hat{\mathbf{j}}\cdot(\sqrt{\rho}\mathbf{u})_h^{n+1}\right)\mathrm{d}\mathbf{x} - \frac{1}{Re}||\nabla(\sqrt{\rho}\mathbf{u})_h^{n+1}||_{L^2}^2 - \frac{1}{3Re}||\nabla\cdot(\sqrt{\rho}\mathbf{u})_h^{n+1}||_{L^2}^2.
\end{aligned} \tag{4.58}$$

Taking $\psi = -(\rho_h^{n+1/2}-\rho_0)\alpha y/Fr^2 - \alpha\hat{p}_h^{n+1/2}/M + \mu_h^{n+1/2}/M$ *in Eq.(4.49) leads to*

$$\begin{aligned}
&\left(\int_\Omega\left(\frac{1}{Fr^2}\rho^{n+1}y\right)\mathrm{d}\mathbf{x}\right)_{\bar{t}} = \int_\Omega\left(\frac{\alpha}{Fr^2Pe}\nabla\mu_h^{n+\frac{1}{2}}\cdot\nabla(\rho_h^{n+\frac{1}{2}}y) - \frac{1}{Fr^2}y(\sqrt{\rho}\mathbf{u})_h^{n+1}\cdot\nabla\rho_h^{n+\frac{1}{2}}\right.\\
&+\frac{1}{Fr^2}\frac{\rho_0 y}{\rho_h^{n+\frac{1}{2}}}\rho_{\bar{t}}^{n+1} + \frac{1}{M}\frac{\rho_0 y}{\alpha\rho_h^{n+\frac{1}{2}}}(\sqrt{\rho}\mathbf{u})_h^{n+1}\cdot\nabla\rho_h^{n+\frac{1}{2}} - \frac{\alpha}{Fr^2Pe}\nabla\mu_h^{n+\frac{1}{2}}\cdot\nabla(\rho_0 y)\\
&-\frac{1}{M}\frac{\hat{p}_h^{n+1/2}}{\rho_h^{n+\frac{1}{2}}}\rho_{\bar{t}}^{n+1} - \frac{1}{M}\frac{\hat{p}_h^{n+1/2}}{\rho_h^{n+\frac{1}{2}}}(\sqrt{\rho}\mathbf{u})_h^{n+1}\cdot\nabla\rho_h^{n+\frac{1}{2}} + \frac{\alpha}{MPe}\nabla\mu_h^{n+\frac{1}{2}}\cdot\nabla\hat{p}_h^{n+\frac{1}{2}}\\
&\left.+\frac{1}{M}\frac{\mu_h^{n+\frac{1}{2}}}{\alpha\rho_h^{n+\frac{1}{2}}}\rho_{\bar{t}}^{n+1} + \frac{1}{M}\frac{\mu_h^{n+\frac{1}{2}}}{\alpha\rho_h^{n+\frac{1}{2}}}(\sqrt{\rho}\mathbf{u})_h^{n+1}\cdot\nabla\rho_h^{n+\frac{1}{2}}\right)\mathrm{d}\mathbf{x} - \frac{1}{MPe}||\nabla\mu_h^{n+\frac{1}{2}}||_{L^2}^2.
\end{aligned} \tag{4.59}$$

By taking $\chi = c_{\bar{t}}^{n+1}/M$ *in Eq.(4.50), we obtain*

$$\begin{aligned}
&\left(\frac{C}{2M}||\sqrt{\rho_h^{n+1}}\nabla c_h^{n+1}||_{L^2}^2 + \frac{1}{M}\int_\Omega\left(\rho_h^{n+1}F(c_h^{n+1})\right)\mathrm{d}\mathbf{x}\right)_{\bar{t}} =\\
&\int_\Omega\left(-\frac{1}{M}\frac{1}{\alpha\rho_h^{n+\frac{1}{2}}}\rho_{\bar{t}}^{n+1}\mu_h^{n+\frac{1}{2}} + \frac{1}{M}\frac{\hat{p}_h^{n+1/2}}{\rho_h^{n+\frac{1}{2}}}\rho_{\bar{t}}^{n+1} - \frac{1}{Fr^2}\frac{\rho_0 y}{\rho_h^{n+\frac{1}{2}}}\rho_{\bar{t}}^{n+1}\right)\mathrm{d}\mathbf{x}.
\end{aligned} \tag{4.60}$$

Taking $q = \hat{p}_h^{n+1/2}/M + (\rho_h^{n+1/2} - \rho_0)y/Fr^2$ *in Eq.(4.47) and using integration by parts, we obtain*

$$0 = \int_\Omega \Bigg(-\nabla\cdot(\sqrt{\rho}\mathbf{u})_h^{n+1}\Big(\frac{1}{M}\hat{p}_h^{n+1/2} + \frac{1}{Fr^2}(\rho-\rho_0)y\Big) - \frac{\alpha}{Pe}\nabla\mu_h^{n+\frac{1}{2}}\cdot\nabla\Big(\frac{1}{M}\hat{p}_h^{n+1/2} + \frac{1}{Fr^2}(\rho-\rho_0)y\Big)\Bigg)\mathrm{d}\mathbf{x}. \quad (4.61)$$

Combing Eqs.(4.58)-(4.61) together, we finally obtain the discrete energy law (4.57) for the weak form (4.47)-(4.50),

$$\begin{aligned}\widehat{E}_{\bar{t}}^{n+1} &= \Bigg(\frac{1}{2}||\sqrt{\rho_h^{n+1}}\mathbf{u}_h^{n+1}||_{L^2}^2 + \frac{C}{2M}||\sqrt{\rho_h^{n+1}}\nabla c_h^{n+1}||_{L^2}^2 + \int_\Omega\Big(\frac{1}{M}\rho_h^{n+1}F(c_h^{n+1}) \\ &\quad + \frac{1}{Fr^2}\rho_h^{n+1}y\Big)\mathrm{d}\mathbf{x}\Bigg)_{\bar{t}} \\ &= -\frac{1}{Re}||\nabla(\sqrt{\rho}\mathbf{u})_h^{n+1}||_{L^2}^2 - \frac{1}{3Re}||\nabla\cdot(\sqrt{\rho}\mathbf{u})_h^{n+1}||_{L^2}^2 - \frac{1}{MPe}||\nabla\mu_h^{n+\frac{1}{2}}||_{L^2}^2.\end{aligned}$$

This completes the proof. □

Note that the numerical scheme (4.47)-(4.50) is used for our computations later. Another energy-law preserving numerical method with respect to the continuous energy law (4.32) may be also designed, see Remark 4.4.2.

Remark 4.4.1. *We now remark about how to implement the scheme (4.47)-(4.50) and how to choose continuous finite element spaces based on the above derivation of the discrete energy law. From the weak form (4.47)-(4.50) we observe that* $\mathbf{u}$ *appears in the form of* $\sqrt{\rho}\mathbf{u}$ *and* $\hat{p}$ *appears in the form (or can be made in the form) of* $\hat{p}/\rho$*. We can thus introduce new variables* $\tilde{\mathbf{u}} = \sqrt{\rho}\mathbf{u}$ *and* $\tilde{p} = \hat{p}/\rho$*, and denote the corresponding finite element spaces as* $\tilde{\mathbf{U}}^h$ *and* $\tilde{P}^h$ *respectively.*

Remark 4.4.2. *If we want to solve the model based on equation (4.1b) instead of (4.1a), we can also design a method which can preserve the energy law (4.32) at the discrete level. With* $\mathbf{u}_h^{n+1}, p_h^{n+1}, c_h^{n+1}, \mu_h^{n+1}, \mathbf{v}, q, \psi, \chi$ *in the appropriate spaces, we seek solutions* $(\mathbf{u}_h^{n+1}, p_h^{n+1}, c_h^{n+1}, \mu_h^{n+1})$ *by computing the following finite element scheme*

$$\int_\Omega \left(\rho_{\bar{t}}^{n+1} q\right) \mathrm{d}\mathbf{x} = \int_\Omega \left(-\nabla\cdot\left(\rho_h^{n+\frac{1}{2}} (\sqrt{\rho}\mathbf{u})_h^{n+1}\right) q \right) \mathrm{d}\mathbf{x}, \tag{4.62}$$

$$\begin{aligned}
&\int_\Omega \Bigg(\sqrt{\rho}_h^{n+\frac{1}{2}} (\sqrt{\rho}\mathbf{u})_{\bar{t}}^{n+1}\cdot\mathbf{v} + \rho_h^{n+\frac{1}{2}} \Big((\sqrt{\rho}\mathbf{u})_h^{n+1}\cdot\nabla \Big) (\sqrt{\rho}\mathbf{u})_h^{n+1}\cdot\mathbf{v} \\
&\qquad + \frac{1}{2}\nabla\cdot\left(\rho_h^{n+\frac{1}{2}} (\sqrt{\rho}\mathbf{u})_h^{n+1}\right)(\sqrt{\rho}\mathbf{u})_h^{n+1}\cdot\mathbf{v} \Bigg) \mathrm{d}\mathbf{x} \\
&= \int_\Omega \Bigg(\frac{1}{M} p_h^{n+\frac{1}{2}} (\nabla\cdot\mathbf{v}) - \frac{1}{Re}\nabla(\sqrt{\rho}\mathbf{u})_h^{n+1} : \nabla\mathbf{v} - \frac{1}{3Re}\Big(\nabla\cdot(\sqrt{\rho}\mathbf{u})_h^{n+1}\Big)(\nabla\cdot\mathbf{v}) \\
&+ \frac{1}{M}\rho_h^{n+\frac{1}{2}} \mu_h^{n+\frac{1}{2}} (\mathbf{v}\cdot\nabla) c_h^{n+\frac{1}{2}} + \frac{1}{2M}\Big(F(c_h^{n+1}) + F(c_h^n)\Big)\nabla\cdot(\rho_h^{n+\frac{1}{2}}\mathbf{v}) \\
&+ \frac{1}{M}\frac{p_h^{n+\frac{1}{2}}}{\rho_h^{n+\frac{1}{2}}} (\mathbf{v}\cdot\nabla)\rho_h^{n+\frac{1}{2}} + \frac{C}{4M}(\nabla c_h^{n+1}\cdot\nabla c_h^{n+1} + \nabla c_h^n\cdot\nabla c_h^n)\nabla\cdot(\rho_h^{n+\frac{1}{2}}\mathbf{v}) \\
&\qquad + \frac{\rho_0\alpha}{Fr^2} y \rho_h^{n+\frac{1}{2}}\mathbf{v}\cdot\nabla c_h^{n+\frac{1}{2}} - \frac{1}{Fr^2}(\rho_h^{n+\frac{1}{2}} - \rho_0)\hat{\mathbf{j}}\cdot\mathbf{v} \Bigg) \mathrm{d}\mathbf{x},
\end{aligned} \tag{4.63}$$

$$\int_\Omega \left(\rho_h^{n+\frac{1}{2}} c_{\bar{t}}^{n+1}\psi + \rho_h^{n+\frac{1}{2}} \Big((\sqrt{\rho}\mathbf{u})_h^{n+1}\cdot\nabla \Big) c_h^{n+\frac{1}{2}}\psi \right) \mathrm{d}\mathbf{x} = \int_\Omega \left(-\frac{1}{Pe}\nabla\mu_h^{n+\frac{1}{2}}\cdot\nabla\psi \right) \mathrm{d}\mathbf{x}, \tag{4.64}$$

$$\begin{aligned}
\int_\Omega \left(\rho_h^{n+\frac{1}{2}} \mu_h^{n+\frac{1}{2}} \chi \right) \mathrm{d}\mathbf{x} = \int_\Omega \Bigg(&\rho_h^{n+\frac{1}{2}} g(c_h^{n+1}, c_h^n)\chi - \frac{1}{\rho_h^{n+\frac{1}{2}}} r(c_h^{n+1}, c_h^n) p_h^{n+\frac{1}{2}}\chi \\
&+ C\rho_h^{n+\frac{1}{2}}\nabla c_h^{n+\frac{1}{2}}\cdot\nabla\chi - \frac{M\rho_0\alpha}{Fr^2} y \rho_h^{n+\frac{1}{2}}\chi \Bigg) \mathrm{d}\mathbf{x},
\end{aligned} \tag{4.65}$$

where, instead of Eq.(4.1a), Eq.(4.1b) is used for the weak form, $\rho_{\bar{t}}^{n+1} = (\rho_h^{n+1} - \rho_h^n)/\Delta t$, *and* $p_h^{n+1/2} = (p_h^{n+1} + p_h^n)/2$. *Note that when taking* $\mathbf{v} = (\sqrt{\rho}\mathbf{u})_h^{n+1}, \psi =$

$\mu_h^{n+1/2}/M+\rho_0\alpha y/Fr^2, \chi = c_{\bar{t}}^{n+1}/M$ *and* $q = p_h^{n+1/2}/M\rho_h^{n+1/2} + \Big(F(c_h^{n+1})+F(c_h^n)\Big)/2M + C(\nabla c_h^{n+1}\cdot\nabla c_h^{n+1} + \nabla c_h^n\cdot\nabla c_h^n)/4M$ *in the weak form (4.62)-(4.65) respectively, we can obtain the discrete energy law corresponding to the continuous energy law (4.32),*

$$
\begin{aligned}
E_{\bar{t}}^{n+1} &= \left(\frac{1}{2}||\sqrt{\rho_h^{n+1}}\mathbf{u}_h^{n+1}||_{L^2}^2 + \frac{C}{2M}||\sqrt{\rho_h^{n+1}}\nabla c_h^{n+1}||_{L^2}^2 + \int_\Omega\Big(\frac{1}{M}\rho_h^{n+1}F(c_h^{n+1})\Big)\mathrm{d}\mathbf{x}\right)_{\bar{t}} \\
&= -\frac{1}{Re}||\nabla(\sqrt{\rho}\mathbf{u})_h^{n+1}||_{L^2}^2 - \frac{1}{3Re}||\nabla\cdot(\sqrt{\rho}\mathbf{u})_h^{n+1}||_{L^2}^2 - \frac{1}{MPe}||\nabla\mu_h^{n+\frac{1}{2}}||_{L^2}^2 \\
&- \int_\Omega\left(\frac{1}{Fr^2}(\rho_h^{n+\frac{1}{2}}-\rho_0)\hat{\mathbf{j}}\cdot(\sqrt{\rho}\mathbf{u})_h^{n+1} + \frac{\rho_0\alpha}{Fr^2Pe}\hat{\mathbf{j}}\cdot\nabla\mu_h^{n+\frac{1}{2}}\right)\mathrm{d}\mathbf{x}. \qquad (4.66)
\end{aligned}
$$

4.5 Implementation Issues

As the weak form (4.47)-(4.50) is a highly nonlinear system consisting of the variable density Navier-Stokes equation with extra stress term, an advective Cahn-Hilliard equations, we employ Newton's method to linearise the system. We first briefly introduce a Newton's linearisation for time-dependent nonlinear equations associated with the unknowns, $\tilde{\mathbf{u}}$, $\tilde{p}$, c and μ at the implicit time level,

$$
\mathbf{F}(\tilde{\mathbf{u}}^{n+1}, \tilde{p}^{n+\frac{1}{2}}, c^{n+1}, \mu^{n+1}) = 0, \qquad (4.67)
$$

where $\mathbf{F}$ is a vector function corresponding to the weak form equations (4.47)-(4.50) respectively, $\tilde{\mathbf{u}}$ and $\tilde{p}$ are the new variables defined in Remark 4.4.1. and $\tilde{p}_h^{n+1/2} = \hat{p}_h^{n+1/2}/\rho_h^{n+1/2}$ (treating it as a solution for $\tilde{p}$ at the $(n+1/2)$th time step in our computations). The solutions at the $(n+1)$st time step ($(n+1/2)$th for $\tilde{p}$) $(\tilde{\mathbf{u}}^{n+1}, \tilde{p}^{n+\frac{1}{2}}, c^{n+1}, \mu^{n+1})$ are unknown, and $(\tilde{\mathbf{u}}^n, \tilde{p}^{n-\frac{1}{2}}, c^n, \mu^n)$ at the nth ($(n-1/2)$th for $\tilde{p}$) time step are obtained. If $n=0$ the initial conditions for $\tilde{\mathbf{u}}, \tilde{p}, c, \mu$ are taken as the initial guess $(\tilde{\mathbf{u}}^0, \tilde{p}^0, c^0, \mu^0)$ for the nonlinear iteration with $\tilde{p}^0 = \hat{p}^0$. For the iteration of Eq.(4.67) at the $(n+1)$th

time step, the Newton's method is

$$
\begin{aligned}
0 &= \mathbf{F}(\tilde{\mathbf{u}}_{s+1}^{n+1}, \tilde{p}_{s+1}^{n+\frac{1}{2}}, c_{s+1}^{n+1}, \mu_{s+1}^{n+1}) \\
&\approx \mathbf{F}'_{\tilde{\mathbf{u}}^{n+1}}(\tilde{\mathbf{u}}_s^{n+1}, \tilde{p}_s^{n+\frac{1}{2}}, c_s^{n+1}, \mu_s^{n+1})(\tilde{\mathbf{u}}_{s+1}^{n+1} - \tilde{\mathbf{u}}_s^{n+1}) \\
&+ \mathbf{F}'_{\tilde{p}^{n+\frac{1}{2}}}(\tilde{\mathbf{u}}_s^{n+1}, \tilde{p}_s^{n+\frac{1}{2}}, c_s^{n+1}, \mu_s^{n+1})(\tilde{p}_{s+1}^{n+\frac{1}{2}} - \tilde{p}_s^{n+\frac{1}{2}}) \\
&+ \mathbf{F}'_{c^{n+1}}(\tilde{\mathbf{u}}_s^{n}, \tilde{p}_s^{n+\frac{1}{2}}, c_s^{n}, \mu_s^{n})(c_{s+1}^{n+1} - c_s^{n+1}) \\
&+ \mathbf{F}'_{\mu^{n+1}}(\tilde{\mathbf{u}}_s^{n+1}, \tilde{p}_s^{n+\frac{1}{2}}, c_s^{n+1}, \mu_s^{n+1})(\mu_{s+1}^{n+1} - \mu_s^{n+1}) \\
&+ \mathbf{F}(\tilde{\mathbf{u}}_s^{n+1}, \tilde{p}_s^{n+\frac{1}{2}}, c_s^{n+1}, \mu_s^{n+1}).
\end{aligned}
$$

Further we can have

$$
\begin{aligned}
&\mathbf{F}'_{\tilde{\mathbf{u}}^{n+1}}(\tilde{\mathbf{u}}_s^{n+1}, \tilde{p}_s^{n+\frac{1}{2}}, c_s^{n+1}, \mu_s^{n+1})\tilde{\mathbf{u}}_{s+1}^{n+1} + \mathbf{F}'_{\tilde{p}^{n+\frac{1}{2}}}(\tilde{\mathbf{u}}_s^{n+1}, \tilde{p}_s^{n+\frac{1}{2}}, c_s^{n+1}, \mu_s^{n+1})\tilde{p}_{s+1}^{n+\frac{1}{2}} \\
&+ \mathbf{F}'_{c^{n+1}}(\tilde{\mathbf{u}}_s^{n+1}, \tilde{p}_s^{n+\frac{1}{2}}, c_s^{n+1}, \mu_s^{n+1})c_{s+1}^{n+1} \\
&+ \mathbf{F}'_{\mu^{n+1}}(\tilde{\mathbf{u}}_s^{n+1}, \tilde{p}_s^{n+\frac{1}{2}}, c_s^{n+1}, \mu_s^{n+1})\mu_{s+1}^{n+1} \\
&= \mathbf{F}'_{\tilde{\mathbf{u}}^{n+1}}(\tilde{\mathbf{u}}_s^{n+1}, \tilde{p}_s^{n+\frac{1}{2}}, c_s^{n+1}, \mu_s^{n+1})\tilde{\mathbf{u}}_s^{n+1} \\
&+ \mathbf{F}'_{\tilde{p}^{n+\frac{1}{2}}}(\tilde{\mathbf{u}}_s^{n+1}, \tilde{p}_s^{n+\frac{1}{2}}, c_s^{n+1}, \mu_s^{n+1})\tilde{p}_s^{n+\frac{1}{2}} \\
&+ \mathbf{F}'_{c^{n+1}}(\tilde{\mathbf{u}}_s^{n+1}, \tilde{p}_s^{n+\frac{1}{2}}, c_s^{n+1}, \mu_s^{n+1})c_s^{n+1} + \mathbf{F}'_{\mu^{n+1}}(\tilde{\mathbf{u}}_s^{n+1}, \tilde{p}_s^{n+\frac{1}{2}}, c_s^{n+1}, \mu_s^{n+1})\mu_s^{n+1} \\
&- \mathbf{F}(\tilde{\mathbf{u}}_s^{n+1}, \tilde{p}_s^{n+\frac{1}{2}}, c_s^{n+1}, \mu_s^{n+1}),
\end{aligned}
\tag{4.68}
$$

where $(\tilde{\mathbf{u}}_s^{n+1}, \tilde{p}_s^{n+\frac{1}{2}}, c_s^{n+1}, \mu_s^{n+1})$ are the solutions obtained after the s'th iteration step at the $(n+1)$th time step. In the two dimensional case, we define the differentiation operator for the velocity $\mathbf{u}$ as

$$
\mathbf{F}'_{\tilde{\mathbf{u}}_{s+1}^{n+1}}(\tilde{\mathbf{u}}_{s+1}^{n+1} - \tilde{\mathbf{u}}_s^{n+1}) = \mathbf{F}'_{\tilde{u}_1}(\tilde{u_1}_{s+1}^{n+1} - \tilde{u_1}_s^{n+1}) + \mathbf{F}'_{\tilde{u}_2}(\tilde{u_2}_{s+1}^{n+1} - \tilde{u_2}_s^{n+1}). \tag{4.69}
$$

In accordance with the local quadratic convergence theory of Newton's method, Eq.(4.68) should converge rapidly with good initial guesses. Note that the initial guesses of iteration at the $(n+1)$th time step are usually given as the solutions of PDE at the previous nth time step

$$(\tilde{\mathbf{u}}_0^{n+1}, \tilde{p}_0^{n+\frac{1}{2}}, c_0^{n+1}, \mu_0^{n+1}) = (\tilde{\mathbf{u}}^n, \tilde{p}^{n-\frac{1}{2}}, c^n, \mu^n).$$

We then solve Eq.(4.68) by treating $(\tilde{\mathbf{u}}_{s+1}^{n+1}, \tilde{p}_{s+1}^{n+\frac{1}{2}}, c_{s+1}^{n+1}, \mu_{s+1}^{n+1})$ as an approximation for the solution at the $(n+1)$th time step $(\tilde{\mathbf{u}}^{n+1}, \tilde{p}^{n+\frac{1}{2}}, c^{n+1}, \mu^{n+1})$, where, in the end, we expect

$$(\tilde{\mathbf{u}}^{n+1}, \tilde{p}^{n+\frac{1}{2}}, c^{n+1}, \mu^{n+1}) = \lim_{s\to\infty} (\tilde{\mathbf{u}}_{s+1}^{n+1}, \tilde{p}_{s+1}^{n+\frac{1}{2}}, c_{s+1}^{n+1}, \mu_{s+1}^{n+1}).$$

Note that the solutions of velocity $\mathbf{u}$ and pressure $\hat{p}$ at the $(n+1)$th time step can then be obtained by

$$\mathbf{u}^{n+1} = \frac{\tilde{\mathbf{u}}^{n+1}}{\sqrt{\rho^{n+1}}},\ \hat{p}^{n+\frac{1}{2}} = \tilde{p}^{n+\frac{1}{2}} \rho^{n+\frac{1}{2}}.$$

In practice, we introduce a stopping criteria for the inner nonlinear iteration

$$\Big(||\tilde{\mathbf{u}}_{s+1}^{n+1} - \tilde{\mathbf{u}}_s^{n+1}||_{H^1}^2 + ||\tilde{p}_{s+1}^{n+\frac{1}{2}} - \tilde{p}_s^{n+\frac{1}{2}}||_{H^1}^2 + ||c_{s+1}^{n+1} - c_s^{n+1}||_{H^1}^2 + ||\mu_{s+1}^{n+1} - \mu_s^{n+1}||_{H^1}^2 \Big)^{\frac{1}{2}} < tol. \tag{4.70}$$

With a sufficiently small tolerance (here we set $tol = 10^{-5}$ in Eq.(4.70)) and proper initial guess, our numerical method for (4.47)-(4.50) converges rapidly in practice. Several examples are presented in the next section to demonstrate the capability of our method.

4.6 Numerical Experiments

With the help of the FreeFem++ platform [61] and MATLAB, the computations are carried out using the P_2 (piecewise quadratic) continuous finite element for the velocity $\tilde{\mathbf{u}}$, the phase variables c, μ and the pressure $\tilde{p}$. Note that in this computation, the same order elements are used for the velocity $\mathbf{u}$ and the pressure p, which is not a normal stable combination for the computations of incompressible NS equations. The model we consider here is quasi-incompressible, where the velocity is not divergence free anymore, and the chemical potential appears in the continuous equations (4.47). Therefore we use the p_2 elements for chemical potential and velocity. As the pressure term appears in the chemical potential equation (4.50), and the pressure is linearly related to the chemical potential, we therefore use the P_2 elements for the pressure as well. On the square domain $\Omega = [-1,1] \times [-1,1]$, we apply Dirichlet boundary conditions for the velocity ($\tilde{\mathbf{u}} = 0$) and Neumann boundary conditions for the phase variables ($\nabla c \cdot \hat{\mathbf{n}} = 0$, $\nabla \mu \cdot \hat{\mathbf{n}} = 0$). Moreover the initial condition for the velocity is set to be zero ($\tilde{\mathbf{u}}|_{t=0} = 0$). For the phase variable c, different initial conditions will be supplied as appropriate for the examples considered.

The solutions to the Cahn-Hilliard equations are nearly constant in the so called bulk region, which typically comprise the largest part of the domain. Between the bulk regions, the solutions exhibit thin transition layers, through which their values can change rapidly but continuously between their values in the bulk regions. In many cases, it is sufficient to finely resolve only the transition layers, and a fixed grid meshing represents a waste of computational resources. Thus, efficient adaptive mesh which resolves only the thin layers near the interface is desirable [76]. In this paper, we adopt a variable metric/Delaunay automatic meshing algorithm for all the examples, which is built in the FreeFem++ platform (see [60] for details of this method). All the examples are computed using adaptive meshes. Snapshots for the adaptive mesh together with

the evolution of the phase variable c at different times are presented in Example 6.2 below.

Example 6.1 We study the coalescence of two kissing drops with different density ratios: (a) 1 : 1 (density matched case, $\rho_1 = \rho_2 = 1$); (b) 1 : 10 (variable case, $\rho_1 = 1$, $\rho_2 = 10$), where the heavier drop is set in a lighter medium. The effect of gravity is ignored in this experiment. Moreover we set $\varepsilon = 0.01$, $C = 100\varepsilon^2$, $M = 1/(10\varepsilon)$, and $Pe = 100/\varepsilon$, $\Delta t = 0.01$ for the time step. Here ε is a small parameter related to the interface thickness. In [87], the stationary solutions for the phase field and pressure were given, which can be used as the approximations for the initial conditions. Based on their work, we use the following as the initial condition for the phase variable c,

$$c = \frac{1}{2}\tanh\left(\frac{-r+\sqrt{(x-a_x)^2+(y-a_y)^2}}{2\sqrt{2}\varepsilon}\right) + \frac{1}{2}\tanh\left(\frac{-r+\sqrt{\left((x-b_x)^2+(y-b_y)^2\right.}}{2\sqrt{2}\varepsilon}\right), \tag{4.71}$$

where r is the drop radius, (a_x, a_y) and (b_x, b_y) are the initial centre positions of two drops. Here we set $r = 0.2\sqrt{2}$, $(a_x, a_y) = (-r/\sqrt{2}, r/\sqrt{2})$ and $(b_x, b_y) = (r/\sqrt{2}, -r/\sqrt{2})$. For simplicity, we set $p = 0$ as the initial iteration of Newton's method for the pressure. Here we refer [87] for detailed study of the pressure. This example is computed using the adaptive mesh, where the shortest edge of all the grids is set to be $1/128 < \varepsilon$.

Fig. 4.1 shows the evolution of the $c = 0.5$ contours (black solid line) together with the velocity field for the density matched case and the variable density case from times $t = 0.01$ to $t = 260$ and $t = 0.05$ to $t = 70$, respectively. Because their interfaces overlap, the two drops coalesce into one larger drop for both cases with slightly visual differences.

In [87], a sharp-interface asymptotic analysis was carried out for the quasi-incompressible

NSCH system, where the interface was assumed to be normal to the z-axis and the fluid velocity, pressure and concentration are independent of time, x and y. At the equilibrium, they used the excess free energy to identify the surface tension σ of the system, which can be given as

$$\sigma = \frac{C}{M}\int_{+\infty}^{-\infty} \rho(c) c_z^2 dz. \tag{4.78}$$

We see that the surface tension for the quasi-incompressible NSCH system is density dependent, where to be specific, for our example, the surface tension for the density matched case ($\rho_1 = \rho_2 = 1$) is smaller than that for the variable density case ($\rho_1 = 1$, $\rho_2 = 10$). As can be seen from Fig.4.1, our numerical example agrees with this analysis, where the effects of surface tension are stronger in the variable density case leading to a higher rate of interface coalescence, and the corresponding velocity fields are stronger as well. Moreover, the magnitude of the velocity is decreasing as the time passes for both cases, which states that the systems are approaching to the equilibrium. From Fig. 4.2, we observe that the volume of the drop in the entire domain is preserved well, where $\int_\Omega c d\mathbf{x} = constant = 3.49321$ for the kissing drop examples in the whole time interval of computation.

We also examined the time evolution of the total energy (with the discrete energy law defined in Eq.(4.57)) for both cases. The discrete energy functional is shown in Fig. 4.3. As the interface deforms, we observe that the total energy is decreasing monotonically as predicted by Theorem 4.1, and tends to a constant value corresponding to a single larger drop near the equilibrium. Moreover, the case for variable density has a larger total energy than that of the density matched case, which is consistent with the density dependence of the total energy of the quasi-incompressible NSCH system (Eq.(4.10)). We have also tested different mesh sizes and can conclude that the energy law (the decay of the energy) for this variable density model is indeed preserved very

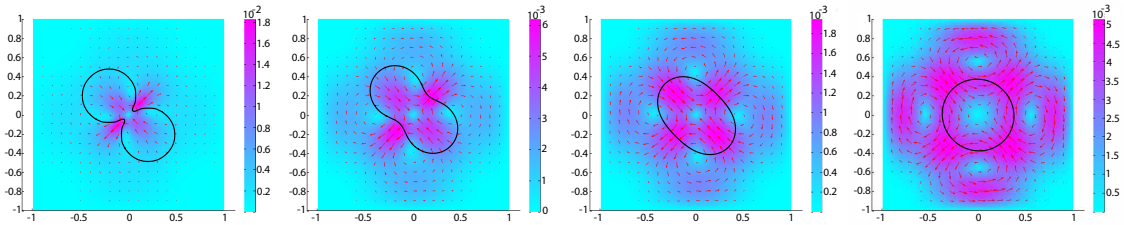

t=0.01 t=8 t=40 t=260

(a) Density matched case ($\rho_1 = \rho_2 = 1$)

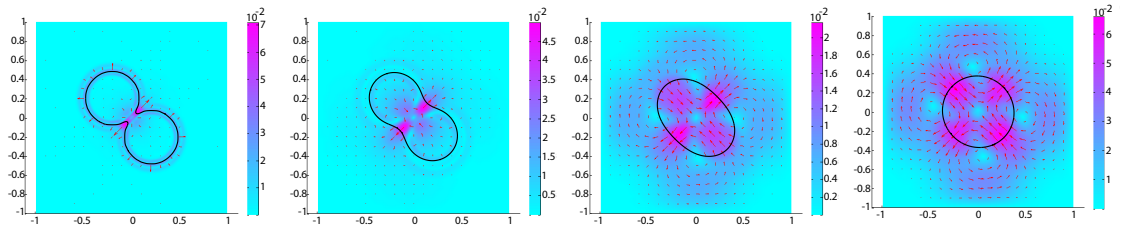

t=0.05 t=4 t=13.5 t=70

(b) Variable density case ($\rho_1 = 1, \rho_2 = 10$)

Figure 4.1: The deformed drop interfaces (black solid line) with the velocity fields (with arrows representing the velocity vectors and color representing the norm value) for kissing drops. $\varepsilon = 0.01$, $C = 100\varepsilon^2$, $M = 1/(10\varepsilon)$, $Pe = 100/\varepsilon$ and $\Delta t = 0.01$.

well using our energy preserving numerical scheme.

Example 6.2 We now consider a drop of lighter fluid rising in a heavier medium with different density ratios: (a) $1:2$ ($\rho_1 = 1$, $\rho_2 = 2$) and (b) $1:50$ ($\rho_1 = 1$, $\rho_2 = 50$). Moreover we set $\varepsilon = 0.01$, $C = 200\varepsilon^2$, $M = 1/(20\varepsilon)$, $Pe = 1000/\varepsilon$, and $1/Fr^2 = 10$. And we set the time step to be $\Delta t = 0.001$ in (a) and $\Delta t = 0.00025$ in (b). The initial

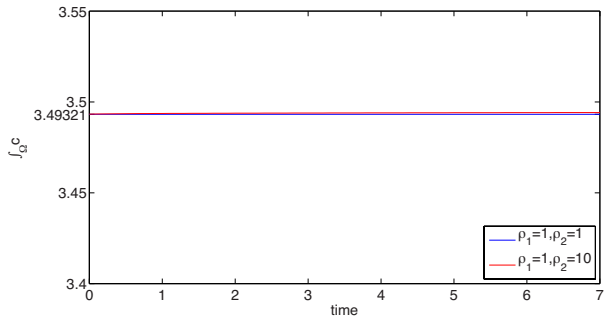

Figure 4.2: The integral of the volume fraction c for kissing drop example in Fig.4.1.

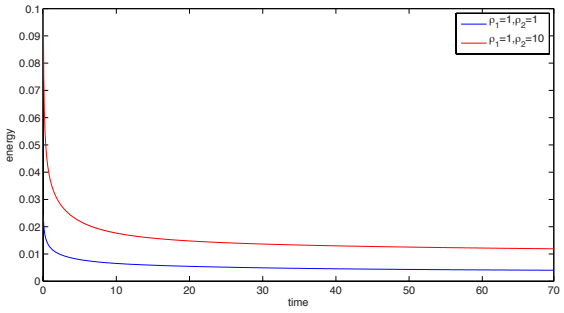

Figure 4.3: The energy for both cases in Fig.4.1.

condition for the phase variable c

$$c = \frac{1}{2}\tanh\left(\frac{r-\sqrt{(x-c_x)^2+(y-c_y)^2}}{2\sqrt{2}\varepsilon}\right)+\frac{1}{2}, \tag{4.79}$$

where r is the radius of the drop and (c_x, c_y) is the initial position of the drop centre. Here we set $r = 0.2$ and $(c_x, c_y) = (0, -0.6)$.

For a drop rising in a liquid, it is often desirable to study the long-time behaviour and the temporal evolution of the interface. The drops may move a relatively long distance. Thus the computational domain must be correspondingly large which is likely to be computationally infeasible, and this constraint may therefore prevent the desired long time simulation. A non-inertial reference frame [66, 67] that moves with the interface can be employed as a remedy for this problem. In this paper, we enlarge the effect of the gravity as an alternative, so that the dramatic deformation can be detected in a relatively short time period. $1/Fr^2$ is therefore set to be 10 in this example, whereas in [77], $1/Fr^2 = 1$.

The square domain $\Omega = [-1,1]\times[-1,1]$ is discretized using an adaptive mesh, where we use a variable metric/Delaunay automatic meshing algorithm built in the FreeFem++ platform. Since the values of phase variable c can change rapidly but continuously across the interface, the mesh is adapted according to the value of $|\nabla c|$ after every 10

time steps, in order to track the features of the phase variable as the computation progresses. The shortest edge of all the grids is set to be $1/128 < \varepsilon$, so that at least one grid cell is located across the interface to ensure accuracy. An example of the dynamic adaptive mesh can be seen in Fig.4.9.

Snapshots of the deformed interface (black solid line) together with the $\nabla \cdot \mathbf{u}$ are presented in Fig. 4.4 and Fig. 4.5, where we observe that the drop with a low density ratio deforms slowly, resulting in a mushroom shape by time $t = 1.4$. On the other hand, the high density ratio drop rises much faster and has deformed into a mushroom shape by the time $t = 0.225$. Our results are similar to those found in [114] when the effects of density ratio in rising drops were simulated using a level-set method. In the large density ratio case, the upwelling motion continues to deform the drops which attain a horseshoe shape around $t = 0.4$. As the drop broadens, we observe drop pinch-off around $t = 0.85$, as the tips of the drop roll up and smaller drops eventually detach.

The divergence of velocity $\nabla \cdot \mathbf{u}$ (color representing its value) are presented in Fig. 4.4 and Fig. 4.5. Recall that the divergence-free condition does not hold for quasi-incompressible fluids with different densities because the fluids may mix slightly across the interface. The two incompressible fluids can be compressible across the interface where the two components are mixed. It can be observed that $\nabla \cdot \mathbf{u} = 0$, such that the fluid is incompressible almost everywhere except along the moving interface. Near the interface, waves of expansion ($\nabla \cdot \mathbf{u} > 0$) and compression ($\nabla \cdot \mathbf{u} < 0$) are observed. Note that in the case of the larger density ratio, the distribution of $\nabla \cdot \mathbf{u} > 0$ is found to be larger and more spatially localized than in the case with smaller density ratio. Further, the compression and expansion waves tend to trail the drop in the large density ratio case whereas in the smaller density ratio case, the waves tend to be ahead of the drop. The divergence free condition is satisfied in the bulk regions for each component during the pinch-off (from $t = 0.85$ to $t = 0.915$), where the distribution of $\nabla \cdot \mathbf{u}$ with non-zero value tends to appear around three drops. We expect that a smaller value

for parameter C and corresponding finer mesh grids causes a narrower distribution of non-zero values of $\nabla \cdot \mathbf{u}$ around the drop boundary.

The flow field and the vorticity contours are presented in Fig.4.6-Fig.4.8, where we can observe that the velocity field for the second case with the lager density ratio are much more enhanced than that for the smaller matched case, with strong spinning motions of the fluid distributed across the drop boundary. Both cases have vorticity contours along the wall and the boundary of the drop, where the positive value stands for the clockwise rotation and the negative for the counterclockwise rotation. The rising of the drop seems to affect the shape of the streamwise vortices, where the concentration of vorticity becomes more apparent near the rear as the drop rises.

For the second case with larger density ratio, the vorticity contours are much more condensed with the absolute value being increased significantly. At $t = 0.5$, we can observe that, as the drop broadens, a pair of co-rotating streamwise vortices begin to appear at the rounded bottom of the drop. They gain strength as they grow along the bottom boundary, where, on the other hand, another pair of vortices that are associated with the rotation of the elongating trailing arms of the drops tends to diminish the dominance. It is interesting to note that, during the pinch-off (from $t = 0.85$ to $t = 0.915$), two pairs of co-rotating vortices seem to balance and both concentrate near the rear of the larger drop.

The adaptive meshes for the rising drop of density ratio $1 : 50$ are presented in Fig. 4.9, where a grid structure that adapts to the locations of the moving interfaces is generated automatically and adapts around the isolated drops after break-up.

In addition, we also examined the time evolution of the total energy (with the discrete energy law defined in Eq.(4.57)) for the case of density 1:2. The discrete energy functional is shown in Fig. 4.10. As the bubble rises, we observe that the total energy is decreasing monotonically as predicted by Theorem 4.1

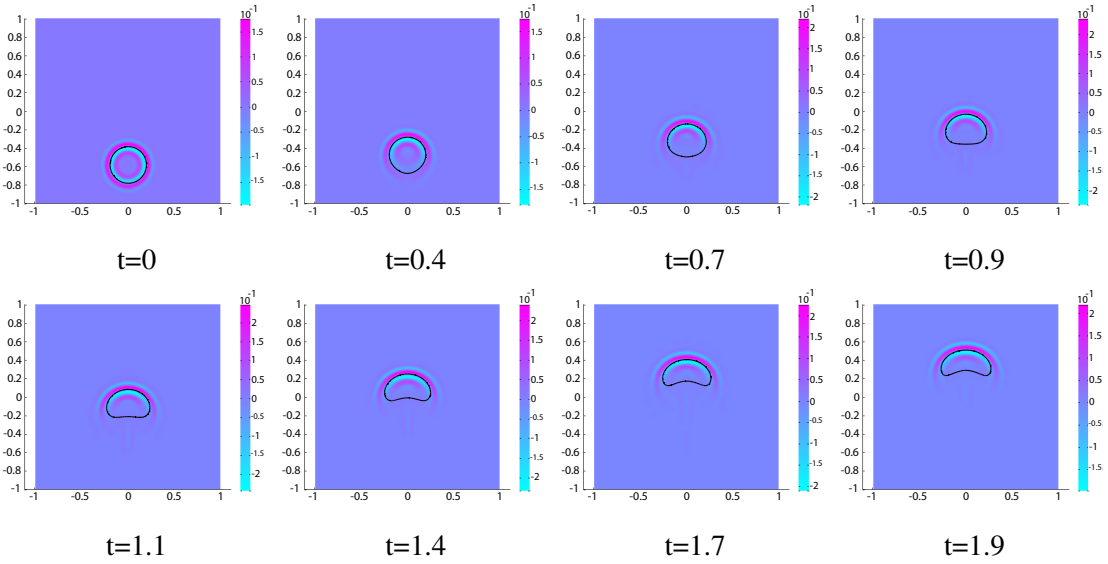

Figure 4.4: The drop interfaces (black solid line) with $\nabla \cdot \mathbf{u}$ (with colour representing the value distribution) for the rising drop with density ratio $1:2$, $\rho_1 = 1, \rho_2 = 50$, $\varepsilon = 0.01$, $C = 200\varepsilon^2$, $M = 1/(20\varepsilon)$, $Pe = 1000/\varepsilon$, $1/Fr^2 = 10$ and $\Delta t = 0.00025$.

4.7 Discussion

In this chapter, we designed a new numerical method to solve two-phase flow using the quasi-incompressible NSCH system with a variable density. Gravitational forces are incorporated into the system in a thermodynamically consistent way. We reformulated the continuous system that enabled the use of C^0 finite elements. We designed a C^0 finite element method and a special temporal scheme that ensured that the scheme has an energy law at the discrete level, which is analogous to the one in the continuous level. To our knowledge, this is the first such scheme for the quasi-incompressible NSCH flow system.

Two examples are computed to test our energy law preserving adaptive numerical scheme for this variable density two-phase model and to see the effects of the density ratio. In the case of kissing drops, increasing the density ratio increases the rate of coalescence because the surface tension also increases. The drop volumes are well-preserved by the numerical scheme. Simulations also confirm that the discrete energy

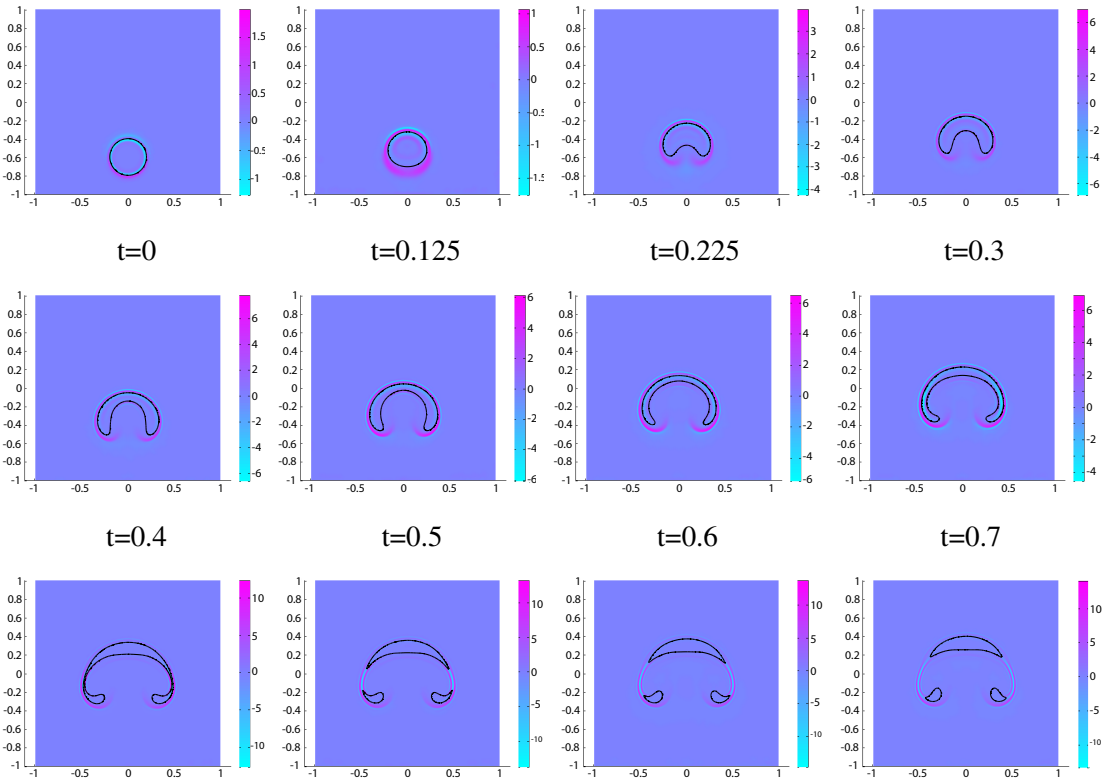

Figure 4.5: The drop interfaces (black solid line) with $\nabla \cdot \mathbf{u}$ (with colour representing the value distribution) for the rising drop with density ratio $1:50$, $\rho_1 = 1, \rho_2 = 50$, $\varepsilon = 0.01$, $C = 200\varepsilon^2$, $M = 1/(20\varepsilon)$, $Pe = 1000/\varepsilon$, $1/Fr^2 = 10$ and $\Delta t = 0.00025$.

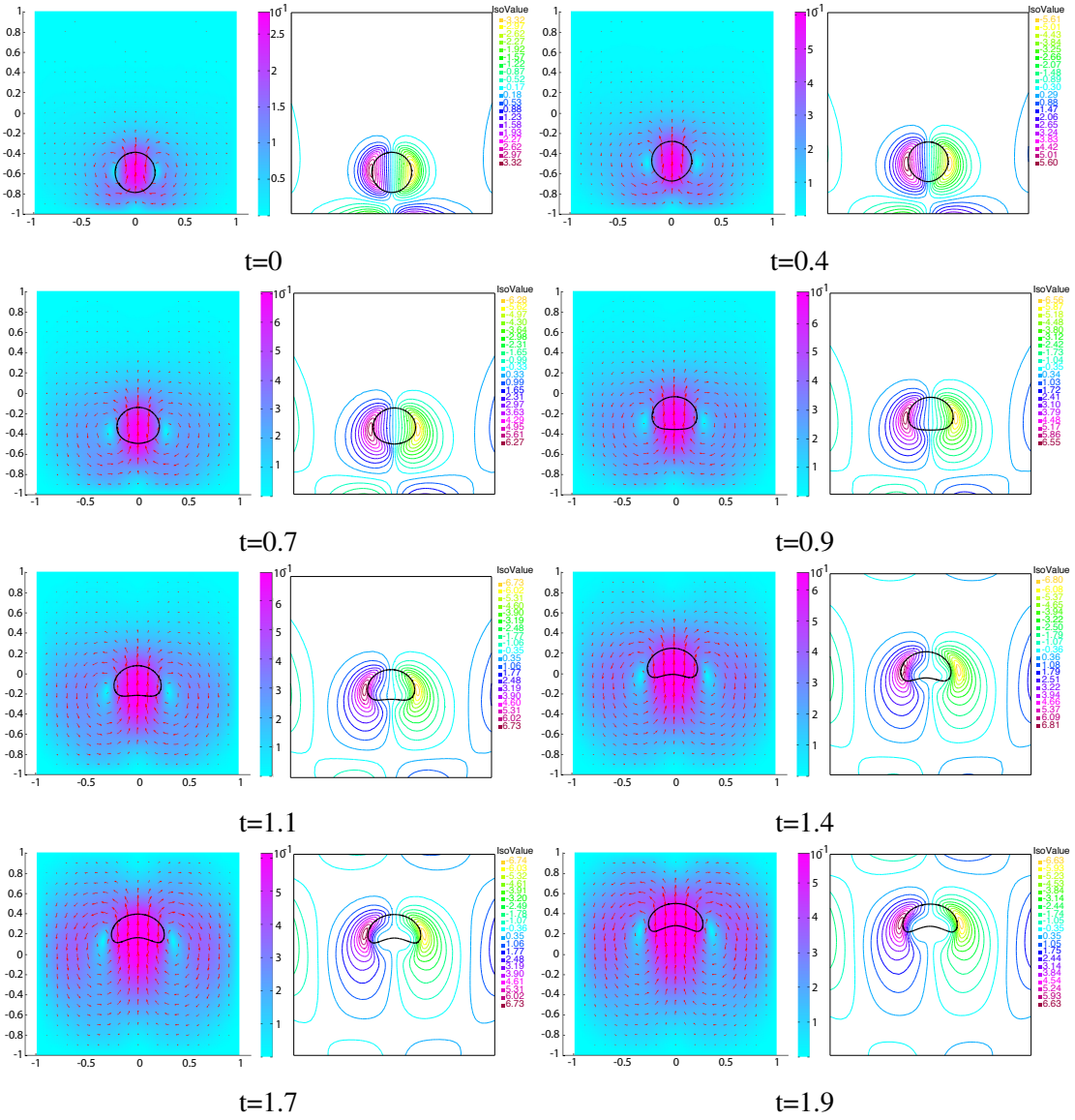

Figure 4.6: The flow field (with arrows representing the velocity vectors and colour representing the norm value) and vorticity contours for the rising drop with density ratio $1:2$, $\rho_1 = 1, \rho_2 = 2$, $\varepsilon = 0.01$, $C = 200\varepsilon^2$, $M = 1/(20\varepsilon)$, $Pe = 1000/\varepsilon$, $1/Fr^2 = 10$ and $\Delta t = 0.001$.

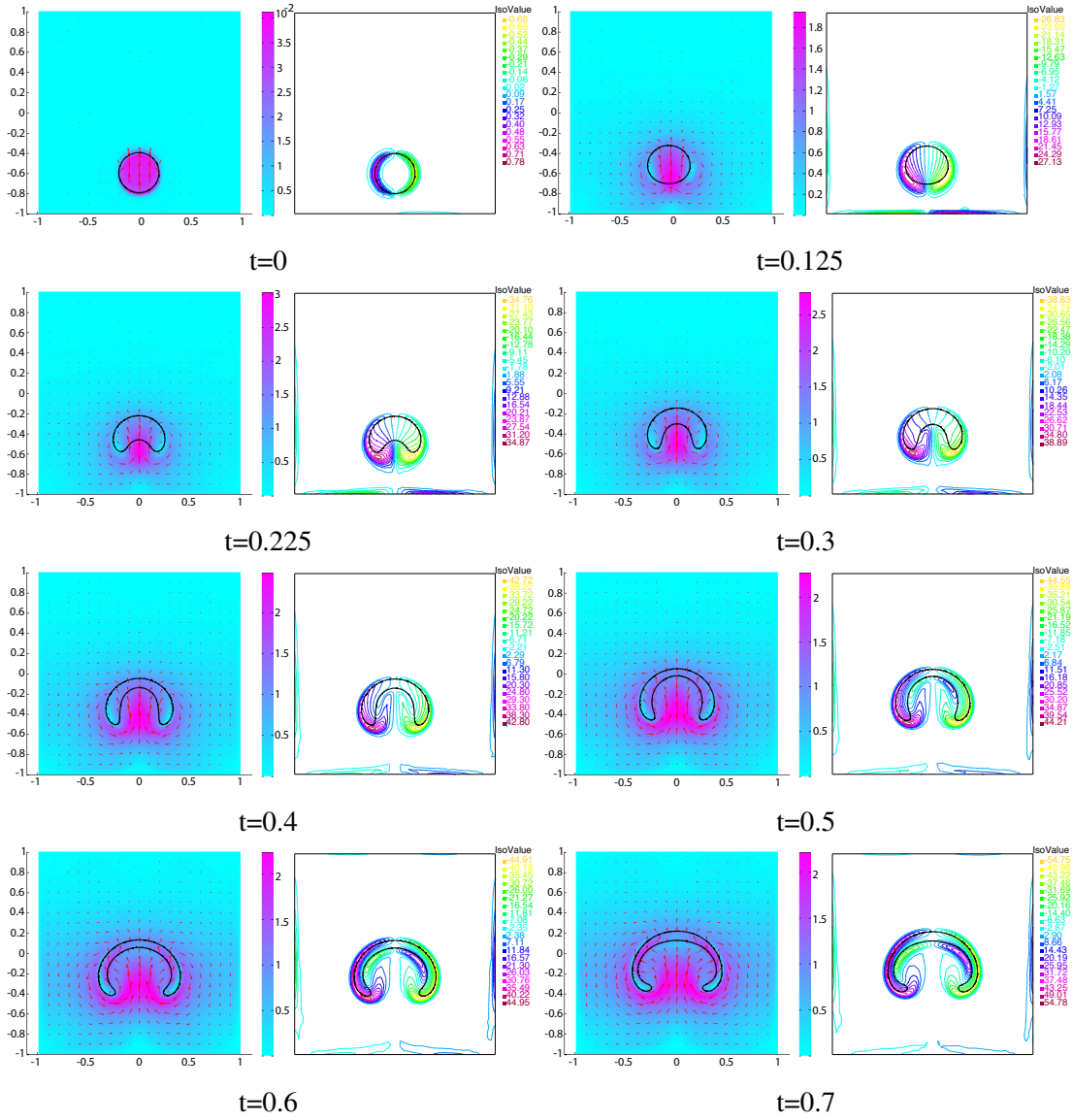

Figure 4.7: The flow field (with arrows representing the velocity vectors and colour representing the norm value) and vorticity contours for the rising drop with density ratio $1:50$ from $t=0$ to $t=0.7$. $\rho_1=1, \rho_2=50$, $\varepsilon=0.01$, $C=200\varepsilon^2$, $M=1/(20\varepsilon)$, $Pe=1000/\varepsilon$, $1/Fr^2=10$ and $\Delta t=0.00025$.

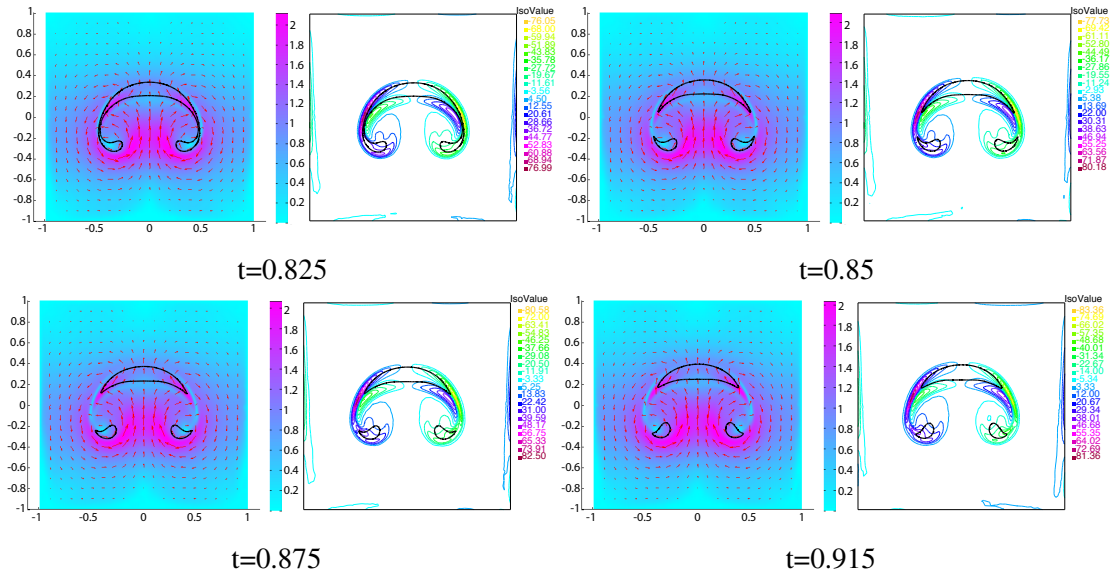

Figure 4.8: The flow field (with arrows representing the velocity vectors and colour representing the norm value) and vorticity contours for the rising drop with density ratio $1:50$ from $t=0.825$ to $t=0.915$ $\rho_1=1, \rho_2=50$, $\varepsilon=0.01$, $C=200\varepsilon^2$, $M=1/(20\varepsilon)$, $Pe=1000/\varepsilon$, $1/Fr^2=10$ and $\Delta t=0.00025$.

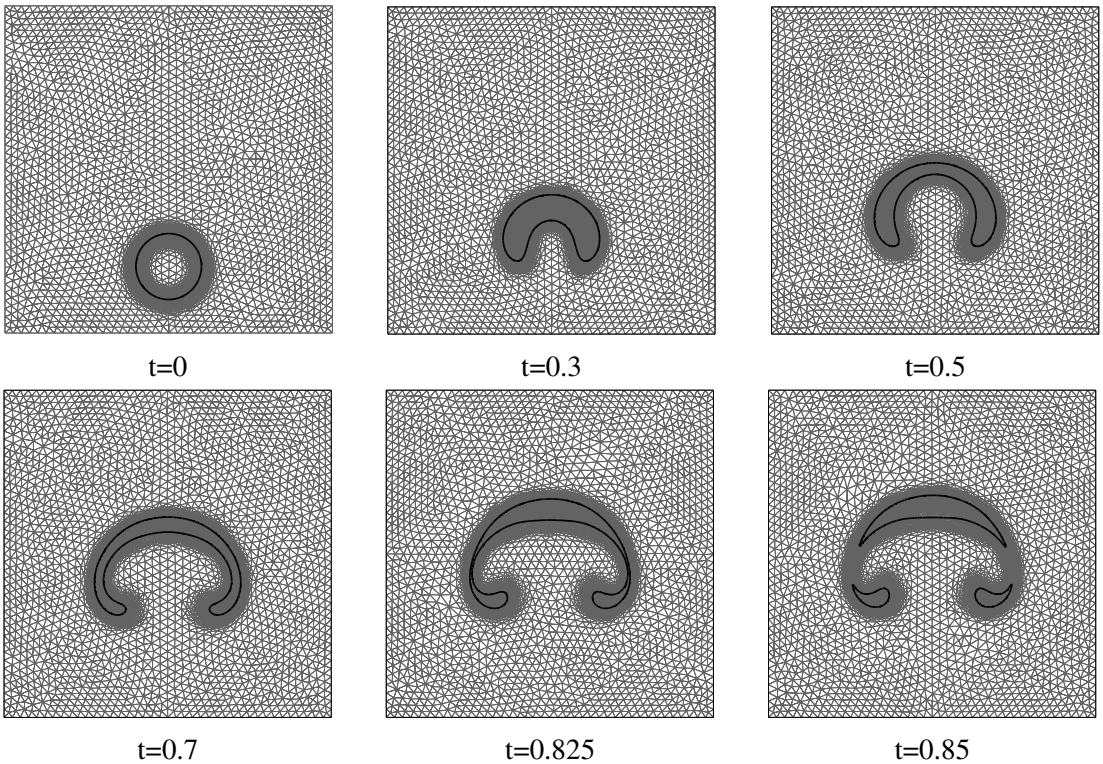

Figure 4.9: The adaptive mesh for the rising drop with density ratio $1:50$. $\varepsilon=0.01$, $C=200\varepsilon^2$, $M=1/(20\varepsilon)$, $Pe=1000/\varepsilon$ and $1/Fr^2=10$.

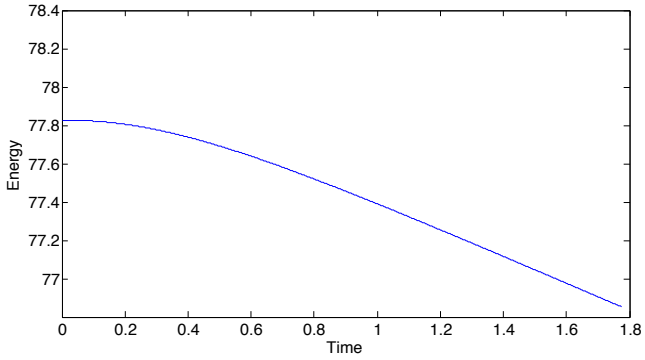

Figure 4.10: The energy for the case of density ratio 1:2 in Fig.4.4.

functional is non-increasing, as predicted by our theory. In the example of the rising drop, the effects of the density ratio are much more obvious, where the shape of the drop deforms faster with larger density ratio compared to the case where the density ratio is smaller. Moreover, in the case of the density ratio $1:50$, the pinch-off event is smoothly captured by the numerical scheme. In the NSCH model, the velocity is not solenoidal near interfaces because fluids of different densities may mix. Our simulations capture this feature. Namely, the numerical results reveal that away from interfaces the fluid is incompressible, while near interfaces waves of expansion and contraction are observed. Increasing the density ratio results in narrower waves with larger magnitudes.

In future work, we will perform extensive studies of the two-phase problems with more complicated interface dynamics, e.g., the moving contact line problems, where the fluid-fluid interface interacts with a solid wall, and the dynamics of interfaces with Marangoni effects, where surface tension gradients are induced by inhomogeneous temperature distributions or surfactants that can be absorbed at the liquid/gas or liquid/liquid interfaces. Our algorithm may also be implemented using supercomputers so as to possibly simulate an air bubble in water.

Chapter 5

A thermodynamically consistent phase-field model for two-phase flows with thermocapillary effects

5.1 Introduction

In this chapter, we develop a phase-field model for a binary incompressible (quasi-incompressible) fluid with thermocapillary effects, which allows for different properties (densities, viscosities and heat conductivities) of each component while maintaining thermodynamic consistency. The governing equations of the model including the Navier-Stokes equations, Cahn-Hilliard equations and energy balance equation are derived within a thermodynamic framework based on entropy generation, which guarantees thermodynamic consistency. A sharp-interface limit analysis is carried out to show that the interfacial conditions of the classical sharp-interface models can be recovered from our phase-field model. Moreover, some numerical examples including thermocapillary migration of a drop and thermocapillary convections in a two-layer

fluid system are computed using a continuous finite element method. The results are compared to the corresponding analytical solutions and theoretical predictions as validations for our model.

5.2 Variable density and mass-averaged velocity

In phase-field modelling, an order parameter (phase variable) is normally introduced to distinguish different phases and the diffuse interface. Lowengrub and Truskinovsky [87] have argued for the advantage of using a physically realistic scalar field instead of an artificial smoothing function for the interface. Several physically realistic scalar fields have been suggested as the order parameters for phase-field modelling, e.g. the mass density ρ for the case of a single compressible fluid with different phases [7], the mass concentration c of one of the constituents for the case of compressible and incompressible binary fluid [87, 2], or an alternative phase variable, the volume fraction ϕ for the case of a incompressible binary fluid [85] and solidification of single materials [123]. Here we choose the mass concentration c of one of the constituents as the phase variable, and begin by introducing the variable density for the mixture. We consider a mixture of two fluids in a domain Ω, and take a sufficient small material volume $V \in \Omega$. We then have the following theorem that was introduced in section 2.3.7 (e.g. [90]),

Theorem 5.2.1. *For a smooth function $f(\mathbf{x},t)$ in the Eulerian coordinate,*

$$\frac{\mathrm{d}}{\mathrm{d}t}\int_{V(t)} f(\mathbf{x},t)\mathrm{d}V = \int_{V(t)}\left(\frac{\mathrm{D}f}{\mathrm{D}t} + f(\nabla\cdot\mathbf{u})\right)\mathrm{d}V = \int_{V(t)}\left(\frac{\partial f}{\partial t} + \nabla\cdot\Big(f\mathbf{u}\Big)\right)\mathrm{d}V, \quad (5.1)$$

where $\mathrm{D}/\mathrm{D}t = \partial/\partial t + \mathbf{u}\cdot\nabla$ is the material derivative and $\mathbf{u}$ is the velocity of the moving volume $V(t)$.

In the control volume, the two fluids are labeled by $i = 1, 2$ and they fill the volumes V_i separately. We then introduce the volume fraction γ_i for the ith fluid such that

$$\gamma_i = \frac{V_i}{V}. \tag{5.2}$$

Further we assume that two fluids can mix along the interfacial region and the volume occupied by a given amount of mass of the single fluid does not change after mixing. Then within the material volume V, γ_i satisfy the following condition

$$\gamma_1 + \gamma_2 = 1. \tag{5.3}$$

Let $M = M_1 + M_2$ be the total mass of the mixture, and M_i be the mass of the ith fluid in the volume. We now introduce the local volume-averaged mass density taken over the sufficient small volume V for each fluid

$$\tilde{\rho}_i = \frac{M_i}{V}, \tag{5.4}$$

and the actual local mass density for each fluid

$$\rho_i = \frac{M_i}{V_i}. \tag{5.5}$$

Note that for incompressible components, we assume that ρ_i are uniform constants. Having in mind Eq.(5.2), we obtain the relation between the volume-averaged mass densities and the local mass densities

$$\gamma_i = \frac{\tilde{\rho}_i}{\rho_i} \text{ and } \frac{\tilde{\rho}_1}{\rho_1} + \frac{\tilde{\rho}_2}{\rho_2} = 1. \tag{5.6}$$

We then define the volume-averaged mass density for the mixture as

$$\rho = \tilde{\rho}_1 + \tilde{\rho}_2 = \frac{M_1 + M_2}{V} = \frac{M}{V}. \tag{5.7}$$

Let c_i be the mass concentration for the ith fluid, such that

$$c_i = \frac{M_i}{M} = \frac{\tilde{\rho}_i}{\rho} \quad \text{and} \quad c_1 + c_2 = 1. \tag{5.8}$$

Using Eqs. (5.6) and (5.8), we obtain

$$\frac{c_1\rho}{\rho_1} + \frac{c_2\rho}{\rho_2} = 1 \;\Rightarrow\; \frac{c_1}{\rho_1} + \frac{c_2}{\rho_2} = \frac{1}{\rho}. \tag{5.9}$$

Here we chose the mass concentration of fluid 1 as the phase variable for our phase-field model, such that $c = c_1 = 1 - c_2$. The variable density for the mixture of two fluids can then be given as

$$\frac{1}{\rho(c)} = \frac{c}{\rho_1} + \frac{1-c}{\rho_2}. \tag{5.10}$$

It can be seen that, for two incompressible components of different densities, the variable density $\rho(c)$ for the mixture is constant almost everywhere except that near the interfacial region. For simplicity, we write the variable density $\rho(c)$ as ρ in all the following derivations.

Now we suppose that the two fluids move with different velocities $\mathbf{u}_i(\mathbf{x},t)$. The equation of mass balance for each fluid within the material volume V can then be written in the form [87, 26, 2]

$$\frac{\partial \tilde{\rho}_i}{\partial t} + \nabla \cdot (\tilde{\rho}_i \mathbf{u}_i) = 0. \tag{5.11}$$

We then introduce the mass-averaged velocity for the mixture as

$$\rho\mathbf{u} = \tilde{\rho}_1\mathbf{u}_1 + \tilde{\rho}_2\mathbf{u}_2 \quad \text{or} \quad \mathbf{u} = c_1\mathbf{u}_1 + c_2\mathbf{u}_2. \tag{5.12}$$

Substituting the density (5.7) and mass-averaged velocity (5.12) of the mixture into Eq. (5.11), we obtain the mass balance for the mixture of two fluids

$$\frac{\partial \rho}{\partial t} + \nabla \cdot (\rho \mathbf{u}) = 0. \tag{5.13}$$

In the following derivations, we consider the mixture as a single fluid moving with velocity $\mathbf{u}$. Note that if we consider a binary incompressible fluid (assuming the two fluids of the mixture are incompressible, and the temperature effects on the densities of both fluids are negligible), then ρ_1 and ρ_2 are constants, and the above equation (5.13) can be further written as

$$\nabla \cdot \mathbf{u} = -\frac{1}{\rho}\frac{\mathrm{D}\rho}{\mathrm{D}t} = -\frac{1}{\rho}\frac{\mathrm{d}\rho}{\mathrm{d}c}\frac{\mathrm{D}c}{\mathrm{D}t} = \alpha\rho\frac{\mathrm{D}c}{\mathrm{D}t}, \tag{5.14}$$

where $\alpha = (\rho_2 - \rho_1)/\rho_2\rho_1$ is constant. We note that, due to the variations of phase variable c, the mass-averaged velocity for the mixture is non-solenoidal ($\nabla \cdot \mathbf{u} \neq 0$) near the interfacial region, which introduces the compressibility effects into the model, and this compressibility is caused by the variations of phase variable rather than pressure. Such binary incompressible fluid is termed as a quasi-incompressible fluid and was introduced by Antanovskii [12], and by Lowengrub and Truskinovsky [87] who developed a phase-field model for two-phase flows where the two fluids have different densities (quasi-incompressible NSCH model). In the previous chapter, we have presented a numerical method for the quasi-incompressible NSCH system with a discrete thermodynamic law [54], where the quasi-incompressibility near interfaces was captured. Namely, the fluid is incompressible away from interfaces, while near interfaces waves of expansion and contraction are observed.

We remark that as well as this mass-averaged velocity, another velocity for the mixture, the volume-averaged velocity was considered by Abels et. al. [1, 2], Boyer et. al. [26] and Ding et. al. [35], where the volume fraction γ instead of the mass concentration c

is used to relate the velocity of single fluids and the mixture. This volume-averaged velocity of binary incompressible fluid is solenoidal ($\nabla \cdot \mathbf{u} = 0$) over the whole domain, where an extra term that accounts for the mass flux relative to the volume-averaged velocity appears in the Navier-Stokes equations (see, for details, [2]).

5.3 Phase-field model for binary compressible fluid with thermocapillary effects

In this section, we develop a system of equations for a binary fluid with thermocapillary effects, in which both components are compressible and Cahn-Hilliard diffusion is coupled with fluid motion.

5.3.1 Derivation of the model

We first consider a mixture of two fluids moving with the mass-averaged velocity $\mathbf{u}$ in a domain Ω, and we take an arbitrary material volume $V \in \Omega$ that moves with the mixture. Within the material volume, we define the properties for the binary compressible fluid as

$$M = \int_{V(t)} \rho \, \mathrm{d}V, \tag{5.15}$$

$$\mathbf{P} = \int_{V(t)} \rho \mathbf{u} \, \mathrm{d}V, \tag{5.16}$$

$$E = \int_{V(t)} \left(\frac{1}{2}\rho |\mathbf{u}|^2 + \rho g z + \rho \hat{u} \right) \mathrm{d}V, \tag{5.17}$$

$$S = \int_{V(t)} \rho \hat{s} \, \mathrm{d}V, \tag{5.18}$$

$$C = \int_{V(t)} \rho c \, \mathrm{d}V, \tag{5.19}$$

where M, $\mathbf{P}$, E, S is the total mass, momentum, energy, and entropy of the mixture, C is the constituent mass of fluid 1, $\rho(c)$ is the variable density of the mixture (Eq.(5.10)), $\mathbf{u}$ is the mass-averaged velocity of the mixture, $|\mathbf{u}|^2/2$ is the kinetic energy per unit mass, gz is the gravitational potential energy per unit mass, z is z-coordinate, $\hat{u}$ is the internal energy per unit mass, $\hat{s}$ is the entropy per unit mass, c is the phase variable (here we chose the mass concentration of fluid 1, and we set $c = c_1$). For our phase-field model, we chose mass concentration c as the phase variable and let $c = c_1$. Substituting the mass concentration (5.8) into Eq.(5.19) gives

$$C = \int_{V(t)} \rho c \, \mathrm{d}V = \int_{V(t)} \rho c_1 \, \mathrm{d}V = \int_{V(t)} \tilde{\rho}_1 \, \mathrm{d}V, \tag{5.20}$$

where we see that C stands for the constituent mass of fluid 1 within the material volume $V(t)$. In phase-field modelling, as well as the classical free energy density for bulk phases, an extra gradient term is typically added into the model accounting for part of the free energy of the diffuse interface [28]. Several ways have been suggested to introduce the gradient term into the phase-field model, e.g. by introducing it into the entropy functional [12, 123], free energy functional [87] or internal energy functional [8, 122]. In the present work, as the thermocapillary effects (Marangoni effects) along the interface are investigated, we expect that the surface free energy (serving as the surface tension (See section 5.5.2) of our phase-field model is temperature dependent (linearly). Therefore, according to the thermodynamic relations, we introduce the gradient term as the nonclassical contributions into both the internal energy and entropy of our model. The specific internal energy, entropy and free energy can then be given in the form

$$\hat{u}(s,\rho,c,\nabla c) = u(s,\rho,c) + u^{nc}(\nabla c),\ u^{nc} = \lambda_u \frac{1}{2}|\nabla c|^2, \tag{5.21}$$

$$\hat{s}(T,\rho,c,\nabla c) = s(T,\rho,c) + s^{nc}(\nabla c),\ s^{nc} = \lambda_s \frac{1}{2}|\nabla c|^2, \tag{5.22}$$

$$\hat{f}(T,\rho,c,\nabla c) = f(T,\rho,c) + f^{nc}(T,\nabla c),\ f^{nc} = \lambda_f(T)\frac{1}{2}|\nabla c|^2, \qquad (5.23)$$

where u, s and f stand for the classical parts of the specific internal energy, entropy and free energy separately. Here f is the Helmholtz free energy, where, for compressible flows, f is depending on the density as it has contributions from both the compressible components of the mixture. The nonclassical parts u^{nc}, s^{nc} and f^{nc} are the gradient terms analogous to the Landau-Ginzburg [49] or Cahn-Hilliard [28] gradient energy. In addition, λ_u and λ_s are constant parameters, $\lambda_f(T)$ is a parameter depending on the temperature and will lead to the thermocapillary effects along the interface. Note that λ_u, λ_s and $\lambda_f(T)$ can be further used to relate the surface tension of the phase-field model to that of the sharp-interface model when the phase-field model reduces to its sharp-interface limit (see section 5.5.2 for details). As $u(\rho,s,c)$ is the classical contribution to the specific internal energy $\hat{u}$, we have the thermodynamic relation

$$\begin{aligned} \mathrm{d}u(s,\rho,c) &= \left.\frac{\partial u}{\partial s}\right|_{\rho,c}\mathrm{d}s + \left.\frac{\partial u}{\partial \rho}\right|_{s,c}\mathrm{d}\rho + \left.\frac{\partial u}{\partial c}\right|_{s,\rho}\mathrm{d}c \\ &= T\mathrm{d}s + \frac{p}{\rho^2}\mathrm{d}\rho + \left.\frac{\partial u}{\partial c}\right|_{s,\rho}\mathrm{d}c, \end{aligned} \qquad (5.24)$$

where the subscripts indicate which variables are held constant when the various partial derivatives are taken. This relation states that the heat $T\mathrm{d}s$, the pressure-volume work $(p/\rho^2)\mathrm{d}\rho$, and chemical work $(\partial u/\partial c)\mathrm{d}c$ that accounts for the variation of the phase variable c all contribute to the changes in the internal energy. Further, we have the following thermodynamic relation for the Helmholtz free energy

$$f = u - Ts. \qquad (5.25)$$

Having in mind the relation (5.24), we obtain

$$\mathrm{d}f = \mathrm{d}u - \mathrm{d}(Ts) = \mathrm{d}u - s\mathrm{d}T - T\mathrm{d}s = \frac{p}{\rho^2}\mathrm{d}\rho - s\mathrm{d}T + \left.\frac{\partial u}{\partial c}\right|_{s,\rho} \mathrm{d}c, \tag{5.26}$$

such that

$$\left.\frac{\partial f}{\partial \rho}\right|_{T,c} = \frac{p}{\rho^2},\ \left.\frac{\partial f}{\partial T}\right|_{\rho,c} = -s \text{ and } \left.\frac{\partial f}{\partial c}\right|_{T,\rho} = \left.\frac{\partial u}{\partial c}\right|_{s,\rho}. \tag{5.27}$$

Similarly, we assume that the same thermodynamic relations, which hold for the classical terms also hold for the general terms, such that

$$\hat{f} = \hat{u} - T\hat{s} \quad \text{and} \quad \left.\frac{\partial \hat{f}}{\partial T}\right|_{s,\rho,c,\nabla c} = -\hat{s}. \tag{5.28}$$

With the relations (5.25) and (5.27), we must also have the relations for the nonclassical terms

$$f^{nc} = u^{nc} - Ts^{nc} \quad \text{and} \quad \left.\frac{\partial f^{nc}}{\partial T}\right|_{\nabla c} = -s^{nc}, \tag{5.29}$$

and for the corresponding parameters

$$\lambda_f(T) = \lambda_u - T\lambda_s \quad \text{and} \quad \frac{\mathrm{d}\lambda_f(T)}{\mathrm{d}T} = -\lambda_s. \tag{5.30}$$

For simplicity, we omit all the subscripts in the following derivations. Under the assumptions above, the general forms of physical balance associated with M, $\mathbf{P}$, E, S and C can be given as follows

$$\frac{\mathrm{d}M}{\mathrm{d}t} = 0, \tag{5.31}$$

$$\frac{\mathrm{d}\mathbf{P}}{\mathrm{d}t} = \int_{\partial V(t)} \mathbf{m}\cdot\hat{\mathbf{n}}\,\mathrm{d}A - \int_{V(t)} \rho g\hat{\mathbf{z}}\,\mathrm{d}V, \tag{5.32}$$

$$\frac{\mathrm{d}E}{\mathrm{d}t} = \int_{\partial V(t)} \left(\mathbf{u}\cdot\mathbf{m}\cdot\hat{\mathbf{n}} - \mathbf{q}_E\cdot\hat{\mathbf{n}} - \mathbf{q}_E^{nc}\cdot\hat{\mathbf{n}}\right)\mathrm{d}A, \tag{5.33}$$

$$\frac{\mathrm{d}S}{\mathrm{d}t} = -\int_{\partial V(t)} \left(\frac{\mathbf{q}_E}{T}\cdot\hat{\mathbf{n}} + \mathbf{q}_S^{nc}\cdot\hat{\mathbf{n}}\right)\mathrm{d}A + \int_{V(t)} S_{gen}\,\mathrm{d}V\ \left(S_{gen} \geqslant 0\right), \tag{5.34}$$

$$\frac{\mathrm{d}C}{\mathrm{d}t} = -\int_{\partial V(t)} \mathbf{q}_C \cdot \hat{\mathbf{n}}\, \mathrm{d}A, \tag{5.35}$$

where $\mathbf{m}$ is the stress tensor, $\hat{\mathbf{n}}$ is the unit outward normal vector of the boundary, $\rho g \hat{\mathbf{z}}$ is the gravitational forces, g is the gravitational constant, $\hat{\mathbf{z}}$ is the vertical component of the unit normal vector, $\mathbf{q}_E$ ($\mathbf{q}_E^{nc}$) is the classical (non-classical) contribution to the internal energy flux, $\mathbf{q}_E/T$ ($\mathbf{q}_S^{nc}$) is the classical (non-classical) contribution to the entropy flux, $S_{gen}(\geqslant 0)$ is the local entropy generation within the volume, and $\mathbf{q}_C$ is the mass flux of fluid 1 with the velocity ($\mathbf{u}_1 - \mathbf{u}$).

Eq.(5.31) represents the mass balance of the mixture within the volume. Eq.(5.32) represents the momentum balance, stating that the rate of the change in total momentum equals to the force (surface forces $\mathbf{m}$ and body forces $\rho g \hat{\mathbf{z}}$) acting on the volume. Here only the gravitational forces are considered. The energy balance equation (5.33) states that the change in total energy equals to the rate of work done by the forces ($\mathbf{m}$) on the boundary plus the energy flux (classical $\mathbf{q}_E$ and non-classical $\mathbf{q}_E^{nc}$ internal energy flux) through the boundary. The entropy balance (5.34) states that the rate of change of entropy in the control volume during the process equals to the net entropy transfered through the boundary (classical $\mathbf{q}_E/T$ and nonclassical $\mathbf{q}_S^{nc}$ entropy flux) plus the local entropy generation (S_{gen}) within the control volume (e.g. [92]). Based on the second law of thermodynamics, the local entropy generation is non-negative for a dissipative system (or say for an irreversible process), which is key to the thermodynamic frame that we used for the derivations. For the constituent mass balance (5.35), we use Eq.(5.20) and theorem 5.2.1 to obtain

$$\frac{\mathrm{d}C}{\mathrm{d}t} = \frac{\mathrm{d}}{\mathrm{d}t}\int_{V(t)} \tilde{\rho}_1 \mathrm{d}V = \int_{V(t)} \left(\frac{\partial \tilde{\rho}_1}{\partial t} + \nabla \cdot (\tilde{\rho}_1 \mathbf{u}) \right) \mathrm{d}V = -\int_{\partial V(t)} \mathbf{q}_C \cdot \hat{\mathbf{n}}\, \mathrm{d}A. \tag{5.36}$$

Substituting (5.11) into (5.36), we obtain

$$\mathbf{q}_C = \tilde{\rho}_1 (\mathbf{u}_1 - \mathbf{u}), \tag{5.37}$$

where we see that $\tilde{\rho}_1\mathbf{u}_1$ stands for the mass flux of fluid 1 with velocity $\mathbf{u}_1$ through the boundary of the control volume, $\tilde{\rho}_1\mathbf{u}$ stands for the mass flux of fluid 1 with velocity $\mathbf{u}$ through the boundary. We then identify $\mathbf{q}_C$ as the mass flux of fluid 1 with velocity $(\mathbf{u}_1-\mathbf{u})$, or say the net mass of fluid 1 that transported by velocity $(\mathbf{u}_1-\mathbf{u})$ through the boundary of the control volume. Note that in the following derivations, the constituent mass flux q_C will be related to the chemical potential of the phase-field, which is analogous to the standard derivations for the Cahn-Hilliard equations (see, for examples, [8], [56] and [87]).

In what follows, we use the definitions (5.15)-(5.19) and the balance laws (5.31)-(5.35) to obtain the equations that expressed in terms of the above unknowns, including $\mathbf{m}$, $\mathbf{q}_E$, $\mathbf{q}_E^{nc}$, $\mathbf{q}_S^{nc}$, $\mathbf{q}_C$ and S_{gen}. We then specify those unknowns with respect to the second law of thermodynamics (ensuring $S_{gen}\geqslant 0$) and the concept of thermodynamic consistency of the phase-field model.

For mass balance (5.31), we use theorem 5.2.1 to obtain

$$\frac{\mathrm{D}\rho}{\mathrm{D}t}=-\rho(\nabla\cdot\mathbf{u}), \tag{5.38}$$

based on which, we have the following theorem

Theorem 5.3.1. (Transport Theorem 2) *For a smooth function $f(\mathbf{x},t)$ in the Eulerian coordinate,*

$$\frac{\mathrm{d}}{\mathrm{d}t}\int_{V(t)}\rho f(\mathbf{x},t)\,\mathrm{d}V=\int_{V(t)}\rho\frac{\mathrm{D}f}{\mathrm{D}t}\,\mathrm{d}V=\int_{V(t)}\rho\left(\frac{\partial f}{\partial t}+(\mathbf{u}\cdot\nabla)f\right)\mathrm{d}V, \tag{5.39}$$

where ρ is the density of the mixture defined in the volume $V(t)$ and satisfies the mass balance (5.38).

Note that as theorem 5.2.1 and theorem 5.3.1 are frequently used, we will not refer them in the following derivations.

For momentum balance (5.32), we simply have

$$\rho \frac{\mathrm{D}\mathbf{u}}{\mathrm{D}t} = \nabla \cdot \mathbf{m} - \rho g \hat{\mathbf{z}}. \tag{5.40}$$

For energy balance (5.33), we obtain

$$\begin{aligned} &\rho \frac{\mathrm{D}\mathbf{u}}{\mathrm{D}t} \cdot \mathbf{u} + \rho g \hat{\mathbf{z}} \cdot \mathbf{u} + \rho \frac{\mathrm{D}u}{\mathrm{D}t} + \nabla \cdot (\rho \lambda_u \frac{\mathrm{D}c}{\mathrm{D}t} \nabla c) - \rho \lambda_u (\nabla c \otimes \nabla c) : \nabla \mathbf{u} - \lambda_u \nabla \cdot (\rho \nabla c) \frac{\mathrm{D}c}{\mathrm{D}t} \\ &= \nabla \cdot (\mathbf{u} \cdot \mathbf{m}) - \nabla \cdot \mathbf{q}_E - \nabla \cdot \mathbf{q}_E^{nc}, \end{aligned} \tag{5.41}$$

where the following identities are used

$$\frac{\mathrm{d}}{\mathrm{d}t} \int_{V(t)} \rho g z \, \mathrm{d}V = \int_{V(t)} \rho g \mathbf{u} \cdot \nabla z \, \mathrm{d}V = \int_{V(t)} \rho g \mathbf{u} \cdot \hat{\mathbf{z}} \, \mathrm{d}V, \tag{5.42}$$

and

$$\begin{aligned} \rho \frac{\mathrm{D}}{\mathrm{D}t} (\frac{1}{2} \lambda_u |\nabla c|^2) &= \rho \lambda_u \nabla c \cdot \frac{\mathrm{D}\nabla c}{\mathrm{D}t} = \rho \lambda_u \nabla c \cdot \Big[\frac{\partial \nabla c}{\partial t} + \mathbf{u} \cdot \nabla (\nabla c) \Big] \\ &= \nabla \cdot (\rho \lambda_u \frac{\mathrm{D}c}{\mathrm{D}t} \nabla c) - \rho \lambda_u (\nabla c \otimes \nabla c) : \nabla \mathbf{u} - \lambda_u \nabla \cdot (\rho \nabla c) \frac{\mathrm{D}c}{\mathrm{D}t}. \end{aligned} \tag{5.43}$$

Here " : " stands for the double dot product of the stress tensor (e.g. [90]). Multiplying the momentum balance equation (5.40) by $\mathbf{u}$ and substituting into (5.41), we obtain the simplified energy balance equation

$$\begin{aligned} \rho \frac{\mathrm{D}u}{\mathrm{D}t} = &-\nabla \cdot (\rho \lambda_u \frac{\mathrm{D}c}{\mathrm{D}t} \nabla c) + \Big(\mathbf{m} + \rho \lambda_u (\nabla c \otimes \nabla c) \Big) : \nabla \mathbf{u} \\ &+ \lambda_u \nabla \cdot (\rho \nabla c) \frac{\mathrm{D}c}{\mathrm{D}t} - \nabla \cdot \mathbf{q}_E - \nabla \cdot \mathbf{q}_E^{nc}, \end{aligned} \tag{5.44}$$

where we have used the identity

$$\nabla \cdot (\mathbf{u} \cdot \mathbf{m}) = (\nabla \cdot \mathbf{m}) \cdot \mathbf{u} + \mathbf{m} : \nabla \mathbf{u}. \tag{5.45}$$

Having in mind the thermodynamic relation (5.24), the energy equation (5.44) in terms of the entropy density can be expressed as

$$\begin{aligned}\rho T\frac{\mathrm{D}s}{\mathrm{D}t} =& -\nabla\cdot(\rho\lambda_u\frac{\mathrm{D}c}{\mathrm{D}t}\nabla c)+\Big(\mathbf{m}+\rho\lambda_u\nabla c\otimes\nabla c)\Big):\nabla\mathbf{u}\\ &+\lambda_u\nabla\cdot(\rho\nabla c)\frac{\mathrm{D}c}{\mathrm{D}t}-\nabla\cdot\mathbf{q}_E-\nabla\cdot\mathbf{q}_E^{nc}-\rho\frac{\partial u}{\partial c}\frac{\mathrm{D}c}{\mathrm{D}t}-\frac{p}{\rho}\frac{\mathrm{D}\rho}{\mathrm{D}t}.\end{aligned} \tag{5.46}$$

For entropy balance (5.34), we obtain

$$\begin{aligned}\rho\frac{\mathrm{D}s}{\mathrm{D}t} =& -\nabla\cdot(\rho\lambda_s\frac{\mathrm{D}c}{\mathrm{D}t}\nabla c)+\rho\lambda_s(\nabla c\otimes\nabla c):\nabla\mathbf{u}\\ &+\lambda_s\nabla\cdot(\rho\nabla c)\frac{\mathrm{D}c}{\mathrm{D}t}-\nabla\cdot(\frac{\mathbf{q}_E}{T})+S_{gen}-\nabla\cdot\mathbf{q}_S^{nc},\end{aligned} \tag{5.47}$$

where, similar to Eq.(5.43), the following identity is used,

$$\rho\frac{\mathrm{D}}{\mathrm{D}t}(\frac{1}{2}\lambda_s|\nabla c|^2) =\nabla\cdot(\rho\lambda_s\frac{\mathrm{D}c}{\mathrm{D}t}\nabla c)-\rho\lambda_s(\nabla c\otimes\nabla c):\nabla\mathbf{u}-\lambda_s\nabla\cdot(\rho\nabla c)\frac{\mathrm{D}c}{\mathrm{D}t}. \tag{5.48}$$

For constituent mass balance (5.35), we simply have

$$\rho\frac{\mathrm{D}c}{\mathrm{D}t}=-\nabla\cdot\mathbf{q}_C. \tag{5.49}$$

We then use Eq.(5.47) and Eq.(5.49) to substitute the terms $\rho\mathrm{D}s/\mathrm{D}t$ and $\rho\mathrm{D}c/\mathrm{D}t$ in (5.46), and use the relation (5.30) to obtain the expression for the entropy generation,

$$\begin{aligned}S_{gen}=&\frac{1}{T}\left(\mathbf{m}+\rho\Big(\lambda_u-T\lambda_s\Big)\mathbf{T}+p\mathbf{I}\right):\nabla\mathbf{u}+\left(\rho\lambda_u\frac{\mathrm{D}c}{\mathrm{D}t}\nabla c+\mathbf{q}_E+\mathbf{q}_E^{nc}-\mu_C\mathbf{q}_C\right)\cdot\nabla\frac{1}{T}\\ &-\nabla\cdot\left[\frac{1}{T}\rho\Big(\lambda_u-T\lambda_s\Big)\frac{\mathrm{D}c}{\mathrm{D}t}\nabla c+\frac{1}{T}\mathbf{q}_E^{nc}-\frac{1}{T}\mu_C\mathbf{q}_C-\mathbf{q}_S^{nc}\right]-\frac{1}{T}\mathbf{q}_C\cdot\nabla\mu_C.\end{aligned} \tag{5.50}$$

To ensure the non-negativity of the entropy generation $S_{gen} \geqslant 0$ (second law of thermodynamics), we specify the unknown terms in the form

$$\mathbf{q}_E = -k(c)\nabla T, \qquad \mathbf{q}_E^{nc} = -\rho\lambda_u \frac{\mathrm{D}c}{\mathrm{D}t}\nabla c + \mu_C \mathbf{q}_C, \tag{5.51}$$

$$\mathbf{q}_S^{nc} = -\rho\lambda_s \frac{\mathrm{D}c}{\mathrm{D}t}\nabla c, \qquad \mathbf{m} = -\rho(\lambda_u - T\lambda_s)\mathbf{T} + \sigma, \tag{5.52}$$

$$\mu_C = \frac{\partial f}{\partial c} - (\lambda_u - T\lambda_s)\frac{1}{\rho}\nabla\cdot(\rho\nabla c), \qquad \mathbf{q}_C = -m_C\nabla\mu_C, \tag{5.53}$$

$$\mathbf{T} = \nabla c \otimes \nabla c, \qquad \sigma = -p\mathbf{I} + \tau, \tag{5.54}$$

$$p = \rho^2 \frac{\partial f}{\partial \rho}, \qquad \tau = \mu(c)(\nabla\mathbf{u} + \nabla\mathbf{u}^T) - \frac{2}{3}\mu(c)(\nabla\cdot\mathbf{u})\mathbf{I}. \tag{5.55}$$

Note that τ is the deviatoric stress tensor from the classical Navier-Stokes equations (e.g. [17]). Here we use the thermodynamic relation (5.27) to obtain the chemical potential μ_C. The pressure p can be obtained immediately through the thermodynamic relation (5.27).

By substituting the above specifications into (5.31)-(5.35), we obtain the system of equations for the phase-field model governing binary compressible flows with thermo-capillary effects

$$\frac{\mathrm{D}\rho}{\mathrm{D}t} = -\rho(\nabla\cdot\mathbf{u}), \tag{5.56}$$

$$\rho\frac{\mathrm{D}\mathbf{u}}{\mathrm{D}t} = \nabla\cdot\mathbf{m} - \rho g\hat{\mathbf{z}}, \tag{5.57}$$

$$\rho\frac{\mathrm{D}u}{\mathrm{D}t} = (\sigma + \rho T\lambda_s\mathbf{T}) : \nabla\mathbf{u} + \lambda_u\nabla\cdot(\rho\nabla c)\frac{\mathrm{D}c}{\mathrm{D}t} + \nabla\cdot(k(c)\nabla T + m_C\mu_C\nabla\mu_C), \tag{5.58}$$

$$\rho\frac{\mathrm{D}s}{\mathrm{D}t} = \frac{1}{T}(\tau + \rho T\lambda_s\mathbf{T}) : \nabla\mathbf{u} + \lambda_s\nabla\cdot(\rho\nabla c)\frac{\mathrm{D}c}{\mathrm{D}t} + \frac{1}{T}\nabla\cdot(k(c)\nabla T), \tag{5.59}$$

$$\rho\frac{\mathrm{D}c}{\mathrm{D}t} = m_C\Delta\mu_C, \tag{5.60}$$

$$\mu_C = \frac{\partial f}{\partial c} - (\lambda_u - T\lambda_s)\frac{1}{\rho}\nabla\cdot(\rho\nabla c). \tag{5.61}$$

Here, the stress tensor $\mathbf{m}$ is defined by

$$\mathbf{m} = -\rho(\lambda_u - T\lambda_s)(\nabla c \otimes \nabla c) + \sigma, \tag{5.62}$$

where the first term is the extra reactive stress (Ericksen's stress) to mimic the surface tension. This stress term is associated with the presence of concentration gradients energy (Cahn-Hilliard energy). We note that the coefficient of this stress is a linear function of temperature, which leads to the thermocapillary effects along the interface (see section 5.5.2 for details), m_C is a positive constant standing for the mobility of the diffusing interface. Note that in the non-classical heat (entropy) flux $\mathbf{q}_E^{nc}$ ($\mathbf{q}_S^{nc}$), the term $\rho\lambda_u \nabla c \ \mathrm{D}c/\mathrm{D}t$ ($\rho\lambda_s \nabla c \ \mathrm{D}c/\mathrm{D}t$) is associated with the gradient energy (entropy) and is in the direction of the gradient of phase variable. Similar terms were obtained by Wang et. al. [123] who used a phase-field model to study the solidification of single material, and by Anderson et. al. [7] who used a phase-field model to study a single compressible fluid with different phases near its critical point. They identified the term as an energy (entropy) flux associated with variations in the phase-field at the boundary of the control volume. In addition, a non-classical energy flux term $m_C\mu_C\nabla\mu_C$ appears in our energy balance equation (5.58). The same energy flux term was obtained by Gurtin et. al. [56] (see Eq.(28)), who re-derived the Model H in the framework of classical continuum mechanics. A "counterpart" entropy flux term was identified by Lowengrub and Truskinovsky [87] when deriving a phase-field model for binary compressible fluid, where it was assumed in this form to keep the derivations compatible with the second law of thermodynamics. In the latter work, the isothermal fluid flow was studied, such that the temperature T in the entropy flux was treated as constant, whereas in our term, the temperature is not a constant as the thermocapillary effects are considered here. They identified it as the energy flux transported through the boundary by chemical diffusion. Our model agrees with these works well and therefore we identify this non-classical energy flux term as the energy that is carried

into the control volume by the chemical diffusion.

Similar to the approach that defines the variable density (5.10), we define the variable viscosity $\mu(c)$ and the variable thermal diffusivity $k(c)$ for the mixture in the form of the harmonic average,

$$\mu(c) = \frac{\mu_1\mu_2}{(\mu_2-\mu_1)c+\mu_1},\ k(c) = \frac{k_1k_2}{(k_2-k_1)c+k_1}, \tag{5.63}$$

where μ_1, μ_2, k_1 and k_2 are the viscosities and thermal conductivities of fluid 1 and 2 respectively.

5.4 Thermodynamic consistency and Galilean invariance

As our phase-field model (5.56)-(5.61) is derived within a thermodynamic framework, which implies that the first and second thermodynamic laws are naturally underlying the model. However, from the numerical point of view, thermodynamic consistency can be further served as a criterion to design the numerical methods. In our phase-field model, the Navier-Stokes equations are coupled with the Cahn-Hilliard equations and energy balance equation, which leads to a nonlinear system. Moreover, as the rapid variations in the solutions of the phase variable occur near the interfacial region, the stability of the numerical method is critical. Recently, the preservation of the thermodynamic laws at discrete level has been reported to play an important role in the designing of numerical methods (e.g. [83, 84] for liquid crystal model, [65, 54] for phase-field model), which not only immediately implies the stability of the numerical scheme, but also ensures the accuracy of the solutions. Hence, in contrast to the derivations, we now show that the first and second laws of thermodynamics can be derived from the system of equations (5.56)-(5.61), which can be further used to design the

numerical methods.

5.4.1 The laws of thermodynamics

Here we show that our phase-field model satisfy the first and second laws of thermodynamics. Multiplying the mass balance (5.56) by $p/\rho + \mathbf{u}\cdot\mathbf{u}/2 + u$, we obtain

$$(\frac{p}{\rho} + \frac{1}{2}\mathbf{u}\cdot\mathbf{u} + u)\frac{\mathrm{D}\rho}{\mathrm{D}t} = -p\mathbf{I} : \nabla\mathbf{u} - \rho(\nabla\cdot\mathbf{u})(\frac{1}{2}\mathbf{u}\cdot\mathbf{u} + u). \tag{5.64}$$

Multiplying the momentum balance (5.57) by $\mathbf{u}$ gives

$$\rho\frac{1}{2}\frac{\mathrm{D}}{\mathrm{D}t}(\mathbf{u}\cdot\mathbf{u}) + \rho\frac{\mathrm{D}}{\mathrm{D}t}(gy) = \nabla\cdot\mathbf{m}\cdot\mathbf{u}. \tag{5.65}$$

By using the identity (5.43), the entropy balance (5.59) can be rewritten in the form

$$\begin{aligned}\rho\frac{\mathrm{D}s}{\mathrm{D}t} + \frac{1}{T}\rho\frac{\mathrm{D}}{\mathrm{D}t}(\frac{1}{2}\lambda_u|\nabla c|^2) = \frac{1}{T}(\tau + \rho(\lambda_u - T\lambda_s)\mathbf{T}) : \nabla\mathbf{u} + \frac{1}{T}\nabla\cdot(\lambda_u\frac{\mathrm{D}c}{\mathrm{D}t}\nabla c)\\ -\frac{1}{T}(\lambda_u - T\lambda_s)\nabla\cdot(\rho\nabla c)\frac{\mathrm{D}c}{\mathrm{D}t} + \frac{1}{T}\nabla\cdot(k(c)\nabla T) + \frac{m_C}{T}|\nabla\mu_C|^2.\end{aligned} \tag{5.66}$$

Multiplying (5.66) by T gives

$$\begin{aligned}\rho T\frac{\mathrm{D}s}{\mathrm{D}t} + \rho\frac{\mathrm{D}}{\mathrm{D}t}(\frac{1}{2}\lambda_u|\nabla c|^2) = (\tau + \rho(\lambda_u - T\lambda_s)\mathbf{T}) : \nabla\mathbf{u} + \nabla\cdot(\lambda_u\frac{\mathrm{D}c}{\mathrm{D}t}\nabla c)\\ -(\lambda_u(T) - T\lambda_s(T))\nabla\cdot(\rho\nabla c)\frac{\mathrm{D}c}{\mathrm{D}t}.\end{aligned} \tag{5.67}$$

For the Cahn-Hilliard equation (5.60), we multiply by μ_C to obtain

$$0 = -\rho\frac{\mathrm{D}c}{\mathrm{D}t}\mu_C + m_C\mu_C\Delta\mu_C. \tag{5.68}$$

For the chemical potential equation (5.61), we multiply by $\rho \mathrm{D}c/\mathrm{D}t$ to obtain

$$\rho \frac{\partial f}{\partial c}\frac{\mathrm{D}c}{\mathrm{D}t} = \rho \frac{\mathrm{D}c}{\mathrm{D}t}\mu_C + \Big(\lambda_u - T\lambda_s\Big)\nabla\cdot(\rho\nabla c)\frac{\mathrm{D}c}{\mathrm{D}t}. \tag{5.69}$$

Combining Eq.(5.64), (5.65), (5.67)-(5.69) together, and having in mind the definition of the total energy of the system (5.17) and the identity (5.45), we finally obtain the first law of thermodynamics for our phase-field model within the domain Ω

$$\begin{aligned}\frac{\mathrm{d}E}{\mathrm{d}t} &= \frac{\mathrm{d}}{\mathrm{d}t}\int_\Omega \left(\rho\hat{u} + \frac{1}{2}\rho\mathbf{u}\cdot\mathbf{u} + \rho g z\right)\mathrm{d}x \\ &= \nabla\cdot(m\cdot\mathbf{u}) + \nabla\cdot(k(c)\nabla T) + \nabla\cdot\left(\lambda_u\frac{\mathrm{D}c}{\mathrm{D}t}\nabla c\right),\end{aligned} \tag{5.70}$$

which is in agreement with the energy balance law (5.33) that we used to derive the model. If we further assume that there is no stress along the boundary and no heat flux through the boundary of the domain Ω, and the interface does not contact with the boundary, we obtain the energy balance for an isolated system,

$$\frac{\mathrm{d}E}{\mathrm{d}t} = \frac{\mathrm{d}}{\mathrm{d}t}\int_\Omega \left(\rho\hat{u} + \frac{1}{2}\rho\mathbf{u}\cdot\mathbf{u} + \rho g z\right)\mathrm{d}x = 0. \tag{5.71}$$

By substituting the terms, $\mathbf{m}$, $\mathbf{q}_E$, $\mathbf{q}_E^{nc}$, $\mathbf{q}_S^{nc}$ and $\mathbf{q}_C$ into the entropy generation (5.50), we obtain the second law of thermodynamics,

$$\begin{aligned} S_{gen} &= \frac{1}{T}\tau : \nabla\mathbf{u} - \mathbf{q}_E\frac{\nabla T}{T^2} - \mathbf{q}_C\frac{1}{T}\nabla\mu_C \\ &= \frac{1}{T}\tau : \nabla\mathbf{u} + k(c)\Big|\frac{\nabla T}{T}\Big|^2 + \frac{m_C}{T}|\nabla\mu_C|^2 \geqslant 0, \end{aligned} \tag{5.72}$$

where we see that except the contributions from the traditional parts (viscous dissipation and heat transfer), the chemical potential or say the variation of the phase variable also contributes to the entropy generation of our phase-field model. Note that the same entropy generation equation was obtained by Lowengrub and Truskinovsky [87] when

deriving the phase-field model for binary compressible fluid.

5.4.2 Onsager reciprocal relations

From Eq.(5.72), we observe that the entropy generation can be seen as the sum of terms each being a product of a flux and thermodynamic force. The simplest model, based on the linear thermodynamics of non-equilibrium processes [51], assumes linear relations between the fluxes and thermodynamic forces, such that

$$\begin{aligned} \tau &= L_{11}\nabla\mathbf{v} + L_{12}\nabla T + L_{13}\nabla\mu_C, \\ \mathbf{q}_E &= L_{21}\nabla\mathbf{v} + L_{22}\nabla T + L_{23}\nabla\mu_C, \\ \mathbf{q}_C &= L_{31}\nabla\mathbf{v} + L_{32}\nabla T + L_{33}\nabla\mu_C, \end{aligned} \tag{5.73}$$

where the coefficients L_{ij} are chosen to guarantee the non-negativity S_{gen}. Moreover, microscopic reversibility requires the Onsager reciprocal relations $L_{ij} = L_{ji}$ ([51], and see, for examples, [100, 38]). From Eqs.(5.55), (5.51) and (5.53), we see that our choices of $\tau, \mathbf{q}_E$ and $\mathbf{q}_C$ satisfy the linear relation (5.73) and the reciprocal relations. Moreover, the entropy generation (5.72) is zero when the thermodynamic equilibrium conditions are satisfied within the system (i.e. thermodynamic forces are zero at equilibrium).

5.4.3 Galilean invariance

Another requirement which the entropy generation (5.72) must satisfy is that it be invariant under a Galilei transformation [51], since the notions of reversible and irreversible behaviour must be invariant under such a transformation. It can be seen that (5.72) satisfies automatically this requirement. Moreover, the model equations must

be Galilean invariant as well, where, according to the classical mechanics, the balance equations must be the same in the inertia frames.

Here we first briefly introduce the concept of Galilean transformation, and show that our model equations and entropy generation satisfy the Galilean invariance.

Let (x,y,z,t) be the coordinate system of the first observer, and a quantity of fluid (velocity, density...) in this frame be denoted by $\phi(x,y,z,t)$. For the second theoretician, the quantity of fluid in this frame is denoted by $\tilde{\phi}(x',y',z',t')$, and the coordinate system is $x',y'z',t'$ in the frame moving in the $+x$ direction with a constant velocity U, such that

$$x = x' + Ut',\ y = y',\ z = z',\ t = t', \tag{5.74}$$

$$\tilde{\mathbf{u}} = \mathbf{u} - U\mathbf{i}. \tag{5.75}$$

where $\tilde{\mathbf{u}}$ and $\mathbf{u}$ are the velocity of the fluid in the corresponding frames, $\mathbf{i}$ is the unit vector in the x direction. Further we have

$$\tilde{\phi}(x',y',z',t') \xrightarrow{\text{Eq.(5.74)}} \phi(x,y,z,t), \tag{5.76}$$

$$\frac{\partial\tilde{\phi}(x',y',z',t')}{\partial x'} = \frac{\partial\phi(x,y,z,t)}{\partial x}, \tag{5.77}$$

$$\frac{\partial\tilde{\phi}(x',y',z',t')}{\partial y'} = \frac{\partial\phi(x,y,z,t)}{\partial y}, \tag{5.78}$$

$$\frac{\partial\tilde{\phi}(x',y',z',t')}{\partial z'} = \frac{\partial\phi(x,y,z,t)}{\partial z}. \tag{5.79}$$

For the time derivative, we have that

$$\frac{\mathrm{d}\tilde{\phi}(x',y',z',t')}{\mathrm{d}t'} = \frac{\mathrm{d}\phi(x,y,z,t)}{\mathrm{d}t}. \tag{5.80}$$

The left hand of Eq.(5.80) gives us that

$$\frac{\mathrm{d}\tilde{\phi}(x',y',z',t')}{\mathrm{d}t'} = \frac{\partial\tilde{\phi}(x',y',z',t')}{\partial x'}\frac{\partial x'}{\partial t'} + \frac{\partial\tilde{\phi}(x',y',z',t')}{\partial y'}\frac{\partial y'}{\partial t'} + \frac{\partial\tilde{\phi}(x',y',z',t')}{\partial z'}\frac{\partial z'}{\partial t'}$$
$$+ \frac{\partial\tilde{\phi}(x',y',z',t')}{\partial t'} = \frac{\partial\tilde{\phi}}{\partial t'} + \tilde{\mathbf{u}}\cdot\nabla\tilde{\phi}. \tag{5.81}$$

Similarly the right of Eq.(5.80) hand gives us that

$$\frac{\mathrm{d}\phi(x,y,z,t)}{\mathrm{d}t} = \frac{\partial\phi}{\partial t} + \mathbf{u}\cdot\nabla\phi. \tag{5.82}$$

Substituting Eqs (5.81) and (5.82) into Eq.(5.80) gives that

$$\frac{\partial\tilde{\phi}}{\partial t'} + \tilde{\mathbf{u}}\cdot\nabla\tilde{\phi} = \frac{\partial\phi}{\partial t} + \mathbf{u}\cdot\nabla\phi, \tag{5.83}$$

$$\frac{\partial\tilde{\phi}}{\partial t'} + (\mathbf{u} - U\mathbf{i})\cdot\nabla\tilde{\phi} = \frac{\partial\phi}{\partial t} + \mathbf{u}\cdot\nabla\phi, \tag{5.84}$$

$$\frac{\partial\tilde{\phi}}{\partial t'} = \frac{\partial\phi}{\partial t} + U\mathbf{i}\cdot\nabla\phi, \text{ and } \nabla\tilde{\phi} = \nabla\phi. \tag{5.85}$$

For the material derivative we have that

$$\frac{\mathrm{D}\tilde{\phi}}{\mathrm{D}t'} = \frac{\partial\tilde{\phi}}{\partial t'} + \tilde{\mathbf{u}}\cdot\nabla\tilde{\phi} = \frac{\partial\phi}{\partial t} + U\mathbf{i}\cdot\nabla\phi + (\mathbf{u} - U\mathbf{i})\cdot\nabla\phi = \frac{\partial\phi}{\partial t} + \mathbf{u}\cdot\nabla\phi = \frac{\mathrm{D}\phi}{\mathrm{D}t}, \tag{5.86}$$

where we see that the material derivative D/Dt and spatial gradient ∇ are Galilean invariant.

Now we go back to our system equations. Firstly, we note that the scalar fields (temperature T, mass density ρ, phase variable c, pressure p and chemical potential μ_C) are independent of the observer (invariant). For example, temperature at a given point in a

room and at a given time would have the same value for any inertia frames. The gravitational acceleration g is invariant for any inertia frames. We see that all of our equations are invariant. Therefore we can conclude that our system equations satisfy the Galilean invariance. Note that, another phase-field model was developed by Abels et. al. [1] to study the binary incompressible fluid with variable density. In their model, as the volume-averaged velocity is employed for the mixture, which leads to a non-objective scalar term appearing in the chemical potential equation. Therefore a particular formulation for the convective terms is needed to keep the Galilean invariance of their model equations. In our model equations, on the other hand, the mass-averaged velocity is employed for the mixture, and therefore no non-objective terms are involved. Our system equations satisfy the Galilean invariance automatically.

5.5 Phase-field for quasi-incompressible fluid with thermocapillary effects

In this section, we develop a model of a binary Cahn-Hilliard fluids with thermocapillary effects in which both components are incompressible.

5.5.1 Derivation of the model

In order to study situations in which the density in each phase is uniform, it is convenient to adopt a thermodynamic formation which does not employ the density as an independent variable, as in the model of quasi-incompressible flow considered by Lowengrub and Truskinovsky [87]. Following their work, we choose the pressure and temperature as independent variables, and work with the Gibbs free energy. In addition, for a binary incompressible fluid system, the free energy density can appear as

the per unit mass quantity or per unit volume quantity. In most phase-field models for two-phase flows (e.g. [63, 85]), the density of two components are assumed to be constant and equal, and the per unit mass and per unit volume specification of the free energy density are equivalent. However, in the situation we study here, the densities of two fluids of the mixture may not be matched and thus the per unit mass and per unit volume forms are not equivalent. As we mentioned above, several models have been developed for a binary incompressible fluid with different densities, in which the per unit volume form of free energy density was employed in [26, 35, 110, 2] and the per unit mass form in [87]. Here we concentrate on the Gibbs free energy density in the per unit mass form, and denote it by $\hat{g}(T,p,c,\nabla c)$. Again, similar to the definition of the free energy (5.23) for a binary compressible fluid, we introduce the nonclassical terms (gradient energy) into the Gibbs free energy of our model, which can then be given in the form

$$\hat{g}(T,p,c,\nabla c) = g(T,p,c) + g^{nc}(T,\nabla c),\ g^{nc} = f^{nc} = \lambda_f(T)\frac{1}{2}|\nabla c|^2, \qquad (5.87)$$

where g is the classical part of the Gibbs free energy density, and $\lambda_f(T)$ is a temperature dependent coefficient and will lead to the thermocapillary effects along the interface (see section 5.5.2 for details). For the classical part of the internal energy defined by (5.21), we have the following thermodynamic relation

$$u(s,\rho,c) = g(T,p,c) + Ts - \frac{p}{\rho}. \qquad (5.88)$$

Using the thermodynamic relation (5.24) leads to

$$\begin{aligned} \mathrm{d}g(T,p,c) &= \mathrm{d}u(s,\rho,c) - s\mathrm{d}T - T\mathrm{d}s + \frac{1}{\rho}\mathrm{d}p - \frac{p}{\rho^2}\mathrm{d}\rho \\ &= -s\mathrm{d}T + \frac{1}{\rho}\mathrm{d}p + \left.\frac{\partial u}{\partial c}\right|_{\rho,s}\mathrm{d}c, \end{aligned} \qquad (5.89)$$

where we note the relations

$$\left.\frac{\partial g(T,p,c)}{\partial T}\right|_{p,c} = -s,\ \left.\frac{\partial g(T,p,c)}{\partial p}\right|_{T,c} = \frac{1}{\rho} \text{ and } \left.\frac{\partial g(T,p,c)}{\partial c}\right|_{T,p} = \left.\frac{\partial u}{\partial c}\right|_{\rho,s}. \quad (5.90)$$

Here as we assume that the variable density is independent of temperature and pressure, the condition of the incompressibility can then be written in the terms of the Gibbs free energy

$$\frac{\partial^2 g(T,p,c)}{\partial^2 p} = 0, \quad (5.91)$$

where the second condition in (5.90) is used. Condition (5.91) implies that Gibbs free energy is a linear function of pressure, (e.g. [87])

$$g(T,p,c) = g_0(T,c) + \frac{p}{\rho(c)}. \quad (5.92)$$

We then re-define the classical internal energy as a function of T, p and c,

$$\tilde{u}(T,p,c) = u(s,\rho,c) = g(T,p,c) + Ts - \frac{p}{\rho(c)}, \quad (5.93)$$

where the relations (5.89) and (5.90) still hold. Similarly to the definition of the internal energy (5.21) and entropy (5.22) for the binary compressible fluid model, the specific internal energy $\hat{u}$ and the specific entropy $\hat{s}$ for binary incompressible fluids, which contain both the classical and nonclassical contributions, can be re-defined in the form

$$\hat{u}(T,p,c,\nabla c) = \tilde{u}(T,p,c) + u^{nc}(\nabla c),\ u^{nc} = \lambda_u \frac{1}{2}|\nabla c|^2, \quad (5.94)$$

$$\hat{s}(T,p,c,\nabla c) = \tilde{s}(T,p,c) + s^{nc}(\nabla c),\ s^{nc} = \lambda_s \frac{1}{2}|\nabla c|^2, \quad (5.95)$$

where $\tilde{u}$ and $\tilde{s}$ are the classical parts of the specific internal energy and entropy that associated with the Gibbs free energy, λ_u and λ_s are constant. In addition to these

classical contributions, we assume that the same thermodynamics relations that hold for the classical terms also hold for the total terms, such that

$$\hat{g} = \hat{u} - T\hat{s} + \frac{p}{\rho}, \quad \left.\frac{\partial \hat{g}}{\partial T}\right|_{p,c,\nabla c} = -\hat{s}. \tag{5.96}$$

Based on which, we obtain the following relation for the coefficients

$$\lambda_f(T) = \lambda_u - T\lambda_s, \ \frac{\mathrm{d}\lambda_f(T)}{\mathrm{d}T} = -\lambda_s. \tag{5.97}$$

The specifications of these three coefficients will be discussed in section 5.5.2. Note that λ_u, λ_s together with $\lambda_f(T)$ (in Eq.(5.87)) can be further used to relate the surface tension of phase-field model to that of the sharp-interface model when our phase-field model reduces to its sharp-interface limit (see section 5.6.4 for details).

Now we derive the system of equations for the quasi-incompressible phase-field model. We still use (5.15)-(5.19) to define the total properties, namely mass M, momentum $\mathbf{P}$, energy E, entropy S and mass constituent C in a material control volume $V(t)$ of the domain Ω. We further assume that the corresponding general balance laws (5.31)-(5.35) that hold for the binary compressible fluid also hold for the quasi-incompressible fluid, which can then be written as

$$\frac{\mathrm{D}\rho}{\mathrm{D}t} = -\rho(\nabla\cdot\mathbf{u}), \tag{5.98}$$

$$\rho\frac{\mathrm{D}\mathbf{u}}{\mathrm{D}t} = \nabla\cdot\mathbf{m} - \rho g\hat{\mathbf{z}}, \tag{5.99}$$

$$\rho\frac{\mathrm{D}\tilde{u}}{\mathrm{D}t} = -\nabla\cdot(\rho\lambda_u\frac{\mathrm{D}c}{\mathrm{D}t}\nabla c) + \lambda_u\nabla\cdot(\rho\nabla c)\frac{\mathrm{D}c}{\mathrm{D}t} + (\mathbf{m}+\rho\lambda_u\mathbf{T}):\nabla\mathbf{u} - \nabla\cdot\mathbf{q}_E - \nabla\cdot\mathbf{q}_E^{nc}, \tag{5.100}$$

$$\rho\frac{\mathrm{D}\tilde{s}}{\mathrm{D}t} = -\nabla\cdot(\rho\lambda_s\frac{\mathrm{D}c}{\mathrm{D}t}\nabla c) + \lambda_s\nabla\cdot(\rho\nabla c)\frac{\mathrm{D}c}{\mathrm{D}t} - \rho\lambda_s\mathbf{T}:\nabla\mathbf{u} - \nabla\cdot(\frac{\mathbf{q}_E}{T}) - \nabla\cdot\mathbf{q}_S^{nc} + S_{gen}, \tag{5.101}$$

$$\rho\frac{\mathrm{D}c}{\mathrm{D}t} = -\nabla\cdot\mathbf{q}_C, \tag{5.102}$$

where, as the pressure p is not defined in the traditional way, the general stress tensor $\mathbf{m}$ is not defined explicitly.

Note that, in contrast to the case of binary compressible fluid, the classical part of the internal energy $\tilde{u}$ we defined here does not depend on the entropy $\tilde{s}$ directly. However, as our derivations are carried out within the thermodynamic framework that is based on the entropy generation, we still need a thermodynamic relation between the internal energy and entropy. Having in mind the definition of the internal energy (5.93) and using the relations (5.89) and (5.90), we obtain the following relation between the classical part of internal energy $\tilde{u}$, Gibbs free energy g and entropy $\tilde{s}$

$$\rho \frac{\mathrm{D}\tilde{u}}{\mathrm{D}t} = \rho \frac{\partial g_0}{\partial c} \frac{\mathrm{D}c}{\mathrm{D}t} + \rho T \frac{\mathrm{D}\tilde{s}(T,p,c)}{\mathrm{D}t}. \tag{5.103}$$

Then similar to the method used for the binary compressible fluid model, we use the unknowns, including $\mathbf{m}$, $\mathbf{q}_E$, $\mathbf{q}_E^{nc}$, $\mathbf{q}_S^{nc}$ to express the entropy generation in the form

$$\begin{aligned} S_{gen} &= \tfrac{1}{T}\left(\mathbf{m} + \rho\lambda_f(T)\mathbf{T}\right) : \nabla\mathbf{u} + \nabla\tfrac{1}{T} \cdot \left(\rho\lambda_u \tfrac{\mathrm{D}c}{\mathrm{D}t}\nabla c + \mathbf{q}_E + \mathbf{q}_E^{nc} - \tilde{\mu}_C \mathbf{q}_C\right) \\ &\quad -\nabla \cdot \left[\tfrac{1}{T}\left(\rho\lambda_f(T)\tfrac{\mathrm{D}c}{\mathrm{D}t}\nabla c + \mathbf{q}_E^{nc} - \tilde{\mu}_C\mathbf{q}_C - T\mathbf{q}_S^{nc}\right)\right] - \tfrac{1}{T}\mathbf{q}_C \cdot \nabla\tilde{\mu}_C, \end{aligned} \tag{5.104}$$

where we have used Eqs.(5.98)-(5.103), $\tilde{\mu}_C = \gamma_f(T)\partial g_0(c)/\partial c - \lambda_f(T)\nabla\cdot(\rho\nabla c)/\rho$ is the chemical potential, $\mathbf{T} = \nabla c \otimes \nabla c$ is the extra reactive stress (Ericksen's stress) to mimic the surface tension, which is associated with the concentration gradients energy. As the pressure is no longer defined by the thermodynamic formulas in this model, we now derive the pressure in an alternative way to that used by Lowengrub and Truskinovsky [87], where the pressure was obtained from the non-dissipated part of the general stress $\mathbf{m}$. Considering a dissipative process, we denote the general stress tensor by $\mathbf{m} = \mathbf{m}_0 + \tau$, in which τ is the deviatoric stress tensor with zero trace, and $\mathbf{m}_0$ is the unknown part to be defined later. The entropy expression (5.104) can then be

written in the form

$$S_{gen} = \frac{1}{T}\left(\mathbf{m}_0 + \rho\lambda_f(T)\mathbf{T}\right) : \nabla\mathbf{u} + \frac{1}{T}\tau : \nabla\mathbf{u} + \nabla\frac{1}{T}\cdot\left(\rho\lambda_u\frac{\mathrm{D}c}{\mathrm{D}t}\nabla c + \mathbf{q}_E + \mathbf{q}_E^{nc} - \tilde{\mu}_C\mathbf{q}_C\right) - \nabla\cdot\left[\frac{1}{T}\left(\rho\lambda_f(T)\frac{\mathrm{D}c}{\mathrm{D}t}\nabla c + \mathbf{q}_E^{nc} - \tilde{\mu}_C\mathbf{q}_C - T\mathbf{q}_S^{nc}\right)\right] - \frac{1}{T}\mathbf{q}_C\cdot\nabla\tilde{\mu}_C. \tag{5.105}$$

We then denote $\mathbf{Du} = \nabla\mathbf{u} - (\nabla\cdot\mathbf{u})\mathbf{I}/3$ as the deviatoric part of $\nabla\mathbf{u}$ (tr $\mathbf{Dv} = 0$) and substitute into (5.105) to obtain

$$S_{gen} = \frac{1}{T}\left(\mathbf{m}_0 + \rho\lambda_f(T)\mathbf{T}\right) : \mathbf{Dv} + \frac{1}{T}\tau : \nabla\mathbf{u} + \nabla\frac{1}{T}\cdot\left\{\rho\lambda_u\frac{\mathrm{D}c}{\mathrm{D}t}\nabla c + \mathbf{q}_E + \mathbf{q}_E^{nc} - \left[\tilde{\mu}_C + \frac{1}{3}\left(\mathrm{tr}\,\mathbf{m}_0 + \rho\left(\lambda_u - T\lambda_s\right)|\nabla c|^2\right)\frac{1}{\rho^2}\frac{\mathrm{d}\rho}{\mathrm{d}c}\right]\mathbf{q}_C\right\} - \nabla\cdot\left\{\frac{1}{T}\left[\rho\lambda_f(T)\frac{\mathrm{D}c}{\mathrm{D}t}\nabla c + \mathbf{q}_E^{nc} - \left(\tilde{\mu}_C + \left(\mathrm{tr}\,\mathbf{m}_0 + \rho\lambda_f(T)|\nabla c|^2\right)\frac{1}{\rho^2}\frac{\mathrm{d}\rho}{\mathrm{d}c}\right)\mathbf{q}_C - T\mathbf{q}_S^{nc}\right]\right\} - \frac{1}{T}\mathbf{q}_C\cdot\nabla\left[\tilde{\mu}_C + \frac{1}{3}\left(\mathrm{tr}\,\mathbf{m}_0 + \rho\left(\lambda_u - T\lambda_s\right)|\nabla c|^2\right)\frac{1}{\rho^2}\frac{\mathrm{d}\rho}{\mathrm{d}c}\right], \tag{5.106}$$

where we have used the mass balance (5.98) and the following identity

$$\left(\mathbf{m}_0 + \rho\lambda_f(T)\mathbf{T}\right) : \frac{1}{3}(\nabla\cdot\mathbf{u})\mathbf{I} = \frac{1}{3}\left(\mathrm{tr}\,\mathbf{m}_0 + \rho\lambda_f(T)\mathrm{tr}\,\mathbf{T}\right)(\nabla\cdot\mathbf{u}). \tag{5.107}$$

Now we assume the first two terms on the right-hand side of (5.106) are non-dissipative and define the pressure p by

$$-p = \frac{1}{3}\mathrm{tr}\,\mathbf{m} = \frac{1}{3}\mathrm{tr}\left(\mathbf{m}_0 + \rho\lambda_f(T)\mathbf{T}\right) = \frac{1}{3}\left(\mathrm{tr}\,\mathbf{m}_0 + \rho\lambda_f(T)|\nabla c|^2\right), \tag{5.108}$$

such that

$$-p\mathbf{I} = \mathbf{m}_0 + \rho(\lambda_u - T\lambda_s)\mathbf{T}, \tag{5.109}$$

in which the way we use to define the pressure in Eq.(5.108) is analogous to the way that defines the kinematic pressure for the classical Navier-Stokes equations [17]. To ensure our model is consistent with the second law of thermodynamics ($S_{gen} \geqslant 0$), we specify the unknown terms as the following

$$\mathbf{q}_E = -k(c)\nabla T, \qquad \mathbf{q}_E^{nc} = -\rho\lambda_u \frac{\mathrm{D}c}{\mathrm{D}t} + \mu_C \mathbf{q}_C, \tag{5.110}$$

$$\mathbf{q}_S^{nc} = -\rho\lambda_s \frac{\mathrm{D}c}{\mathrm{D}t}\nabla c, \qquad \mathbf{m}_0 = -p\mathbf{I} - \rho\lambda_f(T)\mathbf{T}, \tag{5.111}$$

$$\mu_C = \frac{\partial g_0}{\partial c} - \frac{p}{\rho^2}\frac{\mathrm{d}\rho}{\mathrm{d}c} - \lambda_f(T)\frac{1}{\rho}\nabla\cdot(\rho\nabla c), \qquad \mathbf{q}_C = -m_C\nabla\mu_C, \tag{5.112}$$

$$\mathbf{T} = \nabla c \otimes \nabla c, \qquad \tau = \mu(c)(\nabla\mathbf{u} + \nabla\mathbf{u}^T) - \frac{2}{3}\mu(c)(\nabla\cdot\mathbf{u})\mathbf{I}. \tag{5.113}$$

We observe that, besides the Navier-Stokes equations, the pressure appears in the chemical potential equation as well, which is different to the chemical potential (5.61) for the binary compressible fluid model. Moreover, as the quasi-incompressibility is introduced to our phase-field model, the velocity fields is non-solenoidal (see Eq.(5.14)), the term $2\mu(c)(\nabla\cdot\mathbf{u})\mathbf{I}/3$ does not equal to zero and thus cannot be eliminated from τ. By substituting the above specifications into Eqs.(5.98)-(5.102), we obtain the system of equations for the phase-field model governing the quasi-incompressible fluid with thermocapillary effects

$$\frac{\mathrm{D}\rho}{\mathrm{D}t} = -\rho(\nabla\cdot\mathbf{u}), \tag{5.114}$$

$$\rho\frac{\mathrm{D}\mathbf{u}}{\mathrm{D}t} = \nabla\cdot\mathbf{m} - \rho g\hat{\mathbf{z}}, \tag{5.115}$$

$$\rho\frac{\mathrm{D}\tilde{u}}{\mathrm{D}t} = \lambda_u\nabla\cdot(\rho\nabla c)\frac{\mathrm{D}c}{\mathrm{D}t} + (-p\mathbf{I} + \rho T\lambda_s\mathbf{T} + \tau) : \nabla\mathbf{u} + \nabla\cdot(k(c)\nabla T + m_C\mu_C\nabla\mu_C), \tag{5.116}$$

$$\rho\frac{\mathrm{D}\tilde{s}}{\mathrm{D}t} = \lambda_s\nabla\cdot(\rho\nabla c)\frac{\mathrm{D}c}{\mathrm{D}t} + \frac{1}{T}(\rho T\lambda_s\mathbf{T} + \tau) : \nabla\mathbf{u} + \frac{1}{T}\nabla\cdot(k(c)\nabla T), \tag{5.117}$$

$$\rho\frac{\mathrm{D}c}{\mathrm{D}t} = m_C\Delta\mu_C, \tag{5.118}$$

$$\mu_C = \frac{\partial g_0}{\partial c} - \frac{p}{\rho^2}\frac{\mathrm{d}\rho}{\mathrm{d}c} - \lambda_f(T)\frac{1}{\rho}\nabla\cdot(\rho\nabla c), \tag{5.119}$$

where, similarly to binary compressible model, the coefficient of the Ericksen's stress $\mathbf{T}$ is linearly temperature dependent, leading to the thermocapillary effects along the diffusing interface, m_C is a positive constant stands for the mobility of the diffuse interface. The definitions (5.63) are still employed for the variable viscosity $\mu(c)$ and variable thermal conductivity $k(c)$.

By substituting the terms, including $\mathbf{m}$, $\mathbf{q}_E$, $\mathbf{q}_E^{nc}$, $\mathbf{q}_S^{nc}$ and $\mathbf{q}_C$ into the entropy generation (5.106), we obtain the second law of thermodynamics for our phase-field model,

$$S_{gen} = \frac{1}{T}\tau : \nabla\mathbf{u} + k(c)|\frac{\nabla T}{T}|^2 + \frac{m_C}{T}|\nabla\mu_C|^2 \geqslant 0. \tag{5.120}$$

Similar to the binary compressible model, the choices of the terms $\tau, \mathbf{q}_E$ and $\mathbf{q}_C$ satisfy the linear relation (5.73) and the Onsager reciprocal relations. Moreover, it can be observed that the entropy generation (5.120) and the system equations are Galilean invariant.

As mentioned above, several phase-field models have been developed for two-phase flows with thermocapillary effects. However, in most of these models, the classical energy balance equation

$$\rho c_{hc}\frac{\mathrm{D}T}{\mathrm{D}t} = \nabla\cdot(k\nabla T), \tag{5.121}$$

was incorporated directly into the phase-field model, where thermodynamic consistency can be hardly maintained. Comparing with the classical energy balance equation (5.121), several extra terms appear in our energy balance equation (5.116), which guarantee thermodynamic consistency (see section 5.4). The term $\rho\lambda_u\nabla c\,\mathrm{D}c/\mathrm{D}t$ ($\rho\lambda_s\nabla c\,\mathrm{D}c/\mathrm{D}t$) that appears in the non-classical heat (entropy) flux $\mathbf{q}_E^{nc}$ ($\mathbf{q}_S^{nc}$) is associated with the gradient energy (entropy). Here similar to section 5.3, we identify it as the energy

(entropy) flux associated with variations in the phase-field at the boundary of the control volume. Note that, in the isothermal case, our model reduces to the quasi-incompressible NSCH model [87] (Eq.(4.1)-Eq.(4.4)) which is studied in chapter 4.
By using the variable mass density (5.10), the mass balance equation (5.114) can be further rewritten as

$$\nabla \cdot \mathbf{u} = -\frac{1}{\rho}\frac{\mathrm{D}\rho}{\mathrm{D}t} = \alpha\rho\frac{\mathrm{D}c}{\mathrm{D}t} = \alpha m_C \Delta\mu_C, \tag{5.122}$$

where we have used Cahn-Hilliard equation (5.118) and let $\alpha = (\rho_2 - \rho_1)/\rho_2\rho_1$.
The initial conditions are given by

$$\mathbf{u}|_{t=0} = \mathbf{u}_0,\ c|_{t=0} = c_0,\ \text{and}\ T|_{t=0} = T_0. \tag{5.123}$$

For the velocity, the usual no-slip or no-flow boundary conditions can be posed on $\partial\Omega$

$$\mathbf{u} = \mathbf{v_b},\ \text{or}\ \mathbf{u}\cdot\hat{\mathbf{n}} = \mathbf{v_b}\cdot\hat{\mathbf{n}}. \tag{5.124}$$

For the phase-field, it is normal to employ Neumann boundary conditions on $\partial\Omega$

$$\nabla c\cdot\hat{\mathbf{n}} = h_c,\ \text{and}\ \nabla\mu_C\cdot\hat{\mathbf{n}} = h_\mu. \tag{5.125}$$

For the temperature field, Dirichlet and Neumann boundary conditions can be posed on $\partial\Omega$

$$T = T_b,\ \text{or}\ \nabla T\cdot\hat{\mathbf{n}} = q_b \tag{5.126}$$

for the specified temperature and heat flux on the boundary $\partial\Omega$ respectively, and Robin boundary conditions can be posed as well.

5.5.2 Specifications of the model

We now specify the properties including the Gibbs free energy, entropy and internal energy for our phase-field model (5.114)-(5.119). In [9], a phase-field model for the solidification of a pure material that includes convection in the liquid phase was developed, in which the case of the quasi-incompressibility (assuming that the density in each phase is uniform) was discussed. In their work, the Gibbs free energy was suggested in the form

$$\hat{g}(T,p,c) = g_0(T,c) + \frac{p}{\rho(c)} + \lambda_f(T)\frac{1}{2}|\nabla c|^2, \tag{5.127}$$

$$g_0(T,c) = \Big(u_0 - c_{hc}T_0\Big)(1-\frac{T}{T_0}) - c_{hc}T\ln(\frac{T}{T_0}) + \gamma_f(T)h(c), \tag{5.128}$$

which we adopt for the present work. Here, c_{hc} is the heat capacity, T_0 is the reference temperature, $\tilde{u}_0$ is the reference internal energy corresponds to T_0, and $\gamma(T)$ is a temperature dependent parameter that will be discussed later in this subsection. The free energy function $h(c)$ is a double-well potential and is given by

$$h(c) = \frac{c^2(c-1)^2}{4}, \tag{5.129}$$

where the wells define the phases, and leads to an interfacial layer with large variations for c (e.g. [56]). Note that the form for $\hat{g}$ (5.127) is consistent with the incompressible condition (5.92), which is a linear function of pressure. Moreover, this form for $\hat{g}$ is consistent with an internal energy $\hat{u}$, which is a linear function of temperature and leads to the classical heat equation in the bulk liquid [123, 10]. The corresponding expressions for the entropy and internal energy are assumed in the form

$$\hat{s} = \tilde{s} + s^{nc} = \frac{1}{T_0}u_0 + c_{hc}\ln(\frac{T}{T_0}) + \gamma_s h(c) + \lambda_s\frac{1}{2}|\nabla c|^2, \tag{5.130}$$

$$\hat{u} = \tilde{u} + u^{nc} = \tilde{u}_0 + c_{hc}(T-T_0) + \gamma_u h(c) + \lambda_u\frac{1}{2}|\nabla c|^2, \tag{5.131}$$

where $\tilde{u}_0$ is the reference internal energy corresponds to T_0.

We now specify those coefficients, including $\lambda_f(T)$, λ_s, λ_u, $\gamma_f(T)$, γ_s and γ_u, which are used to define the internal energy, entropy and free energy of the system (Eqs.(5.127)-(5.131)). In a sharp-interface model for the thermocapillary flow, the interface is usually represented as a surface of zero thickness with the surface tension as its physical property. An equation of state is required to relate the surface tension to the temperature, which may be linear or nonlinear. For the sake of simplicity, we only consider a linear relation in this study, such that

$$\sigma(T) = \sigma_0 - \sigma_T(T - T_0), \tag{5.132}$$

where $\sigma(T)$ is the linear function of the temperature, σ_0 is the interfacial tension at the reference temperature T_0, σ_T is the rate of change of interfacial tension with temperature, defined as $\sigma_T = \partial\sigma(T)/\partial T$. In our phase-field model, however, the interface has finite thickness and the extra reactive stress (Ericksen's stress) $\mathbf{T}$ appears in the Navier-Stokes equation to mimic the surface tension, where the coefficient of $\mathbf{T}$

$$\lambda_f(T) = \lambda_u - T\lambda_s, \tag{5.133}$$

is a linear function of temperature. As $\sigma(T)$ and $\lambda_f(T)$ are used to describe the thermocapillary effects in the sharp-interface model and our phase-field model respectively, and both of them are linear functions of temperature, we then try to relate our coefficient $\lambda_f(T)$ to its "sharp-interface counterpart" $\sigma(T)$ by introducing two parameters: the first parameter is ε with respect to the thickness of the diffuse interface, and the second one is a ratio parameter η that relates the surface tension between the two models. As the interface thickness ε goes to zero, our phase-field model can reduce to its sharp-interface limit, and the value of η can then be determined through the relation between the surface tensions of two models (see section 5.6.7 for details). The corresponding

coefficients can be given as

$$\lambda_f(T) = \eta\varepsilon\sigma(T) = \eta\varepsilon\sigma_0 - \eta\varepsilon\sigma_T(T-T_0),\ \gamma_f(T) = \frac{\eta}{\varepsilon}\sigma(T) = \frac{\eta}{\varepsilon}\sigma_0 - \frac{\eta}{\varepsilon}\sigma_T(T-T_0),$$
$$\lambda_s = \eta\varepsilon\sigma_T, \qquad \gamma_s = \frac{\eta}{\varepsilon}\sigma_T,$$
$$\lambda_u = \eta\varepsilon\sigma_0 + \eta\varepsilon\sigma_T T_0, \qquad \gamma_u = \frac{\eta}{\varepsilon}\sigma_0 + \frac{\eta}{\varepsilon}\sigma_T T_0. \tag{5.134}$$

Here the coefficients $\lambda_f(T)$, λ_s and λ_u for the gradient terms are $O(\varepsilon^2)$ approximations to those coefficients $\gamma_f(T)$, γ_s and γ_u for the corresponding classical terms, which agrees with the definition of the Cahn-Hilliard free energy (e.g. [87, 85]). With the specifications above, the total energy E of our phase-field model can now be written as

$$E = \int_{V(t)} \left(\frac{1}{2}\rho|\mathbf{u}|^2 + \rho g z + \rho\tilde{u}_0 + \rho c_{hc}(T-T_0) + \rho\gamma_u h(c) + \rho\lambda_u \frac{1}{2}|\nabla c|^2 \right) \mathrm{d}V. \tag{5.135}$$

5.5.3 Non-dimensionalization

With the help of the specification in Eq.(5.134), we non-dimensionalize the phase-field model (5.114)-(5.116), (5.118) and (5.119) as follows. We let $L^\star$, $V^\star$ and $T^\star$ denote the characteric scales of length, velocity and temperature. Then introduce the dimensionless variables $\bar{\mathbf{x}} = \mathbf{x}/L^\star$, $\bar{t} = V^\star t/L^\star$, and also $\bar{\varepsilon} = \varepsilon L^\star$, $\bar{\mathbf{u}} = \mathbf{u}/V^\star$, $\bar{p} = p\rho_1\mu_C^\star$, $\bar{\mu}_C = \mu_C/\mu_C^\star$. For the variable density $\rho(c)$, viscosity $\mu(c)$ and thermal conductivity $k(c)$(Eqs.(5.10) and (5.63)), we let ρ_i, μ_i and k_i (i=1,2) denote the corresponding properties of the ith fluid, and introduce the non-dimensionless variables $\bar{\rho}_r = \rho(c)/\rho_1$, $\bar{\mu}_r = \mu(c)/\mu_1$ and $\bar{k}_r = k(c)/k_1$. Moreover, for the temperature field, we introduce a new non-dimensonless variable $\bar{T} = (T-T_0)/T^\star$. The surface tension $\sigma(T)$ (Eq.(5.132)) is scaled by σ_0 such that $\bar{\sigma}(T) = \sigma(T)/\sigma_0$, σ_T is then scaled by $\sigma_0/T^\star$, such that $\bar{\sigma_T} = \sigma_T T^\star/\sigma_0$. Omitting the bar notation, our phase-field model can now be

rewritten as

$$\nabla \cdot \mathbf{u} = -\frac{1}{\rho_r}\frac{\partial \rho_r}{\partial c}\frac{\mathrm{D}c}{\mathrm{D}t} \tag{5.136}$$

$$\rho_r \frac{\mathrm{D}\mathbf{u}}{\mathrm{D}t} = -\frac{1}{M}\Big[\nabla p + Ca\nabla \cdot \Big(\rho_r \sigma(T)\mathbf{T}\Big)\Big] + \frac{1}{Re}\nabla \cdot \Big(\mu_r(\nabla \mathbf{u} + \nabla \mathbf{u}^T) - \frac{2}{3}\mu_r(\nabla \cdot \mathbf{u})\mathbf{I}\Big) - \frac{\rho_r}{Fr^2}\hat{\mathbf{z}}, \tag{5.137}$$

$$\rho \frac{\mathrm{D}c}{\mathrm{D}t} = \frac{1}{Pe}\Delta \mu_C, \tag{5.138}$$

$$\mu_C = \frac{Ca}{\varepsilon^2}\sigma(T)\frac{\mathrm{d}h(c)}{\mathrm{d}c} - \frac{p}{\rho_r^2}\frac{\mathrm{d}\rho_r}{\mathrm{d}c} - \frac{Ca}{\rho_r}\sigma(T)\nabla \cdot (\rho_r \nabla c), \tag{5.139}$$

$$\rho_r c_{hc}\frac{\mathrm{D}T}{\mathrm{D}t} = \frac{EcCa}{M}(1+\sigma_T T_0)\nabla \cdot (\rho_r \nabla c)\frac{\mathrm{D}c}{\mathrm{D}t} + \frac{Ec}{M}(-p\mathbf{I} + Ca\rho_r T\sigma_T \mathbf{T} + \frac{1}{Re}\tau) : \nabla \mathbf{u} + \nabla \cdot (\frac{1}{Ma}k_r \nabla T + \frac{Ec}{MPe}\mu_C \nabla \mu_C), \tag{5.140}$$

where $M = V^2/\mu_C$ is an analogue of the Mach number, $Ca = \eta\varepsilon\sigma_0/\mu_C L$ is the Capillary number that measures the thickness of the interface, $Re = \mu_1/\rho_1 VL$ is the Reynolds number, $Fr = V^2/gL$ is the Froude number, $Pe = \rho LV/m_C\mu_C$ is the diffusional Peclet number, $Ec = V^2/c_{ch}T$ is the Eckert number that characterizes dissipation of enrgy, $Ma = \rho c_{ch}VL/k_1$ is the Marangoni number.

5.6 Sharp-interface limits

Theoretically, there are usually two ways to validate the phase-field model. The first, as mentioned above, is to show thermodynamic consistency of the model. The second is to relate the phase-field model to its sharp-interface counterpart. Base on the assumption that a given sharp-interface formulation is the correct description of the physics under consideration, the phase-field model can be justified by simply showing that it is asymptotic to the classical sharp-interface description. In the isothermal case, some sharp-interface limit analysis have been carried out for the phase-field

model of two-phase flow to show that the corresponding sharp-interface equations and jump conditions across the interface can be recovered from the phase-field model (e.g. [87, 124, 2]). However, much less attentions have been paid on the asymptotic analysis of the phase-field model for two-phase flows in the non-isothermal case, (e.g. thermocapillary flows, solidifications). Antanovskii [12] presented a phase-field model to study the thermocapillary flow, and showed that the hydrostatic equilibrium condition for the case of a flat interface and the Laplace-Young condition for the case of a drop in equilibrium can be recovered from his phase-field model. Jasnow and Vinals [70] extended Model-H to study the thermocapillary flow, including the migration of a drop and spinodal decomposition of a binary fluid under a constant temperature gradient. In the corresponding sharp-interface limit, he showed that the additional stress term in the Navier-Stokes equation of their phase-field model is equivalent to the tangential and normal force of the appropriate sharp-interface model. Anderson et. al.[9] developed a phase-field model of solidification with convection in the melt, in which the two phases are considered as viscous liquids. In the sharp-interface analysis [10], they used the matched asymptotic expansions to show that the standard boundary conditions, including Young-Laplace and Stefan conditions can be recovered from their phase-field model.

5.6.1 Pillbox argument

To illustrate this concept, we apply a similar pillbox argument to our phase-field model (5.114)-(5.119). In contrast to sharp-interface model, the interface of the phase-field model is diffusive with a finite thickness ε. The phase variable (here is mass concentration c) is chosen to characterize the different phases, which takes distinct values (here $c = \pm 1$) for the different phases, and changes rapidly through the interfacial region. Within this interfacial region, we chose a contour line of c (here $c = 0.5$) to represent

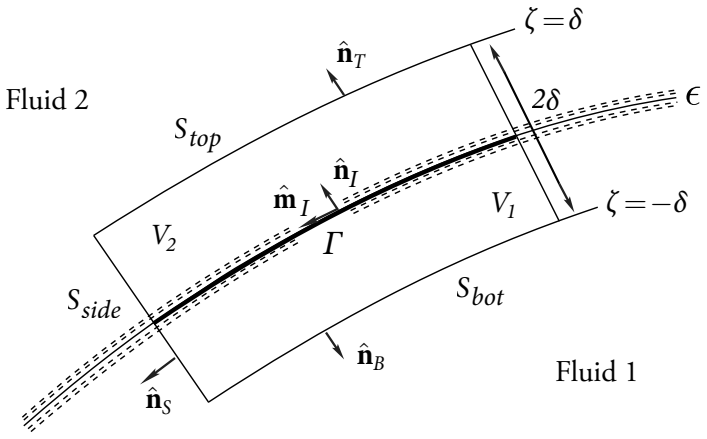

Figure 5.1: A schematic diagram showing a diffuse-interface between two fluids intersecting with a pillbox shaped control volume, $\hat{\mathbf{n}}_T$, $\hat{\mathbf{n}}_B$ and $\hat{\mathbf{n}}_S$ stand for the unit normal vector of the pillbox boundary on its top, bottom and side, respectively. The dotted lines represent the diffuse-interface with thickness ε, 2δ is the thickness of the pillbox. In the limit $\varepsilon \ll \delta \ll L$, the interface thickness goes to zero, and the interface has constant density, $\hat{\mathbf{n}}_I$ and $\hat{\mathbf{m}}_I$ stand for the unit normal and tangent vector of the interface.

the dividing surface Γ for the following derivations (See section 5.6.6 for details of the dividing surface). Moreover, as the largest variations of the phase variable occur in the direction normal to the interface, the side faces of the pillbox need to be treated carefully. Figure 5.1 shows the pillbox shaped control volume designed for our phase-field model, where the surface of the pillbox here is divided into three parts, namely the top S_{top}, bottom S_{bot} and side S_{side} surfaces with their unit normal vector $\hat{\mathbf{n}}_T$, $\hat{\mathbf{n}}_B$ and $\hat{\mathbf{n}}_S$, respectively. The pillbox has thickness of 2δ, where the top of the pillbox is above the dividing surface Γ at a height $\zeta = \delta$ and the bottom is below Γ at a height $\zeta = -\delta$. Here, ζ is a local coordinate normal to the interface S_I. In addition, the pillbox contains a portion of the diffuse-interface with thickness ε, in which Γ stands for the dividing surface with its normal and tangent unit vector $\hat{\mathbf{n}}_I$ and $\hat{\mathbf{m}}_I$. The key limit in the pillbox argument is that $\varepsilon \ll \delta \ll L$, where L is a length scale associated with the outer flow. In this limit, the volume of the pillbox becomes negligible on the outer scales, but the variations in the concentration variable c that define the interfacial region, occur over a region fully contained within the pillbox. Also in this limit, the top (S_{top}) and the

bottom surface (S_{bot}) of the pillbox collapse onto the interface Γ, and have the normal vectors with opposite directions

$$S_{top} = S_{bot} = \Gamma,\ \hat{\mathbf{n}}_T = \hat{\mathbf{n}}_I,\ \hat{\mathbf{n}}_B = -\hat{\mathbf{n}}_I \text{ and } \hat{\mathbf{n}}_S = \hat{\mathbf{m}}_I. \tag{5.141}$$

Moreover, we assume that the interface is moving with the velocity $\mathbf{v}_I$([7, 8]). Note that, as the thermocapillary (Marangoni) effect can be important under the case of microgravity or microdevices, where the surface forces become dominant, we assume that the viscous forces are small comparing to the surface forces.

5.6.2 Governing equations in sharp-interface limit

We first derive the system of equations in the bulk regions away from the interfacial region. Here we only concentrate on the equations of mass, momentum and energy balance. In the limit $\varepsilon \ll 0$, the system of equations (5.114)-(5.116) reduce to the classical equations appropriate for the incompressible flows in bulk regions

$$\nabla \cdot \mathbf{u} = 0, \tag{5.142}$$

$$\rho_i \frac{\mathrm{D}\mathbf{u}}{\mathrm{D}t} = -\nabla p + \nabla \cdot \left(\mu_i(\nabla \mathbf{u} + \nabla \mathbf{u}^T)\right) - \rho_i g \hat{\mathbf{z}}, \tag{5.143}$$

$$\rho_i c_{hc} \frac{\mathrm{D}T}{\mathrm{D}t} = \nabla \cdot (k_i \nabla T) + \mu_i(\nabla \mathbf{u} + \nabla \mathbf{u}^T) : \nabla \mathbf{u}, \tag{5.144}$$

where ρ_i, μ_i and k_i are the corresponding physical properties for the ith fluid.
We now seek to derive the jump conditions for Eqs.(5.142)-(5.144) at the interface from our phase-field model (5.114)-(5.119).

5.6.3 Jump condition for mass balance

In the limit $\varepsilon \ll \delta \ll L$, we have the properties [7, 8]

$$\int_V \frac{\partial \rho}{\partial t} \mathrm{d}V \sim -\int_S \rho \mathbf{u}_I \cdot \hat{\mathbf{n}} \mathrm{d}S, \tag{5.145}$$

$$\int_V \frac{\partial (\rho \mathbf{u})}{\partial t} \mathrm{d}V \sim -\int_S \rho \mathbf{u} \otimes \mathbf{u}_I \cdot \hat{\mathbf{n}} \mathrm{d}S. \tag{5.146}$$

Substituting Eq.(5.145) into Eq.(5.98), we obtain

$$\int_S \rho (\mathbf{u} - \mathbf{u}_I) \cdot \hat{\mathbf{n}} \mathrm{d}S = 0. \tag{5.147}$$

According to the pillbox designed earlier, we break up the above surface integral into pieces for the top, bottom and side surfaces to obtain

$$\int_{S_{top}} \rho (\mathbf{u} - \mathbf{u}_I) \cdot \hat{\mathbf{n}}_T \mathrm{d}S + \int_{S_{bot}} \rho (\mathbf{u} - \mathbf{u}_I) \cdot \hat{\mathbf{n}}_B \mathrm{d}S + \oint_C \int_{-\delta}^{\delta} \rho (\mathbf{u} - \mathbf{u}_I) \cdot \hat{\mathbf{n}}_S \mathrm{d}\zeta \mathrm{d}l = 0. \tag{5.148}$$

Here the surface integral of side portion is further written in term of a line integral on the surface and an integral in the normal direction $\hat{\mathbf{n}}_S$, where the line is a closed curve at the side of the control volume that parallel to the interface. For a viscous fluid under normal operating conditions, it is an experimentally observed fact (like the no-slip boundary conditions at solid walls) that no slip takes place at the interface [119]. Therefore, in the limit $\varepsilon \ll \delta \ll L$, we have

$$\mathbf{v} \cdot \hat{\mathbf{m}}_I \sim \mathbf{v}_I \cdot \hat{\mathbf{m}}_I \tag{5.149}$$

This condition implies that the third left terms in Eq.(5.148) are bounded and do not contribute to the integral. Eq.(5.148) can be reduced to

$$\int_{\Gamma} \Big[\rho(\mathbf{u}-\mathbf{u}_I)\Big] \cdot \hat{\mathbf{n}}_I \mathrm{d}S = 0, \tag{5.150}$$

where $[\chi] = \chi_2 - \chi_1$ refers to the jump of the quantity χ across the singular interface. Since the pillbox control volume V that contains a portion of the diffuse-interface is arbitrary, the integrand in Eq.(5.150) must be zero. This then yields the mass balance jump condition at the interface in a multiphase fluid system

$$\Big[\rho(\mathbf{u}-\mathbf{u}_I)\Big] \cdot \hat{\mathbf{n}}_I = 0. \tag{5.151}$$

Further if we assume that there is no phase change (i.e. no flux) across the interface, Eq.(5.151) reduces jump condition that

$$\Big[\mathbf{u}\Big] \cdot \hat{\mathbf{n}}_I = 0. \tag{5.152}$$

5.6.4 Jump condition for momentum balance

Substituting Eq.(5.145) into the momentum equation (5.115), we obtain

$$\int_S \left(\rho \mathbf{u} \otimes (\mathbf{u}-\mathbf{u}_I) + p\mathbf{I} + \eta\varepsilon\sigma(T)\rho\mathbf{T} - \mu(\nabla\mathbf{u} + \nabla\mathbf{u}^T) + \frac{2}{3}\mu(\nabla\cdot\mathbf{u})\mathbf{I} \right) \cdot \hat{\mathbf{n}} \mathrm{d}S = 0,$$

where, in the limit $\varepsilon \ll \delta \ll L$, we assume that the gravitational term $\rho g\hat{\mathbf{z}}$ is bounded and thus do not contribute to the volume integral. We then break up the above surface

integral into pieces for the top, bottom and sides of the pillbox to obtain

$$\int_{S_{top}} \left(\rho \mathbf{u} \otimes (\mathbf{u} - \mathbf{u}_I) + p\mathbf{I} + \eta \varepsilon \sigma(T) \rho \mathbf{T} - \mu(\nabla \mathbf{u} + \nabla \mathbf{u}^T) + \frac{2}{3}\mu(\nabla \cdot \mathbf{u})\mathbf{I} \right) \cdot \hat{\mathbf{n}}_T \mathrm{d}S$$
$$+ \int_{S_{bot}} \left(\rho \mathbf{u} \otimes (\mathbf{u} - \mathbf{u}_I) + p\mathbf{I} + \eta \varepsilon \sigma(T) \rho \mathbf{T} - \mu(\nabla \mathbf{u} + \nabla \mathbf{u}^T) + \frac{2}{3}\mu(\nabla \cdot \mathbf{u})\mathbf{I} \right) \cdot \hat{\mathbf{n}}_B \mathrm{d}S$$
$$+ \oint_C \int_{-\delta}^{\delta} \Bigg(\rho \mathbf{u} \otimes (\mathbf{u} - \mathbf{u}_I) + p\mathbf{I} + \eta \varepsilon \sigma(T) \rho \mathbf{T} - \mu(\nabla \mathbf{u} + \nabla \mathbf{u}^T)$$
$$+ \frac{2}{3}\mu(\nabla \cdot \mathbf{u})\mathbf{I} \Bigg) \cdot \hat{\mathbf{n}}_S \mathrm{d}\zeta \mathrm{d}l = 0. \tag{5.153}$$

We assume that the most rapid variations in the phase-field take place across the interfacial region with the direction normal to the interface Γ. In the limit $\varepsilon \ll \delta \ll L$, local to the interface we have

$$\nabla \sim \frac{\partial}{\partial \zeta}\hat{\mathbf{n}}_I, \ \nabla c \sim \frac{\partial c}{\partial \zeta}\hat{\mathbf{n}}_I, \ \Delta c \sim \frac{\partial^2 c}{\partial \zeta^2} \text{ and } \frac{\partial}{\partial t} \sim -\mathbf{v}_I \cdot \hat{\mathbf{n}}_I \frac{\partial}{\partial \zeta}, \tag{5.154}$$

such that

$$\mathbf{T} = \nabla c \otimes \nabla c \sim \frac{\partial c}{\partial \zeta}\hat{\mathbf{n}}_I \frac{\partial c}{\partial \zeta}\hat{\mathbf{n}}_I, \ \mathbf{T} \cdot \hat{\mathbf{n}}_I \sim \frac{\partial c}{\partial \zeta}\frac{\partial c}{\partial \zeta}\hat{\mathbf{n}}_I, \text{ and } \mathbf{T} \cdot \hat{\mathbf{m}}_I \sim 0. \tag{5.155}$$

Condition (5.149) implies that the fluid velocity term $\rho \mathbf{v} \otimes (\mathbf{v} - \mathbf{v}_I) \cdot \hat{\mathbf{n}}_S$ is bounded and does not contribute to the integral over the side surface of the pillbox. The tangential derivative terms $-\mu(\nabla \mathbf{v} + \nabla \mathbf{v}^T) \cdot \hat{\mathbf{n}}_S$ are bounded and do not contribute to the side integral. For the term $2/3\mu(\nabla \cdot \mathbf{v}) \cdot \hat{\mathbf{n}}_S$, Eqs.(5.122) and (5.154) gives

$$\frac{2}{3}\mu(\nabla \cdot \mathbf{v}) = \frac{2}{3}\mu\alpha\rho\frac{\mathrm{D}c}{\mathrm{D}t} \sim \frac{2}{3}\mu\alpha\rho c(\mathbf{v} - \mathbf{v}_I)\frac{\partial c}{\partial \zeta}, \tag{5.156}$$

which implies that $2/3\mu(\nabla \cdot \mathbf{v})\mathbf{I} \cdot \hat{\mathbf{n}}_S$ is bounded and does contribute to the side integral. Morevoer, the non-classical stress term $\mathbf{T}$ does not contribute to the integral over the

top and bottom surfaces. Eq.(5.153) reduces to

$$\int_{\Gamma}\left(\Big[\rho\mathbf{u}(\mathbf{u}-\mathbf{u}_I)\Big]\cdot\hat{\mathbf{n}}_I+\Big[p\mathbf{I}\Big]\cdot\hat{\mathbf{n}}_I+\Big[-\mu(\nabla\mathbf{u}+\nabla\mathbf{u}^T)\Big]\cdot\hat{\mathbf{n}}_I\right)\mathrm{d}S + \oint_C\int_{-\varepsilon}^{\varepsilon}p\mathbf{I}\cdot\hat{\mathbf{m}}_I\mathrm{d}\zeta\mathrm{d}l=0, \quad (5.157)$$

where the condition (5.141) is used.

We now seek to identify the last right term in Eq.(5.157) as the surface tension of our phase-field model. At equilibrium, we argue that in the momentum equation, the largest variations in the direction normal to the interface occur in the pressure and the phase-field, so that the terms ∇p and $\nabla\cdot(\eta\varepsilon^2\sigma(T)\rho(\nabla c\otimes\nabla c))$ have the leading order, and the momentum equation (5.115) in the term of the local co-ordinate can then be simplified as

$$\frac{\partial p}{\partial\zeta}+\frac{\partial}{\partial\zeta}\Big(\eta\varepsilon\sigma(T)\rho(\frac{\partial c}{\partial\zeta})^2\Big)=0, \quad (5.158)$$

where we note the conditions

$$p=p_{\pm},\ c=c_{\pm}\text{ and }\frac{\partial c}{\partial\zeta}=0\text{ as }\zeta\to\pm\delta. \quad (5.159)$$

Here $p_{\pm}$ are constant value that p takes at the top and bottom surface of the pillbox, and $c_{\pm}$ are the value of c in the bulk region of fluid 1 and 2 separately. We then integrate (5.158) from $-\delta$ to a position $\zeta\in[-\delta,+\delta]$ to obtain

$$p(\zeta)=p_{-}-\eta\varepsilon\sigma(T)\rho(\frac{\partial c}{\partial\zeta})^2, \quad (5.160)$$

where the condition (5.159) is used. In the limit $\varepsilon \ll \delta \ll L$, we integrate (5.160) from $-\delta$ to δ to obtain

$$\int_{-\delta}^{\delta} p(\zeta)\,\mathrm{d}d = \int_{-\delta}^{\delta} \left(-\eta\varepsilon\sigma(T)\rho(\frac{\partial c}{\partial \zeta})^2 \right) \mathrm{d}\zeta \sim -\eta\sigma(T) \int_{-\delta}^{\delta} \left(\varepsilon\rho(\frac{\partial c}{\partial \zeta})^2 \right) \mathrm{d}\zeta, \tag{5.161}$$

where p_- is bounded and does not contribute to the line integral. Here, for our pill-box argument to make sense, we require that within the pillbox the temperature are continuous and the variations is small over a small distance (of order of the pillbox thickness δ). In the limit $\varepsilon \ll \delta \ll L$, the temperature T is approximately uniform along the direction normal to the interface and thus is independent of the local coordinate ζ. Note that the similar assumption for the temperature was also suggested by [70], where a surface tension term with thermocapillary effects was identified from a phase-field model in its sharp-interface limit. Denoting by

$$\tilde{\sigma}(T) = \eta\sigma(T) \lim_{\varepsilon\to 0} \int_{-\delta}^{\delta} \left(\varepsilon\rho(\frac{\partial c}{\partial \zeta})^2 \right) \mathrm{d}\zeta, \tag{5.162}$$

and substituting into (5.157), we obtain

$$\int_{\Gamma} \left(\Big[\rho\mathbf{u}(\mathbf{u}-\mathbf{u}_I)\Big]\cdot\hat{\mathbf{n}}_I + \Big[p\mathbf{I}\Big]\cdot\hat{\mathbf{n}}_I + \Big[-\mu(\nabla\mathbf{u}+\nabla\mathbf{u}^T)\Big]\cdot\hat{\mathbf{n}}_I \right) \mathrm{d}S - \oint_C \tilde{\sigma}\hat{\mathbf{m}}_I \mathrm{d}l = 0, \tag{5.163}$$

where, in the limit $\varepsilon \ll \delta \ll L$, we assume that the tangential unit vector $\hat{\mathbf{m}}_I$ is independent of ζ and thus can be taken out of the line integral. Using the surface divergence theorem [125] leads to

$$\oint_C \tilde{\sigma}\hat{\mathbf{m}}_I \mathrm{d}l = \int_{\Gamma} \nabla_s\tilde{\sigma}\mathrm{d}S - \int_{\Gamma} (\nabla_s\cdot\hat{\mathbf{n}}_I)\tilde{\sigma}\hat{\mathbf{n}}_I \mathrm{d}S. \tag{5.164}$$

Substituting Eq.(5.164) into Eq.(5.163), we obtain

$$\int_{\Gamma}\left(\Big[\rho\mathbf{u}(\mathbf{u}-\mathbf{u}_I)\Big]\cdot\hat{\mathbf{n}}_I+\Big[p\mathbf{I}\Big]\cdot\hat{\mathbf{n}}_I+\Big[-\mu(\nabla\mathbf{u}+\nabla\mathbf{u}^T)\Big]\cdot\hat{\mathbf{n}}_I\right)\mathrm{d}S$$
$$-\int_{\Gamma}\nabla_s\tilde{\sigma}\mathrm{d}S+\int_{\Gamma}(\nabla_s\cdot\hat{\mathbf{n}}_I)\tilde{\sigma}\hat{\mathbf{n}}_I\mathrm{d}S=0. \tag{5.165}$$

Note that, as the pillbox is arbitrary, the jump condition for the momentum balance at the interface can be given as

$$\Big[\rho\mathbf{u}(\mathbf{u}-\mathbf{u}_I)\Big]\cdot\hat{\mathbf{n}}_I+\Big[p\mathbf{I}\Big]\cdot\hat{\mathbf{n}}_I+\Big[-\mu(\nabla\mathbf{u}+\nabla\mathbf{u}^T)\Big]\cdot\hat{\mathbf{n}}_I=\nabla_s\tilde{\sigma}+\kappa\tilde{\sigma}\hat{\mathbf{n}}_I, \tag{5.166}$$

where ∇_s is the surface gradient, $\kappa=-\nabla_s\cdot\hat{\mathbf{n}}_I$ is the mean curvature of the surface (e.g. [125]). The first term on the right is the tangential thermocapillary (Marangoni) force that accounts for the non-uniform surface tension, while the second is the normal surface tension force. Again if we assume that there is no phase change (i.e. no flux) across the interface, Eq.(5.166) reduces to the jump condition that

$$\Big[p\mathbf{I}\Big]\cdot\hat{\mathbf{n}}_I+\Big[-\mu(\nabla\mathbf{u}+\nabla\mathbf{u}^T)\Big]\cdot\hat{\mathbf{n}}_I=\nabla_s\tilde{\sigma}+\kappa\tilde{\sigma}\hat{\mathbf{n}}_I, \tag{5.167}$$

which is the classical momentum balance jump conditions at the interface for two-phase incompressible fluid with thermocapillary effects. However it still remains to confirm that the term $\tilde{\sigma}$ in Eq.(5.162) stands for the surface tension. In what follows, we will first derive the free energy boundary conditions at equilibrium (5.6.5), based on which we use the excess of interfacial free energy to identify that the term $\tilde{\sigma}$ defined in Eq.(5.162) stands for the surface tension of our phase-field model (section 5.6.6).

5.6.5 Free energy balance

We now rewrite the Cahn-Hilliard equations (5.118) and (5.119) as one equation

$$\int_V \rho \frac{\mathrm{D}c}{\mathrm{D}t} - \left\{ m_C \Delta \left(\frac{\eta}{\varepsilon} \sigma(T) \frac{\mathrm{d}h(c)}{\mathrm{d}c} - \frac{p}{\rho^2} \frac{\mathrm{d}\rho}{\mathrm{d}c} - \eta \varepsilon \sigma(T) \frac{1}{\rho} \nabla \cdot (\rho \nabla c) \right) \right\} \mathrm{d}V = 0 \quad (5.168)$$

At equilibrium, we expect that all the terms in the braces have the leading order. Having in mind the assumption (5.154), the Cahn-Hilliard equation (5.168) can be reduced to

$$\int_V \frac{\partial^2}{\partial \zeta^2} \left(\frac{\eta}{\varepsilon} \sigma(T) \frac{\mathrm{d}h(c)}{\mathrm{d}c} - \frac{p}{\rho^2} \frac{\mathrm{d}\rho}{\mathrm{d}c} - \eta \varepsilon \sigma(T) \frac{1}{\rho} \frac{\mathrm{d}}{\mathrm{d}\zeta} (\rho \frac{\mathrm{d}c}{\mathrm{d}\zeta}) \right) \mathrm{d}V = 0. \quad (5.169)$$

As the pillbox control volume is arbitrary, we have

$$\frac{\partial^2}{\partial \zeta^2} \left(\frac{\eta}{\varepsilon} \sigma(T) \frac{\mathrm{d}h(c)}{\mathrm{d}c} - \frac{p}{\rho^2} \frac{\mathrm{d}\rho}{\mathrm{d}c} - \eta \varepsilon \sigma(T) \frac{1}{\rho} \frac{\mathrm{d}}{\mathrm{d}\zeta} (\rho \frac{\mathrm{d}c}{\mathrm{d}\zeta}) \right) = 0. \quad (5.170)$$

where we note the following boundary conditions

$$h(c) = h(c_\pm) \text{ and } \frac{\mathrm{d}h}{\mathrm{d}c} = h'(c_\pm) \text{ for } c \to \pm\delta. \quad (5.171)$$

Note that in section 5.6.4, Eq.(5.160) is also expressed in the form of local coordinate ζ, we then substitute it into Eq.(5.170) to eliminate the pressure term $-(p/\rho^2)\partial p/\partial c$, so that

$$0 \quad = \frac{\partial^2}{\partial \zeta^2} \left(\frac{\eta}{\varepsilon} \sigma(T) \frac{\mathrm{d}h}{\mathrm{d}c} - \frac{p_-}{\rho^2} \frac{\mathrm{d}\rho}{\mathrm{d}c} - \eta \varepsilon \sigma(T) \frac{\mathrm{d}^2 c}{\mathrm{d}\zeta^2} \right). \quad (5.172)$$

Having in mind the definition of variable density for quasi-incompressible fluid $\rho(c)$ (5.10), we see that the second term $-(p_-/\rho^2)\partial p/\partial c$ in (5.172) is constant, and Eq.(5.172)

can be further simplified as

$$\frac{\partial^2}{\partial\zeta^2}\left(\frac{\eta}{\varepsilon}\sigma(T)\frac{\mathrm{d}h}{\mathrm{d}c}-\eta\varepsilon\sigma(T)\frac{\mathrm{d}^2c}{\mathrm{d}\zeta^2}\right)=0. \tag{5.173}$$

Using the conditions (5.159) and (5.171), we integrate (5.173) twice to obtain

$$0=\frac{\eta}{\varepsilon}\sigma(T)\frac{\mathrm{d}h(c)}{\mathrm{d}c}-\eta\varepsilon\sigma(T)\frac{\mathrm{d}^2c}{\mathrm{d}\zeta^2}-\frac{\eta}{\varepsilon}\sigma(T)h'(c_-), \tag{5.174}$$

or

$$0=\frac{\eta}{\varepsilon}\sigma(T)\frac{\mathrm{d}h(c)}{\mathrm{d}c}-\eta\varepsilon\sigma(T)\frac{\mathrm{d}^2c}{\mathrm{d}\zeta^2}-\frac{\eta}{\varepsilon}\sigma(T)h'(c_+). \tag{5.175}$$

Again, we assume that the temperature T is independent of local coordinate ζ and drop the coefficient $\sigma(T)$ to obtain

$$0=\frac{\eta}{\varepsilon}\frac{\mathrm{d}h(c)}{\mathrm{d}c}-\eta\varepsilon\frac{\mathrm{d}^2c}{\mathrm{d}\zeta^2}-\frac{\eta}{\varepsilon}h'(c_-), \tag{5.176}$$

or

$$0=\frac{\eta}{\varepsilon}\frac{\mathrm{d}h(c)}{\mathrm{d}c}-\eta\varepsilon\frac{\mathrm{d}^2c}{\mathrm{d}\zeta^2}-\frac{\eta}{\varepsilon}h'(c_+). \tag{5.177}$$

Subtracting Eq.(5.176) from Eq.(5.177), we then obtain the boundary conditions for the free energy at the interface

$$h'(c_+)=h'(c_-). \tag{5.178}$$

Again, multiplying Eq.(5.176) by $\partial c/\partial\zeta$ and integrating from $-\delta$ to δ, we have

$$0=\frac{\eta}{\varepsilon}\Big(h(c_+)-h(c_-)\Big)-\frac{\eta}{\varepsilon}h'(c_-)(c_+-c_-), \tag{5.179}$$

where we note that (5.178) and (5.179) are the Gibbs equilibrium conditions for the free energy at the interface (e.g. [39]). In the next subsection, we will use the concept of excess of interfacial free energy to identify the surface tension from our phase-field model, where the Gibbs equilibrium conditions (5.178), (5.179) are used.

5.6.6 Excess of interfacial free energy

In a multiphase fluid system, the surface tension is identical to the surface energy density. As the interface possesses more energy compared to that of the bulk phases, this surface energy can be determined as the excess energy at the surface compared to the corresponding bulk phases [47, 41, 103]. For the phase-field model, as the interfacial region has finite thickness, in which the different phases are mixed, a definition of interface is needed in order to determine the excess energy. For this purpose, the Gibbs dividing surface [47] is typically adopted for the phase-field model (e.g. [7, 87]), where the two phases are thought to be separated by an infinitesimal thin surface.

We begin by introducing the way to determine the exact location of the Gibbs dividing surface. In Gibbs model, the constituent mass of the two-phase fluid can be written as a sum of three components: one of bulk phase 1, one of bulk phase 2, and one of the interfacial region Γ, so that

$$M_i = M_i^1 + M_i^2 + M_i^\Gamma. \tag{5.180}$$

Here as the interface (Γ) is assumed to be ideally thin ($V_\Gamma = 0$) with zero mass, we may have

$$M_i^\Gamma = M_i - M_i^1 - M_i^2 = 0. \tag{5.181}$$

For our phase-field model, as the mass concentration of one fluid component is chosen as the phase variable, we rewrite the balance of constituent mass (5.181) in term of the phase variable

$$\int_{-\delta}^{\delta} \rho c \, \mathrm{d}\zeta - \int_{-\delta}^{\zeta_0} \rho_- c_- \, \mathrm{d}\zeta - \int_{\zeta_0}^{\delta} \rho_+ c_+ \, \mathrm{d}\zeta = 0, \tag{5.182}$$

where $\rho_\pm$ and $c_\pm$ represent the value of ρ and c that take in different bulk phases. The location of the dividing surface Γ is denoted by ζ_0 and can be determined through the above equation. In addition, for the phase variable c, we have two sets of values,

$$c_+ = 0,\ c_- = 1\ (c = c_1) \text{ as } \zeta \to \pm\delta, \tag{5.183}$$

$$c_+ = 1,\ c_- = 0\ (c = c_2) \text{ as } \zeta \to \pm\delta. \tag{5.184}$$

Using Eqs.(5.183) (5.183), Eq.(5.182) can be further written as

$$\int_{-\delta}^{\zeta_0} \Big(\rho - \rho_-\Big) \mathrm{d}\zeta + \int_{\zeta_0}^{\delta} \Big(\rho - \rho_+\Big) \mathrm{d}\zeta = 0, \tag{5.185}$$

where we have used the condition $c_1 + c_2 = 1$. Eq.(5.185) stands for the mass balance of the mixture with the Gibbs dividing surface, which will be used for the derivation later.

With the location of the dividing surface, we now identify the surface tension with respect to the concept of excess of interfacial free energy. Anderson et. al. [7] presented a phase-field model to study a single compressible fluid at different phases, where, at equilibrium, the Helmholtz free energy was used to determine the excess of interfacial free energy. Similarly, Lowengrub and Truskinovsky [87] used the Helmholtz free energy to determine the excess of interfacial free energy and thus to identify the surface tension of quasi-incompressible phase-field model for two-phase flow at equilibrium. Following these works, we use the relation (5.28) and (5.96) to define a Helmholtz

free energy for our phase-field model of quasi-incompressible fluid. Having in mind the Gibbs free energy (5.127), we have

$$\hat{f} = \hat{g} - \frac{p}{\rho} = \Big(u_0 - c_{hc}T_0\Big)(1 - \frac{T}{T_0}) - c_{hc}T\ln(\frac{T}{T_0}) + \frac{\eta}{\varepsilon}\sigma_f(T)h(c) + \varepsilon\eta\sigma_f(T)\frac{1}{2}|\nabla c|^2, \tag{5.186}$$

where we see that the free energy $\hat{f}$ is temperature dependent as the non-isothermal case is considered here. In the isothermal case, (say $T = T_0$), our free energy (5.186) reduces to the classical Cahn-Hilliard free energy (e.g. [28, 87]):

$$\hat{f} = \frac{\eta\sigma}{\varepsilon}h(c) + \eta\sigma\varepsilon\frac{|\nabla c|^2}{2}. \tag{5.187}$$

In what follows, we use the free energy (5.186) and the dividing surface Γ to determine the excess free energy. Let E_{exs} be the excess of interfacial free energy per unit area, then

$$\begin{aligned} E_{exs} &= \int_{-\delta}^{+\delta} \rho\hat{f}\,\mathrm{d}\delta - \int_{-\delta}^{\zeta_0} \rho_-\hat{f}_-\,\mathrm{d}\delta - \int_{\zeta_0}^{+\delta} \rho_+\hat{f}_+\,\mathrm{d}\delta \\ &\sim \sigma(T)\int_{-\delta}^{+\delta}\frac{1}{2}\eta\varepsilon\rho(c)(\frac{\mathrm{d}c}{\mathrm{d}\zeta})^2\mathrm{d}\zeta + \sigma(T)\int_{-\delta}^{\zeta_0}\frac{\eta}{\varepsilon}\Big(\rho(c)h(c) - \rho_-h(c_-)\Big)\mathrm{d}\zeta \\ &\quad + \sigma(T)\int_{\zeta_0}^{\delta}\frac{\eta}{\varepsilon}\Big(\rho(c)h(c) - \rho_+h(c_+)\Big)\mathrm{d}\zeta, \end{aligned} \tag{5.188}$$

where $\hat{f}_\pm$ are the values of the Gibbs free energy that take in the bulk phases corresponding to $c_\pm$. Note that, in the limit of $\varepsilon \ll \delta \ll L$ (or δ is sufficiently small), we assume that the variations of the temperature T along the direction normal to the interface are small and thus independent of the local coordinate ζ. Then the first two terms associated with the temperature in (5.186) are constant and can be eliminated. For the derivations later, we first multiply Eq.(5.176) by $\partial c/\partial\zeta$ and integrate from δ

to a position ζ to obtain

$$\frac{1}{2}\eta\varepsilon(\frac{dc}{\mathrm{d}\zeta})^2 = \frac{\eta}{\varepsilon}\Big(h(c)-h(c_-)\Big) - \frac{\eta}{\varepsilon}h'(c_-)(c-c_-), \tag{5.189}$$

where the condition (5.159) is used. We then rewrite Eq.(5.188) in the form

$$\begin{aligned} E_{exs} = {} & \sigma(T)\int_{-\delta}^{+\delta}\eta\varepsilon\rho(c)(\frac{\mathrm{d}c}{\mathrm{d}\zeta})^2\mathrm{d}\zeta \\ & + \sigma(T)\int_{-\delta}^{\zeta_0}\frac{\eta}{\varepsilon}\left(\rho(c)\Big(h(c_-)-h'(c_-)c_-\Big) - \rho_-\Big(h(c_-)-h'(c_-)c_-\Big)\right)\mathrm{d}\zeta \\ & + \sigma(T)\int_{\zeta_0}^{\delta}\frac{\eta}{\varepsilon}\left(\rho(c)\Big(h(c_-)-h'(c_-)c_-\Big) - \rho_+\Big(h(c_+)-h'(c_-)c_+\Big)\right)\mathrm{d}\zeta, \end{aligned} \tag{5.190}$$

where we have used the balance of constituent mass (5.182). Using the condition (5.179) and mass balance equation (5.185), we finally obtain the expression for the excess of interfacial free energy

$$E_{exs} = \sigma(T)\int_{-\delta}^{+\delta}\eta\varepsilon\rho(c)(\frac{\mathrm{d}c}{\mathrm{d}\zeta})^2\mathrm{d}\zeta = \tilde{\sigma}(T), \tag{5.191}$$

where we identify that the term $\tilde{\sigma}(T)$ in the jump condition for momentum balance (5.167) is identical to the excess of interfacial free energy, and thus stands for the surface tension of our phase-field model. In addition, if we use the specification for the double-well free energy (5.129) and substitute Eq.(5.189) into the excess of interfacial free energy (5.191), we have

$$E_{exs} = \sigma(T)\int_{-\delta}^{+\delta}\left(\frac{1}{2}\eta\varepsilon\rho(c)(\frac{\mathrm{d}c}{\mathrm{d}\zeta})^2 + \frac{\eta}{\varepsilon}\rho(c)h(c)\right)\mathrm{d}\zeta = \tilde{\sigma}(T), \tag{5.192}$$

which reveals that in the free energy (5.186), both the gradient energy $\lambda_f(T)|\nabla c|^2/2$ and the double well free energy $\gamma_f(T)h(c)$ contribute equally to the surface energy

at equilibrium. This agrees with the results obtained by Lowengrub & Truskinovsky [87], and Liu & Shen[85], where the phase-field model for a quasi-incompressible fluid (variable density case) and binary incompressible fluid (density matched case) were studied in the sharp-interface limit, respectively.

With the help of the location of the dividing surface and the excess of interfacial free energy, we can further relate the surface tension of the our phase-field model $\tilde{\sigma}(T)$ (identified in Eq.(5.191)) to that of the sharp-interface model $\sigma(T)$ (defined in Eq.(5.132)) by letting

$$\tilde{\sigma}(T) = \sigma(T) \int_{-\delta}^{+\delta} \eta \varepsilon \rho(c) (\frac{\mathrm{d}c}{\mathrm{d}\zeta})^2 \mathrm{d}\zeta = \sigma(T). \tag{5.193}$$

The value of the ratio parameter η can then be determined through the following equation

$$\eta = \frac{1}{\int_{-\delta}^{+\delta} \varepsilon \rho(c) (\frac{\mathrm{d}c}{\mathrm{d}\zeta})^2 \mathrm{d}\zeta}. \tag{5.194}$$

It has been argued by [29] that in the limit of gently curved interface, and when the motion of the interface is slow, the phase variable c can be approximated by its 1D stationary solution c_0 along the direction normal to the interface. For simplicity, we now assume that the local coordinate ζ coincide with the y direction, and the position of the dividing surface is $y_0 = 0$. In the 1D case, we have the following stationary solution c_0 near the interfacial region,

$$c_0(y) = \frac{1}{2} + \frac{1}{2} \tanh\Big(\frac{y}{2\sqrt{2}\varepsilon}\Big), \text{ for } y \in [-\delta, \delta], \tag{5.195}$$

which is shown in Figure 5.2. Here $y = \delta$ and $y = -\delta$ are the positions of the top and bottom surface of the pillbox separately. In the limit $\varepsilon \ll \delta \ll L$, we note the

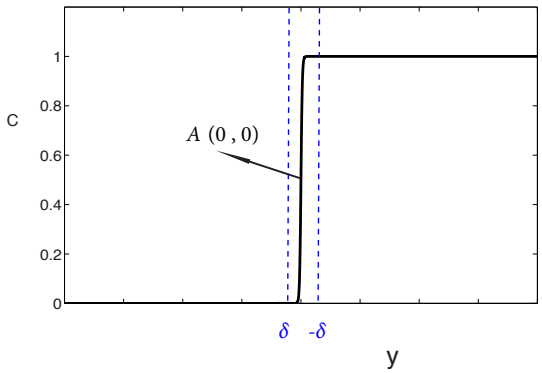

Figure 5.2: The stationary solution c_0 (black solid line) for the phase-field. A is a point on the dividing surface Γ, δ and $-\delta$ are positions of the top and bottom surfaces of the pillbox (blue dotted line).

conditions

$$c = 0 \text{ for } y = \delta, \text{ and } c = 1 \text{ for } y = -\delta. \tag{5.196}$$

Substituting Eq.(5.195) and the variable density (5.10) into (5.194) we obtain

$$\eta = \frac{2\sqrt{2}(\rho_2 - \rho_1)^3}{\rho_1\rho_2\left[\rho_2^2 - \rho_1^2 - 2\rho_1\rho_2 \ln(\frac{\rho_2}{\rho_1})\right]}, \tag{5.197}$$

where the condition (5.196) is used. Note that for the density matched case ($\rho_1 = \rho_2$), Eq.(5.194) leads to a simpler expression for η, which is

$$\eta = 6\sqrt{2}. \tag{5.198}$$

This agrees with the result obtained by [103], [130] and [4]. In next section, we will compute some examples using our phase-field model for quasi-incompressible fluids (5.114)-(5.119). As both examples are computed under the density matched case, we use Eq.(5.198) for the computations. The numerical results will be compared to the analytical solutions that derived for the sharp-interface model to validate this value of η and further to validate our model.

5.6.7 Jump condition for energy balance

To derive the jump condition for the energy balance at the interface, we first substitute the terms E, $\mathbf{m}$, $\mathbf{q}_E$ and $\mathbf{q}_E^{nc}$ ((5.17), (5.110), (5.111) and (5.113)) into the energy balance equation (5.33). In the integral form, we obtain

$$\int_S \Bigg(\rho\hat{u}(\mathbf{v}-\mathbf{v}_I) + \rho\frac{1}{2}|\mathbf{v}|^2(\mathbf{v}-\mathbf{v}_I) - \Big(-p\mathbf{I} - \lambda_f(T)\rho\mathbf{T} + \mu(\nabla\mathbf{v}+\nabla\mathbf{v}^T) \\ -\frac{2}{3}\mu(\nabla\cdot\mathbf{v})\mathbf{I}\Big)\cdot\mathbf{v} - \lambda_u(\rho\nabla c\frac{\mathrm{D}c}{\mathrm{D}t}) - k\nabla T - m_C\mu_C\nabla\mu_C \Bigg)\cdot\mathbf{n}_I \mathrm{d}S = 0, \quad (5.199)$$

where we have used the identities

$$\rho\frac{\mathrm{D}\hat{u}}{\mathrm{D}t} = \frac{\partial(\rho\hat{u})}{\partial t} + \nabla\cdot(\rho\hat{u}\mathbf{v}), \quad (5.200)$$

$$\rho\frac{\mathrm{D}}{\mathrm{D}t}\frac{1}{2}|\mathbf{v}|^2 = \frac{\partial}{\partial t}(\rho\frac{1}{2}|\mathbf{v}|^2) + \nabla\cdot(\rho\frac{1}{2}|\mathbf{v}|^2\mathbf{v}), \quad (5.201)$$

and the following properties which are similar to (5.145) and (5.146),

$$\int_V \frac{\partial(\rho\hat{u})}{\partial t}\mathrm{d}V \sim -\int_S \rho\hat{u}\mathbf{v}_I\cdot\hat{\mathbf{n}}\mathrm{d}S, \quad (5.202)$$

$$\int_V \frac{\partial}{\partial t}(\rho\frac{1}{2}|\mathbf{v}|^2)\mathrm{d}V \sim -\int_S \rho\frac{1}{2}|\mathbf{v}|^2\mathbf{v}_I\cdot\hat{\mathbf{n}}\mathrm{d}S. \quad (5.203)$$

We then break up the above integral into pieces for the top, bottom and sides of the pillbox to obtain

$$\int_{S_{top}} \Bigg(\rho\hat{u}(\mathbf{v}-\mathbf{v}_I) + \rho\frac{1}{2}|\mathbf{v}|^2(\mathbf{v}-\mathbf{v}_I) - \Big(-p\mathbf{I} - \lambda_f(T)\rho\mathbf{T} + \mu(\nabla\mathbf{v}+\nabla\mathbf{v}^T) \\ -\frac{2}{3}\mu(\nabla\cdot\mathbf{v})\mathbf{I}\Big)\cdot\mathbf{v} - \lambda_u(\rho\nabla c\frac{\mathrm{D}c}{\mathrm{D}t}) - k\nabla T - m_C\mu_C\nabla\mu_C \Bigg)\cdot\hat{\mathbf{n}}_T\mathrm{d}S \\ + \int_{S_{bot}} \Bigg(\rho\hat{u}(\mathbf{v}-\mathbf{v}_I) + \rho\frac{1}{2}|\mathbf{v}|^2(\mathbf{v}-\mathbf{v}_I) - \Big(-p\mathbf{I} - \lambda_f(T)\rho\mathbf{T} + \mu(\nabla\mathbf{v}+\nabla\mathbf{v}^T) \quad (5.204)$$

$$-\frac{2}{3}\mu(\nabla\cdot\mathbf{v})\mathbf{I}\Big)\cdot\mathbf{v}-\lambda_u(\rho\nabla c\frac{\mathrm{D}c}{\mathrm{D}t})-k\nabla T-m_C\mu_C\nabla\mu_C\Bigg)\cdot\hat{\mathbf{n}}_B\mathrm{d}S$$
$$+\oint_C\int_{-\delta}^{\delta}\Bigg(\rho\hat{u}(\mathbf{v}-\mathbf{v}_I)+\rho\frac{1}{2}|\mathbf{v}|^2(\mathbf{v}-\mathbf{v}_I)-\Big(-p\mathbf{I}-\lambda_f(T)\rho\mathbf{T}+\mu(\nabla\mathbf{v}+\nabla\mathbf{v}^T)$$
$$-\frac{2}{3}\mu(\nabla\cdot\mathbf{v})\mathbf{I}\Big)\cdot\mathbf{v}-\lambda_u(\rho\nabla c\frac{\mathrm{D}c}{\mathrm{D}t})-k\nabla T-m_C\mu_C\nabla\mu_C\Bigg)\cdot\hat{\mathbf{n}}_S\mathrm{d}\zeta\mathrm{d}l=0, \qquad (5.205)$$

where we assume that the heat capacity c_{hc} is a constant. In the limit $\varepsilon\ll\delta\ll L$, the non-classical terms of the internal energy $\hat{u}$, $\mathbf{T}$, $\lambda_u(\rho\nabla c\frac{\mathrm{D}c}{\mathrm{D}t})$ and $m_C\mu_C\nabla\mu_C$ do not contribute to the top and the bottom surface integrals. So that the terms $\Big(\rho\hat{u}(\mathbf{v}-\mathbf{v}_I)+\rho\frac{1}{2}|\mathbf{v}|^2(\mathbf{v}-\mathbf{v}_I)+\mu(\nabla\mathbf{v}+\nabla\mathbf{v}^T)\cdot\mathbf{v}-\frac{2}{3}\mu(\nabla\cdot\mathbf{v})\mathbf{I}\cdot\mathbf{v}\Big)\cdot\hat{\mathbf{n}}_S$ are bounded and do not contribute to the side integral. Moreover, the non-classical terms $\lambda_f(T)\rho\mathbf{T}$, $\lambda_u(\rho\nabla c\frac{\mathrm{D}c}{\mathrm{D}t})$ and $m_C\mu_C\nabla\mu_C$ do not contribute to the side integral, $k\nabla T$ is bounded and does not contribute to the side integral. Eq.(5.205) then reduces to

$$\int_\Gamma\Bigg(\Big[\rho_i c_{hc}T(\mathbf{v}-\mathbf{v}_I)\Big]+\Big[\rho_i\frac{1}{2}|\mathbf{v}|^2(\mathbf{v}-\mathbf{v}_I)\Big]+\Big[p\mathbf{I}\cdot\mathbf{v}\Big]-\Big[\mu(\nabla\mathbf{v}+\nabla\mathbf{v}^T)\cdot\mathbf{v}\Big]$$
$$-\Big[k_i\nabla T\Big]\Bigg)\cdot\hat{\mathbf{n}}_I\mathrm{d}S+\oint_C\Bigg(\int_{-\delta}^{\delta}p\mathrm{d}\zeta\Bigg)\mathbf{v}_I\cdot\hat{\mathbf{m}}_I\mathrm{d}l=0, \qquad (5.206)$$

where in the last term of Eq.(5.206), we argue that the interface velocity $\mathbf{v}_I$ is independent of the local coordinate ζ and thus can be taken out of the integral in the normal direction. By using Eqs.(5.161) and (5.162), we obtain

$$\int_\Gamma\Bigg(\Big[\rho_i c_{hc}T(\mathbf{v}-\mathbf{v}_I)\Big]+\Big[\rho_i\frac{1}{2}|\mathbf{v}|^2(\mathbf{v}-\mathbf{v}_I)\Big]+\Big[p\mathbf{I}\cdot\mathbf{v}\Big]-\Big[\mu(\nabla\mathbf{v}+\nabla\mathbf{v}^T)\cdot\mathbf{v}\Big]$$
$$-\Big[k_i\nabla T\Big]\Bigg)\cdot\hat{\mathbf{n}}_I\mathrm{d}S+\oint_C\int_{-\delta}^{\delta}\tilde{\sigma}\mathbf{v}_I\cdot\hat{\mathbf{m}}_I\mathrm{d}\zeta\mathrm{d}l=0. \qquad (5.207)$$

The surface divergence theorem gives

$$\int_\Gamma \Bigg(\Big[\rho_i c_{hc} T(\mathbf{v}-\mathbf{v}_I)\Big] + \Big[\rho_i \frac{1}{2}|\mathbf{v}|^2(\mathbf{v}-\mathbf{v}_I)\Big] + \Big[p\mathbf{I}\cdot\mathbf{v}\Big] - \Big[\mu_i(\nabla\mathbf{v}+\nabla\mathbf{v}^T)\cdot\mathbf{v}\Big] - \Big[k_i\nabla T\Big]\Bigg)\cdot\hat{\mathbf{n}}_I \mathrm{d}S - \int_\Gamma \nabla_s\cdot(\tilde{\sigma}\mathbf{v}_I)\mathrm{d}S - \int_\Gamma \kappa\tilde{\sigma}\hat{\mathbf{n}}_I\cdot\mathbf{v}_I \mathrm{d}S = 0, \tag{5.208}$$

where the condition (5.141) is used. As the surface is arbitrary, we obtain the energy balance jump condition at the interface

$$\Big[k_i\nabla T\Big]\cdot\hat{\mathbf{n}}_I = \Bigg(\Big[\rho c_{hc} T(\mathbf{v}-\mathbf{v}_I)\Big] + \Big[\rho_i \frac{1}{2}|\mathbf{v}|^2(\mathbf{v}-\mathbf{v}_I)\Big] + \Big[p\mathbf{I}\cdot\mathbf{v}\Big] - \Big[\mu_i(\nabla\mathbf{v}+\nabla\mathbf{v}^T)\cdot\mathbf{v}\Big]\Bigg)\cdot\hat{\mathbf{n}}_I - \nabla_s\cdot(\tilde{\sigma}\mathbf{v}_I) - \kappa\tilde{\sigma}\hat{\mathbf{n}}_I\cdot\mathbf{v}_I, \tag{5.209}$$

where the energy spent by the interface deformation and the effects of the interface curvature are taken into account in our jump condition for energy balance at the interface. Eq.(5.209) agrees with the result obtained in by [11], where the energy balance condition is derived by using a pillbox for sharp interface model. Again if we assume that there is no phase change across the interface, Eq.(5.209) then reduces to

$$\Big[k_i\nabla T\Big]\cdot\hat{\mathbf{n}}_I = \Bigg(\Big[p\mathbf{I}\cdot\mathbf{v}\Big] - \Big[\mu_i(\nabla\mathbf{v}+\nabla\mathbf{v}^T)\cdot\mathbf{v}\Big]\Bigg)\cdot\hat{\mathbf{n}}_I - \nabla_s\cdot(\tilde{\sigma}\mathbf{v}_I) - \kappa\tilde{\sigma}\hat{\mathbf{n}}_I\cdot\mathbf{v}_I. \tag{5.210}$$

If we further ignore the energy spent by the interface deformation and the effects of interface curvature, we can obtain the classical jump condition for the energy equation,

$$\Big[k\nabla T\Big]\cdot\hat{\mathbf{n}}_I = 0, \tag{5.211}$$

which is widely used for the computations of sharp-interface model (e.g. [115]).

5.7 Computational methods and results

In this section, we investigate numerically our phase-field model through three examples. One is the thermocapillary convection in a micro-channel with two-layer superimposed fluid, and the second (third) one is the thermocapillary migration of a drop with zero (finite) Marangoni number. All examples will be computed by using continuous finite element methods. The numerical results of the first and second examples will be compared to the existing analytical solutions and theoretical predictions.

5.7.1 Simplified model and the weak form

For the sake of simplicity, we assume that the densities of the two fluids are matched. The system equations (5.114)-(5.119) can then be simplified in the form

$$\nabla \cdot \mathbf{v} = 0, \tag{5.212}$$

$$\frac{\mathrm{D}\mathbf{v}}{\mathrm{D}t} = -\nabla p - \nabla \cdot \Big[\lambda_f(T)(\nabla c \otimes \nabla c)\Big] + \nabla \cdot (\mu \nabla \mathbf{v}), \tag{5.213}$$

$$\begin{aligned}\frac{\mathrm{D}\hat{u}}{\mathrm{D}t} &= \lambda_u \nabla \cdot (\nabla c \frac{\mathrm{D}c}{\mathrm{D}t}) + \Big(- p\mathbf{I} - \lambda_f(T)(\nabla c \otimes \nabla c) + \mu \nabla \mathbf{v}\Big) : \nabla \mathbf{v} \\ &\quad + \nabla \cdot (k \nabla T + m_C \mu_C \nabla \mu_C),\end{aligned} \tag{5.214}$$

$$\frac{\mathrm{D}c}{\mathrm{D}t} = m_C \Delta \mu_C, \tag{5.215}$$

$$\mu_C = \gamma_f(T)\frac{\mathrm{d}h(c)}{\mathrm{d}c} - \lambda_f(T)\Delta c, \tag{5.216}$$

where the variable thermal conductivity (5.63) is employed. Here we have rewritten the energy balance equation (5.116) by using Eq.(5.43) and the definition of $\hat{u}$ (5.131). Note that the reason we need to rewrite energy equation is that in the weak formulation of Eq.(5.116), the second order derivative is involved implying that more complicated C^1 finite elements are needed. However in the weak formulation (5.219) below we find that only first order derivatives of c are involved, so that the C^0 finite element method

can be used for our computations. The benefits of using C^0 elements are obvious, that the method can be implemented easily and many existing codes can be incorporated to reduce various complications. Note that Eqs.(5.212)-(5.214) of the system will be computed for the example of thermocapillary convection, Eqs.(5.212)-(5.216) will be computed for the example of thermocapillary migration with zero Marangoni number, and the non-dimensional system equations (5.136)-(5.140) will be computed for the example of thermocapillary migration with finite Marangoni number. For simplicity, we only present the numerical scheme for dimensional system equations (5.212)-(5.216). The numerical method for the non-dimensional system (5.136)-(5.140) can be obtained correspondingly. By multiplying the system (5.212)-(5.216) with the test functions q, $\mathbf{u}$, χ, ϕ and ψ respectively and using integration by parts, the weak form can be derived straightforwardly (where $\mathbf{v}$, p, $\hat{u}$, c, μ and test functions $\mathbf{u}$, q, χ, ϕ and ψ are in appropriate spaces),

$$\int_\Omega \left(\nabla \cdot \mathbf{v} q \right) \mathrm{d}\mathbf{x} = 0, \tag{5.217}$$

$$\int_\Omega \left(\mathbf{v}_t \cdot \mathbf{u} + (\mathbf{v} \cdot \nabla)\mathbf{v} \cdot \mathbf{u} - p\nabla \cdot \mathbf{u} - \lambda_f(T)(\nabla c \otimes \nabla c) : \nabla \mathbf{u} + \mu \nabla \mathbf{v} : \nabla \mathbf{u} \right) \mathrm{d}\mathbf{x} = 0, \tag{5.218}$$

$$\int_\Omega \left(\hat{u}_t \chi + (\mathbf{v} \cdot \nabla)\hat{u}\chi + \lambda_u \frac{\mathrm{D}c}{\mathrm{D}t} \nabla c \cdot \nabla \chi + \lambda_f(T)(\nabla c \otimes \nabla c) : \nabla \mathbf{v}\chi + p\mathbf{I} : \nabla \mathbf{v}\chi \right.$$

$$\left. -\mu \nabla \mathbf{v} : \nabla \mathbf{v}\chi + k\nabla T \cdot \nabla \chi + + m_C \mu_C \nabla \mu_C \cdot \nabla \chi \right) \mathrm{d}\mathbf{x} = 0, \tag{5.219}$$

$$\int_\Omega \left(c_t \phi + (\mathbf{v} \cdot \nabla) c\phi + m_C \nabla \mu_C \cdot \nabla \phi \right) \mathrm{d}\mathbf{x} = 0, \tag{5.220}$$

$$\int_\Omega \left(\mu_C \psi - \gamma_f(T) \frac{\mathrm{d}h(c)}{\mathrm{d}c} \psi - \nabla \lambda_f(T) \cdot \nabla c \psi - \lambda_f(T) \nabla c \cdot \nabla \psi \right) \mathrm{d}\mathbf{x} = 0. \tag{5.221}$$

5.7.2 Temporal schemes and implement issue

The solution of the weak form (5.217)-(5.221) is approximated by a finite difference scheme in time and a conformal C^0 finite element method in space. To ensure the stability of our numerical method, we adopt the fully implicit backward Euler scheme to compute the problem.

We let $\Delta t > 0$ represent a time step size, and $(\mathbf{v}_h^n, p_h^n, \hat{u}_h^n, c_h^n, \mu_{C_h}^n)$ (in a finite dimensional space given by a finite element discretization of the computational domain Ω) is an approximation of $(\mathbf{v}, p, \hat{u}, c, \mu)$ at time $t^n = n\Delta t$, where $\mathbf{v}_h^n = \mathbf{v}(n\Delta t)$, $p_h^n = p(n\Delta t)$, $\hat{u}_h^n = \hat{u}(n\Delta t)$, $c_h^n = c(n\Delta t)$ and $\mu_{C_h}^n = \mu_C(n\Delta t)$. Then the approximation at time t^{n+1} is denoted as $(\mathbf{v}_h^{n+1}, p_h^{n+1}, \hat{u}_h^{n+1}, c_h^{n+1}, \mu_{C_h}^{n+1})$ and computed by the following finite element scheme

$$\int_\Omega \left(\nabla \cdot \mathbf{v}_h^{n+1} q + \delta p_h^{n+1} q \right) \mathrm{d}\mathbf{x} = 0, \tag{5.222}$$

$$\int_\Omega \Bigg(\mathbf{v}_{\bar{t}}^{n+1} \cdot \mathbf{u} + (\mathbf{v}_h^{n+1} \cdot \nabla)\mathbf{v}_h^{n+1} \cdot \mathbf{u} - p_h^{n+1} \nabla \cdot \mathbf{u} - \lambda_f(T_h^{n+1})(\nabla c_h^{n+1} \otimes \nabla c_h^{n+1}) : \nabla \mathbf{u} + \mu \nabla \mathbf{v}_h^{n+1} : \nabla \mathbf{u} \Bigg) \mathrm{d}\mathbf{x} = 0, \tag{5.223}$$

$$\int_\Omega \Bigg(\hat{u}_{\bar{t}}^{n+1} \chi + (\mathbf{v}_h^{n+1} \cdot \nabla)\hat{u}_h^{n+1} \chi + \lambda_u (c_{\bar{t}}^{n+1} + (\mathbf{v}_h^{n+1} \cdot \nabla) c_h^{n+1}) \nabla c_h^{n+1} \cdot \nabla \chi + \lambda_f(T_h^{n+1})(\nabla c_h^{n+1} \otimes \nabla c_h^{n+1}) : \nabla \mathbf{v}_h^{n+1} \chi - \mu \nabla \mathbf{v}_h^{n+1} : \nabla \mathbf{v}_h^{n+1} \chi + k \nabla T_h^{n+1} \cdot \nabla \chi + m_C \mu_{C_h}^{n+1} \nabla \mu_{C_h}^{n+1} \cdot \nabla \chi \Bigg) \mathrm{d}\mathbf{x} = 0, \tag{5.224}$$

$$\int_\Omega \left(c_{\bar{t}}^{n+1} \phi + (\mathbf{v}_h^{n+1} \cdot \nabla) c_h^{n+1} \phi + m_C \nabla \mu_{C_h}^{n+1} \cdot \nabla \phi \right) \mathrm{d}\mathbf{x} = 0, \tag{5.225}$$

$$\int_\Omega \Bigg(\mu_{C_h}^{n+1} \psi - \gamma_f(T_h^{n+1}) h'(c_h^{n+1}) \psi - \nabla \lambda_f(T_h^{n+1}) \cdot \nabla c_h^{n+1} \psi - \lambda_f(T_h^{n+1}) \nabla c_h^{n+1} \cdot \nabla \psi \Bigg) \mathrm{d}\mathbf{x} = 0, \tag{5.226}$$

where $\mathbf{v}_{\bar{t}}^{n+1} = (\mathbf{v}_h^{n+1} - \mathbf{v}_h^n)/\Delta t$, $\hat{u}_{\bar{t}}^{n+1} = (\hat{u}_h^{n+1} - \hat{u}_h^n)/\Delta t$ and $c_{\bar{t}}^{n+1} = (c_h^{n+1} - c_h^n)/\Delta t$. Note that the divergence free equation needs to be treated carefully in incompressible flow computations. Here we rewrite Eq.(5.222) in the penalty formulation, where δ is a relatively small parameter and is set to be $\delta = 10^{-6}$ for all the computations. Note that for every time step, T^{n+1} can be obtained by using Eq.(5.131), such that

$$c_{hc}T^{n+1} = \hat{u}^{n+1} - \gamma_u h(c^{n+1}) - \lambda_u \frac{1}{2}|\nabla c^{n+1}|^2. \tag{5.227}$$

Since the scheme is nonlinearly implicit we need to linearize the system and then solve a linear system iteratively at each time step. We follow the numerical methods designed in [65], where the linear system is symmetric and does not depend on time. Therefore, we only need to calculate the Cholesky factorization for the symmetric linear system at the initial time step. After the initial time we do not need to factorize the linear system again since the coefficient matrix is independent of time.

For a phase-field model, it is sufficient to finely resolve only the transition layers, and a fixed grid represents a waste of computational resources. Therefore, efficient adapting mesh that resolves the thin layers near the interface is desirable. For the example of the thermocapillary convection, we design a mesh that has relatively high-resolution grids near the flat interface. For the example of the thermocapillary migration, as the interface moves as the drop rises, an adaptive mesh is designed, in which there is a smaller frame that moves with the drop. Within the frame, the resolution of grids is much higher than those outside the moving frame, so that the moving interface of the drop can be resolved purposely. Here, only the meshes for the example of thermocapillary migration are shown.

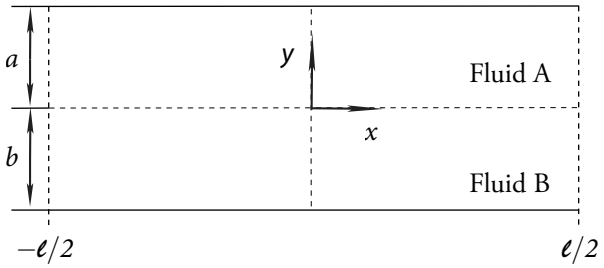

Figure 5.3: The schematic diagram showing two immiscible fluids in a microchannel. The temperatures of the lower and upper plates are $T^b(x,-b) = T_h + T_0 cos(kx)$ and $T^a(x,a) = T_c$, respectively, where $T_h > T_c > T_0$ and $k = 2\pi/l$ is the wave number, and a and b are the heights of the fluid A and B respectively.

5.7.3 Thermocapillary-driven Convection

We now investigate the thermocapillary-driven convection in a heated micro-channel with two-layer superimposed fluids with a planar interface [98]. Considering two-layer fluids (figure 5.3), where the heights of the fluid A (upper) and fluid B (lower) are a and b, respectively, and the fluids are of infinite extension in the horizontal direction. The physical properties of the fluids are their densities, viscosities and heat conductivities. The temperature variations in the present study are considered to be small enough so that the thermophysical properties of each fluid are assumed to remain constant, with the exception of surface tension. The temperature of the lower and upper plates are

$$T^b(x,-b) = T_h + T_0 \cos(\omega x) \text{ and } T^a(x,a) = T_c \tag{5.228}$$

respectively, where $T_h > T_c > T_0 > 0$, and $\omega = 2\pi/l$ is a wave number with l being the channel length. The above temperature boundary conditions establish a temperature field that is periodic in the horizontal direction with a period of l. Therefore, it is sufficient to only focus on the solution in one period, i.e.,$-l/2 < x < l/2$. In the limit of zero Marangoni number and small Reynolds number, it is possible to ignore the convective transport of momentum and energy. In addition, we assume that the

interface is to remain flat. By solving the simplified sharp-interface governing equations with the corresponding jump boundary conditions at the interface, Pendes *et al*, [98] obtained the analytical solutions for temperature field $\bar{T}(x,y)$ and stream-function $\bar{\psi}(x,y)$, where for the upper fluid

$$\bar{T}^A(x,y) = \frac{(T_c - T_h)y + \tilde{k}T_c b + T_h a}{a + \tilde{k}b} + T_0 f(\alpha,\beta,\tilde{k})\,\sinh(\alpha - \omega y)\,\cos(\omega x), \tag{5.229}$$

$$\bar{\psi}^A(x,y) = \frac{U_{max}}{\omega}\frac{1}{\sinh^2(\alpha) - \alpha^2}\Big\{\omega y\,\sinh^2(\alpha)\cosh(\omega y) - \frac{1}{2}\Big[2\alpha^2 + \omega y\Big(\sinh(2\alpha) - 2\alpha\Big)\Big]\sinh(\omega y)\Big\}\sin(\omega x), \tag{5.230}$$

and for the lower fluid

$$\bar{T}^B(x,y) = \frac{\tilde{k}(T_c - T_h)y + \tilde{k}T_c b + T_h a}{a + \tilde{k}b} + T_0 f(\alpha,\beta,\tilde{k})\,\Big[\sinh(\alpha)\cosh(\omega y) - \tilde{k}\sinh(\omega y)\cosh(\alpha)\Big]\,\cos(\omega x), \tag{5.231}$$

$$\bar{\psi}^B(x,y) = \frac{U_{max}}{\omega}\frac{1}{\sinh^2(\beta) - \beta^2}\Big\{\omega y\,\sinh^2(\beta)\cosh(\omega y) - \frac{1}{2}\Big[2\beta^2 - \omega y\Big(\sinh(2\beta) - 2\beta\Big)\Big]\sinh(\omega y)\Big\}\sin(\omega x). \tag{5.232}$$

In the above equations the unknowns are defined by $\tilde{k} = k_A/k_B$, $\alpha = a\omega$, $\beta = b\omega$, $f(\alpha,\beta,\tilde{k}) = 1/(\tilde{k}\sinh(\beta)\cosh\alpha + \sinh(\alpha)\cosh\beta)$, $g(\alpha,\beta,\tilde{k}) = \sinh(\alpha)f(\alpha,\beta,\tilde{k})$ and

$$U_{max} = -\left(\frac{T_0\sigma_T}{\mu_B}\right)g(\alpha,\beta,\tilde{k})h(\alpha,\beta,\tilde{\mu}),$$

$$h(\alpha,\beta,\tilde{\mu}) = \frac{\Big(\sinh^2(\alpha) - \alpha^2\Big)\Big(\sinh^2(\beta) - \beta^2\Big)}{\tilde{k}\Big(\sinh^2(\beta) - \beta^2\Big)\Big(\sinh(2\alpha) - 2\alpha\Big) + \Big(\sinh^2(\alpha) - \alpha^2\Big)\Big(\sinh(2\beta) - 2\beta\Big)}.$$

Based on their work, the simulations for our phase-field model are carried out in a 2D domain $[-l/2, l/2] \times [-b, a]$ with $l = 1.6 \times 10^{-4}$, and $a = b = 4 \times 10^{-5}$. As the

		$\varepsilon = 0.02$	$\varepsilon = 0.01$	$\varepsilon = 0.005$	$\varepsilon = 0.002$	$\varepsilon = 0.001$
k=0.1	$\frac{\|\|T-\bar{T}\|\|_{L^2}}{\|\|\bar{T}\|\|_{L^2}}$	5.445×10^{-3}	2.503×10^{-3}	1.189×10^{-3}	4.551×10^{-4}	2.200×10^{-4}
	$\frac{\|\|\psi-\bar{\psi}\|\|_{L^2}}{\|\|\bar{\psi}\|\|_{L^2}}$	4.309×10^{-2}	2.668×10^{-2}	1.614×10^{-2}	6.94×10^{-3}	6.44×10^{-3}
k=0.5	$\frac{\|\|T-\bar{T}\|\|_{L^2}}{\|\|\bar{T}\|\|_{L^2}}$	1.585×10^{-3}	5.748×10^{-4}	2.098×10^{-4}	5.167×10^{-5}	1.815×10^{-5}
	$\frac{\|\|\psi-\bar{\psi}\|\|_{L^2}}{\|\|\bar{\psi}\|\|_{L^2}}$	6.796×10^{-2}	2.208×10^{-2}	8.682×10^{-3}	3.688×10^{-3}	7.318×10^{-4}

Table 5.1: L^2 norm of the relative difference between the numerical results and the analytical solutions for section 6.3.

interface between the two fluids is assumed to be flat and rigid, the initial conditions for the phase-field is only depending on y, and can be given in the form

$$c(y) = \frac{1}{2} + \frac{1}{2}\tanh\Big(\frac{y}{2\sqrt{2}\varepsilon}\Big), \text{ for } y \in (-b, a), \tag{5.233}$$

where ε is related to the thickness of the diffuse interface. The periodic boundary conditions are applied on the left and right sides of the domain. On the top and bottom walls, the no-slip boundary conditions are imposed such that

$$\mathbf{u} = 0 \text{ for } y = a, -b. \tag{5.234}$$

Eq.(5.228) are used as the boundary conditions for temperature with $T_h = 20$, $T_c = 10$ and $T_0 = 4$. We let the ratio parameter $\eta = 6\sqrt{2}$ (Eq. (5.198)). Moreover, the fluid properties are set as $\mu_A = \mu_B = 0.2$, $k_B = 0.2$, $\sigma_0 = 2.5 \times 10^{-1}$, $\tilde{k} = k_A/k_B$ (thermal conductivity ratio) and $\sigma_T = -5 \times 10^{-3}$ (at $T_{ref} = T_c$).

To show the influences of the thermal conductivity ratio on the stream-function and temperature fields, the simulations are carried for two cases with different value of $\tilde{k}$, where $\tilde{k} = 0.1$ for case 1, and $\tilde{k} = 0.5$ for case 2. Here the variable thermal conductivity $k(c)$ (Eq. (5.63)) is employed, where we fixed $k_B(= 0.2)$, and change the value of k_A for the two cases. The contours of temperature fields and stream function for the

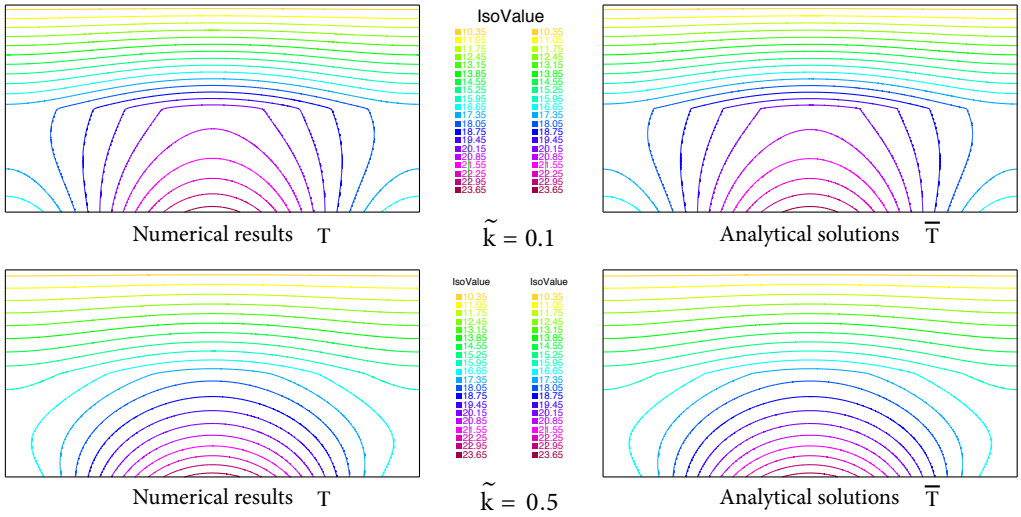

Figure 5.4: Isotherms of the numerical results and analytical solutions for the example of thermocapillary convection in a two-layer fluid system with the different thermal diffusivity ratios, $\tilde{k} = 1$ and $\tilde{k} = 0.2$.

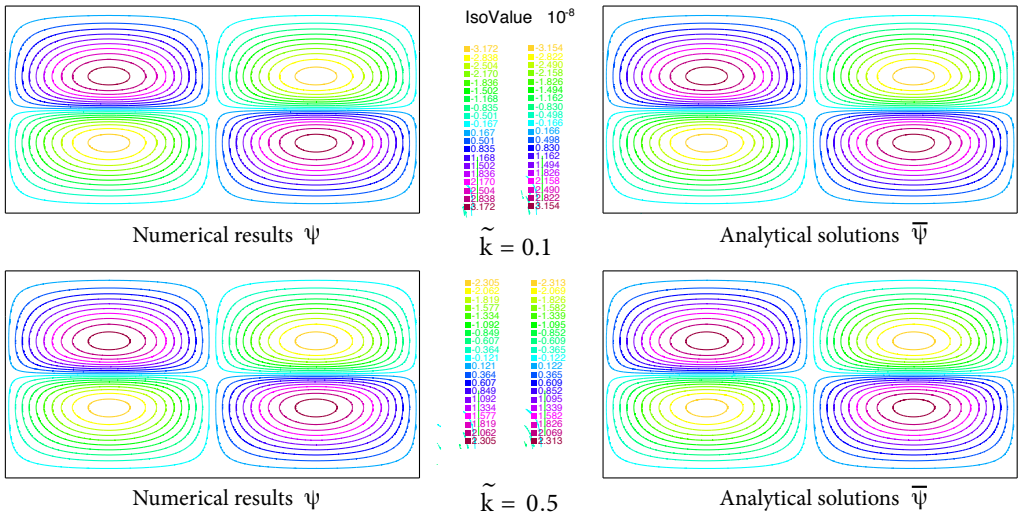

Figure 5.5: Streamlines of the numerical results and analytical solutions for the example of thermocapillary convection in two-layer fluid system with different thermal diffusivity ratios, $\tilde{k} = 1$ and $\tilde{k} = 0.2$. Positive (negative) values of the stream-function indicate the clockwise (the counterclockwise) circulation.

two cases at $\varepsilon = 0.002$ are shown in figure 5.4 and figure 5.5 respectively. It can be seen that our numerical results are in good agreement with the analytical solutions. In order to show that our phase-field model approaches to the sharp-interface model as the thickness of diffuse interface goes to zero, the computations are carried out by using four different values of $\varepsilon(= 0.02, 0.01, 0.005, 0.002)$. The L^2 norm of the relative difference between the numerical results and analytical solutions are shown in table 2. We can observe that as the value of ε decreases, the L^2 norm of relative difference decreases for both temperature field and stream functions. We also note that there are slight differences between our numerical results and the analytical predictions. The reason is two-fold. For one, and most importantly, the thickness of the interface of our model is finite, and the thermal diffusivity changes across it. The second reason is that the viscous heating term is considered in our energy balance equation (5.214). As can be observed from the isotherms in figure 5.4, the cosine like boundary condition for temperature leads to the non-uniform distributions of the temperature along the interface. This results in a shear force along the interface that is from the centre to both sides of the domain. The fluids are set to motion by this shear force and move from the middle toward both sides of the domain. It is then replaced by the fluid flowing downwards (upward) from the top (bottom) boundary. Also as the domain is periodic in the horizontal direction, the velocities of fluid that moves towards both sides decrease and the fluids are forced to move upward (downward) to the top (bottom) of the domain. This mechanism results in the formation of the circulation patterns that can be observed in the stream function fields (figure 5.5), where the fluid flow consists of four counter-rotating circulation that divide the domain into four parts. Moreover, in the context of the thermal conductivity ratio, we find that the decrease of the value of $\tilde{k}$ leads to a more non-uniform distribution of temperature along the interface, and thus strengthens the thermocapillary-driven convection. This agrees with the recent result obtained by Liu *et al*. [86], where the same thermocapillary convection in a two-layer

fluid system was investigated numerically by using a lattice Boltzmann phase-field method.

5.7.4 Thermocapillary migration in the limit of zero Marangoni number

The thermocapillary migration of a gas bubble was first examined experimentally by [129], who derived an analytical expression for the terminal velocity (also known as YGB velocity) of the drop in an infinite domain. In his study, both the Marangoni and Reynolds numbers are assumed to be infinitely small, such that the convective transport of momentum and energy are negligible. Instead, the terminal velocity of the gas bubble is derived in a infinite domain with constant temperature gradient fields, and can be given in the form

$$V_{YGB} = \frac{2U}{(2+\tilde{k})(2+3\tilde{\mu})}, \tag{5.235}$$

where $U = -\sigma_T G_T R/\mu_B$ is chosen as the velocity scale, R is the radius of the drop and G_T stands for the constant temperature gradient, $\tilde{k} = k_A/k_B$ is the thermal conductivity ratio and $\tilde{\mu} = \mu_A/\mu_B$ is the viscosity ratio between the two fluids. In our simulation, we consider a 2D domain Ω of size $[0, 7.5R] \times [0, 15R]$ where a planar 2D circular drop of fluid A with radius $R = 0.1$ is placed inside the medium of fluid B, with the drop's centre located at the center of the box $(x_c, y_c) = (3.75R, 7.5R)$. We set the initial condition for the phase-field as

$$c(x,y) = \frac{1}{2}\tanh\left(\frac{R - \left[(x-x_c)^2 + (y-y_c)^2\right]^{\frac{1}{2}}}{2\sqrt{2}\varepsilon}\right) + \frac{1}{2}, \tag{5.236}$$

where $\varepsilon = 0.001 \times 15R$ stands for the thickness of the diffuse interface. In figure 5.6 we present the initial condition (5.236) for the whole domain (left hand side), and for fixed $x = 3.75R$ (right hand side), where it can be observed that the area with $c = 1$ represents the drop (fluid A) and the area with $c = 0$ represents the medium (fluid B), between which the value of c varies rapidly resulting in a diffuse interface with finite thickness. Within this transition layer, the dotted contour line is at level $c = 0.5$ that represents the dividing surface Γ. No-slip boundary conditions are imposed on the top and bottom wall, and periodic boundary conditions are imposed in the horizontal direction. A linear temperature field is imposed in the y direction

$$T(x,y) = T_b + \frac{T_t - T_b}{15R} y = T_b + G_T y, \tag{5.237}$$

with $T_b = 10$ on the bottom wall and $T_t = 25$ on the top wall, resulting in a constant temperature gradient, $G_T = 10$. Again, we let the ratio parameter $\eta = 6\sqrt{2}$ (Eq.(5.198)). Moreover, the fluid properties are shown as the following:

$$\mu_A = \mu_B = 0.2, \quad k_B = 0.2, \quad \sigma_0 = 2.5 \times 10^{-1},$$
$$\tilde{k} = k_A/k_B \text{ (thermal conductivity ratio)}, \quad \sigma_T = -5 \times 10^{-3} \text{ (at } T_{ref} = T_c),$$

Using these values, the theoretical terminal velocity of a spherical drop can be given as

$$V_{YGB} = 8.333 \times 10^{-4}. \tag{5.238}$$

Numerically, we use the following equation to calculate the rise velocity v_r of the drop for our phase-field model,

$$v_r = \frac{\int_\Omega c\mathbf{u} \cdot \hat{\mathbf{j}} \, \mathrm{d}V}{\int_\Omega c \, \mathrm{d}V}, \tag{5.239}$$

where $\hat{\mathbf{j}}$ is the component of the unit vector in y direction.

Figure 5.7 shows the temporal evolution of the drop velocity normalized by V_{YGB} between two different interface methods, phase-field method and level set method ([62]). Similar to the last example, we compute our model by using two different interfacial thickness corresponding to $\varepsilon = 0.002$ and 0.001. Both the level set method and phase-field method seem to converge to a value of $v_r/V_{YGB} = 0.8$, roughly 20% different from the theoretical prediction. The reason for this discrepancy is two-fold. For one, and most importantly, the theoretical rise velocity is for an axisymmetric sphere, whereas our simulations are carried out for a planar 2D drop. The second reason is that the simulations include small blockage effects from the finite computational domain size as well as minute deformations of the drop, whereas the theoretical formula assumes an infinite domain and a non-deformable drop. As the thickness of the diffuse interface decreases, our results seem to coverage to the that obtained by level-set method ([62]). For the case $\varepsilon = 0.01$, we present the streamlines together with the moving interface at $t = 1$ and $t = 50$ in figure 5.10, where we observe that the streamlines for both cases exhibit the similar patterns, with two asymmetric recirculations around the drop. Figure 5.10 shows the meshes together with the drop interface at $t = 1$ and $t = 50$. Here the size of the smaller frame is set to be $[3R \times 3R]$, in which we take the shortest edge of the grids inside the frame as $15R/1000 = \varepsilon$, so that at least 7-9 grid cell (corresponding to the definition of the interfacial thickness) is located across the interface to ensure accuracy of our computations. In addition, the moving velocity of the frame is set to be equal to the drop rising velocity $v_{frame} = v_r$, such that, through this relative long-term behavior, the rising drop is always kept inside the smaller moving frame.

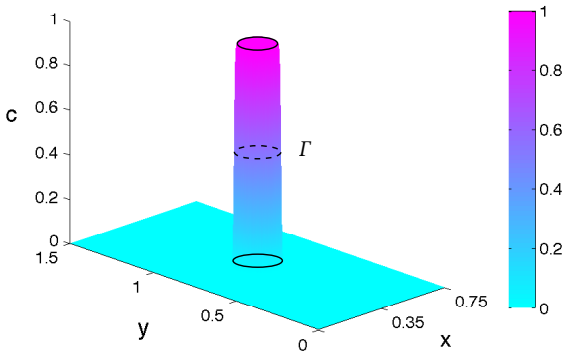

Figure 5.6: Initial condition of the phase variable c for the example of the thermocapillary migration of a drop. The dotted line stands for the dividing surface.

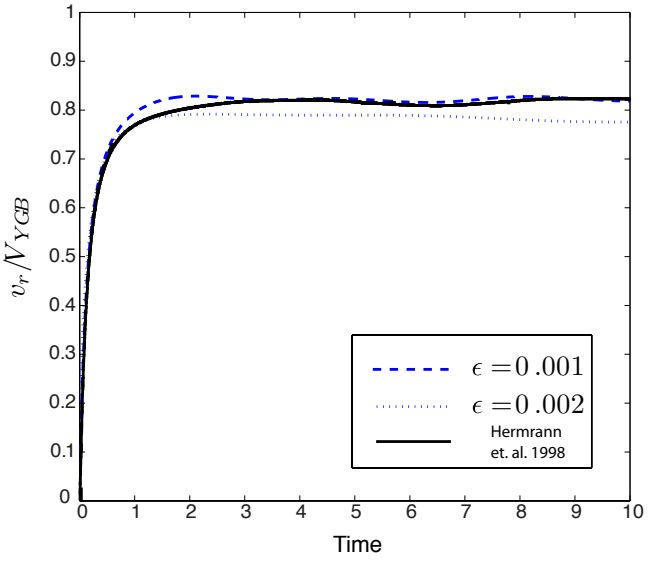

Figure 5.7: The time evolution of the normalized migration velocity of a drop. The dashed line represents the theoretical prediction for a 3D drop (V_{YGB}), while the solid line is our numerical results for a 2D planar drop (v_r).

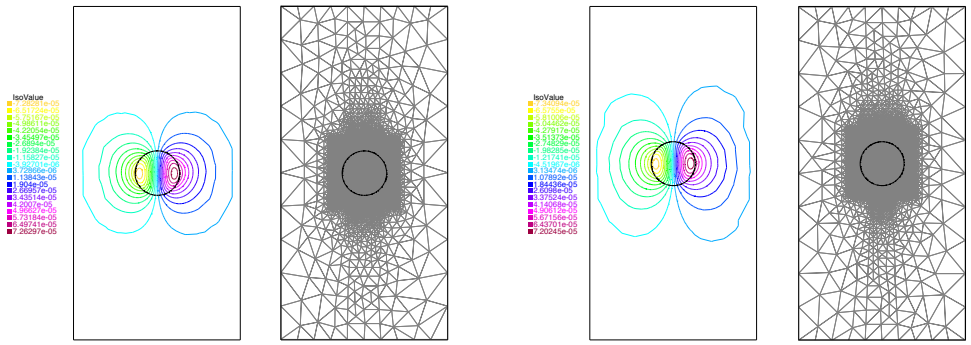

Figure 5.8: The drop interface (black) and the streamlines (colored lines, left), and the meshes (gray lines, right) at $t = 1$ and $t = 50$. Positive values of the stream-function indicate the clockwise circulation and negative values of the stream-function indicate the counterclockwise circulation.

5.7.5 Thermocapillary migration with finite Marangoni number

We now compute the example of the thermocapillary motion of a drop with finite Marangoni numbers. Due to the finite Marangoni numbers, the energy equation is coupled with the Navier-Stokes equations. This is expected to result in a reduction of the tangential temperature gradients at the drop interface due to the interfacial flow driven by the Marangoni stress, which in turn will also be reduced. In this simulation, we consider a 2D domain Ω of size $[0, 10R] \times [0, 15R]$, where a planar 2D circular drop of fluid A with radius $R = 0.5$ is placed inside the medium of fluid B, with the drop's centre located at the centre of the box $(x_c, y_c) = (0, 1.5R)$. At $t = 0$, Eq.(5.236) is employed as the initial condition for phase variable, and a linear temperature distribution from $T_b = 0$ at the bottom to $T_t = 1$ at the top is imposed for the bulk liquid, and we assume that the drop has the same initial linear temperature distribution as the bulk liquid. Again, no slip boundary conditions are imposed on the top and bottom boundaries, and periodic boundary conditions are imposed in the horizontal direction. The two fluids are assumed to have the same densities and viscosities. We set the thermal conductivity $k_1 = 0.1$ for the drop and $k_2 = 1$ for the bulk fluid. Moreover, we set the non-dimensional parameters as $\varepsilon = 0.002$, $Re = 10$, $M = 1$, $Pe = 100/\varepsilon$, $Ca = 1$,

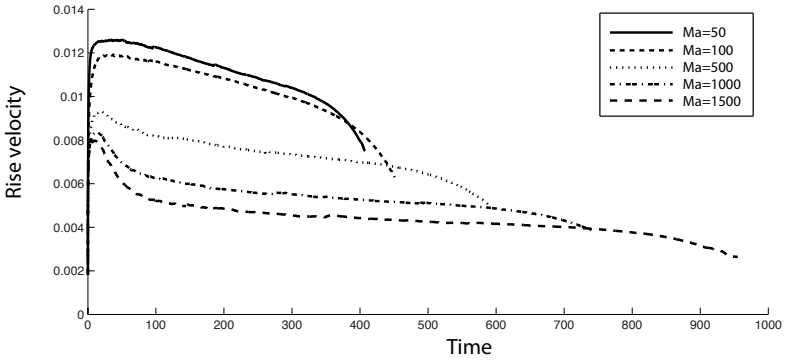

Figure 5.9: The time evolution of rise velocity of a drop with different finite Marangoni number.

$Ec = 1$. Five different values of Marangoni number are employed for the computations, such that $Ma = 50, 100, 500, 1000, 1500$.

Figure 9 shows the velocity of the drop versus time for the five cases. As the time progresses, the rise velocity reduces in all five cases, where we can observe that the increase in Ma leads to the decrease in the rise velocity, which is consistent with the simulations in [62, 128, 135].

Figure 10 shows snapshots of the isotherms at 4 different times for the corresponding three cases, where the dependence of the migration velocity on the Marangoni number can easily be explained. Obviously, the enhanced convective transport of momentum and heat with the increase of the Marangoni number results in more disturbances of the temperature field. Inside the drop, as we increase the Marangoni number, the larger variations can be observed, leading to a substantial reduction in the surface temperature gradient and the corresponding rise velocities.

5.8 Discussion

In this chapter, we present a thermodynamically consistent phase-field model for two-phase flows with thermocapillary effects, which allows the binary incompressible fluid

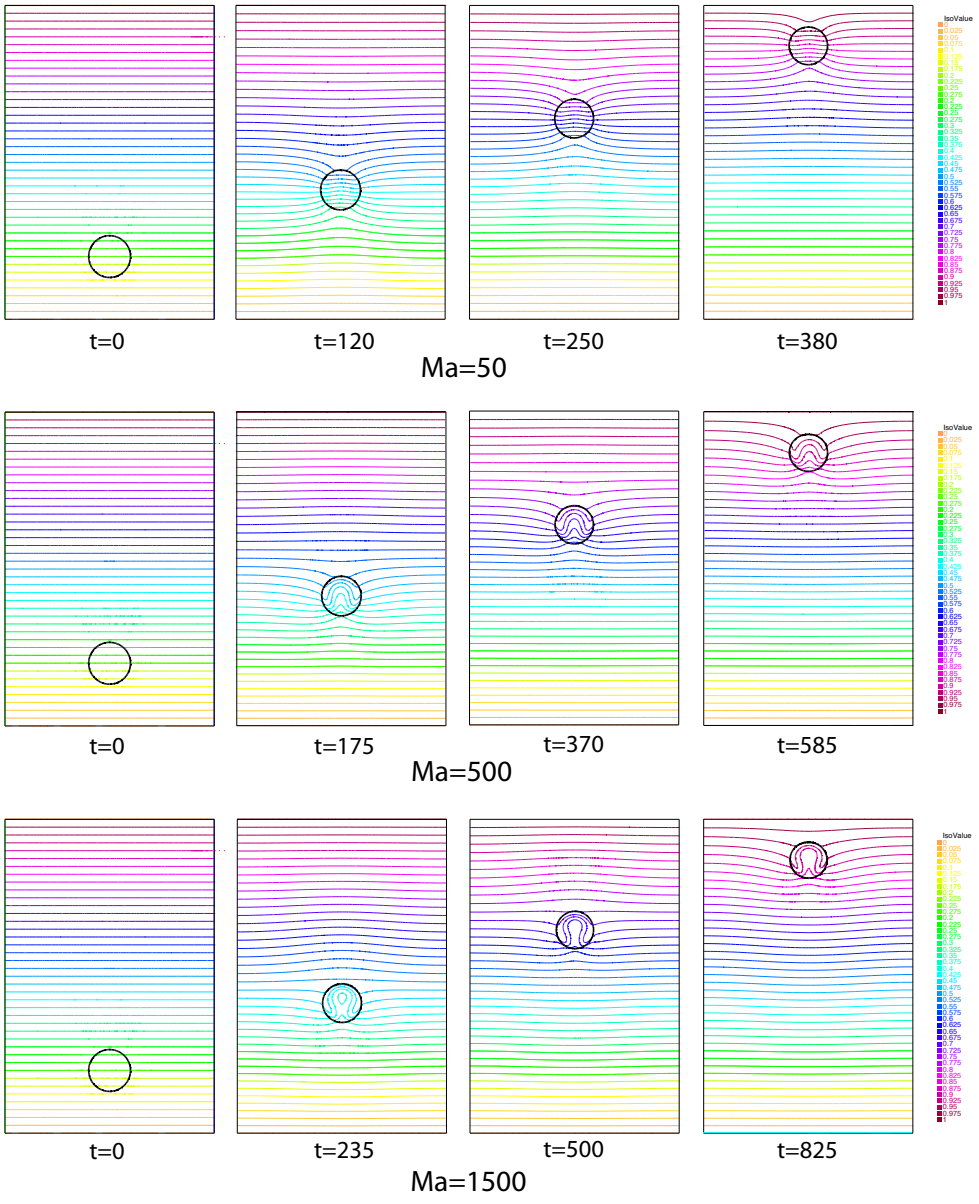

Figure 5.10: The snapshots of drop interface (black) and isotherms (colored lines) for different time and different Ma as indicated.

(quasi-incompressible fluid) to have different physical properties for each component, including densities, viscosities and thermal conductivities. To the best of our knowledge, such a phase-field model is new. We chose the mass concentration as the phase variable, where the corresponding variable density and mass-averaged velocity lead to a quasi-incompressible formulation for the binary incompressible fluid. As the thermocapillary effects are produced by the non-homogenous distribution of a temperature dependent (linearly) surface tension, we introduce the square-gradient (Cahn-Hilliard) term into the internal energy and entropy of our phase-field model, so that the interfacial free energy that is associated with the surface tension in our model, can be linearly dependent on the temperature. Our model equations, including mass balance equation, Navier-Stokes equation with extra stress term, advective Cahn-Hilliard equation, energy balance equation and entropy balance equation, are derived within a thermodynamic frame based on entropy generation. Comparing with the classical energy balance equation employed by other phase-field models, the non-classical terms associated with the square-gradient term appear in our energy balance equation (5.116) accounting for the energy spent by the variations of the phase-field. In addition, we verify the first and second thermodynamic laws from the system of equations to show that thermodynamic consistency is maintained in our model.

In the sharp-interface analysis, we show that the system of equations and jump conditions at the interface for the classical sharp-interface model are recovered from our model, which reveals the underlying physical mechanisms of the phase-field model, and provides a validation of our model. It is worth mentioning that, in the jump condition of the momentum balance, we identify the square-gradient term of the free energy as the surface tension (Eq.(5.162)) of our phase-field model. We further relate it to the physical surface tension through a ratio parameter, where a relation (Eq.(5.194)) is provided to determine the value of this parameter.

We also compute two examples, including thermocapillary convection in a two-layer

fluid system and thermocapillary migration of a drop. The results for both examples are in good agreement with the existing analytical solutions, which validates our phase-field model. Thus, on the whole, we conclude that the phase-field model can be very suitable for simulating multiphase flows with thermocapillary effects.

In the future work, besides exploring various applications and extension of the model, we aim to provide an asymptotic analysis of the solution of the model, and use it as a further validation of our model. We also plan to design a numerical method with respect to thermodynamic consistency at the discrete level. Thermodynamic consistency is critical not only to the phase-field modelling, but also to the numerical method designing. In our previous work [54], the quasi-incompressible NSCH model [87] was investigated. The numerical method that preserves the thermodynamic law (energy law) at the discrete level is presented to show that it captures the pinch off and the feature of quasi-incompressibility of the system, namely, the numerical results reveal that away from interfaces the fluid is incompressible, while near interfaces waves of expansion and contraction are observed. For the phase-field model developed here, we will present a thermodynamic consistency preserving numerical method with the corresponding numerical results in a forthcoming work [52].

Chapter 6

Conclusion and future work

6.1 Conclusion

In this thesis, we have used the phase-field method to study the two-phase flow with the variable density and thermocapillary effects. On the whole, we conclude that the phase-field model can be very suitable for simulating two-phase flows with variable density and thermocapillary effects. Moreover, we show that thermodynamic consistency is a critical feature for the phase-field modelling and also for the designing of numerical methods.

In the case of variable density flows, we show that the energy preserving numerical method can be robust when handling the highly nonlinear and coupled phase-field model equations. Through the numerical examples (kissing drop and rising drop), we show that the coalescence and pinch-off of the interface are captured smoothly using our numerical method, and the discrete energy functional of the system is non-increasing, as predicted by our numerical method. Moreover, in the NSCH model, the velocity is not solenoidal near interfaces because fluids of different densities may mix; our simulations capture this feature. Namely, the numerical results reveal that away

from interfaces the fluid is incompressible, while near interfaces waves of expansion and contraction are observed. Increasing the density ratio results in narrower waves with larger magnitudes.

In the case of thermocapillary effects, we show that, for two-phase flows, the temperature dependence of the surface tension can be coupled easily to the model equations, and can be implemented easily by using the phase-field method. We also show that the thermodynamic framework can be a strong tool for phase-field modelling, where the model equations can be identified by ensuring the non-negativity of the entropy generation, and the model equations satisfy the law of thermodynamics automatically. In the sharp-interface analysis, we show that the system of equations and jump conditions at the interface for the classical sharp-interface model are recovered from our model, which reveals the underlying physical mechanisms of the phase-field model, and provides a validation of our model. It is worth mentioning that, in the jump condition of the momentum balance, we identify the square-gradient term of the free energy as the surface tension of our phase-field model, and we relate it to the physical surface tension through a ratio parameter, where a relation (Eq.(5.194)) is provided to determine the value of this parameter. We also compute two examples, including thermocapillary convection in a two-layer fluid system and thermocapillary migration of a drop. The results for both examples are in good agreement with the existing analytical solutions, which validates our phase-field model.

Together with the energy law preserving numerical method, we show that the adaptive mesh is also very desirable for the computations of the phase-field methods. In chapter 4 and 5, the numerical examples are all computed with the help of the adaptive mesh. For the phase-field model, we show that it is sufficient to finely resolve only the interfacial region, and the relative coarser grids are sufficient for the bulk regions.

6.2 Future work

In future work, we will perform extensive studies of the two-phase problems with more complicated interface dynamics, e.g., the moving contact line problems, where the fluid-fluid interface interacts with solid wall, and the dynamics of interface with Marangoni effects, where surface tension gradients are induced by inhomogeneous distributions of surfactants, which can be absorbed at the liquid/gas or liquid/liquid interfaces. For the model developed in chapter 5, we plan to design a thermodynamically consistent numerical method for the full model, where the energy law of the phase-field model can be preserved at the discrete level. The quasi-incompressibility together with the thermocapillary effects will be studied by using our numerical methods.

Bibliography

[1] H. Abels, H. Garcke, and G. Grun. Thermodyanimcally consistent diffuse interface models for incompressible two-phase flows with different densities. *arXiv:1011.0528*, 2010.

[2] H. Abels, H. Garcke, and G. Grün. Thermodynamically consistent, frame invariant, diffuse interface models for incompressible two-phase flows with different densities. *Mathematical Models and Methods in Applied Sciences*, 22(3):1150013, 2012.

[3] R. A. Adams. *Sobolev Spaces*. Academic Press, New York, 1975.

[4] S. Aland. *Modelling of two-phase flow with surface active particles*. PhD thesis, TU Dresden, 2012.

[5] S. Aland and A. Voigt. Benchmark computations of diffuse interface models for two-dimensional bubble dynamics. *Int. J. Numer. Meth. Fluids*, 69:747–761, 2012.

[6] C. D. Andereck, P. W. Colovas, M. M. Degen, and Y. Y. Renardy. Instabilities in two layer *R*ayleigh-*B*enard convection: Overview and outlook. *Int. J. Eng. Sci.*, 1451(36), 1998.

[7] D. M. Anderson and G. B. McFadden. A diffuse-interface description of fluid systems. *NIST IR 5887 (National Institute of Standards and Technology)*, 1996.

[8] D. M. Anderson, G. B. McFadden, and A. A. Wheeler. Diffuse-inteface methods in fluid mechanics. *Annual Review of Fluid Mechanics*, 30:139–165, 1998.

[9] D. M. Anderson, G. B. McFadden, and A. A. Wheeler. A phase-field model of solidification with convection. *Physica D*, 135:175–194, 2000.

[10] D. M. Anderson, G. B. McFadden, and A. A. Wheeler. A phase-field model with convection: sharp-interface asymptotics. *Phys. D*, 151:305–331, 2001.

[11] D. Andrea. Equations for two-phase flows: a primer. *arXiv:1101.5732v1 [physics.flu-dyn]*, 2011.

[12] L. K. Antanovskii. A phase field model of capillarity. *Phys. Fluids*, 7:747–753, 1995.

[13] R. J. Atkin and R. E. Crane. Continuum theories of mixtures: basic theory and historical development. *Q. J. Mech. Appl. Math.*, 29:209–244, 1976.

[14] H. B*é*nard. Les tourbillons cellulaires dans une nappe liquide. premiere partie: description. *Rev. Gen. Sci. Pure Appl.*, 11:1261–1271, 1900.

[15] V. Baldalassi, H. Ceniceros, and S. Banerjee. Computation of multiphase systems with phase field models. *J. Comput. Phys.*, 190:371–397, 2004.

[16] K. Bao, Y. Shi, S. Sun, and X.-P. Wang. A finite element method for the numerical solution of the coupled *C*ahn-*H*illiard and *N*avier-*S*tokes system for moving contact line problems. *J. Comput. Phys.*, 231:8083–8099, 2012.

[17] G. K. Batchelor. *An introduction to fluid dynamics*. Cambridge University Press, 2000.

[18] G. Beckett, J. A. Mackenzie, and M. L. Robertson. An r-adaptive finite element method for the solution of the two-dimensional phase-field equations. *Comm. Comput. Phys.*, 1:805–826, 2006.

[19] A. Bedford and D. S. Drumheller. Theories of immiscible and structured mixtures. *Int. J. Eng. Sci.*, pages 863–960, 1983.

[20] V. Berejnov, O. M. Lavrenteva, and A. Nir. Interaction of two deformable viscous drops under external temperature gradient. *J. Colloid. Interface Sci.*, 242:202–213, 2001.

[21] A. N. Beris and B. J. Edwards. *Thermodynamics of Flowing Systems: with Internal Microstructure*. Oxford University Press, 1994.

[22] M. J. Block. Surface tension as the cause of *B*enard cells and surface deformation in a liquid film. *Nature*, 178:650–651, 1956.

[23] M. G. Blyth and C. Pozrikidis. Effect of inertia on the *M*arangoni instability of two-layer channel flow, part ii: normal-mode analysis. *J. Eng. Math.*, 50:329–341, 2004.

[24] R. Borcia and M. Bestehorn. Phase-field for marangoni convection in liquid-gas systems with a deformable interface. *Phys. Rev. E*, 67(066307), 2003.

[25] R. Borcia, D. Merkt, and M. Bestehorn. A phase-field description of surface-tension-driven instability. *Int. J. Bifurcat. Chaos*, 14(12):4105–4116, 2004.

[26] F. Boyer. A theoretical and numerical model for the study of incompressible mixture flows. *Computers & Fluids*, 31:41–68, 2002.

[27] J. W. Cahn and S. M. Allen. A microscopic theory for domain wall motion and its experimental verication in fe-al alloy domain growth kinetics. *J. Phys.*, Colloque C:7–51, 1978.

[28] J. W. Cahn and J. E. Hillard. Free energy of a nonuniform system. I. interfacial free energy. *J. Chem. Phys.*, 28:258–267, 1958.

[29] R. Chella and J. Vinals. Mixing of a two-phase fluid by cavity flow. *Phys. Rev. E*, 53:3832–3840, 1996.

[30] F. Chen and J. Shen. Efficient energy stable schemes with spectral discretization in space for anisotropic *C*ahn-*H*illiard systems. *Commun. Comput. Phys.*, 13:1189–1208, 2013.

[31] Z. Chen, R. H. Nochetto, and A. Schmidt. Error control and adaptivity for a phase relaxation model. *M2AN Math. Model. Numer. Anal.*, 34(4):775–797, 2000.

[32] C. Collins, J. Shen, and S. M. Wise. An efficient, energy stable scheme for the *C*ahn-*H*illiard-brinkman system. *Commun. Comput. Phys., 13 (2013), pp. 929-957.*, 13:929–957, 2013.

[33] A. A. Darhuber and S. M. Troian. Principles of microfluidic actuation by modulation of surface stresses. *Annu. Rev. Fluid Mech.*, 2005.

[34] S. H. Davis. Thermocapillary instabilities. *Annu. Rev. Fluid Mech.*, 19:403, 1987.

[35] H. Ding, P. D. M. Spelt, and C. Shu. Diffuse interface model for incompressible two-phase flows with large density ratios. *J. Comput. Phys.*, 226:2078 – 2095, 2007.

[36] S. Dong and J. Shen. A time-stepping scheme involving constant coefficient matrices for phase-field simulations of two-phase incompressible flows with large density ratios. *J. Comput. Phys.*, 231:5788–5804, 2012.

[37] Q. Du and J. Zhang. Adaptive finite element method for a phase field bending elasticity model of vesicle membrane deformations. *SIAM J. Sci. Comput.*, 30(3):1634–1657, 2008.

[38] C. Eck, M. Fontelos, G. Grun, F. Klingbeil, and O. Vantzos. On a phase-field model for electrowetting. *Interfaces Free Bound.*, 11(2):259–290, 2009.

[39] H. Emmerich. *The Diffuse Interface Approach in Materials Science: Thermodynamic Concepts and Applications of Phase-Field Models*. Lecture Notes in Physics Monographs. Springer, 2003.

[40] H. Emmerich. Advances of and by phase-field modeling in condensed-matter physics. *Adv. Phys.*, 57:1–87, 2008.

[41] D. H. Everett. Definitions terminology and symbols in colloid and surface chemistry. *Pure Appl. Chem.*, 31:577, 1972.

[42] X. Feng. Fully discrete finite element approximations of the *N*avier-*S*tokes-*C*ahn-*H*illiard diffuse interface model for two-phase fluid flows. *SIAM J. Numer. Anal.*, 44:1049–1072, 2006.

[43] X. Feng, T. Tang, and J. Yang. Long time numerical simulations for phase-field problems using p-adaptive spectral deferred correction methods. *http://www.math.hkbu.edu.hk/ ttang/Papers/SDC-submit.pdf*, 2014.

[44] T. Gambaryan-Roisman, A. Alexeev, and P. Stephan. Effect of the microscale wall topography on the thermocapillary convection within a heated liquid film. *Exp. Therm Fluid Sci.*, 29:765–772, 2005.

[45] M. Gao and X. Wang. A gradient stable scheme for a phase field model for the moving contact line problem. *J. Comput. Phys.*, 231:1372–1386, 2012.

[46] J. W. Gibbs. On the equilibrium of heterogeneous substances. *Trans. Connect. Acad.*, 111, 1875.

[47] J. W. Gibbs. *The Collected Works of J. W. Gibbs*. Longmans and Green, 1928.

[48] J. Giesselmann and T. Pryer. Energy consistent discontinuous galerkin methods for a quasi-incompressible diffuse two phase flow model. *http://archiv.org/abs/1307.8248*, 2013.

[49] V. L. Ginzburg and L. D. Landau. Theory of superconductivity. *Zh. Eksp. Teor. Fiz.*, 20:1064–1082, 1950.

[50] F. A. Graybill. *Matrices with Applications in Statistics*. Wadsworth International Group, Belmont, California, 2nd edition, 1983.

[51] S. R. De Groot and P. Mazur. *Non-Equilibrium Thermodynamics*. Dover Books on Physics, 1985.

[52] Z. Guo and P. Lin. A thermodynamic consistency preserving numerical method for a phase-field model with thermocapillary effects. *In preparation.*, 2014.

[53] Z. Guo and P. Lin. A thermodynamically consistent phase-field model for two-phase flows with thermocapillary effects. *Under revision of J. Fluid Mech.*, 2014.

[54] Z. Guo, P. Lin, and J. Lowengrub. A numerical method for the quasi-incompressible *C*ahn-*H*illiard-*N*avier-*S*tokes equations for variable density flows with a discrete energy law. *J. Comput. Phys. in press.*, 2014.

[55] Z. Guo, P. Lin, and Y. Wang. Continuous finite element schemes for a phase field model in two-layer fluid *B*enard-*M*arangoni convection computations. *Computer Phys. Comm.*, 185:63–78, 2014.

[56] M. E. Gurtin, D. Poligone, and J. Vinale. Two-phase fluids and immiscible fluids described by an order parameter. *Mathematical Models and Methods in Applied Sciences*, 6:815–831, 1996.

[57] M. E. Guttin. *An Introduction to Continuum Mechanics (Mathematics in Science and Engineering)*. Academic Press, 1981.

[58] H. Haj-Hariri, Q. Shi, and A. Borhan. Thermocapillary motion of deformable drops at finite reynolds and marangoni numbers. *Phys. Fluids*, 9:845–855, 1997.

[59] Q. He, R. Glowinski, and X. Ping. A least-squares/finite element method for the numerical solution of the *N*avier-*S*tokes-*C*ahn-*H*illiard system modeling the motion of the contact line. *J. Comput. Phys.*, 230:4991–5009, 2011.

[60] F. Hecht. The mesh adapting software: bamg. *INRIA report*, 1998.

[61] F. Hecht, O. Pironneau, A. Le Hyaric, and K. Ohtsuka. Freefem++ (version 2.17-1), 2007 (http://www.freefem.org/++/ftp/freefem++doc.pdf).

[62] M. Herrmann, J. M. Lopez, P. Brady, and M. Raessi. Thermocapillary motion of deformable drops and bubbles. *Center for Turbulence Research, Proceedings of the Summer program*, pages 155–170, 2008.

[63] P. C. Hohenberg and B. I. Halperin. Theory of dynamic critical phenomena. *Rev. Mod. Phys.*, 49:435–479, 1977.

[64] T. Y. Hou, J. S. Lowengrub, and M. J. Shelley. Boundary integral methods for multicomponent fluids and multiphase materials. *J. Comput. Phys.*, 169:302–362, 2001.

[65] J. Hua, P. Lin, C. Liu, and Q. Wang. Energy law preserving C^0 finite element schemes for phase field models in two-phase flow computations. *J. Comput. Phys.*, 230:7115–7131, 2011.

[66] J. S. Hua, P. Lin, and J. F. Stene. Numerical simulation of gas bubbles rising in viscous liquids at high *R*eynolds number, moving interface problems and applications in fluid dynamics. *Contemporary Mathematics*, 466:17–34, 2008.

[67] J. S. Hua, J. F. Stene, and P. Lin. Numerical simulation of 3d bubbles rising in viscous liquids using a front tracking method. *J. Comput. Phys.*, 227(6):3358–3382, 2008.

[68] D. Jacqmin. Calculation of two-phase Navier-Stokes flows using phase-field modeling. *J. Comput. Phys.*, 155:96–127, 1999.

[69] D. Jacqmin. Contact-line dynamics of a diffuse fluid interface. *J. Fluid Mech.*, 402:57–88, 2000.

[70] D. Jasnow and J. Vinals. Coarse-grained description of thermo-capillary flow. *Phys. Fluids*, 8:660–669, 1996.

[71] Y. Jiang and P. Lin. Numerical simulation for moving contact line with continuous finite element schemes. *In preparation*, 2014.

[72] D. Johnson and R. Narayanan. A tutorial on the Rayleigh-Marangoni-Bénard problem with multiple layers and side-wall effects. *Chaos*, 124(9), 1999.

[73] A. Juel, J. M. Burgess, W. D. McCormick, J. B. Swift, and H. L. Swinney. Surface tension-driven convection patterns in two liquid layers. *Physica D*, 169(143), 2000.

[74] J. Kim. A continuous surface tension force formulation for diffuse-interface models. *J. Comput. Phys.*, 204:784–804, 2005.

[75] J. Kim. Phase-field models for multi-component fluid flows. *Commun. Comput. Phys.*, 12(3):613–661, 2012.

[76] J. Kim, K. Kang, and J. Lowengrub. Conservative multigrid methods for *C*ahn-*H*illiard fluids. *J. Comput. Phys.*, 193:511–543, 2004.

[77] J. Kim and J. Lowengrub. Phase field modelling and simulation of three-phase flows. *Interface and Free Boundary*, 7:435–466, 2005.

[78] H. G. Lee, J. S. Lowengrub, and J. Goodman. Modeling pinchoff and reconnection in a *H*ele-*S*haw cell. i. the models and their calibration. *Phys. Fluids*, 14(2):492, 2002.

[79] H. Y. Lee, J. Lowengrub, and J. Goodman. Modeling pinchoff and reconnection in a *H*ele-*S*haw cell. ii. analysis and simulation in the nonlinear regime. *Phys. Fluids*, 14(2):514, 2002.

[80] V. G. Levich. *Physicochemical hydrodynamics*. Englewood Cliffs, N. J., Prentice-Hall, 1962.

[81] F. H. Lin and C. Liu. Static and dynamic theories of liquid crystals. *J. Partial Diff. Eqns.*, 14:289–330, 2001.

[82] P. Lin. A sequential regularization method for time-dependent incompressible Navier-Stokes equations. *SIAM J. Numer. Anal.*, 34:1051–1071, 1997.

[83] P. Lin and C. Liu. Simulation of singularity dynamics in liquid crystal flows: a C^0 finite element approach. *J. Comput. Phys.*, 215(1):348–362, 2006.

[84] P. Lin, C. Liu, and H. Zhang. An energy law preserving C^0 finite element scheme for simulating the kinematic effects in liquid crystal flow dynamics. *J. Comput. Phys.*, 227(2):1411–1427, 2007.

[85] C. Liu and J. Shen. A phase field model for the mixture of two incompressible fluids and its approximation by a Fourier-Spectral method. *Physica D*, 179:211–228, 2002.

[86] H. Liu, A. J. Valocchi, Y. Zhang, and Q. Kang. Lattice *B*oltzmann phase-field modeling of thermocapillary flows in a confined microchannel. *J. Comput. Phys.*, 256:334–356, 2014.

[87] J. Lowengrub and L. Truskinovsky. Quasi-incompressible Cahn-Hilliard fluids and topological transitions. *Proc. R. Soc. Lond. A*, 454:2617–2654, 1998.

[88] C. Ma and D. Bothe. Numerical modeling of thermocapillary two-phase flows with evaporation using a two-scalar approach for heat transfer. *J. Comput. Phys.*, 233:552–573, 2013.

[89] J.A. Mackenzie and M.L. Robertson. A moving mesh method for the solution of the one-dimensional phase-field equations. *Journal of Computational Physics*, 181(2):526–544, 2002.

[90] G. E. Mase and G. T. Mase. *Continuum Mechanics for Engineers, Second Edition*. CRC Press, 1999.

[91] R. Mittal and G. Iaccarino. Immersed boundary methods. *Ann. Rev. Fluid Mech.*, 37:239–361, 2005.

[92] M. J. Moran, H. N. Shapiro, D. D. Boettner, and M. Bailey. *Fundamentals of Engineering Thermodynamics*. Wiley, 7 edition, 2010.

[93] S. Nas, M. Muradoglu, and G. Tryggvason. Pattern formation of drops in thermocapillary migration. *Int. J. Heat Mass Transfer*, 49:2265–2276, 2006.

[94] S. Nas and G. Tryggvason. Thermocapillary interaction of two bubbles or drops. *Int. J. Multiphase Flow*, 29:1117–1135, 2003.

[95] S. J. Osher and R. P. Fedkiw. Level set methods: An overview and some recent results. *J. Comput. Phys.*, 169:463–502, 2001.

[96] S. R. Palit. Thermodynamic Interpretation of the Eötvös constant. *Nature*, 177:1180, 1956.

[97] J. R. A. Pearson. On convection cells induced by surface tension. *J. Fluid Mech.*, 4:489–500, 1958.

[98] B. Pendse and A. Esmaeeli. An analytical solution for thermocapillary-driven convection of superimposed fluids at zero *R*eynolds and *M*arangoni numbers. *Int. J. Therm. Sci.*, 49:1147–1155, 2010.

[99] C. Pozrikidis. Effect of inertia on the marangoni instability of two-layer channel flow, part i: numerical simulations. *J. Eng. Math.*, 50:311–327, 2004.

[100] T. Qian, X. Wang, and P. Sheng. Molecular hydrodynamics of the moving contact line in two-phase immiscible flows. *Comm. Comput. Phys.*, 1(1):1–52, 2006.

[101] J. N. Reddy. *An Introduction to Continuum Mechanics*. Cambridge University Press, 2007.

[102] M. A. Rother, A. Z. Zinchenko, and R. H. Davis. A three-dimensional boundary-integral algorithm for thermocapillary motion of deformable drops. *J. Colloid Interface Sci.*, 245:356–364, 2002.

[103] J. S. Rowlinson and B. Widom. *Molecular Theorey of Capillarity*. Dover Publications, INC. Mineola, New York., 1982.

[104] R. Scardovelli and S. Zaleski. Direct numerical simulation of free surface and interfacial flows. *Ann. Rev. Fluid Mech.*, 31:567–603, 1999.

[105] M. F. Schatz and G. P. Neitzel. Experiments on thermocapillary instabilities. *Annu. Rev. Fluid Mech.*, 33:93–127, 2001.

[106] L. E. Scriven and C. V. Sternling. On cellular convection driven by surface tension gradient: effects of mean surface tension and viscousity. *J. Fluid Mech.*, 19:321–340, 1964.

[107] R. F. Sekerka. Notes on entropy production in mutlicomponent fluids. *unpublished*, 1993.

[108] J. A. Sethian and P. Smereka. Level set methods for fluid interfaces. *Annu. Rev. Fluid Mech.*, 35:341–372, 2003.

[109] J. Shen and X. Yang. An efficient moving mesh spectral method for the phase-field model of two-phase flows. *J. Comput. Phys.*, 228:2978–2992, 2009.

[110] J. Shen and X. Yang. A phase-field model and its numerical approximation for two-phase incompressible flows with different densities and viscosities. *SIAM Journal of Scientific Computing*, 33:1159 – 1179, 2010.

[111] C. V. Sternling and L. E. Scriven. Interfacial turbulence: hydrodynamic instability and the *M*arangoni effect. *AIChE J.*, 5:514–523, 1959.

[112] R. S. Subramanian and R. Balasubramaniam. *The motion of Bubbles and Drops in Reduced Gravity*. Cambridge University Press, 2001.

[113] P. Sun, C. Liu, and J. Xu. Phase field model of thermo-induced *M*arangoni effects in the mixtures and its numerical simulations with mixed finite element method. *Commun. Comput. Phys.*, 6:1095–1117, 2009.

[114] M. Sussman, P. Smereka, and S. Osher. A level set approach for computing solutions to incompressible two-phase flow. *J. Comput. Phys.*, 114:146–159, 1994.

[115] S. J. Tavener and K. A. Cliffe. Two-fluid Marangoni–Bénard convection with a deformable interface. *J. Comput. Phys.*, 182:277–300, 2002.

[116] K. E. Teigen, P. Song, J. Lowengrub, and A. Voigt. A diffuse-interface method for two-phase flows with soluble surfactants. *J. Comput. Phys.*, 230:375 – 393, 2011.

[117] R. Temam. *Navier-Stokes Equations : Theory and Numerical Analysis*. North-Holland, 1977.

[118] G. Tryggvason, B. Bunner, A. Esmaeeli, D. Juric, N. Al-Rawahi, W. Tauber, J. Han, S. Nas, and Y. J. Jan. Front tracking method for the computation of multiphase flow. *J. Comput. Phys.*, 169:708–759, 2001.

[119] G. Tryggvason, R. Scardovelli, and S. Zaleski. *Direct Numerical Simulations of Gas-Liquid Multiphase Flows*. Cambridge University Press, 2011.

[120] van der R. Sman and van der S. Graaf. Diffuse interface model of surfactant adsorption onto flat and droplet interfaces. *Rheol. Acta.*, 46:3–11, 2006.

[121] J. D. van der Waals. The thermodynamic theory of capilliary flow under the hypothesis of a continuous variation of density, english translaion. *J. Statist. Phys.*, 20:197, 1979.

[122] M. Verschueren, F. N. van de Vosse, and H. E. H. Meijer. Diffuse-interface modelling of thermo-capillary flow instabilities in a *H*ele-*S*haw cell. *J. Fluid Mech.*, 434:153–166, 2001.

[123] S. L. Wang, R. F. Sekerka, A. A. Wheeler, B. T. Murray, S. R. Coriell, R. J. Braun, and G. B. McFadden. Thermodynamically-consistent phase-field models for solidification. *Phys. D*, 69:189–200, 1993.

[124] X.-P. Wang and Y.-G. Wang. The sharp interface limit of a phase field model for moving contact line problem. *Methods Appl. Anal.*, 14(3):285–292, 2007.

[125] C. E. Weatherburn. *Differential Geometry of Three Dimensions*. Cambridge University Press, 1939.

[126] H. Wu, X. Xu, and C. Liu. On the general *E*ricksen-*L*eslie system: Parodi's relation, well-posedness and stability. *Arch. Rational. Mech. Anal.*, in press, 2012.

[127] X. F. Yang, J. J. Feng, C. Liu, and J. Shen. Numerical simulations of jet pinching-off and drop formation using an energetic variational phase-field method. *J. Comput. Phys.*, 218(1):417–428, 2006.

[128] Z. Yin, P. Gao, W. Hu, and L. Chang. Thermocapillary migration of nondeformable drops. *Phys. Fluids*, 20:082101, 2008.

[129] N. O. Young, J. S. Goldstein, and M. J. Block. The motion of bubbles in a vertical temperature gradient. *J. Fluid Mech.*, 6:350–356, 1959.

[130] P. T. Yue, J. J. Feng, C. Liu, and J. Shen. A diffuse interface method for simulating two phase flows of complex fluids. *J. Fluid Mech.*, 515:293–317, 2004.

[131] P. T. Yue, C. F. Zhou, J. J. Feng, C. F. Ollivier-Gooch, and H. H. Hu. Phase-field simulations of interfacial dynamics in viscoelastic fluids using finite elements with adaptive meshing. *J. Comput. Phys.*, 219(1):47–67, 2006.

[132] J. Zhang, S. Das, and Q. Du. A phase field model for vesicle–substrate adhesion. *J. Comput. Phys.*, 228:7837–7849, 2009.

[133] Y. Zhang, H. Wang, and T. Tang. Simulating two-phase viscoelastic flows using moving finite element methods. *Commun. Comput. Phys.*, 7(2):333–349, 2010.

[134] Z. Zhang and H. Tang. An adaptive phase field method for the mixture of two incompressible fluids. *Computers & Fluids*, 36:1307–1318, 2007.

[135] J. Zhao, Z. Li, H. Li, and J. Li. Thermocapillary migration of deformable bubbles at moderate to large *M*arangoni number in microgravity. *Microgravity Sci. Technol.*, 22:295–303, 2010.

[136] H. Zhou and R. H. Davis. Axisymmetric thermocapillary migration of two deformable viscous drops. *J. Colloid Interface Sci.*, 181:60–72, 1996.